Optical analysis of biological media
- continuous wave techniques

Jan Sørensen Dam

Department of Physics
Lund Institute of Technology

SIGILLVM VNIVERSITATIS GOTHORVM CAROLINÆ
AD VTRVMQVE
1666

Optical analysis of biological media
- continuous wave diffuse spectroscopy

Jan Sørensen Dam

Lund Reports on Atomic Physics

LRAP-265

Doctoral Thesis

Department of Physics

Lund Institute of Technology

November 2000

ISBN 91-628-4546-2

Preface

The work presented in this thesis was carried out in the framework of the Danish Industrial PhD Fellowship Programme, which is administered and financially supported by the Danish Academy of Technical Sciences. The project took place, partly at Bang & Olufsen Medicom a/s, and partly at Lund institute of Technology.

Bang & Olufsen Medicom has carried out research and development of various techniques for optical biopsy and spectroscopic analysis of biological media since 1990. The efforts have been aimed primarily at applications such as non-invasive tissue glucose monitoring, extracorporeal hemodynamic monitoring, and optical immunoassays. Likewise, the Medical Optics Group at Lund institute of Technology has, for more than a decade, performed extensive research in a wide range of techniques for optical biopsies and spectroscopic analyses of biological media.

Being a joint project between industry and academia, the objectives and the outcome of the work presented here therefore had to comply with scientific standards as well as the demands to commercial potential. Accordingly, the overall goal of this project has been to develop and improve optical methods and techniques for non- or minimal-invasive real-time medical diagnosis and monitoring of patients. In order to meet the commercial interests, the work has been specifically aimed at so-called *Home Care* and *Doctors Office* applications. Consequently, the presented methods have been based on continuous wave measurements, because such techniques in general imply relatively simple technology, which in turn enables compact, robust, and cost-effective implementation.

The introduction in Chapter 1 provides further details of the background, the objectives, and the applied methods of the project. Chapter 2 discusses the physical basis of light interacting with biological media. Next, a description of various light propagation models is given in Chapter 3. Then, the applied instrumentation and some practical aspects of carrying out bio-optical measurements are discussed in Chapter 4. Finally, various multivariate analysis techniques that have been applied to extract information from the measurements are presented in Chapter 5.

Contents

Abstract

The main topic of this thesis is real-time quantification of relevant chromophores and light scattering elements in biological media. The presented methods and instrumentation are based on continuous wave (steady-state) optical measurements of (a) spatially-resolved diffuse reflectance from bulk media and (b) combined spatially-resolved and goniometric measurements of re-emitted light from thin samples. These two configurations address applications for non-invasive medical diagnostics (optical biopsy), and *in vitro* diffuse spectroscopy of turbid samples (e.g. whole blood analysis and immunoassays), respectively.

The physical basis of light-tissue interaction, i.e. absorption and scattering, is discussed, as well as various theoretical models for light propagation in turbid biological media, e.g. Monte Carlo simulations, diffusion theory, and the adding-doubling method. The optical properties are extracted from the measurements using multivariate calibration and analysis techniques. Therefore, a general introduction to such methods is also included, e.g. principal component analysis, multiple polynomial regression, and Newton-Raphson prediction algorithms. Finally, some of the prototype instrumentation developed during the project is presented, e.g. a fiber probe system, an integrating sphere setup, and a hybrid goniometric/spatially-resolved system.

List of papers

I. J.S. Dam, P.E. Andersen, T. Dalgaard and P.E. Fabricius, Determination of tissue optical properties from diffuse reflectance profiles by multivariate calibration, *Appl. Opt.* 37, 772-778 (1998).

II. J.S. Dam, T. Dalgaard, P.E. Fabricius and S. Andersson-Engels, Multiple polynomial regression method for determination of biomedical optical properties from integrating sphere measurements, *Appl. Opt.* 39, 1202-1209 (2000).

III. J.S. Dam, C.B. Pedersen, T. Dalgaard, P. Aruna and S. Andersson-Engels, Fiber optic probe for non-invasive real-time determination of tissue optical properties at multiple wavelengths, *Appl. Opt.* (Accepted, Oct. 2000).

IV. T.H. Pham, F. Bevilacqua, T. Spott, J.S. Dam, B.J. Tromberg and S. Andersson-Engels, Quantifying the absorption and reduced scattering coefficients of tissue-like turbid media over a broad spectral range using a non-contact Fourier interferometric, hyperspectral imaging system, *Appl. Opt.* (In press, vol. **39** 2000).

V. J.S. Dam, C.B. Pedersen, T. Dalgaard, P.E. Fabricius and S. Andersson-Engels, Monte Carlo study on optical characterization of thin turbid samples using angular and spatially- resolved measurements. (Manuscript for Appl. Opt.).

VI. P.E. Andersen, J.S. Dam, P.M. Petersen and P. Bjerring, Local diffuse reflectance from three-layered skin tissue structures, "*Optical Tomography and Spectroscopy of Tissue: Theory, Instrumentation, Model, and Human Studies II*", SPIE Proc. 2979, 515-526 (1997).

VII. J. Swartling, C. Klinteberg, J.S. Dam, T. Johansson, J. Roth, and S. Andersson-Engels. Comparison of spatially and temporally resolved diffuse reflectance measurement systems for determination of biomedical optical properties at 785 nm, (Manuscript in preparation)

Additional material is presented in:

- J.S. Dam, C.B. Pedersen, P.E. Fabricius and S. Andersson-Engels, Fiber optic system *in vivo* real-time determination of tissue optical properties from steady-state diffuse reflectance measurements, *"Photon Migration, Diffuse Spectroscopy, and Optical Coherence Tomography: Imaging and Functional Assessment",* SPIE Proc. 4160, (2000).
- J.S. Dam, Biomedical Optics Research at Bang & Olufsen Technology a/s, Poster, *Second regional Bio-Conference*, Medicon Valley Academy, Lund (1998).

Nomenclature

	Basic quantities		**Units**
t	Time		s
ω	Angular frequency		rad/s
r	Distance		m
$\mathbf{r}$	Position vector		m
V	Volume		m^3
A	Area		m^2
$\mathbf{n}$	Normal vector		-
$\mathbf{s}$	Direction vector		-
s	Solid angle		sr
Q	Energy		J
W	Energy density	$W = Q / V$	$\mathrm{J/m}^3$
P	Power	$P = Q / t$	J/s (=W)
	Electromagnetic terms		
$\mathbf{E}$	Electric field		V/m
$\mathbf{H}$	Magnetic field		A/m
$\mathbf{J}$	Electric current density	$\mathbf{J} = \sigma\mathbf{E}$	$\mathrm{A/m}^2$
$\mathbf{P}$	Polarization	$\mathbf{P} = \varepsilon_0\chi\mathbf{E}$	$\mathrm{As/m}^2$
$\mathbf{S}$	Poynting vector	$\mathbf{S} = \mathbf{E}\times\mathbf{H}$	$\mathrm{W/m}^2$
$\mathbf{k}$	Wave vector		rad/m
k	Wavenumber	$k = \lvert\mathbf{k}\rvert = 2\pi / \lambda$	rad/m
c	Speed of light in medium	$c = c_0 / n$	m/s
λ	Wavelength	$\lambda = 2\pi c / \omega$	m
χ	Electric susceptibility		-
σ	Electric conductivity		A/Vm
ε_r	Relative permittivity		-
n_c	Complex refractive index	$n_c = \sqrt{\varepsilon_r}$	-
n	Refractive index	$\mathrm{Re}(n_c)$	-
c_0	*In vacuo* speed of light	$c_0 = 1/\sqrt{\varepsilon_0\mu_0}$	m/s
μ_0	*In vacuo* permeability		Vs/Am
ε_0	*In vacuo* permittivity		As/Vm

Optical properties

μ_a	Absorption coefficient	$\mu_a = \rho_a C_a$	m^{-1}
μ_s	Scattering coefficient	$\mu_s = \rho_s C_s$	m^{-1}
g	anisotropy factor	$g =< \cos\theta >$	-
μ'_s	Reduced scattering coefficient	$\mu'_s = (1-g)\mu_s$	m^{-1}
θ	Scattering angle		rad
$p(\cos\theta)$	Scattering phase function		-
mfp	Mean free path	$mfp = (\mu_a + \mu_s)^{-1}$	m
C	Absorption/scattering cross-section	$C = \delta A$	m^2
ρ	Absorber/scatter volume density		m^{-3}
δ	Absorption/scattering efficiency factor		
R	Diffuse reflectance		W/m^2
T	Diffuse transmittance		W/m^2

Radiometric quantities

$\mathbf{F}$	Radiant flux	W/m^2
E	Irradiance	W/m^2
ϕ	Fluence rate	W/m^2
I	Intensity	W/sr
L	Radiance	W/m^2sr
N	Photon distribution	$m^{-3}sr^{-1}$

Multivariate data analysis notation

$\mathbf{X}$	Data matrix	-
$\mathbf{Y}$	System matrix	-
$\mathbf{K}, \mathbf{B}$	Calibration coefficient matrices	-
$\mathbf{p}$	Loading vectors	-
$\mathbf{T}$	Score matrix	-
x	Explicit (independent) variables	-
y	Implicit (dependent) variables	-
$\hat{y}$	Predicted (estimated) implicit variables	-
I	Number of samples	-
J	Number of explicit variables x	-
M	Number of implicit variables y	-

Chapter 1

Introduction

During the recent years optical techniques, especially lasers, have found increasing applications in the medical field, and a new interdisciplinary field denoted *biomedical optics* has evolved. This field covers a wide range of therapeutic and diagnostic techniques, as illustrated in Figure 1.1.

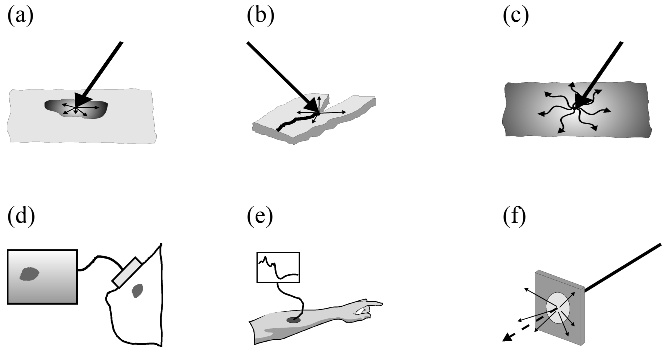

Figure 1.1. *Schematic illustrations of optical applications in medicine: (a) photodynamic therapy, (b) laser surgery, (c) thermotherapy, (d) optical tomography, (e) optical biopsy, and (f) in vitro diffuse spectroscopy.*

In general, it is common to all medical applications of optical methods that they may relieve the patients of some of the discomfort associated with the more conventional counterparts of the optical methods. For instance:

a) Photodynamic therapy (optical/chemical treatment of tumors) causes less pain and less subsequent cicatrization.

b) Laser surgery (cutting, removal, and/or welding of tissue) provides pinpoint selectivity and causes minimal bleeding.

c) Optical tomography (e.g. optical mammography) is non-ionizing as opposed to radiography.

d) Optical thermotherapy enables rapid and selective deposition of heat energy.

e) Optical biopsies (non- or minimal-invasive spectroscopic analysis of biological tissue) are performed without any cutting or removal of tissue.

f) Medical applications of *in vitro* diffuse spectroscopy (e.g. optical immunoassays) require relatively small samples and provide fast analysis.

Thus, optical methods in general exhibit a substantial potential for a wide range of medical diagnostic and therapeutic applications. However, only optical biopsies and *in vitro* diffuse spectroscopy, that is item (e) and (f) from the above list, will be considered in this context.

Optical biopsy encompasses several techniques, for example: laser-induced fluorescence spectroscopy, Raman spectroscopy, and traditional transmission- or reflectance spectroscopy in the visible (VIS), near-infrared (NIR), or the infrared (IR) wavelength region. These techniques each have a series of advantages and drawbacks; e.g. Raman spectroscopy has high specificity but low sensitivity, whereas IR spectroscopy is hampered by high water absorption and pour transmission in optical fibers. Furthermore, several of these techniques also imply complex instrumentation, which makes clinical implementation awkward. Applying so-called spatially resolved continuous wave techniques, as demonstrated in the following chapters, can circumvent many of these inconveniences.

The light propagation in turbid biological media is jointly governed by the absorption and scattering properties of the medium. In Figure 1.2 it is illustrated how a beam of light enters a bulk turbid medium and migrates in a diffuse manner due to scattering elements within the medium. In turn, the light that is not absorbed by the medium will be re-emitted back through the surface as diffuse reflectance. Consequently, diffuse reflectance measurements on skin tissue carries information on various tissue constituents such as glucose, melanin, oxyhemoglobin, bilirubin etc.

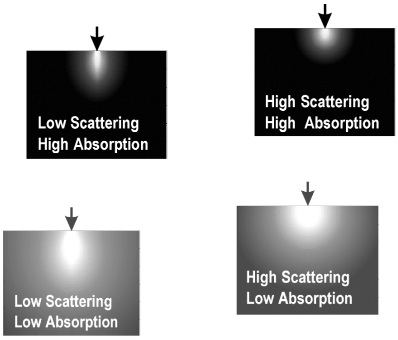

Figure 1.2. *Light propagation in a turbid media with varying absorption and scattering properties*

Since the diffuse reflectance is jointly governed by the absorption and scattering properties in an obscure manner, it is imperative to be able to determine both properties simultaneously, even if the desired information is embedded in the absorption properties exclusively. Naturally, the absorption and scattering properties also determine light propagation, and with that, the deposition of energy during therapeutic applications. In order to optimize the treatment in such applications, accurate determination of the absorption and scattering properties is therefore important in these cases as well.

In conventional *in vitro* absorption spectroscopy on turbid media, the effect of scattering is often ignored; or rather simple correction schemes are adopted. In both cases, this leads to errors in the spectroscopic analysis. Therefore, analogous to the diffuse reflectance measurements, the accuracy of such applications would also benefit from simultaneous determination of the absorption and scattering properties. Accordingly, the work presented in the following focus partly on methods for optical biopsy and patient monitoring based on spatially resolved diffuse reflectance measurements as illustrated in Figure 1.3(a), and partly on methods for diffuse *in vitro* spectroscopy on thin turbid biological samples as illustrated in Figure 1.3 (b).

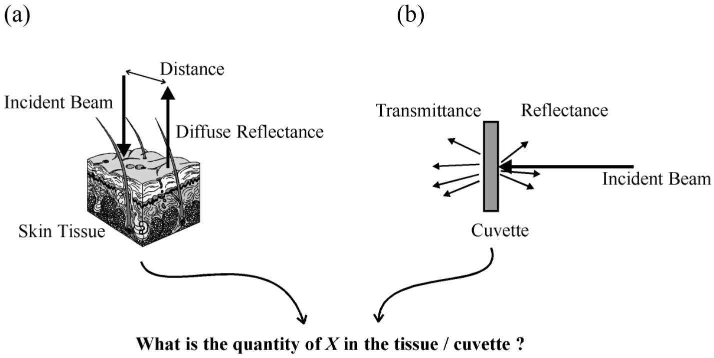

Figure 1.3. *The primary measurement configurations discussed in this thesis: (a) Diffuse reflectance measurements on bulk samples and (b) goniometric and spatially resolved measurements on thin samples*

It has been shown that the optical properties (the absorption and scattering properties) may be extracted with good accuracy using time-resolved or frequency-domain methods. However, these methods also typically imply bulky and expensive equipment, thus steady state; also called continuous wave methods are advantageous in many practical applications, because the relatively simple technology promotes design of cost-efficient and portable equipment. Consequently, all methods and techniques presented in this work are based on continuous wave measurements.

The task of extracting information on biological constituents from diffuse reflectance and transmittance measurements is a so-called inverse problem. In order to adopt a suitable inversion scheme for this problem, proper light propagation models must be employed. While the geometric configuration of the cuvette/slab setup in Figure 1.3(b) is fairly regular, and therefore can be described by relatively simple models, the morphology of the skin tissue in Figure 1.3(a) is rather complex and consequently implies complex models too. As a compromise between accuracy and simplicity, single or multi-layered models are often implemented using either Monte Carlo simulations or diffusion theory as discussed in *Paper VI.*

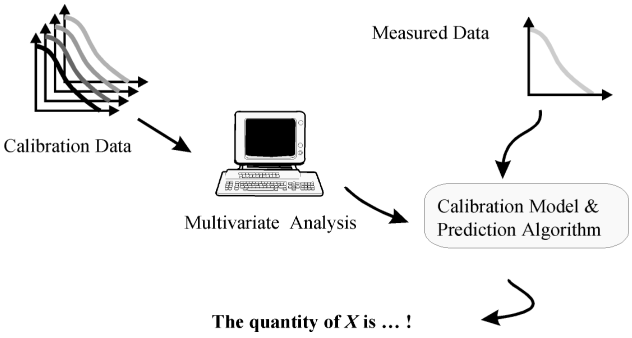

Figure 1.4. *Illustration of the inversion scheme for extracting absorption and scattering properties using multivariate calibration and analysis.*

When a suitable light propagation model has been chosen, the final step in solving the inverse problem is to associate the measured output from the setups in Figure 1.3 to the optical properties of the medium in question. If the light propagation models provide closed form analytic expressions the inversion scheme is simple. However, if the models provide numerical solutions only, such as Monte Carlo simulations, the inversion scheme has to be based on some sort of multivariate calibration and prediction algorithms as illustrated in Figure 1.4.

Integrating spheres are widely used to measure the total diffuse reflectance and transmittance from thin slabs or cuvettes in setups equivalent to Figure 1.3(b). The optical properties may then be determined from such measurements using e.g. the inverse adding-doubling method. This method may, however, prove to be to slow for real-time applications involving hyper-spectral measurements. Thus, *Paper II* presents a novel, faster and even more accurate algorithm for optical property predictions from integrating sphere measurements. The actual integrating sphere setup may also prove to be too bulky and inconvenient for clinical use. Hence, *Paper V* presents a method for extracting the optical properties from slab geometries using goniometric measurements in combination with spatially resolved measurements of the transmittance and reflectance. This hybrid method thus enables more compact and handy implementation than analogous integrating sphere setups.

In order to measure diffuse reflectance profiles as illustrated in Figure 1.3(a), and to carry out immediate extraction of the optical properties, a fiber optic probe system was also developed during the project, as described in *Paper III*. The design and geometric configuration of this probe was determined on the basis of the investigations described in *Paper I*. The probe system was calibrated and tested on a matrix of liquid phantoms with well-known optical properties, and preliminary clinical tests were also performed. The fiber probe is capable of extracting the optical properties at four arbitrary wavelengths, which is sufficient for numerous clinical diagnostic applications. But in some instances, a broader wavelength range is needed. Hence, *Paper IV* provides a presentation of hyper-spectral measurements and analysis of reflectance profiles using a Fourier spectrometer.

Chapter 2

Optical response of biological media

For more than a century it has been demonstrated that light has a dual nature. In many instances it is convenient to describe light as a particle phenomenon, i.e. as photons carrying discrete packets of energy. The particle model is well suited for treating light-matter interaction on a microscopic level, e.g. energy transitions in atoms and molecules. In other instances it is more appropriate to consider light as electromagnetic waves, especially when describing the polarization, phase, and interference properties of the light. Moreover, the wave model is also convenient for describing light-matter interactions on the macroscopic level, such as specular reflection, refraction, etc. Hence, it is possible to consider light propagation and interaction both as a particle and a wave phenomenon. It is difficult, though, to set up any rules for which approach to employ in a specific situation. In general, it is often convenient to adopt both the wave and the particle approach, either simultaneously or consecutively, to obtain the best overall picture. As it appears from the discussion in the next chapter, the task of modeling multiple scattered light by wave theory is intractable and does not yield any solutions of practical relevance. Thus, most optical modeling of light in turbid media is based on so-called transport theory, which basically builds on the photon approach. The photon migration within a turbid medium, as described by transport theory[1], is governed by a set of macroscopic optical properties: [2] the absorption coefficient μ_a, the scattering coefficient μ_s, and the anisotropy factor g (sometimes referred to as the asymmetry factor). Although transport theory basically is empirical and hence also the optical properties, they can principle be derived from electromagnetic wave theory. Therefore, this chapter will first give a review of some basic concepts of electromagnetic wave theory, and thereby provide a fundamental physical understanding of the optical properties introduced subsequently. Finally, examples and spectra of biological important chromophores (absorbing molecules) and scattering components will also be given. The definitions and concepts introduced in this chapter will thus provide a platform for the discussions of multiple scattering and the light propagation models introduced in Chapter 3.

2.1 Electromagnetic wave theory

In electromagnetic terms a bulk non-scattering medium may be approximated by a homogeneous and isotropic continuum of free charges and small dipoles[3-5] as shown in Figure 2.1.

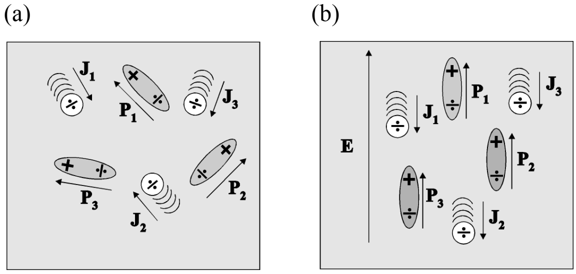

Figure 2.1. *(a) Medium with a homogeneous distribution of dipoles and free charges. (b) Same medium exposed to an electric field* **E**

When the medium in Figure 2.1(a), is exposed to the electric field **E** the directions of the free charges and the orientations of the dipoles seek to align in the direction of **E** as shown in Figure 2.1(b). The "willingness" of the dipoles to align and of the charges to move in the direction of **E** is quantified by the electric susceptibility χ and the electric conductivity σ of the specific medium, respectively. The net polarization **P** and the net electric current density **J** is then given by the so-called constitutive relations.

$$\begin{aligned} \mathbf{J} &= \sigma \mathbf{E} \\ \mathbf{P} &= \varepsilon_0 \chi \mathbf{E} \end{aligned} \tag{2.1}$$

Where ε_0 is the *in vacuo* permittivity. In Eq.(2.1), it is assumed that the electric field **E** (along with **J** and **P)** is time harmonic.

$$\mathbf{E}(t) = \mathrm{Re}\{\mathbf{E}(\omega) e^{-i\omega t}\} \tag{2.2}$$

Where, ω is the angular frequency of the harmonic fields and t is the time.

In real life, certainly not all fields are time harmonic, but fortunately it can be shown that any anharmonic field can be composed from superposition of time harmonic fields by Fourier techniques.

2.1.1 *Maxwell equations*

Any electromagnetic field and thus also electromagnetic waves must satisfy the Maxwell equations. In the time harmonic case, these may be written in complex form as[6]:

$$\begin{aligned} &\nabla \cdot (\varepsilon_r \varepsilon_0 \mathbf{E}(\mathbf{r},\omega)) = 0 \\ &\nabla \times \mathbf{E}(\mathbf{r},\omega) = i\omega\mu_0 \mathbf{H}(\mathbf{r},\omega) \\ &\nabla \cdot \mathbf{H}(\mathbf{r},\omega) = 0 \\ &\nabla \times \mathbf{H}(\mathbf{r},\omega) = -i\omega\varepsilon_r \varepsilon_0 \mathbf{E}(\mathbf{r},\omega) \end{aligned} \tag{2.3}$$

Where, $\mathbf{H}$ is the magnetic field, $\mathbf{r}$ is the position vector, ε_r is the relative complex permittivity, and μ_0 is the *in vacuo* permeability. In the above, it was implicitly assumed that the medium was non-magnetic, i.e.

$$\mathbf{B} = \mu_0 \mathbf{H} \tag{2.4}$$

Hence, the behavior of the time-harmonic electromagnetic fields, in the unbounded medium shown in Figure 2.1, is fully described by the Maxwell equations in Eq. (2.3). Where, the medium specific properties, given by the constitutive relations in Eq. (2.1), are embodied in ε_r.

$$\varepsilon_r = 1 + \chi(\omega) + i\frac{\sigma(\omega)}{\varepsilon_0 \omega} \tag{2.5}$$

2.1.2 *Electromagnetic waves*

From the Maxwell equation it can be shown that any electromagnetic wave propagation must satisfy the following wave equations.

$$\begin{aligned} &\nabla^2 \mathbf{E}(\mathbf{r},\omega) + \frac{\omega^2 n_c^2}{c_0^2} \mathbf{E}(\mathbf{r},\omega) = 0 \\ &\nabla^2 \mathbf{H}(\mathbf{r},\omega) + \frac{\omega^2 n_c^2}{c_0^2} \mathbf{H}(\mathbf{r},\omega) = 0 \end{aligned} \tag{2.6}$$

Where c_0 is the *in vacuo* speed of light, and n_c is the complex refractive index

$$n_c = n + i\kappa = \sqrt{\varepsilon_r} \tag{2.7}$$

The simplest solutions to Eq. (2.6) yield the equations of the plane harmonic wave.

$$\begin{aligned} \mathbf{E} &= \mathbf{E}_0 \, e^{i(\mathbf{k}\cdot\mathbf{r}-\omega t)} \\ \mathbf{H} &= \mathbf{H}_0 \, e^{i(\mathbf{k}\cdot\mathbf{r}-\omega t)} \end{aligned} \tag{2.8}$$

Where **k** is the wave vector indicating the direction of propagation, and $\mathbf{E}_0$ and $\mathbf{H}_0$ are constant vectors. In fact, plane waves are physically unrealizable, because they are infinite in time and space. However, they are very useful, because any finite physical wave can be constructed by superposition of harmonic plane waves with different wavelengths, directions, and polarizations.

2.1.3 The Poynting vector

In many cases involving electromagnetic waves, the main interest is the energy transport. This is quantified readily by the Poynting vector **S**.

$$\mathbf{S} = \mathbf{E} \times \mathbf{H} \tag{2.9}$$

Hence, **S** specifies the magnitude and the direction of the rate of transfer of electromagnetic energy. For time-harmonic fields, **S** oscillates with ω, it is therefore often more convenient to apply the time averaged Poynting vector.

$$\langle \mathbf{S} \rangle = \tfrac{1}{2} \mathrm{Re}\{\mathbf{E} \times \mathbf{H}^*\} \tag{2.10}$$

The magnitude of the time averaged Poynting vector is equal to the irradiance *E*, which is a widely used quantity in the framework of transport theory discussed in the next chapter.

$$E = \left| \langle \mathbf{S} \rangle \right| \tag{2.11}$$

Finally, the time-averaged Poynting vector for a plane harmonic wave is given by.

$$\left\langle \mathbf{S}_{plane} \right\rangle = \tfrac{1}{2} n c_0 \varepsilon_0 \left| \mathbf{E}_0 \right|^2 e^{-\frac{4\pi\kappa z}{\lambda_0}} \mathbf{e}_z \tag{2.12}$$

Naturally, in this case, the direction of the energy flux is the same as the direction of propagation; i.e. $\mathbf{e}_z$ is parallel to **k**.

2.2 Absorption

From Eq. (2.12) it appears that there is an exponential attenuation of the irradiance of the plane wave as a function of the distance in the propagation direction. This relation is commonly known as Beer's law

$$E(z) = E_0 \, e^{-\mu_a z} \tag{2.13}$$

Where E_0 is the irradiance at the distance $z = 0$, and μ_a is the absorption coefficient.

$$\mu_a = \frac{4\pi \kappa}{\lambda_0} \tag{2.14}$$

Thus, the absorption coefficient μ_a of a medium at a given wavelength λ is proportional to the imaginary part κ of the complex refractive index n_c. Note that the irradiance *E*, which is a scalar, should not be confused with the electric field vector **E**. Moreover, *E* is often referred to as intensity, but in this context, the intensity *I* denotes power per solid angle, as stated in Section 3.1.2.

2.2.1 Absorption coefficient, cross-section, and mean free path length

The above definition of μ_a is derived on the basis of macroscopic electromagnetic terms where the medium is assumed to be a continuum. However, from a microscopic point of view, absorption takes place in discrete elements (atoms and molecules) as illustrated in Figure 2.2. In this approach, it is convenient to define μ_a in probabilistic terms[1]. Accordingly, μ_a is defined such that when a photon travels an infinitesimal distance *dz*, the probability for absorption by a chromophore is given by $\mu_a dz$. This is analogous to defining μ_a as the reciprocal of the absorption mean free path length mfp_a

$$\mu_a = \frac{1}{mfp_a} = \frac{i}{fp_1 + fp_2 + ...fp_i} \tag{2.15}$$

Where $fp_1 ... fp_i$ are the distances (free path lengths) traveled by each photon before absorption occurs (see Figure 2.2(a)).

The volume density of absorbing elements ρ_a and μ_a are connected through the absorption cross-section[6] C_a

$$\mu_a = C_a \rho_a \tag{2.16}$$

Which in turn is defined by

$$C_a = q_a A_a \tag{2.17}$$

Where, A_a is the geometrical cross-section of the absorbing element and q_a is the absorption efficiency as shown in Figure 2.2(b).

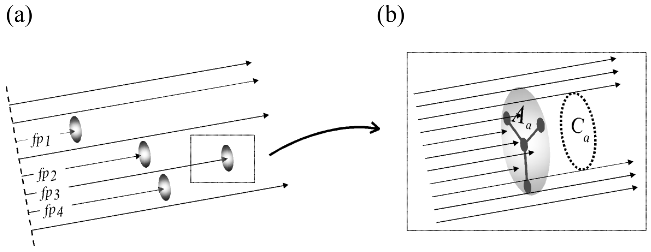

Figure 2.2. *Graphical illustration of (a) absorption free path lengths, and (b) the absorption cross-section*

2.2.2 Photons and molecular transitions

The quantum theory states that the energy of a photon is given by

$$e_{photon} = h\frac{c_0}{\lambda_0} \tag{2.18}$$

It is also stated that a molecule only can absorb photons with energies corresponding to transitions between the specific energy levels of the molecules, as indicated by the Jablonski diagram in Figure 2.3. The transitions can in general be divided into high-energy electronic transitions corresponding to light in the UV and VIS region, and low-energy vibrational or rotational transitions corresponding to light in the NIR and IR region[7,8]. The Jablonski diagram also shows how the energy from an incident photon is either dissipated through internal heat conversion or partly re-emitted leading to fluorescence or phosphorescence. The energy may also be converted by photochemical reactions, but heat dissipation is normally the dominant effect.

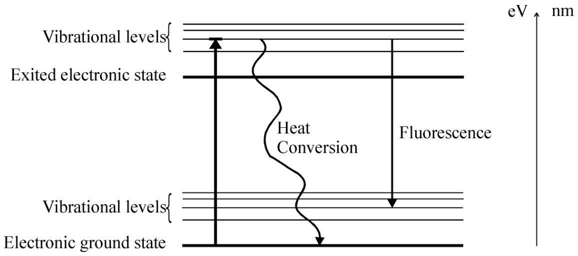

Figure 2.3. *Jablonski diagram illustrating the energy levels of chromophores*

Accordingly, absorption spectra may be considered as optical fingerprints that reveal important information on the molecular structure, configuration, and quantity of the various chromophores in a medium.

2.2.3 Biological chromophores

Figure 2.4 shows various absorption spectra of some important chromophores in human skin tissue. Water constitutes about 75 % of the tissue[9] and is therefore a major chromophore, but, as it appears from Figure 2.4, the water absorption is significant in the upper part of the near-infrared (NIR) region only ($\lambda > 1400$ nm). In the lower part of the visual (VIS) and ultraviolet (UV) region ($\lambda < 500$ nm) various proteins, such as melanin[10] and hemoglobin[11], dominate the absorption. The main function of melanin in the skin is to protect the organism from UV radiation. Although melanin is a very strong absorber it is only localized in a very thin layer (the epidermis) as discussed in Section 4.1.1. Thus, the overall effect of hemoglobin is moderate, but naturally there are large individual variations due to race, suntan, etc. Hemoglobin is also a strong absorber situated in the red blood cells. However, the blood content of tissue may be as low as a few percent. Thus the over-all effect of hemoglobin absorption is also moderate. As it appears from Figure 2.4, the spectra of oxy-hemoglobin and deoxy-hemoglobin deviates. This is widely used to measure the local blood oxygenation states of tissues optically, normally by recording the diffuse reflectance at $\lambda \approx$ 660 nm and at the isobestic point at $\lambda \approx$ 805 nm, where the two hemoglobin spectra coincide. The perhaps most import feature of the spectra shown in Figure 2.4 is the in general relatively low absorption in the lower NIR region (600 nm < λ < 1400 nm). This region facilitates deep light penetration into the tissue and is therefore called the diagnostic and therapeutic window.

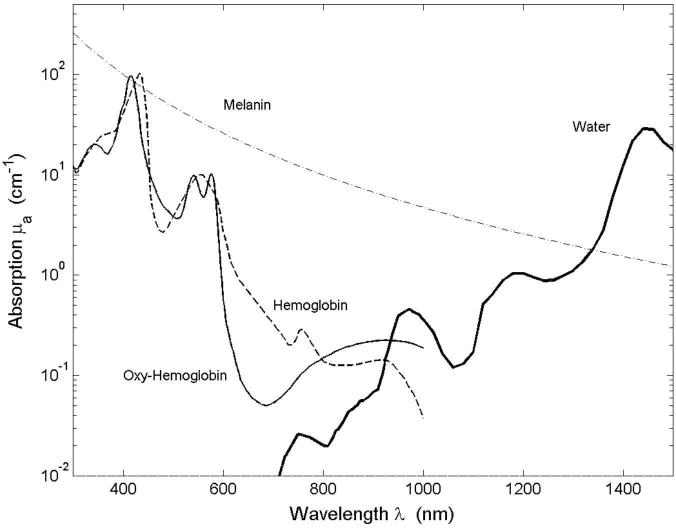

Figure 2.4. *Absorption spectra of typical skin tissue chromophores: water*[12]*, melanin*[10]*, oxyhemoglobin, and deoxy-hemoglobin*[11]*. Note that the spectra is scaled to the typical volume fractions of the chromophores in the tissue.*

2.3 Scattering

Snell's law of refraction is well known in the field of geometrical optics. It states that a ray of ray of light entering a medium with a different refractive index, as illustrated in Figure 2.5(a) is refracted and reflected according to

$$n_1 \sin\theta_1 = n_2 \sin\theta_2 \tag{2.19}$$

In case of unpolarized light, the fraction of the reflected power also called the specular reflectance r, is given by Fresnel's formula

$$r = \frac{1}{2}\left(\frac{\tan^2(\theta_1 - \theta_2)}{\tan^2(\theta_1 + \theta_2)} + \frac{\sin^2(\theta_1 - \theta_2)}{\sin^2(\theta_1 + \theta_2)} \right) \tag{2.20}$$

Note that any references to the refractive index henceforward simply imply the real part n of the complex refractive index n_c, as defined by Eq. (2.7). Typical values of n relevant for biomedical optics are: $n_{water} = 1.33$, $n_{tissue} = 1.4$, and $n_{glass} = 1.52$.

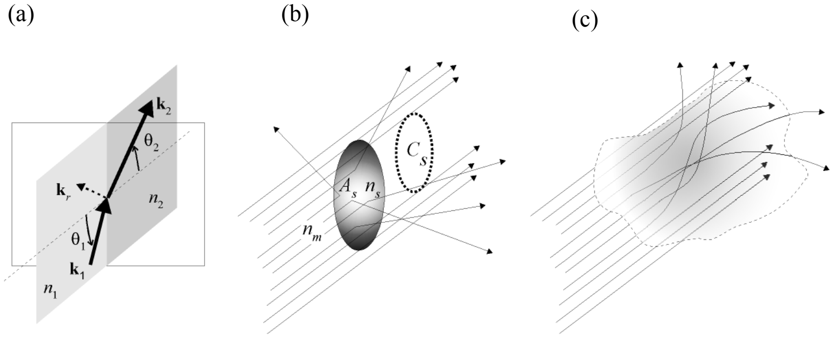

Figure 2.5. *Graphical illustration of (a) refraction at a well-defined boundary, (b) scattering by a discrete particle, and (c) scattering by continuous refractive index variations*

Light refraction may serve as a simple analogy to elastic light scattering, which also are caused by variations in n. The term elastic indicates that the light energy is preserved during the scattering event. Inelastic scattering, such as Raman scattering, will not be considered here[8]. Hence, a scattering medium may be conceived as an ensemble of discrete randomly distributed scattering particles with a refractive index n_s different from that of the surrounding medium n_m, i.e.

$$m = \frac{n_s}{n_m} \neq 1 \tag{2.21}$$

Where, m denotes the relative refractive index. A scattering medium may, however, also be described as continuum with refractive index fluctuations as shown in Figure 2.5(c). Although, the latter approach probably provides a more accurate description of turbid biological media it also involves complex mathematical calculations and modeling[6,13]. Consequently, the major part of the scattering calculations applied in biomedical optics is based on the discrete scattering element approach illustrated by Figure 2.5(b).

2.3.1 Scattering coefficient, cross-section, and mean free path length

Analogous to absorption cross-section, the effective scattering cross-section and the scattering coefficient may be defined as

$$C_s = q_s A_s \tag{2.22}$$

Where C_s is related to the geometrical cross-section of the scattering element A_s through the scattering efficiency q_s. Still analogous the absorption case, the scattering coefficient μ_s can be interpreted as.

$$\mu_s = C_s \rho_s \tag{2.23}$$

Where, ρ_s is the volume density of the scattering elements. Finally, the scattering mean free path length is defined as

$$mfp_s = \frac{1}{\mu_s} \tag{2.24}$$

2.3.2 Amplitude scattering matrix

The incident and scattered electric field ($\mathbf{E}_i$ and $\mathbf{E}_s$) may be described by their components in the directions parallel and perpendicular to the scattering plane defined by the direction vectors $\mathbf{k}_i$ and $\mathbf{k}_s$ of the incident and the scattered photons. This is illustrated in Figure 2.6. The relationship between $\mathbf{E}_i$ and $\mathbf{E}_s$ is for far-field observations readily quantified by

$$\begin{pmatrix} \mathbf{E}_{\parallel,s} \\ \mathbf{E}_{\perp,s} \end{pmatrix} = \frac{e^{ik(r-z)}}{-ikr} \begin{pmatrix} S_2(\theta,\alpha_a) & S_3(\theta,\alpha_a) \\ S_4(\theta,\alpha_a) & S_1(\theta,\alpha_a) \end{pmatrix} \begin{pmatrix} \mathbf{E}_{\parallel,i} \\ \mathbf{E}_{\perp,i} \end{pmatrix} \tag{2.25}$$

Where the complex amplitude functions $S_1 \dots S_4$ constitute the amplitude scattering matrix, and θ is the scattering angle, and α_a is the azimuth angle. The exponential term in Eq. (2.25) accounts for spherical wave form of the scattered light, hence this term is constant[6] for observations at constant radial distance[13] r.

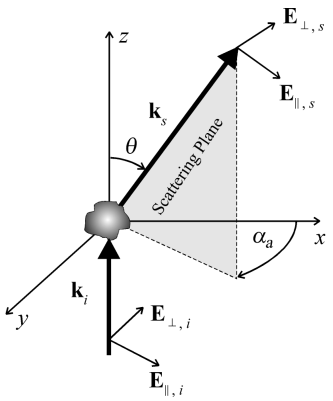

Figure 2.6. *Illustration of the definition of the scattering plane and the parallel and perpendicular electric field components (*$\mathbf{E}_{\parallel}$ *and* $\mathbf{E}_{\perp}$*).*

For the sake of brevity and clarity, only scattering from homogeneous spheres will be discussed in the following, In this case, S_3 and S_4 equal zero and S_1 and S_2 are invariant to α_a. By replacing the electric field $\mathbf{E}$ with the irradiance E, Eq. (2.25) can be reduced to

$$\begin{pmatrix} E_{\parallel,s} \\ E_{\perp,s} \end{pmatrix} = \frac{1}{k^2 r^2} \begin{pmatrix} |S_2|^2 & 0 \\ 0 & |S_1|^2 \end{pmatrix} \begin{pmatrix} E_{\parallel,i} \\ E_{\perp,i} \end{pmatrix} \tag{2.26}$$

For unpolarized incident light it can be shown that

$$E_s = \frac{S_{11}}{k^2 r^2} E_i \tag{2.27}$$

Where S_{11} is identical to the first element in the so-called Mueller matrix and in this case defined by

$$S_{11} = \tfrac{1}{2}(|(S_1(\theta)|^2 + |(S_2(\theta)|^2) \tag{2.28}$$

2.3.3 The anisotropy factor

The scattering phase function $p(\theta)$ may be calculated from S_{11} by

$$p(\theta) = \frac{S_{11}(\theta)}{c}, \quad c = \int_0^{\pi} S_{11} 2\pi \sin(\theta)\, d\theta \tag{2.29}$$

Such that $p(\cos\theta)$ is normalized according to

$$\int_{-1}^{1} p(\cos\theta) d(\cos\theta) = 1 \tag{2.30}$$

The anisotropy factor g is defined as the mean value of the cosine of the scattering angle[1].

$$g = \langle \cos(\theta) \rangle = \int_{-1}^{1} p(\cos\theta) \cos\theta \, d(\cos\theta) \tag{2.31}$$

Thus g varies in the range [-1, 1] and is a measure of the amount of forward scattering, e.g. $g = 0$ denotes isotropic scattering. The phase function of the scattering elements in a medium may be determined by goniometric measurements of single scattering events (e.g. see Figure 4.7(b)). However, in biomedical optics and other fields the actual phase function may often be approximated well by the *Henyey-Greenstein* (H-G) scattering phase function[14]

$$p_{HG}(\cos\theta) = \frac{1}{2} \frac{1 - g^2}{(1 + g^2 - 2g\cos\theta)^{3/2}} \tag{2.32}$$

Where, g, together with θ, directly specifies the scattering phase function.

2.3.4 The reduced scattering coefficient

In some types of scattering measurements, various combinations of μ_s and g yield identical observable results. This effect is encountered, for instance in diffuse reflectance measurements (following many scattering events as illustrated in Figure 2.7), when the so-called similarity principle[15,16] applies[17]

$$(1 - g_1)\mu_{s,1} = (1 - g_2)\mu_{s,2} \tag{2.33}$$

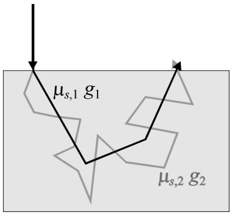

Figure 2.7. *The effect of the similarity principle in diffuse reflectance measurements*

In such cases it is convenient to characterize the medium by the reduced scattering coefficient μ'_s, which combines μ_s and g into a single parameter.

$$\mu'_s = (1-g)\mu_s \tag{2.34}$$

2.3.5 Mie theory

The scattering properties of homogeneous spheres can also be calculated rigorously by applying Mie theory[6,13,18]. According to Mie theory the scattering properties of non-absorbing homogeneous can be calculated from the relative refractive index m (see also Eq. (2.21)), and the size parameter x.

$$x = ka = \frac{2\pi n_m a}{\lambda}, \quad m = \frac{n_s}{n_m} \tag{2.35}$$

Where a is the radius of the sphere, while n_s and n_m are the real part of the refractive indices of the sphere and the surrounding medium, respectively. Although, Mie theory applies for all x, cases with $a << \lambda$ are termed Rayleigh scattering, while cases with $a \approx \lambda$ are termed Mie scattering. Rayleigh scattering is characterized by nearly isotropic scattering ($g \approx 0$) and that μ_s is proportional to λ^{-4}. The underlying formalism of Mie theory is complex and comprehensive. So only the headlines will be given here. The central parameters of the Mie formulas concerning scattering from non-absorbing homogeneous spheres are the Mie scattering coefficients a_n and b_n defined by.

$$\begin{aligned} a_n &= \frac{m\psi_n(mx)\psi'_n(x) - \psi_n(x)\psi'_n(mx)}{m\psi_n(mx)\xi'_n(x) - \xi_n(x)\psi'_n(mx)} \\ b_n &= \frac{\psi_n(mx)\psi'_n(x) - m\psi_n(x)\psi'_n(mx)}{\psi_n(mx)\xi'_n(x) - m\xi_n(x)\psi'_n(mx)} \end{aligned} \tag{2.36}$$

Where the Riccati-Bessel functions ψ_n and ξ_n are defined as

$$\varnothing_n(\eta) = \eta\, j_n(\eta),\ \xi_n(\eta) = \eta\, h_n^{(1)}(\eta) \tag{2.37}$$

Here j_n and $h_n^{(1)}$ are spherical Bessel and Hankel functions, respectively. The scattering cross-section C_s of the sphere can now be calculated from

$$C_{sca} = \frac{2\pi}{k^2} \sum_{n=1}^{\infty} (2n+1)(|a_n|^2 + |b_n|^2) \tag{2.38}$$

While the scattering matrix components S_1 and S_2 are calculated from

$$\begin{aligned} S_1 &= \sum_n \frac{2n+1}{n(n+1)} (a_n \pi_n + b_n \tau_n) \\ S_2 &= \sum_n \frac{2n+1}{n(n+1)} (a_n \tau_n + b_n \pi_n) \end{aligned} \tag{2.39}$$

Where

$$\pi_{\text{n}} = \frac{P_n^1(\cos\theta)}{\sin\theta},\quad \tau_{\text{n}} = \frac{dP_n^1(\cos\theta)}{d\theta} \tag{2.40}$$

And P_n^1 is the associated Legendre function. Now, by inserting Eq. (2.39) into Eqs. (2.28) and (2.29) the scattering phase function $p(\cos\theta)$ and in turn the anisotropy factor g of the homogeneous spheres can be calculated[6,13].

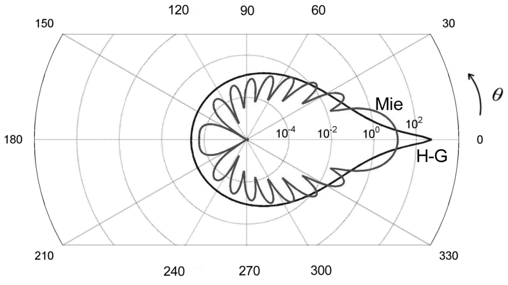

Figure 2.8. *Comparison of scattering phase functions for a homogeneous sphere based on Mie theory and the H-G approximation, respectively. The data of the sphere are a= 1μm, n_s = 1.35, and n_m = 1.4. This yields C_s = 0.48 and g = 0.98.*

Figure 2.8 shows the scattering phase function for a sphere calculated using Mie theory algorithms[19] and the corresponding H-G approximation. It appears from Figure 2.8, that there is good over-all correlation between the Mie - and H-G scattering phase function. There are, however, discrepancies, especially for small angles θ, so the H-G approximation should not be applied uncritically.

2.3.6 Biological spectra

The scattering properties of biological media reflect the ultrastructure of the media. This structure is very complex and includes elements such as cell organelles, nuclei, cell membranes and the cells themselves. Extra-cellular components, such as collagen fibers, and lipid droplets also play an important role in tissue scattering[20-22].

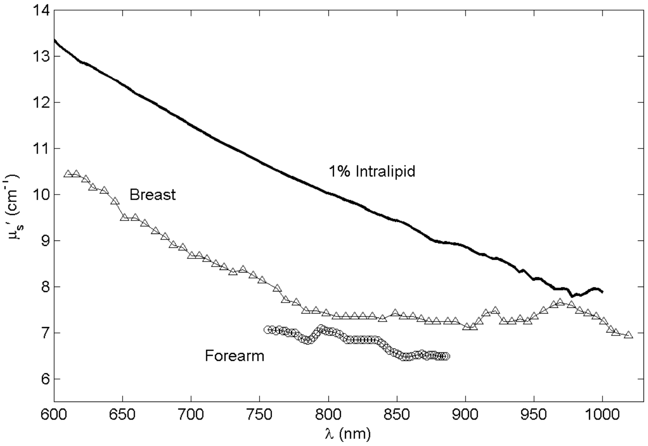

Figure 2.9. *Reduced scattering spectra of breast*[23] *and forearm tissue*[24] *determined from diffuse reflectance measurements, and a 1% Intralipid spectrum determined from integrating sphere measurements (Paper II).*

None of the mentioned biological scattering structures resembles homogeneous spheres. However, it can be advantageous to apply sphere equivalents to the various biological structures, and thus use Mie theory or H-G approximations for qualitative estimations of the structures, e.g. by relating the size of the structures to the amount of forward scattering etc. Most biological tissue is strongly forward scattering ($0.7 < g$ 0.99), with $g = 0.9$ as a representative value for skin tissue. In general, the μ_s of biological media varies considerably, yet $\mu_s \approx 100\,\mathrm{cm}^{-1}$ applies, as a rule of thumb, for a wide range of media. Consequently, $\mu'_s \approx 10\,\mathrm{cm}^{-1}$ also applies as typical value for skin tissue[2,25]. Many reported studies on tissue scattering properties are based on *in vitro* measurements, but since the scattering components of tissue are structural elements of *in vivo* tissue, it is difficult to obtain reliable results from such measurements. Hence, accurate methods for noninvasive scattering measurements are desirable. Figure 2.9 shows examples of μ'_s spectra of breast[23] and skin tissue[24] as well as intralipid[26]. The latter substance is widely used for tissue simulating scattering phantoms[27,28]. All three spectra exhibit a characteristic decrease in μ'_s for increasing λ .

Chapter 3

Light propagation models

While the main topic of the previous chapter was the basic interaction of light with the chromophores and single scattering elements, this chapter proceeds with light propagation modeling in multiple scattering bulk media. As stated in the introduction in Chapter 1, such models are imperative for extracting the optical properties from real measurements on biological media. In the previous chapter, the dual nature of light, i.e. the wave versus the photon approach, was discussed in relation to the basic absorption and scattering properties of biological media. Light propagation in a multiple scattering medium is also fundamentally governed by Maxwell's equations. Although, the electromagnetic theory approach is attractive since it preserves the wave properties of the light as illustrated in Figure 3.1(a), the complexity of the mathematical formalism is overwhelming. Instead models based on photon transport are frequently used in biomedical optics. These are expressed as differential or integro-differential equations; e.g. the transport equation[1], which is derived from simple phenomenological considerations on the basis of the radiative transport theory[29-31].

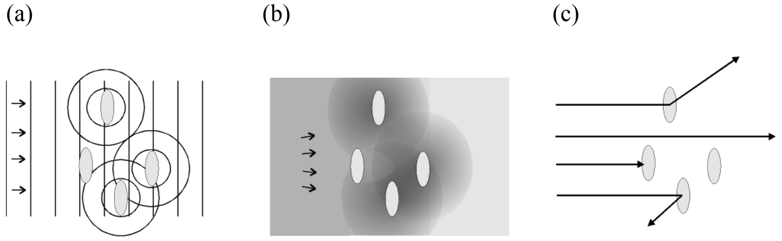

Figure 3.1. *Schematics of light propagation in multiple scattering media described, respectively, as (a) interfering waves by electromagnetic theory, (b) as energy flux by diffusion theory, and (c) as photon trajectories by Monte Carlo simulations.*

The transport equation has no exact closed analytical solutions relevant for any practical applications. However, the diffusion approximation[29] (diffusion theory) [32,33]provides useful solutions, although certain restrictions apply. In diffusion theory, the photon migration is modeled as a gradient-driven diffusion of energy, which is illustrated in Figure 3.1(b). Monte Carlo (MC) simulations[34] are also widely used in biomedical. While diffusion theory models light propagation as a diffuse photon flux, MC simulations, which is a purely numerical and stochastic approach, models light as discrete photons bouncing around in the scattering medium as illustrated by Figure 3.1(c)

Both diffusion theory and MC simulations are capable of handling light propagation in both two and three dimensions. Still, purely one-dimensional models also play an important role in biomedical optics, especially for *in vitro* spectroscopy measurements on turbid media. One-dimensional numerical models, such as the adding-doubling method[17,35,36] presented in Section 3.4, typically lead to mathematical simplifications compared to two- and three-dimensional models. This leads to faster calculations, which in turn promotes determination of optical properties based on iterative forward calculations, as exemplified by the inverse adding-doubling method[37,38] applied in Paper II.

During the following discussions and the work presented in the accompanying papers, some general simplifications regarding the applied models are assumed. First, it is assumed that the scattering and absorbing elements of a medium are sufficiently separated, so that the optical properties of one element is unaffected by the scattered fields and the physical presence of other elements. Second, it is also assumed that all scattering elements may be described by one scattering phase function only. Although, it in principle is possible to include several such functions in MC simulations and thus model different scattering patterns, all MC simulations discussed here assume a single scattering phase function. Third, all media below are assumed be homogeneous. Again, MC simulations, and to some extent diffusion theory also, allow non-homogeneous media, but this is not applied in the following either (except for simulating glass/plastic cuvette walls). Hardly any of the above assumptions is strictly valid for biological media in general. However, the work presented in Papers III and IV as well as several other studies[39,40] demonstrate that at least MC simulations correlate well with measured results, although not all conditions are rigorously fulfilled.

3.1 Transport theory

Transport theory has been applied in several fields of physics[29-31] and has proven to be advantageous for modeling light propagation in turbid media as well. In short, the fundamental difference between transport theory and electromagnetic theory is that, while electromagnetic theory describes light propagation by superposition of electromagnetic fields, transport theory basically relies on superposition of energy fluxes. Thus, wave phenomena (e.g. polarization, phase, and interference) are normally not considered in transport theory. In the discussion on electromagnetic theory in Chapter 2 it was demonstrated how the Poynting vector **S** expressed the energy transport of electromagnetic waves and it was stated that the rate of energy (radiant power *P*) transferred through a surface with the area *A* could be determined from

$$P = \int_A \mathbf{S} \cdot \mathbf{n} \, dA \tag{3.1}$$

Where **n** is the normal vector of the surface. The transport theory equivalent of **S** is the flux vector **F.** Here the power *P* transferred through a surface with the area *A* is defined as

$$P = \int_A \mathbf{F} \cdot \mathbf{n} \, dA \tag{3.2}$$

It is beyond the scope here to discuss the underlying theoretical connection between electromagnetic theory and transport theory. So the above analogy just serves to illustrate the fact that **S** and **F** express the same quantity i.e. the direction and rate of energy transfer per unit area perpendicular to the direction.

3.1.1 Radiometric terms

In Eq. (3.2) the flux **F** was introduced, in order to describe the incident power *P* on a surface with the area *A* and the normal vector **n**, which is illustrated graphically in Figure 3.2(a). The power per unit area of the surface in Figure 3.2(a) is denoted the irradiance *E* (see also Eq. (2.13)) and is defined as

$$E(\mathbf{r},t) = \mathbf{F}(\mathbf{r},t) \cdot \mathbf{n}(\mathbf{r}) \tag{3.3}$$

Where **r** is the position vector and *t* is the time. As noted previously, $E(\mathbf{r},t)$ should not be confused with the intensity $I(\mathbf{r},\mathbf{s},t)$, which is defined as the power per solid angle in direction **s** at time *t* at position *r*.

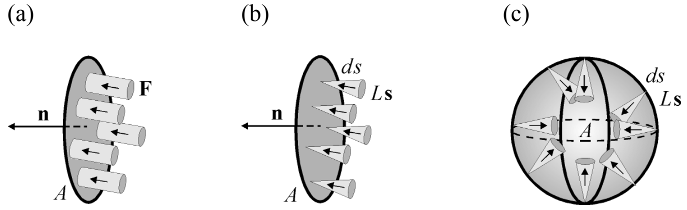

Figure 3.2. *Illustration of incident power P on an area A, described by three key quantities of transport theory: (a) the flux* **F***, (b) the radiance L, and (c) the fluence rate ϕ*

In transport theory, light is often modeled in terms of the radiance $L(\mathbf{r},\mathbf{s},t)$, which expresses power per solid angle and area in direction **s** at position **r** at time *t*. As a mnemonic rule, *L* may be considered to be a hybrid of *E* and *I*. The net flux $\mathbf{F}$ expressed in terms of radiance is given by.

$$\mathbf{F}(\mathbf{r},t) = \int_{4\pi} L(\mathbf{r},\mathbf{s},t)\mathbf{s}\, ds \tag{3.4}$$

Where *ds* denotes an infinitesimal solid angle. The power incident on the right-hand side of surface *A* in Figure 3.2(b) can now be calculated by

$$P(t) = \int_{A}\int_{2\pi} L(\mathbf{r},\mathbf{s},t)(\mathbf{s}\cdot\mathbf{n})\, ds\, dA \tag{3.5}$$

Light in a highly scattering medium, such as human tissue, is almost completely diffuse, which means that the incident light on a small volume element a given position comes from arbitrary directions. In this case, it is convenient to introduce the fluence rate ϕ defined by

$$\phi(\mathbf{r},t) = \int_{4\pi} L(\mathbf{r},\mathbf{s},t)\, ds \tag{3.6}$$

This means that ϕ expresses the total power incident on a small sphere at position **r** and time t divided by the cross-sectional area A of the sphere, as illustrated in Figure 3.2(c). The practical importance of ϕ finds expression in

$$W(\mathbf{r}) = \int \mu_a(\mathbf{r})\phi(\mathbf{r},t)\,dt \tag{3.7}$$

Where, W is the deposited energy density at position **r** in the medium.

3.1.2 The transport equation

The governing equation of transport theory is the transport equation, which is equivalent to the Boltzmann equation widely used to describe particle transport, e.g. neutrons[31]. In this particular case the particles are photons. During the following the photon flux will, however, be described in terms of the radiance L. By using Eq. (2.18), the relationship between photon distribution function $N(\mathbf{r},\mathbf{s},t)$, which is the volume density of the photons at time t traveling within the solid angle ds in direction **s** at position **r**, is given by

$$L(\mathbf{r},\mathbf{s}) = N(\mathbf{r},\mathbf{s})\frac{hc^2}{\lambda} \tag{3.8}$$

Where h is Planck's constant, while c and λ is the speed and the wavelength of the light in the medium, respectively.

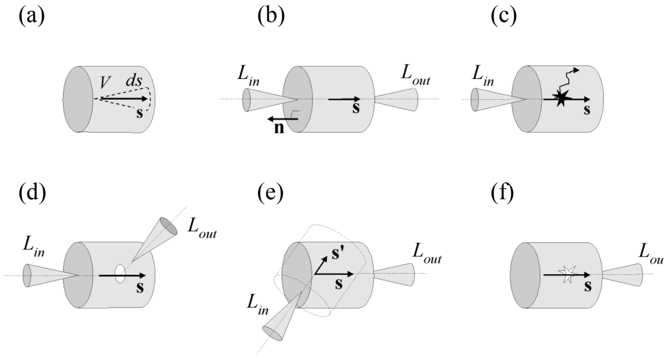

Figure 3.3. S*chematics of the component terms of the transport equation. That is, (a) the energy of the photons in volume V, (b) losses through the boundaries, (c) losses due to absorption, (d) losses due to scattering, (e) gain from light scattered into the direction in question, and (f) gain due to sources within volume V.*

Consider the photons traveling at speed c in direction $\mathbf{s}$ within the small cylinder with volume V in Figure 3.3(a). The total energy Q_a of the photons per solid angle s at time t is given by

$$\frac{dQ_a(\mathbf{s},t)}{ds}=\frac{1}{c_0}\int_V L(\mathbf{r},\mathbf{s},t)dV \tag{3.9}$$

In Figure 3.3(b) the decrease in intensity ΔI_b due to losses through the surfaces S of the cylinder is

$$\Delta I_b(\mathbf{s},t)=\int_S L(\mathbf{r},\mathbf{s},t)\mathbf{s}\cdot\mathbf{n}dS=\int_V \nabla L\cdot\mathbf{s}dV \tag{3.10}$$

Where, Gauss' theorem was employed to convert the surface integral to a volume integral. The intensity decrease ΔI_c Figure 3.3(c) due to absorption is given by

$$\Delta I_c(\mathbf{s},t)=\int_V \mu_a L(\mathbf{r},\mathbf{s},t)dV \tag{3.11}$$

Likewise, the intensity decrease ΔI_d due to photons being scattered away from the direction of $\mathbf{s}$ in Figure 3.3(d) is given by

$$\Delta I_d(\mathbf{s},t)=\int_V \mu_s L(\mathbf{r},\mathbf{s},t)dV \tag{3.12}$$

In Figure 3.3(e), the intensity increase ΔI_e gained through photons scattered from other directions $\mathbf{s}'$ into $\mathbf{s}$ is expressed as

$$\Delta I_e(\mathbf{s},t)=\int_V \mu_s \int_{4\pi} L(\mathbf{r},\mathbf{s}',t)p(\mathbf{s},\mathbf{s}')ds'dV \tag{3.13}$$

Where $p(\mathbf{s},\mathbf{s}')$ is identical to the scattering phase function $p(\cos\theta)$. Finally, the intensity increase ΔI_f due to light sources q within the cylinder Figure 3.3(f) is

$$\Delta I_f(\mathbf{s},t)=\int_V q(\mathbf{r},\mathbf{s},t)dV \tag{3.14}$$

Now, the rule of energy conservation applied on Eqs. (3.9)-(3.14) leads to

$$\frac{\partial}{\partial t}\left(\frac{dQ_a}{ds}\right)+\Delta I_b+\Delta I_c+\Delta I_d=\Delta I_e+\Delta I_f \tag{3.15}$$

Dropping the volume integrals in Eq. (3.15) finally yields the time-dependent transport equation.

$$\frac{1}{c}\frac{\partial L(\mathbf{r},\mathbf{s},t)}{\partial t}+\mathbf{s}\cdot\nabla L(\mathbf{r},\mathbf{s},t)+(\mu_a+\mu_s)L(\mathbf{r},\mathbf{s},t)=\mu_s\int_{4\pi}L(\mathbf{r},\mathbf{s}',t)p(\mathbf{s},\mathbf{s}')ds'+q(\mathbf{r},\mathbf{s},t) \tag{3.16}$$

As pointed out previously, there are no closed form analytic solutions to the transport equation for relevant three-dimensional problems and therefore approximation methods must be employed, for example MC simulations (probabilistic method), diffusion theory (expansion method), or adding-doubling (discretization method).

3.2 Monte Carlo simulations

Monte Carlo (MC) simulations[34,41] is the perhaps most intuitive of commonly employed approaches to light transport modeling in multiple scattering media. The basic idea of MC simulations is to consecutively launch a huge number of virtual photons into a scattering and absorbing medium, and record either the energy deposition in the medium as illustrated by Figure 3.4, or the energy flux re-emitted from the medium, as demonstrated in Paper I-V.

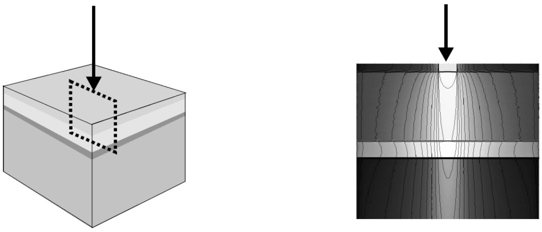

Figure 3.4. *Illustration of Monte Carlo simulated photon distribution in a simplified multi-layered tissue model.*

3.2.1 Step sizes and scattering angles

During MC simulations, each single photon performs a random walk in the scattering medium determined by iterative decisions on (a) how far to move before any interaction with the medium should take place and (b) in which direction to proceed after the interaction. This random walk of numerous photons in a medium leads to the characteristic jagged photon trajectories shown in Figure 3.5(a).

The decisions governing the photon propagation are based on random sampling of a set of probability distributions derived from the macroscopic optical properties (μ_a, μ_s, and g) of the medium in question. In order to sample these probability distributions a random variable η that varies between [0,1] is introduced. The relationship between η and the probability density functions *p(x)* which characterizes the optical properties of the medium is given by

$$\eta = \int_a^x p(x)dx \tag{3.17}$$

In this way, η is the "dice" of the MC simulations that is rolled every time a photon has to be moved, and x represents the photon step size Δz or the deflection angles θ and α_a , as shown below.

In the previous chapter it was stated that μ_a and μ_s could be defined such that, when a photon travels an infinitesimal distance *dz*, the probability for absorption or scattering is given by $\mu_a dz$ and $\mu_s dz$, respectively. Thus, the probability for any interaction (absorption and/or scattering) is given by $(\mu_a + \mu_s)dz$. From this, it can be shown that the probability density function of the step size Δz is defined as.

$$p_s = (\mu_a + \mu_s)\exp(-(\mu_a + \mu_s)\Delta z) \tag{3.18}$$

The step size, which is the free path length of the photon between to interactions, as shown in Figure 3.5(b), may now be sampled randomly by inserting Eq. (3.18) in to Eq. (3.17).

$$\Delta z = \frac{-\ln(\eta)}{\mu_a + \mu_s} \tag{3.19}$$

During the photon-matter interaction some of the photon energy is absorbed. This accomplished by decrementing the weight *w* (the energy) of the photon according to.

$$w_2 = w_1 \Delta w \tag{3.20}$$

Where, w_1 and w_2, as illustrated in Figure 3.5(b), represent the photon energy before and after interaction, respectively, and where the deposited energy Δw is given by

$$\Delta w = 1 - \frac{\mu_a}{\mu_a + \mu_s} = \frac{\mu_s}{\mu_a + \mu_s} \tag{3.21}$$

Note that the right-hand term of Eq. (3.21) also is known as the albedo of the medium. By applying the absorption scheme in Eqs. (3.20) and (3.21), it is assumed that absorption and scattering takes place during a single event. This is evidently not true, but the above approach implies substantial computational advantages compared to applying separate step sizes for absorption and scattering. Moreover, the net simulation results of the two approaches are identical.

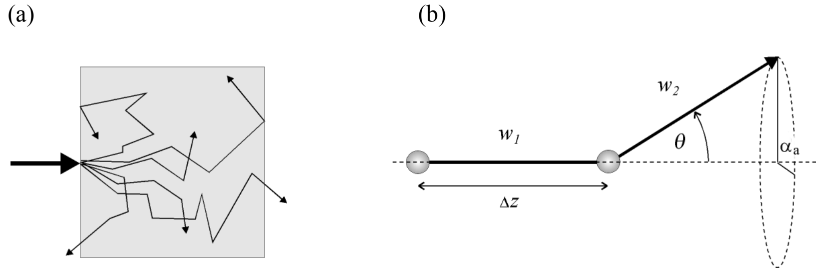

Figure 3.5. *Schematic of Monte Carlo simulations showing (a) random walks of multiple photons, and (b) the basic stochastic parameters governing the photon migration, i.e. step size* Δz*, scattering angle* θ*, and azimuth angle* α_a.

After an absorption-scattering event, a new direction of the decremented photon has to be selected, that is, the scattering angle θ and the azimuth angle α_a depicted in Figure 3.5(b) have to be calculated. The determination of θ is based on the scattering phase function of the scattering elements in the medium. As mentioned in Section 0, the Henyey-Greenstein (H-G) function is a widely used approximation to the actual scattering phase functions of biological media. In this case, the probability density function of θ is identical to the H-G function (see Eq. (2.32)) and is thus given by

$$p_{HG}(\cos\theta) = \frac{1}{2}\frac{1-g^2}{(1+g^2-2g\cos\theta)^{3/2}} \tag{3.22}$$

The scattering angle θ may thus be sampled as

$$\cos\theta = \begin{cases} \frac{1}{2g}\left(1+g^2-\left(\frac{1-g^2}{1-g+2g\eta}\right)^2\right) & \text{if } g \neq 0 \\ 2\eta - 1 & \text{if } g = 0 \end{cases} \tag{3.23}$$

The H-G approximation implies symmetric scattering around the direction of propagation, i.e. α_a is evenly distributed within [$0,2\pi$]. Consequently, α_a are sampled as

$$\alpha_a = 2\pi\eta \tag{3.24}$$

After this cycle of calculations the photon is moved and a new set of Δz, θ, and α_a is calculated. This continues repeatedly until the photon either leaves the medium, or it is terminated due to a w value below a predefined threshold. If the refractive index of the medium n_m differs from the index of the surroundings or if n_m varies across boundaries in the medium, specular reflections occur, as indicated in Figure 3.5(a). In such cases, refraction calculations according to the Fresnel boundary conditions have to be employed in addition to the above calculations (Eqs. (2.19) and (2.20)).

3.2.2 Advantages and drawbacks

MC simulations are stochastic by nature and provide numerical solutions only. Still, the method is highly flexible and truly three-dimensional[42]. Consequently, practically any geometry can be simulated as exemplified in Figure 3.4. Moreover, provided that a sufficient number of photons are launched, MC simulations have proven to be very accurate as well[39,40]. Although the photons in most applications are treated as neutral non-interacting particles carrying energy only, it is, however, possible to include wave phenomena such as phase and polarization in MC simulations also[43,44]. Besides the numerical results, the major drawback of MC simulations is the computation time/power needed to obtain precise results. However, as novel accelerated MC algorithms evolve[45], and computers are getting faster, this inconvenience gradually becomes less restrictive.

3.3 Diffusion Theory

The diffusion approximation[29,32,33] has been widely used in biomedical optics and has led to a considerable insight into light propagation in tissue. However, as discussed in Section 3.3.3 below there are also several drawbacks related to the use of the diffusion approximation.

3.3.1 Spherical harmonics expansion

The basic idea of diffusion theory is to expand the functions L, p and q of the transport equation (Eq. (3.16)) into spherical harmonics[32], e.g.

$$L(\mathbf{r},\mathbf{s},t) = \sum_{l=0}^{\infty} \sum_{m=-l}^{l} \sqrt{\frac{2l+1}{4\pi}} \psi_{lm}(\mathbf{r},t) Y_{lm}(\mathbf{s}) \tag{3.25}$$

Truncation of Eq. (3.25) at $l \leq 1$ yields the so-called P_1 approximation.

$$L(\mathbf{r},\mathbf{s},t) = \sqrt{\frac{1}{4\pi}} \psi_{00}(\mathbf{r},t) Y_{00}(\mathbf{s}) + \sqrt{\frac{3}{4\pi}} \sum_{m=-1}^{1} \psi_{1m}(\mathbf{r},t) Y_{1m}(\mathbf{s}) \tag{3.26}$$

The four unknowns ψ_{00} and ψ_{1m} may now be found by inserting Eq. (3.26) into the transport equation (Eq. (3.16). Alternatively, it is also possible to take advantage of the fact that Y_{00} is a scalar, while Y_{1m} are components of a vector, and thus express the radiance as

$$L(\mathbf{r},\mathbf{s},t) = A(\mathbf{r},t) + \mathbf{B}(\mathbf{r},t) \cdot \mathbf{s} \tag{3.27}$$

Eq. (3.27) suggests that L is composed of a isotropic part A and an an-isotropic part $\mathbf{B} \cdot \mathbf{s}$, as illustrated geometrically in Figure 3.6. Now, inserting Eq. (3.27) into Eq. (3.4) yields

$$\mathbf{F}(\mathbf{r},t) = \int_{4\pi} A(\mathbf{r},t)\mathbf{s} + \left(\mathbf{B}(\mathbf{r},t) \cdot \mathbf{s}\right)\mathbf{s} \, ds = \frac{4\pi}{3} \mathbf{B}(\mathbf{r},t) \, . \tag{3.28}$$

Here, it appears that $\mathbf{F} \neq 0$, i.e. there is a net transport of energy in the direction of $\mathbf{B}$ as long as $\mathbf{B} \neq 0$.

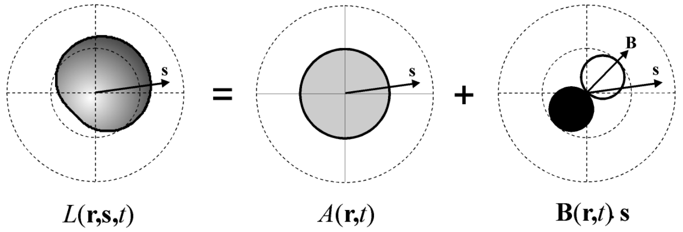

Figure 3.6. *Graphical illustration of the diffusion theory approximation of the radiance L as a superposition of a major isotropic part A and a minute anisotropic part* $\mathbf{B}\cdot\mathbf{s}$.

Using Eq. (3.6) the fluence rate ϕ is calculated as

$$\phi(\mathbf{r},t)=\int_{4\pi} A(\mathbf{r},t)+\mathbf{B}(\mathbf{r},t)\cdot\mathbf{s}\;ds=4\pi A(\mathbf{r},t) \tag{3.29}$$

By inserting Eqs. (3.28) and (3.29) into Eq. (3.27), the radiance can now be expressed as

$$L(\mathbf{r},\mathbf{s},t)=\frac{1}{4\pi}\left(\phi(\mathbf{r},t)+3\mathbf{F}(\mathbf{r},t)\cdot\mathbf{s}\right) \tag{3.30}$$

As mentioned, the source term q in Eq. (3.16) may also be expanded into spherical harmonics

$$q(\mathbf{r},\mathbf{s},t)=\frac{1}{4\pi}\left(q_0(\mathbf{r},t)+3\mathbf{q}_1(\mathbf{r},t)\cdot\mathbf{s}\right) \tag{3.31}$$

However, for the sake of clarity, only isotropic point sources are considered in the following, so the $\mathbf{q}_1$ term in Eq. (3.31) is assumed to be equal to zero. Thus, inserting Eqs. (3.30) and (3.31) into Eq. (3.16) and rearranging yields

$$\frac{1}{c}\frac{\partial}{\partial t}(\phi+3\mathbf{F}\cdot\mathbf{s})=-\mathbf{s}\cdot\nabla(\phi+3\mathbf{F}\cdot\mathbf{s})-(\mu_a+\mu_s)(\phi+3\mathbf{F}\cdot\mathbf{s})+\mu_s\int_{4\pi}p(\mathbf{s}'\cdot\mathbf{s})(\phi+3\mathbf{F}\cdot\mathbf{s}')ds'+q_0 \tag{3.32}$$

Where $\mathbf{F}$ and ϕ still are functions of $\mathbf{r}$ and t, while μ_a and μ_s are functions of $\mathbf{r}$ only. By applying Eqs. (2.30) and (2.31) on the scattering phase function *p*, Eq. (3.32) reduces to

$$\frac{1}{c}\frac{\partial}{\partial t}(\phi + 3\mathbf{F}\cdot\mathbf{s}) = -(\mathbf{s}\cdot\nabla + \mu_a)\phi - 3(\mathbf{s}\cdot\nabla + \mu_a + \mu'_s)\mathbf{F}\cdot\mathbf{s} + q_0 \tag{3.33}$$

Integration of Eq. (3.33) over all $\mathbf{s}$ yields

$$\frac{1}{c}\frac{\partial\phi}{\partial t} = -\mu_a\phi - \nabla\cdot\mathbf{F} + q_0 \tag{3.34}$$

Likewise, multiplying Eq. (3.33) with $\mathbf{s}$ and subsequent integration over all $\mathbf{s}$ leads to

$$\frac{1}{c}\frac{\partial\mathbf{F}}{\partial t} = -\frac{1}{3}\nabla\phi - (\mu_a + \mu'_s)\mathbf{F} \tag{3.35}$$

Here, the steady-state version of Eq. (3.35) is recognized as Fick's law from the diffusion theory.

$$\mathbf{F} = -D\nabla\phi \tag{3.36}$$

Where the diffusion coefficient *D* is defined as

$$D = \frac{1}{3(\mu_a + \mu'_s)} \tag{3.37}$$

By inserting the instantaneous flux $\mathbf{F}$ from Eq. (3.36) into Eq. (3.34) the time-resolved diffusion equation finally emerges

$$\frac{1}{c}\frac{\partial\phi(\mathbf{r},t)}{\partial t} - D\nabla^2\phi(\mathbf{r},t) + \mu_a\phi(\mathbf{r},t) = q_0(\mathbf{r},t) \tag{3.38}$$

Now, consider an ultra-short pulse from an isotropic point source within an infinite and homogeneous medium.

$$q_0(\mathbf{r},t) = \delta(0,0) \tag{3.39}$$

Where δ is Dirac's delta function. The solution to Eq. (3.38) using the source defined by Eq. (3.39) yields the following Green's function (impulse response).

$$\phi(r,t) = Q_s c (4\pi Dct)^{-3/2} e^{-\frac{r^2}{4Dct} - \mu_a c t} \tag{3.40}$$

Where, Q_s is the energy of the pulse from the point source and r is the radial distance from the source. This relatively simple expression may be used to derive solutions for more complex geometric configurations with greater practical relevance. The steady-state equivalent of Eq. (3.40) is

$$\phi(r) = P_s \frac{1}{4\pi Dr} e^{-\sqrt{\frac{\mu_a}{D}}r} \tag{3.41}$$

Here, P_s is the power of the continuous wave point source

3.3.2 Time-independent diffuse reflectance

In general, the work presented in Papers I-V concerns either diffuse reflectance measurements of bulk media or *in vitro* diffuse spectroscopy on relatively thin samples. Due to the restrictions discussed in Section 3.3.3 below, diffusion theory is not suited to model the thin-sample geometry. However, the theory may be used to estimate the reflectance from a collimated beam incident on a semi-infinite medium, provided that the source-detector configuration and the optical properties conform to the restrictions in Eq. (3.44). Several attempts have been made to include Fresnel boundary conditions, etc. into diffusion theory. One of the more successful approaches[46] is based on so-called *dipole sources* and *extrapolated boundaries* as illustrated in Figure 3.7.

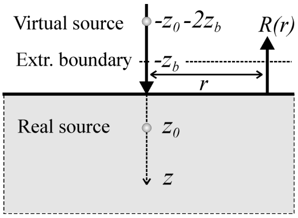

Figure 3.7. *Schematic of diffusion theory model of the diffuse reflectance R(r) as a function of radial distance r. The model is based the extrapolated boundary and virtual dipole source approach.*

Thus, it can be shown (using Eq. (3.41)) that the spatially-resolved diffuse reflectance from the geometry shown in Figure 3.7 can be expressed as

$$R(r)=\frac{1}{4\pi}\left[z_0\left(\mu_{eff}+\frac{1}{r_1}\right)\frac{e^{-\mu_{eff}r_1}}{r_1^2}+(z_0+2z_b)\left(\mu_{eff}+\frac{1}{r_2}\right)\frac{e^{-\mu_{eff}r_2}}{r_2^2}\right] \tag{3.42}$$

Where

$$\mu_{eff}=\sqrt{\frac{\mu_a}{D}}\ ,\ r_1=\sqrt{z_0^2+r^2}\ ,\ r_2=\sqrt{(z_0+2z_b)^2+r^2}\ ,\ z_0=\frac{1}{\mu'_s},\ \ z_b\approx bz_0 \tag{3.43}$$

Here, b is dependent on the actual Fresnel reflection coefficient, e.g. $b\approx 2$ for a typical tissue-air boundary.

3.3.3 *Accuracy and limitations*

Diffusion theory is an important workhorse in the field of biomedical optics. It has been shown, however, that it is inaccurate in several instances, particularly for applications that involve structures near the surface of the medium, small source-detector distances[47], or geometrical configuration with sharp discontinuities of the scattering properties. Furthermore, it is laborious to model even moderately complex geometries using diffusion theory. In any case, two basic conditions have to be fulfilled in order to obtain valid results from diffusion theory[33]. First, scattering must prevail absorption; secondly, sufficient source-detector distances have to be insured.

$$\mu'_s >> \mu_a \quad , \qquad r_{s-d}>\frac{2\sim 3}{\mu'_s} \tag{3.44}$$

These restrictions are a consequence of the basic assumption of the P_1 approximation (see Eq. (3.27)), that the radiance in a scattering medium is composed of a major isotropic part and a minute anisotropic part.

3.4 The Adding-Doubling Method

As mentioned previously, one-dimensional light propagation models are important i*n vitro* spectroscopy on turbid samples. Although MC simulations may also be used for this, application of a dedicated one-dimensional method normally provides much faster calculations. Besides providing fast calculations, the adding-doubling (A-D) method[35,38] described here, permits anisotropic scattering and arbitrary sample thicknesses, and handles refractive index mismatch also.

3.4.1 Reflection and transmission functions

The basic idea of the A-D method is that once the angle-dependent reflection *R* and transmission *T* for a thin slab are known, then *R* and *T* for a slab of arbitrary thickness maybe found by repeatedly doubling the thickness of the original thin slab. If this original slab is sufficiently thin then single scattering approximations can be used to determine *R* and *T*.

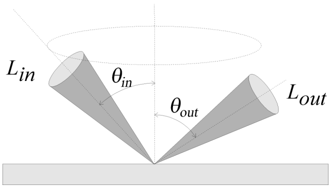

Figure 3.8. *Angularly resolved incident and reflected radiance for a thin slab.*

Consider the slab geometry in Figure 3.8, the resulting irradiance E from conical incident light at angle θ is given by

$$E = \int_0^{\pi/2} L_{in}(\theta_{in})\cos\theta_{in}\, 2\pi \sin\theta_{in}\, d\theta_{in} \tag{3.45}$$

Which may also be expressed as

$$E = \int_0^{1} 2\pi L_{in}(v_{in}) v_{in} dv_{in} \tag{3.46}$$

Where, $v_{in} = \cos\theta$.

Thus, for constant diffuse incident radiance $L_{in} = 1$, the irradiance is

$$E_{diff} = 2\pi \int_0^1 \nu_{in} \, d\nu_{in} = \pi \tag{3.47}$$

The reflection function $R(\nu_{in}, \nu_{out})$ of the slab is defined as the reflected radiance L_{out} in direction ν_{out} as a function of the irradiance E of light incident from direction ν_{in} normalized to I_{diff}.

$$R(\nu_{in}, \nu_{out}) = \frac{dL_{out}(\nu_{out})}{dE(\nu_{in})} \pi \tag{3.48}$$

From this definition of R and by applying Eq. (3.46), the reflected radiance $L_{out}(\nu_{out})$ for an azimuth-independent incident radiance L_{in} is given by

$$L_{out}(\nu_{out}) = \int_0^1 R(\nu_{in}, \nu_{out}) 2\nu_{in} L_{in}(\nu_{in}) \, d\nu_{in} \tag{3.49}$$

Analogous expressions for the transmission function T and the transmitted radiance can be derived in a similar manner.

3.4.2 Matrix approximation and quadrature integration

One of the assumptions, that the A-D method builds on, is that the reflectance and transmittance properties of a thin slab may be approximated well by matrix operations on L_{in}, L_{out}, R and T at a discrete set of angles ν_1, ν_2 … ν_n, i.e.

$$\begin{bmatrix} L_{out}(\nu_1) \\ L_{out}(\nu_2) \\ \cdots \\ L_{out}(\nu_l) \end{bmatrix} = \frac{1}{l} \begin{bmatrix} R(\nu_1,\nu_1) & R(\nu_2,\nu_1) & \cdots & R(\nu_n,\nu_1) \\ R(\nu_1,\nu_2) & R(\nu_2,\nu_2) & \cdots & R(\nu_n,\nu_2) \\ \cdots & \cdots & \cdots & \cdots \\ R(\nu_1,\nu_l) & R(\nu_2,\nu_l) & \cdots & R(\nu_l,\nu_l) \end{bmatrix} \cdot \begin{bmatrix} 2\nu_1 & 0 & \cdots & 0 \\ 0 & 2\nu_2 & \cdots & 0 \\ \cdots & \cdots & \cdots & \cdots \\ 0 & 0 & \cdots & 2\nu_l \end{bmatrix} \cdot \begin{bmatrix} L_{in}(\nu_1) \\ L_{in}(\nu_2) \\ \cdots \\ L_{in}(\nu_l) \end{bmatrix} \tag{3.50}$$

Where $\nu_1 = 1$ and $\nu_l = 0$. However an unlimited number of angles l is not practical, and since the adding-doubling method implies integration of numerous functions it is convenient to choose a limited set of angles $\nu_1, \nu_2, \ldots \nu_{l'}$ based on integration by quadrature.

The principle of e.g. Gauss quadrature[48] is that the integral of a function $f(\nu)$ may be approximated by:

$$\int_a^b f(\nu)d\nu \approx \sum_{i=0}^{l'} w_i f(\nu_i) \tag{3.51}$$

Where the angles ν_i and the weight coefficients w_i are determined simultaneously by solving the equation system

$$\int_a^b \nu^m d\nu = \sum_{i=0}^{l'} w_i f(\nu_i)\,, \quad m = 0,1,2...(2l'-1) \tag{3.52}$$

3.4.3 Adding the layers

Once a proper set of discrete angles have been determined using quadrature, the reflected radiance may be approximated by the matrix expression

$$\mathbf{L}_{out} = \mathbf{R}\mathbf{L}_{in} \tag{3.53}$$

Note, that the multiplication of the reflection function R, the scaling factor $1/n$, and the 2ν factor in Eq. (3.50) all have been compiled into $\mathbf{R}$ in Eq. (3.53). Figure 3.1 illustrates the A-D notation of the reflected and transmitted radiance of a thin slab.

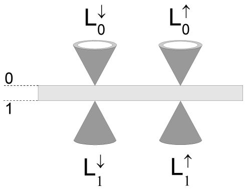

Figure 3.9. *Schematic of reflected and transmitted radiances L of a thin slab at boundary 0 and 1, respectively.*

Now, the matrix equations describing the reflection and transmittance properties of the slab can be written as

$$\begin{aligned} \mathbf{L}_1^{\downarrow} &= \mathbf{T}_{01}\mathbf{L}_0^{\downarrow} + \mathbf{R}_{10}\mathbf{L}_1^{\uparrow} \\ \mathbf{L}_0^{\uparrow} &= \mathbf{T}_{10}\mathbf{L}_1^{\uparrow} + \mathbf{R}_{01}\mathbf{L}_0^{\downarrow} \end{aligned} \tag{3.54}$$

Analogous expressions apply to a second layer with boundaries 1 and 2. Consequently, Juxtaposition of layer_{01} and layer_{12} yields

$$\begin{aligned} \mathbf{L}_2^{\downarrow} &= \mathbf{T}_{02}\mathbf{L}_0^{\downarrow} + \mathbf{R}_{20}\mathbf{L}_1^{\uparrow} \\ \mathbf{L}_0^{\uparrow} &= \mathbf{T}_{20}\mathbf{L}_2^{\uparrow} + \mathbf{R}_{02}\mathbf{L}_0^{\downarrow} \end{aligned} \tag{3.55}$$

Where the transmission and reflectance operators are defined by

$$\begin{aligned} \mathbf{T}_{02} &= \frac{\mathbf{T}_{12}\mathbf{T}_{01}}{\mathbf{I}-\mathbf{R}_{10}\mathbf{R}_{12}} & \mathbf{T}_{20} &= \frac{\mathbf{T}_{10}\mathbf{T}_{21}}{\mathbf{I}-\mathbf{R}_{12}\mathbf{R}_{10}} \\ \mathbf{R}_{20} &= \frac{\mathbf{T}_{12}\mathbf{R}_{10}\mathbf{T}_{21}}{\mathbf{I}-\mathbf{R}_{10}\mathbf{R}_{12}} + \mathbf{R}_{21} & \mathbf{R}_{02} &= \frac{\mathbf{T}_{10}\mathbf{R}_{12}\mathbf{T}_{01}}{\mathbf{I}-\mathbf{R}_{12}\mathbf{R}_{10}} + \mathbf{R}_{01} \end{aligned} \tag{3.56}$$

And $\mathbf{I}$ denotes the identity matrix

$$\mathbf{I} = \begin{bmatrix} 1 & 0 & \dots & 0 \\ 0 & 1 & \dots & 0 \\ \vdots & \vdots & \ddots & \vdots \\ 0 & 0 & \dots & 1 \end{bmatrix} \tag{3.57}$$

In this way, once $\mathbf{R}$ and $\mathbf{T}$ of the thin slab in Figure 3.9 has been determined using an appropriate method. Then the reflectance and the transmittance of a sample with arbitrary thickness may be determined by repeatedly using Eq. (3.54)-(3.56).

Chapter 4

Instrumentation and measurements

As pointed out in Chapter 1, the main subject of this thesis is optical characterization of biological tissue and fluids, partly from non-invasive diffuse reflectance measurements, and partly from goniometric and spatially resolved diffuse spectroscopy on thin slabs or cuvettes. As discussed in Section 3.3.3 the use of diffusion theory for light propagation modeling in turbid biological media is strongly limited by requirements to the range of optical properties and the specific geometry of the setup. Most of the light transport modeling presented here (Paper I-V) is therefore based on numerical Monte Carlo simulations. Consequently, all data analysis is based on multivariate calibration and prediction techniques as well. These analysis techniques are described in detail in Chapter 5, whereas this chapter provides a presentation of the design and development of the applied instrumentation. Furthermore, practical aspects and problems encountered when performing non-invasive reflectance measurements and diffuse in vitro spectroscopy are also discussed. The wavelengths of the presented instrumentation are primarily within the upper visible and the lower near-infrared range ($500 < \lambda < 1000$ nm). Nevertheless, the discussion and argumentation below, in principle, also applies to wavelengths in the vicinity of this range, e.g. the biologically interesting middle and upper near-infrared region ($1.0 < \lambda < 2.5$ µm).

4.1 Skin tissue optical biopsy

Several studies have shown that important information on skin tissue constituents may be extracted from diffuse reflectance measurements on the tissue. However, as a consequence of the similarity principle[15-17], normally only the absorption coefficient μ_a and the reduced scattering coefficient μ'_s can be extracted from such measurements. While, μ_a may provide information on important chromophores, such as, melanin, oxyhemoglobin, and bilirubin[49-55], μ'_s and may be used to characterize the size and concentration of various scattering components in the tissue[20,21,56-60]. Moreover, tissue glucose concentrations may also be correlated to the scattering properties of the tissue[61,62].

4.1.1 Structure and functions of skin tissue

The quantification of tissue chromophores and scattering elements, from diffuse reflectance measurements, is impeded by the fact that human skin tissue is a not a regular homogenous medium. As illustrated by the cross-section in Figure 4.1, skin tissue consists basically of three main layers denoted epidermis, dermis and hypodermis.

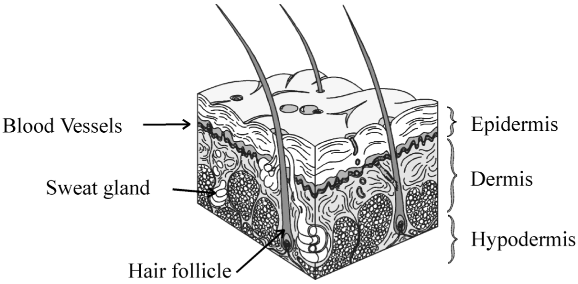

Figure 4.1. *Schematic cross-section of human skin tissue*

The epidermis, which is 50-100 µm thick, may be further divided into three sub-layers: the stratum corneum, the stratum spinosum, and the stratum germinatum (alias the basal layer). The stratum corneum (the outer layer) is about 10-40 µm thick and made up of a compact fibrous configuration of nonviable cells (keratinocytes), which form an effective main barrier to the surroundings. The living keratinocytes are created by in the basal layer, after which they slowly move outward and gradually transform into anuclear nonviable cells. This migration from the basal layer to the stratum corneum takes approximately 14 days. Also located in the basal layer are the melanocytes that produce the pigment melanin, which protects against UV radiation and also is responsible for the skin color. The epidermis is bloodless; hence the nutrition for the cell production in the basal layer diffuses outward from the blood vessels of the dermis.

The dermis, which typically has a thickness of 500 - 3000 µm, is highly vascularized. Besides the rich blood supply, the dermis is made up of skin appendages such as hair follicles and sweat glands, surrounded by fibrous supporting tissue and collagen. Accordingly, the dermis is responsible for most of the skin's mechanical strength.

The subcutaneous tissue (hypodermis) beneath the dermis is mainly composed of lobules of fat separated by collagen bundles and traversed by larger blood vessels, lymphatic vessels, and nerves. As opposed to the vascular system of the dermis, that serve nutritional purposes only, the blood vessels of the subcutaneous capillary and venous plexus also play an important role in the temperature regulation of the human body[63,64].

4.1.2 Diffuse reflectance techniques

Determination of optical properties from diffuse reflectance measurements may be roughly divided into methods based on either time-resolved, frequency-domain, or continuous wave (CW) techniques. Time resolved measurements[65-67] provide information on the path lengths traveled by the photons since the time-of-flight in a homogenous medium is directly proportional to the path length. Hence, it is in principle possible to apply Beer's law (Eq. (2.13)) on the recorded photons path lengths and calculate μ_a.

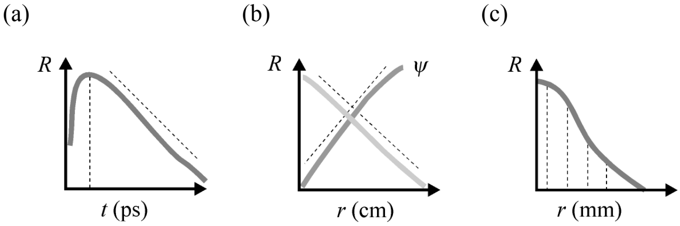

Figure 4.2. *Schematics illustrating the recorded signals from (a) time-resolved, (b) frequency-domain, and (c) spatially resolved diffuse reflectance measurements.*

The schematic in Figure 4.2(a) shows the reflected intensity *R(r)* as a function of the time *t* at a given distance *r*. By means of time-dependent diffusion theory, it can be shown, that the time delay of the peak value of *R(t)* can be related directly to μ'_s, and that μ_a can be determined directly from the slope of the "tail" of the *R(t)* graph[68,69]. However, determination of μ_a and μ'_s in the biological relevant range requires a time-resolution of about 100 ps, thus relatively fast and expensive instrumentation is required.

Determination of μ_a and μ'_s using frequency-domain methods[54,70,71] implies a modulated light source and are based on phase ψ and amplitude measurements of *R(r)* as depicted in Figure 4.2(b). The data obtained from frequency-domain measurements are basically analogous to the Fourier transform of the data from corresponding time-resolved measurements, i.e. no additional information is gained from frequency-domain measurements. Still, compared to time-resolved methods, frequency-domain methods may offer some advantages regarding acquisition time and subsequent data analysis[72]. On the other hand, frequency-domain measurements typically require source-detector separations in the cm range and hence relatively large sample volumes are required.

In the case of CW diffuse reflectance measurements[39,46,73-79] (Figure 4.2(c)), the information on μ_a and μ'_s is embedded in *R(r)* in a nontrivial way (see Eq.(3.42)). A considerable part of the work on determination of optical properties from diffuse reflectance measurements has been focused on either time-resolved or frequency-domain techniques. However, as mentioned above, methods based on these techniques, also require more bulky and expensive equipment, and/or larger sample volumes, which may restrict their implementation in some biomedical applications. Recent work[73,77] (Papers I, III, and VII) has shown that CW based methods may yield absolute determination of the optical properties of tissue with accuracies comparable to time-resolved and frequency-domain techniques. Moreover, CW techniques also imply relatively simple technology and thus enable compact implementation. This make CW based methods well suited for long-time monitoring of skin tissue optical properties, because a probe may be fixed to the skin of a patient and still allow him to move around. Optical biopsies of body cavities or organs are also favored by CW techniques since they allow small-size probes to be implemented in endoscopic instrumentation.

4.1.3 Geometry considerations

The extraction of μ_a and μ'_s from CW *R(r)* measurements is a nontrivial problem, which calls for advanced data analysis in order to determine the optimum positions and number of detectors. There is, however, some regularity in the *R(r)* dependence of μ_a and μ'_s (Paper III), as illustrated in Figure 4.3. The schematic in Figure 4.3(a) shows that $R(r \approx 0)$ is practically invariant with respect to μ_a when μ'_s is kept constant, i.e. there is a virtual "hinge" situated at the source. Likewise, Figure 4.3(b) shows that $R(r_{pivot})$ is practically invariant with respect to μ'_s when μ_a is kept constant, i.e. there is a virtual "pivot joint" situated at r_{pivot}. The experiments in Paper III showed that $r_{pivot} \sim 3$ mm for a biological relevant range of optical properties ($0 < \mu_a < 0.35$ cm^{-1} and $6 < \mu'_s < 16$ cm^{-1}). The graph in Figure 4.3(a) suggests that μ'_s may be determined with good accuracy from *R(r)* data at the hinge exclusively. In order to determine μ_a also, Figure 4.3(b) suggest that $R(r)$ measurements at the pivot joint should be included as well, since $R(r)$ is almost independent of μ'_s here. Although, other authors[78,80] support this argumentation, the experiments in Paper I showed that *R(r)* data at the hinge in conjunction with data well beyond the pivot joint yielded better robustness and accuracy than $R(r)$ data close to the pivot joint. Consequently, source-detector distances well beyond the pivot joint (for typical skin tissue optical properties) were included in the development and design of the instrumentation presented in Paper III.

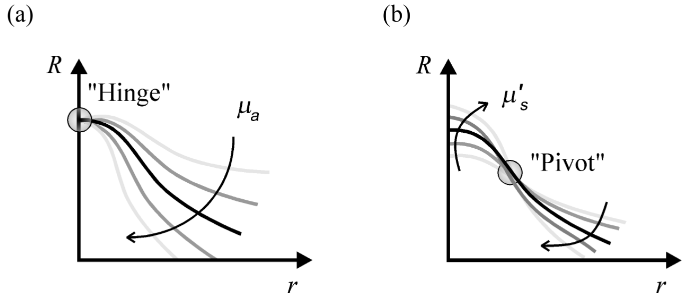

Figure 4.3. *Spatially resolved diffuse reflectance R(r) as a function of μ_a and μ'_s for (a) constant values of μ'_s, and (b) for constant values of μ_a. The "hinge" and "pivot" marks indicate R(r) invariance.*

4.1.4 Contact probes and image reflectometry.

Instrumentation based on CW diffuse reflectance measurements may in general be divided into probes in physical contact with the sample[46,74,76,77,81,82] and non-contact methods[39,83-85] (image reflectometry). The latter type of methods is advantageous in clinical applications because of the non-contact and thus sterile properties, while the former type is superior for compact and portable equipment for long term monitoring. Studies on both type of instrumentation have been carried out in Paper III and Paper IV, respectively. Figure 4.4(a) shows the fiber optic probe system for contact measurements presented in Paper III, and Figure 4.4(b) shows the Fourier transform interferometric imaging system (FTIIS) used for the hyperspectral image reflectometry experiments presented in paper IV. In addition to the sterile advantages of image reflectometry systems, the non-contact operation does not induce any mechanical pressure on the tissue either. Thus the blood perfusion of the tissue is not affected either, as opposed to contact measurements, where this may cause serious interference, when contact measurements are carried out. Another advantage of image reflectometry systems is that the diffuse reflectance from areas of arbitrary size can be collected, simply by using a zoom lens to collect the light. Moreover, complementary conventional images (with diffuse irradiation of the tissue surface) are easy to record. As a result, the tissue samples may be further evaluated by simple visual inspection and/or the optical homogeneity of the samples may be quantified by applying image analysis techniques.

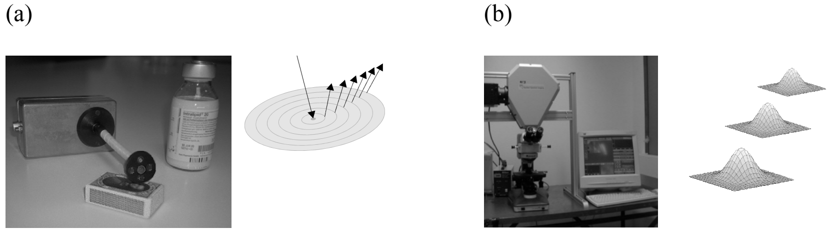

Figure 4.4. *Pictures of (a) the fiber probe system and (b) the Fourier transform interferometric imaging system (SpectraCube ® ASI) applied in Paper III and IV, respectively.*

Figure 4.5 shows a schematic of the fiber optic probe system presented in Paper III. The fiber probe collects the diffuse reflectance in six concentric rings around the source in the range 0.6 - 7.8 mm, in concordance with the discussion in Section 4.1.3. In comparison with a simpler linear configuration; the ring configuration makes the system more robust to any inhomogeneity in the sample. Moreover, it also increases the signal sensitivity at the larger source-detector separations. The light source(s) consists of 4 multiplexed replaceable diode lasers. Thus the wavelengths of the probe may be chosen arbitrarily among available diode lasers. The reflectance is collected simultaneously at all 6 rings and one cycle of successive measurements at the four wavelengths may be performed with a rate of about 100 Hz. This speed is sufficient to record the dynamics of most natural occurring physiological activity including pulse, breathing etc. Thus, in conjunction with appropriate calibration and prediction techniques, the system is capable of real-time determination of μ_a and μ'_s. The fiber probe system was intended as a versatile research tool, and although it is relatively compact it is not designed as a portable tool for long-term monitoring. However, by using LED light sources and integrated electronics, the technology is readily implemented into portable probes dedicated for fixation on the skin and hence suitable for long-term monitoring.

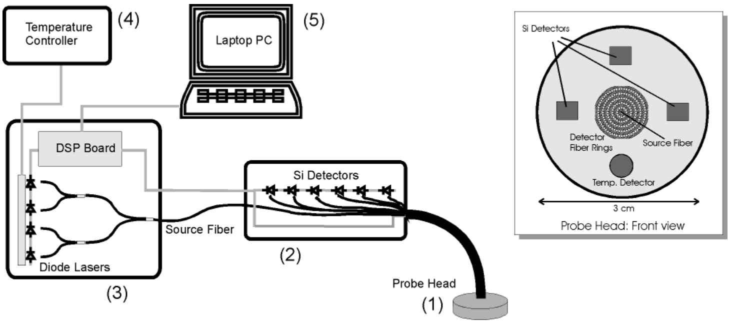

Figure 4.5. *Diagram of fiber optic system for CW R(r) measurements applied in Paper III. (1) Probe head with source and detector optical fibers. (2) Handheld box with photo diodes and amplifier electronics. (3) Stationary box containing a digital signal processing board and diode lasers. (4) External temperature controller. (5) Laptop PC to analyze, display, and store the acquired R(r) data.*

4.1.5 Practical aspects, problems and interferences.

When using the above-mentioned setups for practical measurements a number of problems and interferences are encountered. Some are specific for either the FTIIS setup or the probe system, and some apply in general. The problems and interferences common to both types of setups are mainly associated with the local morphology and physiological dynamics of the skin tissue. First of all, skin tissue is highly inhomogeneous, as pointed out in Section 4.1.1. This makes light modeling complex, i.e. it is difficult to generate proper calibration models and in turn to perform accurate predictions of μ_a and μ'_s . Layered models can be applied, but it has been shown (Paper VI) that the generic form of *R(r)* from a multi-layered geometry is similar to *R(r)* from a single-layer geometry, i.e. it is difficult to distinguish the optical properties of the separate layers and also to determine whether any variation in *R(r)* originate from changes in μ_a or changes in μ'_s. Furthermore, structures such as hair, sweat glands, and blood vessels add to the inhomogeneity as well. In short, any extracted values of μ_a and μ'_s from *R(r)* measurements on skin tissue are a composite of the optical properties of each individual type of tissue in the sample volume. Moreover, according to the discussion in Section 4.1.3, μ'_s is mainly determined from short source-detector separations, while μ_a is determined from larger separations, i.e. different tissue volumes are sampled in order to determine μ_a and μ'_s simultaneously. Both topical and subject-to-subject variations in the skin composition (e.g. melanin content and layer thicknesses) further complicate accurate determination of μ_a and μ'_s. Another frequently occurring problem during measurements of optically weak signals (e.g. scattering due to tissue glucose) is interference from blood perfusion variations. Such variations may be simple pulsatory variations as well as more subtle variations associated with thermoregulation or the psychic state (e.g. shock, blushing, etc).

In addition to the above, there are a number of problems specifically related to optical biopsy on skin tissue using contact probes. First, the static mechanical pressure of the probe may influence the tissue optical properties, e.g. by displacing blood in the sample volume. Second, physical activities of the patient may cause movements of the probe relative to the skin tissue (motion artifacts). Finally, the obstruction of the tissue-air interface, in combination with sweating, may cause long-term changes in the tissue-probe optical coupling. In fact, proper and reproducible tissue-probe coupling is of paramount importance in order to obtain valid results. This is rendered difficult by the rugged and highly scattering structure of the stratum corneum, therefore some sort of fluid or creme is often applied in order to provide a better refractive index match between the probe and the skin. This problem may also be confronted by stripping off the stratum corneum before the probe is mounted. But, as mentioned in Section 4.1.1 above, the stratum corneum will regenerate completely in about 14 days, leaving this approach suitable for relatively short-term measurements only. Because of the coupling difficulties, it would be opportune to employ relative instead of absolute reflectance measurements, that is, to consider the form and shape of *R(r)* only. However, the investigations in Paper I showed that this lead to a significant decrease in the prediction accuracy of μ_a and μ'_s. The problems due to coupling and inhomogeneity may also be addressed either by individual calibration to each patient or by considering relative changes in μ_a and μ'_s only. Still, the basic background optical properties may change considerably during long term monitoring.

There are also several practical problems and drawbacks specifically related to image reflectometry systems as well. First, the measurements have to be corrected for the point-spread function of the imaging system. Secondly, the equipment is not portable. Finally, the acquisition rate is typically relatively low and a considerable amount of data is produced leading to a low analysis rate as well.

4.2 *In vitro* diffuse spectroscopy

In the above discussion on diffuse reflectance measurements, only μ_a and μ'_s were extracted, i.e. μ'_s could not be separated into μ_s and the anisotropy factor g. Consequently, important information on the size and shape of the scattering elements in a sample could not be extracted. As an alternative, all three optical properties (μ_a, μ_s, and g) may be obtained from combined *in vitro* transmittance and reflection measurements on thin samples (e.g. tissue slices or solutions in cuvettes). Such methods are not only interesting for medical purposes, but also for applications in industry and environmental technology. Nevertheless, most present available conventional methods are not able to extract μ_a, μ_s and g simultaneously and hence focus on either the absorption- or the scattering properties; i.e. the scattering effects are treated as interference during absorption measurements or vice versa. Figure 4.6 shows some commonly applied setups for absorption and scattering characterization.

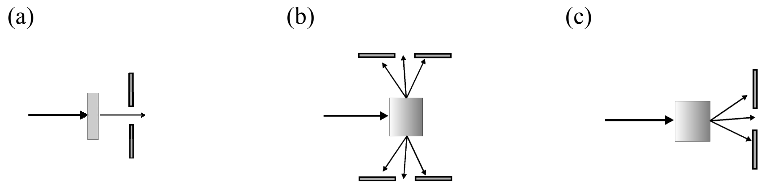

Figure 4.6. *Schematic setups for (a) absorption spectroscopy, and scattering measurements based on (b) turbidimetry, and (c) nephelometry.*

4.2.1 Absorption spectroscopy

Absorption spectroscopy is characterized by measuring the attenuation of light through a cuvette with a well-defined optical path length. It is one of the most commonly used optical techniques for analysis of biological solutions. The solutions are normally quantified by using Beer's law (see Eq. (2.13)), i.e. a linear relationship between the concentration and μ_a is assumed. However, many biological solutions contain scattering components, which also contribute to the attenuation of the light through the samples. In some cases the scattering contribution is either ignored, or more or less effective correction schemes are employed[86,87]. In other cases, the scattering components are removed before the absorption measurements. As an example, this is carried out as in various types of clinical blood analysis, where the blood cells are hemolysed (i.e. the cell walls are crushed either mechanically or chemically) and removed from the sample either by means of sedimentation or centrifugation before the spectroscopic analysis is performed.

4.2.2 Turbidimetry and nephelometry

The concentration or size of scattering components in turbid solutions, may be determined using turbidimetric and nephelometric methods. These methods are based on simplified goniometric *in vitro* measurements of the light re-emitted from a scattering sample. As illustrated by Figure 4.6(b) and (c), turbidimetry is characterized by measuring the attenuation of a collimated beam passing through the sample, while nephelometry is characterized by measuring the intensity of the scattered light, typically at a 90° relative to the incident beam. At hospital laboratories, turbidimetric and nephelometric methods are widely used for so-called optical immunoassays, i.e. procedures measuring the light scattering effects due to formation of immune complexes from antigen-antibody reactions. These measurements are used to quantify human proteins in biological fluids, such as plasma, serum, cerebrospinal fluid, and urine, and thus serve as an important tool for diagnosing diseases and monitoring the effect of treatment. Analogous to unwanted scattering components during absorption spectroscopy, absorption effects may cause serious interference during turbidimetry and nephelometry

4.2.3 Integrating sphere measurements

Diffuse transmittance (T_d) and reflectance (R_d) measurements on thin samples using integrating sphere (IS) setups (see Figure 4.7(a)) have been widely used as a research and reference tool for *in vitro* quantification of μ_a and μ'_s [88-92]. By supplementing IS measurements with collimated transmittance (T_c) measurements, μ'_s may be further separated into μ_s and g.

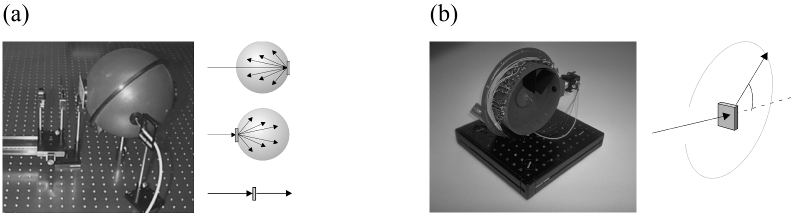

Figure 4.7. *Pictures of (a) the integrating sphere setup. and (b) the goniometer system applied in Paper II and V, respectively.*

Several approaches have been applied to model the transmittance and reflectance properties of thin samples, e.g. methods based on Kubelka-Munk theory[93] and diffusion theory[94], which both provide analytic expression for R_d and T_d. However, these methods are characterized by moderate accuracy and hence most contemporary techniques for extraction of μ_a, μ_s, and g from IS and collimated transmittance measurements are based on more accurate numerical methods such as the inverse adding-doubling (IAD) method[38] or Monte Carlo based methods[89,95]. The IAD method is based on iterative calculations of R_d and T_d, which, however, may prove to be to slow for some applications involving hyperspectral analysis. To this end, a new method, based on a pre-made Monte Carlo database and multiple polynomial fitting, which is faster and more accurate than the IAD method, is presented in Paper II.

4.2.4 Combined spatially resolved and goniometric measurements

As mentioned above, IS measurements are widely used as a reference method for in vitro determination of μ_a, μ_s, and g. Implementation in practical *in vitro* diffuse spectroscopy applications is, however, less prevalent, partially due to the inconvenience of the bulky geometry. Moreover, the sample has to be moved from one port of the sphere to another to accomplish both transmittance and reflectance measurements. Double-sphere setups may be applied to avoid this, but then the measurement accuracy is decreased, due to optical cross-talk between the two spheres. Furthermore, in order to separate μ'_s into μ_s and g collimated transmittance measurements have to be carried out also. Besides being difficult to perform, such measurements also imply moving the sample to a separate setup. The conventional methods for *in vitro* optical characterization of turbid samples, i.e. absorption spectroscopy, turbidimetry, and nephelometry, do not suffer from the inconvenient sample handling of the IS method. Still, they are not capable of simultaneous determination of μ_a, μ_s, and g. Accurate and handy methods for *in vitro* optical characterization of turbid samples is not only interesting for purely medical applications, but also has considerable potentials in areas such as environmental technology and process control in the food industry (e.g. breweries and dairies). To this end, two methods for simultaneous real-time determination of μ_a, μ_s, and g is presented in Paper V. The first method is based on conventional goniometric measurements at multiple angles. The experiments showed that μ_a, μ_s, and g may be determined with good accuracy from the diffuse transmittance at three angles, i.e. 0°, 3°, and 60°, relative to the optical axis. However, measurements at 60° may be inconvenient to implement, thus a second setup, shown in Figure 4.8, was also developed and tested. This method is based on two spatially resolved measurements of the transmittance $T(r)$ and the reflectance $R(r)$ in combination with goniometric transmittance measurements at two relatively small angles (α_1 and α_2). By applying a 1 mm thick cuvette, the data analysis in Paper V showed that the optimum radial distances of the T_d and R_d measurements were about 2.5 mm and that optimum angles α_1 and α_2 were 0° and 3°, respectively, for typical biological optical properties.

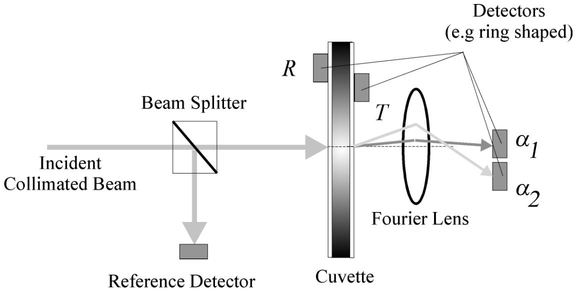

Figure 4.8. *Setup for simultaneous determination of μ_a, μ_s, and g based on spatially resolved reflectance and transmittance measurements in combination with goniometric transmittance measurements.*

As it appears, the output from the setup in Figure 4.8 generates four variables, while in theory only three are needed to determine μ_a, μ_s, and g. Therefore, the dimension of output data are reduced by principal component analysis (see Section 5.2.2), which in turn makes the method more robust to measurement noise interferences. Moreover, as opposed to the collimated transmittance measurements of the IS method, the α_1 and α_2 measurements rely on finite numerical apertures. This all together, enables compact implementation and robust operation of the hybrid goniometric/spatially resolved setup.

Chapter 5

Multivariate data analysis

As described earlier, the task of extracting the optical properties from either diffuse reflectance measurements on a bulk medium or *in vitro* measurements on a thin sample can be broken down to consecutively solving a direct and an inverse problem. The direct problem, i.e. modeling the light propagation, was discussed in Chapter 3. In this chapter the inverse problem is addressed by means of multivariate data analysis (MDA), which, in general terms, deals with optimum extraction of information from a set of measured data by application of relevant mathematical and statistical tools. This rather broad characterization reflects the fact that the many techniques constituting MDA have evolved from a number of rather diverse fields, e.g. economics, psychology, and chemistry. For example, MDA is also frequently referred to as chemometrics due to the extensive use by chemists. Hence, MDA lacks a distinctive definition. Naturally, there exists also a considerable overlap to the more strictly defined methods and techniques in the field of mathematical statistics. In the comprehensive framework of MDA, the inverse problem of extracting the optical properties may be approached in numerous ways, e.g. by applying neural networks[39,96,97] or cluster analysis[97,98]. Both of these approaches can be very effective, especially for describing non-linear relationships. However, they are also somewhat of a "black box" mathematically speaking. In this chapter, the inverse problem is addressed by means of more mathematically "transparent" multivariate calibration techniques[99-101], which give a better insight into the works of the inversion scheme. In the following, there will be a general introduction to some of the traditional methods as well as a presentation of the specific methods and techniques applied in Papers I-VI. Because the principles of conventional spectroscopy is commonly known, this particular application will be used to exemplify the principles of the discussed MDA techniques in parallel with the various applications presented in the papers.

5.1 Framework and basic principles

In short, calibration is to relate a set of implicit properties of a system to a set of explicit properties, or, in other words, to relate some more or less concealed characteristics of the system to a set of directly measurable parameters. These implicit and explicit properties are quantified by a set of so-called dependent and independent variables, denoted y and x, respectively. These are the appellations normally used in MDA, but for mnemonic reasons y and x will be denoted the implicit and explicit variables, respectively, in this context. Moreover, matrices will be denoted by bold capital letters (**X**), vectors by bold lower-case letters (**x**), and the single elements of matrices or vectors by italics (x). Unless otherwise is stated, vectors are assumed to be column vectors. Furthermore, in order to distinguish between known and estimated values of the implicit variables, estimated values are indicated by the "hat" symbol ($\hat{y}$).

The starting point for creating a calibration model is the data matrix **X** containing recorded data from the system in question.

(a)

$$\mathbf{X}=\begin{bmatrix} x_{1,1} & x_{1,2} & \cdots & x_{1,J} \\ x_{2,1} & x_{2,2} & \cdots & x_{2,J} \\ \cdots & \cdots & \cdots & \cdots \\ x_{I,1} & x_{I,2} & \cdots & x_{I,J} \end{bmatrix} \downarrow \text{Samples}$$

$$\rightarrow \text{Explicit (independent) variables}$$

(b)

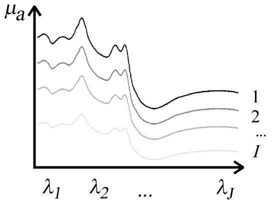

Figure 5.1. *Analogy between (a) data matrix and (b) recorded spectra in the absorption spectroscopy case.*

In the equation in Figure 5.1(b), each row corresponds to a measurement on one sample and the columns are the measured variables collected from each sample. That is, **X** consists of I samples with J explicit variables, which in the spectroscopy example correspond to a series of I spectra measured at J wavelengths, as illustrated in Figure 5.1(b). Analogous to **X**, the inherent properties of the analyzed system, i.e. the implicit variables may be arranged in a system matrix **Y**.

$$\mathbf{Y} = \underset{\rightarrow \text{ Implicit (dependent) variables}}{\begin{bmatrix} y_{1,1} & y_{1,2} & \cdots & y_{1,M} \\ y_{2,1} & y_{2,2} & \cdots & y_{2,M} \\ \cdots & \cdots & \cdots & \cdots \\ y_{I,1} & y_{I,2} & \cdots & y_{I,M} \end{bmatrix}} \downarrow \text{Samples} \tag{5.1}$$

In the absorption spectroscopy case, the M implicit variables of **Y** are identical to the concentrations of M chromophores in the analyzed substance.

5.2 Preprocessing techniques

In some cases it may be convenient or even necessary to carry out data preprocessing, i.e. to prepare the data in **X** in some way before any calibration is performed. In its simplest form preprocessing can be a visual inspection of the data in order to exclude any outliers (i.e. obviously flawed data), from **X** before the calibration. Since, missing data also can corrupt the calibration, it may also be advantageous to fill in qualified guesses, e.g. the mean value of the nearby data. However, such procedures should be carried out with caution, and it should be stressed that missing unique information cannot be restored. If the data appears to be is noisy, it may also be helpful to smooth out the data, e.g. by using Fourier transform filtering or spline interpolation.

5.2.1 Linearization, centering, and scaling

If there is a non-linear relationship between the **Y** and the **X** variables, it can be necessary to perform a linearization of **X** in order to obtain data with a simpler distribution and a more stable variance. In absorption spectroscopy, there is an exponential relationship between the implicit and explicit variables, i.e. the concentrations of the chromophores and the measured transmittances. In this case, the **X** variables are linearized using Beer's law (Eq. (2.13)), i.e. the calibration is not based on the raw transmittance measurements, but on the absorbance $A = -\log_{10}(P_{out} / P_{in})$, i.e.

$$\mathbf{X}_l = -\log_{10}(\mathbf{X}) \tag{5.2}$$

Figure 5.2(a) illustrates the effect of linearization, by taking the logarithm of the **X** data depicted in Figure 5.1.

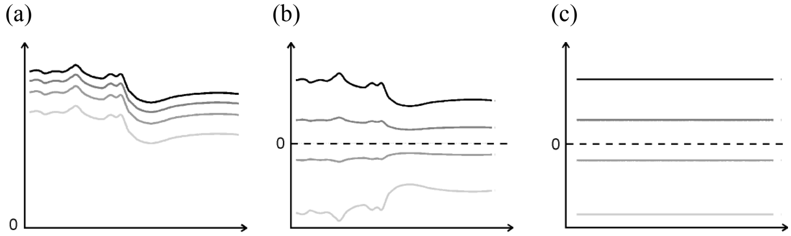

Figure 5.2. *Various types of common preprocessing techniques applied on the spectra in Figure 5.1*; *(a) linearization, (b) centering, and (c) autoscaling.*

During a calibration it often advantageous to remove any baseline, i.e. any constant level in the **X** data, so that the variations in the data are favored over the absolute levels. This can be accomplished by differentiating the **X** data once or twice or, more commonly, by centering the **X** matrix.

$$\mathbf{X}_c = \mathbf{X} - \mathbf{X}_m \tag{5.3}$$

Where

$$\mathbf{X}_m = \mathbf{u}[\bar{x}_1 \quad \bar{x}_2 \quad \ldots \quad \bar{x}_J] \tag{5.4}$$

Here, $\bar{x}_1 \ldots \bar{x}_J$ are the sample means of the J variables in **X** and **u** is a column vector with I elements all equal to one. Thus $\mathbf{X}_m$ becomes a (I,J)-dimensional matrix like **X**. Figure 5.2(b) shows the centered data of the absorption spectra in Figure 5.1. For instance, centering would typically be employed to remove the approximately constant background water absorption during absorption spectroscopy on aqueous solutions. Moreover, centering is also a prerequisite of the very useful principal component analysis method presented in Section 5.3.3 below. Finally, $\mathbf{X}_c$ is also used in the definition of the important covariance matrix of **X**.

$$\mathbf{S} = \frac{1}{I-1}\mathbf{X}'_c\,\mathbf{X}_c \tag{5.5}$$

Where I still denotes the number of samples in **X**.

The covariance matrix **S** provide important information on the spread and the covariance of the variable values in **X.** For instance, the J diagonal elements in **S** are the sample variances var_s of **X**.

$$var_s(\mathbf{X}) = \lfloor s_1^2 \quad s_2^2 \quad \ldots \quad s_J^2 \rfloor = diag(\mathbf{S}) \tag{5.6}$$

Where $s_1 \ldots s_J$ are the standard deviations of the samples in **X**.

In some instances, it may also prove to be necessary to weight, i.e. scale the explicit variables, especially if the explicit variables are measured in different units with large numerical differences. Scaling is accomplished by multiplying each column of **X** by a column specific scaling factor. The scaling factors may be determined in several ways, e.g. by letting the variance of each variable in $\mathbf{X}_c$ be one. This widely used approach is termed autoscaling.

$$\mathbf{X}_{as} = \mathbf{X}_c \mathbf{u} \begin{bmatrix} \frac{1}{s_1} & \frac{1}{s_2} & \ldots & \frac{1}{s_J} \end{bmatrix} \tag{5.7}$$

Where, **u** again is column vector with I elements all equal to one. The effect of autoscaling the spectra from Figure 5.1 is illustrated in Figure 5.2(c).

Finally, when any prediction is performed on the basis of preprocessed calibration data, the measured prediction data should be prepared accordingly. For instance, if the calibration model is based on a centered **X** matrix, the mean values of the calibration data should be subtracted from the $\mathbf{X}_{pred}$ data from which $\hat{\mathbf{Y}}$ is to be predicted, i.e..

$$\mathbf{X} = \mathbf{X}_{pred} - \mathbf{X}_{m,cal} \tag{5.8}$$

5.2.2 Principal component analysis

Principal component analysis (PCA) is a major workhorse in MDA[86,102]. In short, the PCA procedure decomposes the original coordinate system of a centered data matrix $\mathbf{X}_c$ into a new system defined by a set of orthogonal unit vectors ($\mathbf{p}_1$, $\mathbf{p}_2$, …$\mathbf{p}_J$). These vectors are chosen so that the direction of $\mathbf{p}_1$ is the direction where the samples of **X** has the largest variance, while the direction of $\mathbf{p}_2$ is the direction with the second largest variance, etc. The change of coordinate system results in a new set of so-called latent variables, also denoted principal components (PC1, PC2, …etc). The scatter plots in Figure 5.3 illustrates how a data swarm in a three-dimensional **X** system (i.e. $J = 3$) spanned by the vectors $\mathbf{e}_x$, $\mathbf{e}_y$, and $\mathbf{e}_z$ is transformed into the principal component system spanned by $\mathbf{p}_1$, $\mathbf{p}_2$, and $\mathbf{p}_3$.

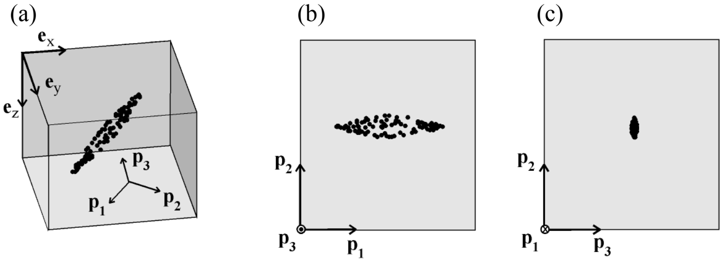

Figure 5.3. *Scatter plots illustrating the PCA decomposition of coordinates from the original* $\mathbf{X}_c$ *system in (a) into the principal components in (b) and (c). Note that, due to the implicit centering in PCA,, the origins of the coordinates systems in (b) and (c) in fact are situated at the center of the data swarm.*

The elements of the **p** vectors are denoted loadings, and the vectors themselves are called loading vectors, since they express the coordinates of the new system in terms of the coordinates of the original **X** space as illustrated in Figure 5.3. Analogous to the explicit variables in the $\mathbf{X}_c$ data matrix, the principal components are arranged in a so-called score matrix **T** defined by:

$$\mathbf{T} = \mathbf{X}_c\mathbf{P} \tag{5.9}$$

Where,

$$\mathbf{P} = [\mathbf{p}_1 \quad \mathbf{p}_2 \quad \cdots \quad \mathbf{p}_J] \tag{5.10}$$

Similarly, the original centered data matrix can be calculated from:

$$\mathbf{X}_c = \mathbf{TP'} \tag{5.11}$$

It can be shown that the loading vectors are the eigenvectors of the covariance matrix **S** of **X** (see Eq. (5.5)) and hence they are characterized by:

$$\lambda_j\mathbf{S} = \mathbf{S}\mathbf{p}_j \tag{5.12}$$

The eigenvalues of **S** in Eq. (5.12), i.e. $\lambda_1 \ldots \lambda_J$, are measures of the variance of the PC's directed along the corresponding loading vectors $\mathbf{p}_1$, $\mathbf{p}_2$, …$\mathbf{p}_J$. Thus, the **P** matrix in

Eqs. (5.9)–(5.11) is determined by sorting the loading vectors according to decreasing eigenvalues. The full set of latent variables of the score matrix **T** **(**i.e. the principal components) carry exact the same amount of information on the analyzed system as the original explicit variables in **X**. So nothing is gained by just shifting from **X** coordinates to principal components. However, as stated above, during PCA the principal components are sorted according to the amount of sample variance in the variable values. Thus, it is likely that, any redundant information in the **X** is isolated in the main principal components, i.e. PC1 or PC2. Likewise, any random noise or interference in **X** is most likely transferred to the inferior higher-numbered principal components. Owing to this, PCA may be used for effective dimension reduction of data matrices with many variables, by including only a few main principal components when generating calibration models.

$$\mathbf{T}_F = \mathbf{X}_c[\mathbf{p}_1 \quad \mathbf{p}_2 \quad \ldots \quad \mathbf{p}_F], \quad F < J \tag{5.13}$$

Thus, PCA may in turn lead to simpler calibration models and more robust predictions. The data analysis presented in Paper III and V provide examples of such dimension reduction using PCA. Furthermore, PCA is also an integral part of the PCR calibration models described in Section 5.3.3 below. Analogous to the other preprocessing techniques discussed above, in any predictions involving PCA, the **X** data used for the predictions based has to be prepared accordingly before the prediction is carried out, i.e.

$$\mathbf{T} = (\mathbf{X}_{pred} - \mathbf{X}_{m,cal})\mathbf{P} \tag{5.14}$$

5.3 Linear calibration models

As stated in Section 5.1 the basic task of calibration and multivariate modeling is to mathematically describe the relationship between the explicit variables of the data matrix **X** and the implicit variables of the system matrix **Y.** The MDA literature provides a variety of methods and techniques for accomplishing this. Many of these are based on variations of one of the four methods introduced in the following. These four methods are denoted; classical least squares (CLS), multiple linear regression (MLR), principal component regression (PCR), and partial least squares (PLS), respectively. All four methods basically assume linear relationships between the explicit and the implicit variables, and furthermore rely on least square regression techniques. However, they are often (with more or less success) applied on non-linear systems as well. But, in most such cases it will be more appropriate to apply an actual non-linear model as discussed in Section 5.4 below.

5.3.1 Classical least squares

The simplest and most intuitive of the four basic calibration models is the classical least squares (CLS) method, which is also referred to as total calibration, because all components of the analyzed medium is determined simultaneously. The mathematical formulation of the CLS model is:

$$\mathbf{X} = \mathbf{YK} + \mathbf{E}_x \tag{5.15}$$

As stated above, and as indicated by the name of the method, the calibration coefficient matrix **K** is determined by least squares regression during which the residual part $\mathbf{E}_x$ representing random noise, non-linearities, etc in **X** is minimized. The CLS model assumes that the contributions from every component of the analyzed system including interferences are known during the calibration. In absorption spectroscopy this implies that the concentrations of all occurring chromophores in the samples have to be included as implicit variables in the system matrix **Y** during calibration, which in some cases is most inconvenient or even impossible. Prediction of $\hat{\mathbf{y}}_i$ from a measured sample $\mathbf{x}_i$ using CLS is described by:

$$\hat{\mathbf{y}}_i = (\mathbf{KK}')^{-1}\mathbf{K}\mathbf{x}_i \tag{5.16}$$

With reference to the spectroscopy example shown in Figure 5.1(b), $\mathbf{x}_i$ is thus a row vector containing the absorption spectrum from the unknown sample i, and $\hat{\mathbf{y}}_i$ is a row vector with the predicted values of the concentrations of the chromophores in the sample.

5.3.2 Multiple linear regression

In the multiple linear regression (MLR) model[103] the problem is turned upside-down as compared to the CLS, i.e. the model is described by:

$$\mathbf{Y} = \mathbf{XB} + \mathbf{E}_y \tag{5.17}$$

This means that a single implicit variable y, can be estimated as a weighted sum of a set of measured explicit variables by using:

$$\hat{y}_{i,m} = \mathbf{x}_i \mathbf{b}_m \tag{5.18}$$

Naturally, the full set of variables $\hat{\mathbf{Y}}$ of a series of samples may also be determined by replacing the row vector $\mathbf{x}_i$ and the column vector $\mathbf{b}_m$ with the matrices **X** and **B** in Eq. (5.18). During MLR, the y-residuals $\mathbf{E}_y$ are minimized, as opposed to the x-residuals $\mathbf{E}_\mathrm{x}$

using the CLS model. Consequently, it is not necessary to quantify all interfering components during calibration, which is the main advantage of MLR compared to CLS. However, in order to obtain valid results using the MLR model, it is important that any interfering agents present in the prediction samples also are included during calibration. The major drawback of the MLR model is that the number of explicit variables is not allowed to exceed the number of samples during calibration, i.e. $J < I$ must apply for $\mathbf{X}$.

5.3.3 Principal component regression

The principal component regression (PCR) model seeks to combine the advantages of the CLS model and the MLR model by applying PCA prior to prediction, and thus circumvent the drawback of the MLR model regarding the limited number of variables. This is accomplished by using the equations in Section 5.2.2 above to reduce the J explicit variables in $\mathbf{X}$ to F principal components in $\mathbf{T}$. In analogy with the MLR model in Eq. (5.17), the PCR model is thus described by

$$\mathbf{Y} = \mathbf{TB} + \mathbf{E}_y \tag{5.19}$$

Again parallel to the MLR model, y may be estimated using

$$\hat{y}_{i,m} = \mathbf{t}_i \mathbf{b}_m \tag{5.20}$$

Where $\mathbf{t}_i$ and $\mathbf{b}_m$ are row- and column vectors, respectively. In this way, the MLR model's advantage of not having to quantify any interferences, and the CLS model's capacity for handling numerous variables is thus both incorporated into the PCR model.

5.3.4 Partial least square regression

The loading vectors, i.e. $\mathbf{p}_1$, $\mathbf{p}_2$… in PCA and thus PCR are determined on the basis of the variations in $\mathbf{X}$ only. Still, if a major part of the variations in $\mathbf{X}$ are not correlated to variations in $\mathbf{Y}$, but caused by random noise, then any structured information on the system may be smeared out into some of the inferior principal components and thus be practically lost. In such cases, it is favorable to apply the partial least squares regression (PLS) model[104], because, it not only seeks to describe the major variations in **X,** but also attempts to isolate the part of the variations which is relevant for the description of $\mathbf{Y}$. Analogous to the PCA method, this is realized by shifting to a new coordinate system defined using a set of unit loading vectors $\mathbf{w}$. However, in the PLS approach, the directions of $\mathbf{w}$ are not determined on the basis of the variance of $\mathbf{X}$, but on the basis of the covariance between $\mathbf{X}$ and $\mathbf{Y}$, i.e.

$$\mathbf{W} = \frac{\mathbf{X'Y}}{|\mathbf{X'Y}|} \tag{5.21}$$

Where

$$\mathbf{W} = [\mathbf{w}_1 \quad \mathbf{w}_2 \quad \dots \quad \mathbf{w}_J] \tag{5.22}$$

The component loading vectors of **W** may also be determined separately by substituting **Y** with **y** in Eq. (5.21), which sometimes provides a better model. The latter approach is termed PLS1, and the former PLS2. The score matrix **T** in the PLS2 approach is defined as

$$\mathbf{T} = \mathbf{X}_c\mathbf{W} \tag{5.23}$$

Hence, the PLS model is characterized by

$$\mathbf{Y} = \mathbf{TB} + \mathbf{E}_y \tag{5.24}$$

And the implicit variables may be estimated using

$$\hat{y}_{i,m} = \mathbf{t}_i\mathbf{b}_m \tag{5.25}$$

Like in Eq. (5.20) all $\hat{y}_{i,m}$ may be determined simultaneously by substituting $\mathbf{t}_i$ and $\mathbf{b}_m$ with **T** and **B** in Eq. (5.25). However, it should be noted that $\mathbf{t}_i$ in Eq. (5.25) is not equal to $\mathbf{t}_i$ in Eq. (5.20).

5.4 Non-linear calibration and prediction

The previous section considered linear calibration models and used traditional absorption spectroscopy and thus predictions of μ_a as a general example. This section will proceed with a presentation of non-linear multivariate methods suitable for predicting, either μ_a and μ'_s, or all three basic optical properties (i.e. μ_a, μ_s, and g) from various combinations of diffuse reflectance and transmittance measurements. Paper II deals with calibration and predictions of μ_a and μ'_s using integrating sphere measurements, i.e. measurements of the total diffuse reflectance R and transmittance T from thin slabs or cuvettes. By applying the terminology lined out previously, the rows of **X** are defined as:

$$\mathbf{x}_i = [R_i \quad T_i] \tag{5.26}$$

Repeated recordings of R and T in the given (μ_a, μ'_s) range thus yield the full data matrix **X** illustrated graphically in Figure 5.4(a). In Paper III, μ_a and μ'_s are extracted from spatially resolved diffuse reflectance measurements. Here, the main part of the analysis was carried out using the reflectance data from the first and sixth detector of the fiber probe described in Paper III. Thus, the rows of **X** are defined as:

$$\mathbf{x}_i = \left[d_{1,i} \quad d_{6,i} \right] \tag{5.27}$$

Where, the full data matrix is illustrated by the surface plots in Figure 5.4. The system matrix **Y** corresponding to the **X** matrices depicted in and Figure 5.4(a) and (b) are in both cases given by

$$\mathbf{y}_i = \left[\mu_{a,i} \quad \mu'_{s,i} \right] \tag{5.28}$$

The **X** - **Y** relationships depicted in Figure 5.4(a) and (b) are clearly non-linear. Hence, in order to carry out proper calibration and prediction either effective linearization of the **X** data, or nonlinear models must be employed, e.g. multiple polynomial regression as demonstrated in Paper II and III.

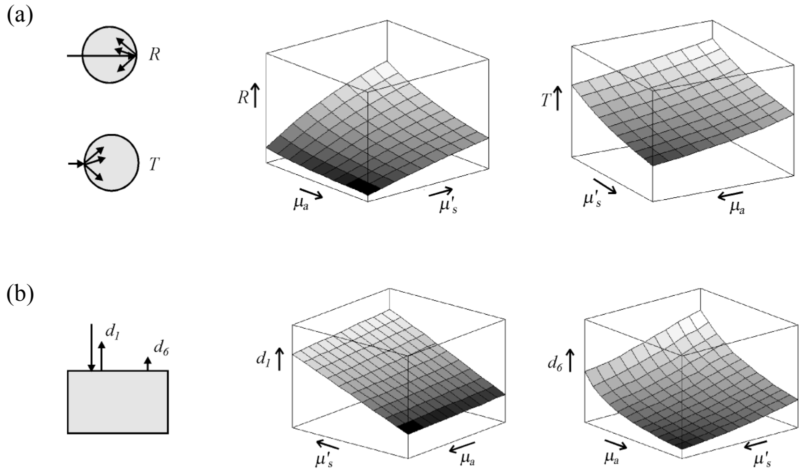

Figure 5.4. *Surface plots as a function of μ_a and μ'_s for (a) integrating sphere measurements of the total diffuse reflectance R and the total diffuse transmittance T, (Paper II) and for (b) spatially resolved diffuse reflectance measurements at detector d_1 and d_6 of the fiber probe system (Paper III).*

5.4.1 Multiple polynomial regression

The non-linear regression approach applied in Paper II, III, and V is based on fitting two functions (g_1 and g_2) of μ_a and μ'_s to **X**, e.g. the data illustrated in Figure 5.4(a) and (b), respectively.

$$\mathbf{X}=\begin{bmatrix} x_{1,1} & x_{1,2} \\ x_{2,1} & x_{2,2} \\ \cdots & \cdots \\ x_{I,1} & x_{I,2} \end{bmatrix}=\begin{bmatrix} g_1(\mu_{a,1},\mu'_{s,1}) & g_2(\mu_{a,1},\mu'_{s,1}) \\ g_1(\mu_{a,2},\mu'_{s,2}) & g_2(\mu_{a,2},\mu'_{s,2}) \\ \cdots & \cdots \\ g_1(\mu_{a,I},\mu'_{s,I}) & g_2(\mu_{a,I},\mu'_{s,I}) \end{bmatrix} \tag{5.29}$$

Where, the functions g_1 and g_2 are double-polynomials defined as

$$g_1(\mu_a,\mu'_s)=\sum_{k=0}^{n}\sum_{l=0}^{n}a_{kl}\mu_a^k\mu'^l_s \quad , \qquad g_2(\mu_a,\mu'_s)=\sum_{k=0}^{n}\sum_{l=0}^{n}b_{kl}\mu_a^k\mu'^l_s \tag{5.30}$$

Accordingly, a_{kl} and b_{kl} are the fitting, i.e. the calibration coefficients determined by least square regression in Eq. (5.29), and n is the order of the resulting double-polynomials. The equation system in Eq. (5.29) may also be expressed in short form by the matrix equation:

$$\mathbf{X}=\mathbf{Y}_{pol}\mathbf{B} \tag{5.31}$$

Where, $\mathbf{Y}_{pol}$ consists of i rows each with $(n+1)^2$ elements, which are identical to the products $\mu_a^k\mu'^l_s$ in Eq. (5.30), while **B** consists of two column vectors, where the elements are a_{kl} and b_{kl}, respectively.

The procedure lined out in Eqs. (5.29) and (5.30) is based on two y variables ($M=2$). However, the procedure may in principle be expanded to any number of y variables, and hence it is denoted multiple polynomial regression (MPR). For instance, MPR with $M=3$ was applied in Paper V to create models using triple-polynomials of the form

$$g_1(\mu_a,\mu_s,g)=\sum_{k=0}^{n}\sum_{l=0}^{n}\sum_{q=0}^{n}a_{klq}\mu_a^k\mu_s^l g^q \ , \qquad g_2=\ldots \ , \qquad g_3=\ldots \tag{5.32}$$

5.4.2 Newton-Raphson method

By applying the MPR method to create non-linear calibration models, it is not possible to carry out subsequent predictions by simple matrix manipulations; instead some sort of numerical root-locating method must be applied in order to estimate $\hat{y}$ from x. There are numerous algorithms for this, each with specific advantages regarding accuracy, speed, and robustness. The Newton-Raphson (N-R) method is perhaps the most widely used, and it turned out to be the best choice for the analyses described in Paper II, III, and V as well. The first step in N-R method is to define the functions $\mathbf{f}(\hat{\mathbf{y}}_i)$ from the fitting functions $\mathbf{g}(\hat{\mathbf{y}}_i)$, e.g. as defined by Eq. (5.30), and the prediction samples x_i from which the $\hat{\mathbf{y}}_i$ variables are to be estimated.

$$\mathbf{f}(\hat{\mathbf{y}}_i) = \begin{bmatrix} g_1(\hat{\mathbf{y}}_i) \\ g_2(\hat{\mathbf{y}}_i) \\ \cdots \\ g_M(\hat{\mathbf{y}}_i) \end{bmatrix} - \begin{bmatrix} x_{i,1} \\ x_{i,2} \\ \cdots \\ x_{i,M} \end{bmatrix} \tag{5.33}$$

The next step is to perform converging iterative estimation of the $\hat{y}$ variables using

$$\left.\begin{aligned} -\mathbf{f}(\hat{\mathbf{y}}_{i,k}) &= \mathbf{J}\mathbf{h}_k \\ \hat{\mathbf{y}}'_{i,k+1} &= \hat{\mathbf{y}}'_{i,k} + \mathbf{h}_k \end{aligned}\right\} k = 1,2,3..... \tag{5.34}$$

Where, $\mathbf{h}$ contains correction terms of $\hat{\mathbf{y}}'_i$, and $\mathbf{J}$ is the Jacobi matrix

$$\mathbf{J} = \begin{bmatrix} \frac{\partial f_1}{\partial y_1} & \cdots & \frac{\partial f_1}{\partial y_j} \\ \vdots & \ddots & \vdots \\ \frac{\partial f_j}{\partial y_1} & \cdots & \frac{\partial f_j}{\partial y_j} \end{bmatrix} \tag{5.35}$$

Naturally, the N-R method can also be used in conjunction with non-polynomial functions, if such provide better calibration models. However, the N-R method always requires that the number of x variables equals the number y variables, i.e. $J = M$ with reference to Figure 5.1(a) and Eq. (5.1). This may be a considerable drawback in applications involving numerous x variables. Still, as it was demonstrated in parts of the analyses in Paper III and V, PCA may be utilized to reduce J explicit variables to M principal components during calibration, and thus subsequently allow the N-R algorithm to be employed for prediction.

5.5 Model validation and optimization

Once a calibration model has been created it is important to characterize the performance of the model as regards prediction errors, robustness, etc. For instance, accuracy and robustness often behave in a diametrical manner; i.e. detailed models may be too sensitive to noise in the prediction measurements and thus produce false or non-converging results. A too detailed model will also track all the noise variations in addition to the structured **X-Y** variations during calibration and lead to incorrect models. Therefore, it is imperative to perform prediction tests yielding quantitative measures of the model performance in order to evaluate and optimize the model for a specific application. In order to get reliable results, any final prediction test should in principle always be carried out using independent sets of calibration and prediction samples. However, for economical reasons or during preliminary analysis of the model it may be convenient to apply the so-called leave-one-out cross validation test, which implies calibration and prediction tests using the same set of samples. However, during a cross validation test, the particular sample used for prediction is excluded from the calibration set, i.e. in case of I samples, cross validation yields I predictions using I different calibration models each based on $I-1$ samples.

5.5.1 Errors, accuracy and precision

The root mean square error e_{RMS} is a widely used measure of errors in MDA and statistics. It has the same units as y and embodies errors of the calibration model, measurement errors, interferences, etc.

$$e_{RMS} = \sqrt{\frac{1}{I}\sum(\hat{y}_i - y_i)^2} \tag{5.36}$$

The mean relative error e_{MR} is also frequently used

$$e_{MR} = \frac{1}{I}\sum\frac{|\hat{y}_i - y_i|}{y_i} \tag{5.37}$$

However, one should be careful in the interpretation of e_{MR}, especially because y_i values close to zero yield much higher relative errors, than y_i values far from zero, despite equal absolute errors. Therefore it often more favorable to apply the mean, relative to the range, error e_{MRR}.

$$e_{MRR} = \frac{1}{I}\sum \frac{|\hat{y}_i - y_i|}{(y_{\max} - y_{\min})} \tag{5.38}$$

When evaluating the performance of calibration models and prediction algorithms it is advantageous to clearly distinguish between accuracy and precision. These two concepts are illustrated graphically in Figure 5.5.

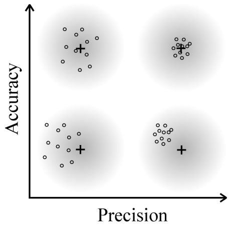

Figure 5.5.
The concepts of accuracy and precision. The "+" *symbol represents the true value, while the* "o" *symbols are predicted values.*

The inaccuracy of a set of predictions is defined as systematic deviation of the estimated values from the true value, and is expressed mathematically by the bias of the estimated values

$$bias(\hat{y}) = \frac{1}{I}\sum \hat{y}_i - y_i \tag{5.39}$$

On the other hand, the imprecision (also called uncertainty) of the predictions refer to the spread of the estimated values around the mean of the estimations. This is expressed mathematically by the population variance of the predictions.

$$var_p(\hat{y}) = \frac{1}{I}\sum (\hat{y}_i - \bar{\hat{y}})^2 \tag{5.40}$$

Note, that the population variance in Eq. (5.40) is not equal to the sample variance defined in Eq. (5.6), i.e.

$$var_p = \frac{I-1}{I} var_s \tag{5.41}$$

Using Eq. (5.36), (5.39), and (5.40) the root mean square error can be rewritten as

$$e_{RMS}(\hat{y}) = \sqrt{var_p(\hat{y}) + bias(\hat{y})^2} \tag{5.42}$$

Thus, while $e_{RMS}(\hat{y})$ is an over-all measure of the calibration and prediction performance of a specific model and a given set of samples, then, as exemplified in Paper II, the bias and the variance may be utilized to evaluate a specific calibration model and prediction algorithm separately. That is, a relatively high $bias(\hat{y})$ value often implies a flawed calibration model, e.g. a poor fit, while a relatively high $var(\hat{y})$ indicates a precarious prediction algorithm and/or a high noise level in the prediction samples.

5.5.2 Over - and underfitting

So-called overfitting or underfitting is a common pitfall when performing calibration and prediction analyses. In all practical applications, the calibration samples contain a certain amount of noise with no relevant information regarding the analyzed system. However, the least squares regression algorithms normally used for calibration do not distinguish between variations due to the structured **X-Y** relationships and random variations due to noise. Thus, if the calibration is too detailed, i.e. the data are overfitted; it will result in a winding calibration model, as illustrated by Figure 5.6(c). Consequently, such a model represents the calibration data exactly, but is a poor approximation to the true **X-Y** relations represented by the dashed line in Figure 5.6(c). Furthermore, the winding form of an overfitted model may put greater demands on the prediction algorithm and cause it to fail occasionally. Note that the same arguments apply to spline interpolation techniques, which is practically equivalent to overfitting (Paper II).

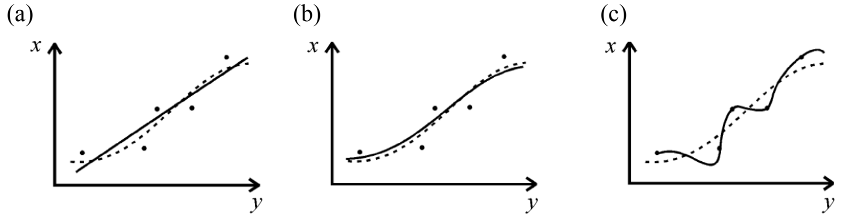

Figure 5.6. *Schematics illustrating (a) underfitted, (b) optimum, and (c) overfitted calibration models. The dashed line represent the true values, the dots are the measured values used for calibration, and the continuous line shows the resulting fit.*

On the other hand, a too simplified calibration, e.g. using a linear model on non-linear data, will produce an underfitted model as illustrated in Figure 5.6(a). Such a model will also yield incorrect predictions. Still, predictions on underfitted models are often more robust than on corresponding overfitted models. Figure 5.6(b) shows an optimum model, which seeks to track the structured information in the data and at the same time ignore any random oscillations due to noise.

The analyses presented in Paper III complements the above discussion on over - and underfitting by concluding that calibration models based on third order polynomials (i.e. $n = 3$ in Eq. (5.29)) were superior to both first and second as well as higher order polynomials.

Acknowledgements

First, I would like to thank the *Danish Academy of Technical Sciences* for granting financial support to the work presented here.

I would also like to thank Erik Bækgaard at *Bang & Olufsen Medicom* for making it possible for me to concentrate on this project for three years. Moreover, I am also grateful for the rewarding discussions and the prompt help provided by my colleagues at B&O Medicom: Paul Erik Fabricius, Torben Dalgaard, and Carsten B. Pedersen.

Finally, I would like to thank Stefan Andersson-Engels and all the other people in the *Medical Optics Group* at *Lund Institute of Technology* for making me feel welcome and for their indulgence regarding the occasional inter-Scandinavian language clutter during the years.

Summary of papers

Paper I describes a method for determining the reduced scattering and absorption coefficients of turbid biological media from the spatially resolved diffuse reflectance. A Sugeno Fuzzy Inference System in conjunction with data pre-processing techniques is employed to perform multivariate calibration and prediction on reflectance data generated by Monte Carlo simulations. The pre-processing consists of, either Principal Component Analysis, or a new extended curve-fitting procedure originating from diffusion theory. With reference to practical applications it is also discussed how the prediction accuracy is affected by (a) using relative instead of absolute reflectance data, (b) by imposing measurement noise on the reflectance data, and (c) by changing the number and position of detectors.

Paper II presents a new method for extracting optical properties from integrating sphere measurements on thin biological samples. The method is based on multivariate calibration techniques involving Monte Carlo simulations, multiple polynomial regression, and a Newton-Raphson algorithm for solving nonlinear equation systems. Similar tests using data from integrating sphere measurements on dye/latex micro-sphere phantoms lead to mean errors less than 1.7 % between predicted and theoretically calculated values. Comparisons showed that the new method was more robust and typically 5- 10 times as fast and accurate as two other analogous methods, i.e. the Inverse Adding-Doubling method and the Monte Carlo Spline Interpolation method.

Paper III describes a compact, fast, and versatile fiber optical probe system for real-time determination of tissue optical properties from spatially resolved continuous wave diffuse reflectance measurements. The system collects one set of reflectance data from six source-detector distances at four arbitrary wavelengths with a maximum overall sampling rate of 100 Hz. The four wavelengths of the current configuration are 660, 785, 805 and 974 nm, respectively. Multivariate calibration techniques based on 2-D polynomial fitting are employed to extract and display the absorption and reduced scattering coefficients in real-time mode. Results from preliminary *in vivo* skin tissue measurements are also presented and discussed.

Paper IV reports on how absorption and reduced scattering spectra of turbid media was quantified using a non-contact imaging approach based on a Fourier transform interferometric imaging system (FTIIS). The system was used to collect hyperspectral images of the steady-state diffuse reflectance from a set of homogenous, semi-infinite turbid phantoms within the spectral region of 550-850 nm. Monte Carlo simulations were fit to the recorded hyperspectral images in order to quantify the absorption and scattering spectra. A simple and effective calibration approach was introduced to account for the instrument response. Using reflectance data both close to and far from the source (0.5-6.5 mm), The absorption and reduced scattering coefficients could be predicted with an error of 7% and 3%, respectively.

Paper V presents a novel and accurate method for real-time determination of the absorption coefficient, the scattering coefficient, and the anisotropy factor of thin turbid samples. The three optical properties are determined using multivariate calibration on on Monte Carlo simulated recordings of the angularly resolved transmittance and the spatially resolved diffuse reflectance and transmittance. The applied calibration and prediction techniques are based on multiple polynomial regression in combination with a Newton-Raphson algorithm. Numerical test showed mean prediction errors of approximately 0.5 % for all three optical properties within ranges typical for biological media. Finally, a setup for practical implementation of the presented method is suggested.

Paper VI considers two different skin structure models. The first structure consists of epidermis, dermis/blood, and subcutaneous tissue. The second structure consists of epidermis/dermis, adipose tissue and muscle tissue. A new solution based on diffusion theory of the CW local diffuse reflectance from a three-layered skin tissue structure is presented. Comparisons with Monte Carlo simulations were carried out favorably. It is shown that the functional form of the radial dependence of the diffuse reflectance from multilayer and single layer models are identical. The sensitivity of the local diffuse reflectance as a function of the optical properties of separate layers is also discussed. As well as the influence on the local diffuse reflectance with changes in the optical properties corresponding to normal changes in tissue glucose concentration and blood volume.

Paper VII presents a comparative study of the performance of two systems used for determining the absorption and reduced scattering coefficients at 785 nm; one spatially resolved and one time-resolved. The spatially resolved system recorded the diffuse reflectance from a diode laser by means of a fiber-bundle probe in contact with the sample. The time-resolved system utilized ultra-short laser pulses and a single-photon counting detection scheme. Additional measurements were made with an integrating sphere set-up.

The authors contribution to the papers

- All experimental work, data analysis, and writing of Papers II, III, and V.
- All experimental work and writing of Paper I, as well as parts of the data analysis.
- Parts of the experimental work and data analysis of Papers IV, VI, and VII.

References

1. A.J. Welch, M.J.C. van Gemert, W.M. Star and B.C. Wilson, Definitions and overview of tissue optics, in *Optical-Thermal Response of Laser-Irradiated Tissue,* eds. A.J. Welch and M.J.C. van Gemert, (Plenum Press, New York, NY, 1995).

2. V. Tuchin, *Tissue Optics: Light Scattering Methods and Instruments for Medical Diagnosis*, (SPIE, Washington DC, 2000).

3. E. Hecht, *Optics*, (Addison-Wesley, Reading, 1987).

4. D.K. Cheng, *Field and wave electromagnetics*, (Addison-Wesley, Reading, 1989).

5. G. Kristensson, *Elektromagnetisk vågutbredning*, (Studentlitteratur, Lund, 1997).

6. C.F. Bohren and D.R. Huffman, *Absorption and scattering of light by small particles*, (John Wiley & Sons, Inc., New York, NY, 1983).

7. P.W. Atkins, *Physical chemistry*, (Oxford University Press, Oxford, UK, 1982).

8. S. Svanberg, *Atomic and molecular spectroscopy*, (Springer, 1997).

9. F.A. Duck, *Physical Properties of Tissue*, (Academic Press Ltd., London, 1990).

10. S.L. Jacques and D.J. McAuliffe, The melanosome: threshold temperature for explosive vaporization and internal absorption coefficient during pulsed laser irradiation, *Photochem. Photobiol.* **53**, 769-775 (1991).

11. S.A. Prahl, Tabulated molar extinction coefficient for hemoglobin in water, http://omlc.ogi.edu/spectra/hemoglobin/summary.html, Accessed October 6, 1999, (1998).

12. G.M. Hale and M.R. Querry, Optical constants of water in the 200-nm to 200-µm wavelength region, *Appl. Opt.* **12**, 555-563 (1973).

13. H.C. van de Hulst, *Light scattering by small particles*, (Wiley, New York, NY, 1957).

14. L.G. Henyey and J.L. Greenstein, Diffuse radiation in the galaxy, *Astrophys. J.* **93**, 70-83 (1941).

15. R. Graff, J.G. Aarnoudse, M. de and W. Jentink, Similarity relations for anisotropic scattering in absorbing media, *Opt. Eng.* **32**, 244-252 (1993).

16. D.R. Wyman, M.S. Patterson and B.C. Wilson-BC, Similarity relations for anisotropic scattering in Monte Carlo Simulations of deeply penetrating neutral particles, *J. Comp. Phys.* **81**, 137-150 (1989).

17. H.C. van de Hulst, *Multiple Light Scattering*, (Academic, New York, 1980).

18. A. Ishimaru, *Electromagnetic wave propagation, radiation, and scattering*, (Prentice-Hall, Inc., New Jersey, 1991).

19. D. Barnett, Matlab algorithms for Mie scattering calculations, http://www.lboro.ac.uk/departments/el/research/optics/matmie/mfiles.html, (2000).

20. I.S. Saidi, S.L. Jacques and S.K. Tittel, Mie and Rayleigh modeling of visible-light scattering in neonatal skin, *Appl. Opt.* **34**, 7410-7418 (1995).

21. J.R. Mourant, J.P. Freyer, A.H. Hielscher, A.A. Eick, D. Shen and T.M. Johnson, Mechanisms of light scattering from biological cells relevant to noninvasive optical-tissue diagnotics, *Appl. Opt.* **37**, 3586-3593 (1998).

22. B. Beauvoit, S.M. Evans, T.W. Jenkins, E.E. Miller and B. Chance, Correlation between the light scattering and the mitochondrial content of normal tissues and transplantable rodent tumors, *Anal. Biochem.* **226**, 167-174 (1995).

23. R. Cubeddu, A. Pifferi, P. Taroni, A. Torricelli and G. Valentini, Noninvasive absorption and scattering spectroscopy of bulk diffusive media: An application to the optical characterization of human breast, *Appl. Phys. Lett.* **74**, 874-876 (1999).

24. S.J. Matcher, M. Cope and D.T. Delpy, *In vivo* measurements of the wavelength dependence of tissue-scattering coefficients between 760 and 900 nm measured with time-resolved spectroscopy, *Appl. Opt.* **36**, 386-396 (1997).

25. W.-F. Cheong, S.A. Prahl and A.J. Welch, A review of the optical properties of biological tissues, *IEEE J. Quant. Electr.* **26**, 2166-2185 (1990).

26. J.S. Dam, T. Dalgaard, P.E. Fabricius and S. Andersson-Engels, Multiple polynomial regression method for determination of biomedical optical properties from integrating sphere measurements, *Appl. Opt.* **39**, 1202-1209 (2000).

27. S.T. Flock, S.L. Jacques, B.C. Wilson, W.M. Star and M.J.C. van Gemert, Optical properties of Intralipid: A phantom medium for light propagation studies, *Lasers Surg. Med.* **12**, 510-519 (1992).

28. H.J. van Staveren, C.J.M. Moes, J. van Marle, S.A. Prahl and M.J.C. van Gemert, Light scattering in Intralipid-10 % in the wavelength range of 400-1100 nm, *Appl. Opt.* **30** , 4507-4514 (1991).

29. A. Ishimaru, *Wave propagation and scattering in random media*, (Academic Press, New York, NY, 1978).

30. S. Chandrasekar, *Radiative transfer*, (Oxford University Press, London, England, 1960).

31. K.M. Case and P.F. Zweifel, Fundamentals, in *Linear transport theory,* (Addison-Wesley Publishing Co., Reading, MA, 1967).

32. K.M. Case and P.F. Zweifel, Numerical methods, in *Linear transport theory,* (Addison-Wesley Publishing Co., Reading, MA, 1967).

33. W.M. Star, Diffusion theory of light transport, in *Optical-Thermal Response of Laser-Irradiated Tissue,* eds. A.J. Welch and M.J.C. van Gemert, (Plenum Press, New York, NY, 1995).

34. S.L. Jacques and L. Wang, Monte Carlo modeling of light transport in tissues, in *Optical-Thermal Response of Laser-Irradiated Tissue,* eds. A.J. Welch and M.J.C. van Gemert, (Plenum Press, New York, NY, 1995).

35. S.A. Prahl, The adding-doubling method, in *Optical-Thermal Response of Laser-Irradiated Tissue,* eds. A.J. Welch and M.J.C. van Gemert, (Plenum Press, New York, NY, 1995).

36. G.N. Plass, G.W. Kattawar and F.E. Catchings, Matrix operator theory of radiative transfer. 1: Rayleigh scattering, *Appl. Opt.* **12**, 314-329 (1973).

37. J.W. Pickering, S.A. Prahl, N. van Wieringen, J.F. Beek, H.J.C.M. Sterenborg and M.J.C. van Gemert, Double-integrating-sphere system for measuring the optical properties of tissue, *Appl. Opt.* **32**, 399-410 (1993).

38. S.A. Prahl, M.J.C. van Gemert and A.J. Welch, Determining the optical properties of turbid media by using the adding-doubling method, *Appl. Opt.* **32**, 559-568 (1993).

39. A. Kienle, L. Lilge, M.S. Patterson, R. Hibst, R. Steiner and B.C. Wilson, Spatially resolved absolute diffuse reflectance measurements for noninvasive determination of the optical scattering and absorption coefficients of biological tissue, *Appl. Opt.* **35**, 2304-2314 (1996).

40. S.T. Flock, B.C. Wilson and M.S. Patterson, Monte Carlo modeling of light propagation in highly scattering tissue - II: Comparison with measurements in phantoms, *IEEE Trans. Biomed. Eng.* **36**, 1169-1173 (1989).

41. L. Wang, S.L. Jacques and L. Zheng, MCML-Monte Carlo modeling of light transport in multi-layered tissues, *Computer Methods and Programs in Medicine* **47**, 131-146 (1995).

42. T.J. Pfefer, J. Kehlet Barton, E.K. Chan, M.G. Ducros, B.S. Sorg, T.E. Milner and A.J. Welch, A three-dimensional modular adaptable grid numerical model for light propagation during laser irradiation of skin tissue, *IEEE Journal of selected topics in Quantum Electronics* **2**, 934-942 (1996).

43. S. Bartel and A.H. Hielscher, Monte Carlo Simulations of the Diffuse Backscattering Mueller Matrix for Highly Scattering Media, *Appl. Opt.* **39**, 1580-1588 (2000).

44. M.J. Racovic, G.W. Kattawar, M. Mehrubeoglu, B.D. Cameron, L. Wang, S. Rasteger and G. Cote, Light Backscattering Polarization Patterns from Turbid Media: Theory and Experiment, *Appl. Opt.* **38**, 3399-3408 (1999).

45. A. Pifferi, P. Taroni, G. Valentini and S. Andersson-Engels, Real-time method for fitting time-resolved reflectance and transmittance measurements with a Monte Carlo model, *Appl. Opt.* **37**, 2774-2780 (1998).

46. T.J. Farrell, M.S. Patterson and B. Wilson, A diffusion theory model of spatially resolved, steady-state diffuse reflectance for noninvasive determination of tissue optical properties *in vivo*, *Med. Phys.* **19**, 879-888 (1992).

47. L.V. Wang and S.L. Jacques, Source of error in calculation of optical diffuse reflectance from turbid media using diffusion theory, *Comp. Meth. Prog. Biomed.* **61**, 163-170 (2000).

48. S.V. Chapra and R.P. Canale, *Numerical Methods for Engineers*, (MacGraw-Hill, 1997).

49. J.W. Feather, D.J. Ellis and G. Leslie, A portable reflectometer for the rapid quantification of cutaneous haemoglobin and melanin, *Phys. Med. Biol.* **33**, 711-722 (1988).

50. S.L. Jacques, Reflectance spectroscopy with optical fiber devices, and transcutaneous bilirubinometers, in *Biomedical optical instrumentation and laser-assisted biotechnology,* eds. A.M. Verga Scheggi, S. Martellucci, A.N. Chester and R. Pratesi, pp. 83-94 (Kluwer Academic Publishers, Dordrecht, 1996).

51. M.A. Franceschini, E. Gratton and S. Fantini, Noninvasive optical method of measuring tissue and arterial saturation: an application to absolute pulse oximetry of the brain, *Opt. Let.* **24**, 829-831 (1999).

52. C.E. Elwell, M. Cope, A.D. Edwards, J.S. Wyatt, D.T. Delpy and E.O.R. Reynolds, Quantification of adult cerebral hemodynamics by near-infrared spectroscopy, *J. Appl. Physiol.* **77**, 2753-2760 (1994).

53. B. Chance, Near-infrared images using continuous, phase-modulated, and pulsed light with quantitation of blood and blood oxygenation., *Ann. N. Y. Acad. Sci.* **838**, 29-45 (1998).

54. J.B. Fishkin, P.T.C. So, A.E. Cerussi, S. Fantini, M.A. Franceschini and E. Gratton, Frequency-domain method for measuring spectral properties in multiple-scattering

media - Methemoglobin absorption-spectrum in a tissuelike phantom, *Appl. Opt.* **34**, 1143-1155 (1995).

55. R.A. Weersink, J.E. Hayward, K.R. Diamond and M.S. Patterson, Accuracy of noninvasive *in vivo* measurements of photosensitizer uptake based on a diffusion model of reflectance spectroscopy, *Photochem. Photobiol.* **66**, 326-335 (1997).

56. S.L. Jacques, Origins of tissue optical properties in the UVA, Visible, and NIR regions, eds. R.R. Alfano and J.G. Fujimoto, pp. 364-369 (Optical Society of America, 1996).

57. A.H. Hielscher, J.R. Mourant and I.J. Bigio, Influence of particle size and concentration on the diffuse backscattering of polarized light from tissue phantoms and biological cell suspensions, *Appl. Opt.* **36**, 125-135 (1997).

58. J.R. Mourant, J. Boyer, A.H. Hielscher and I.J. Bigio, Influence of scattering phase function on light transport measurements in turbid media performed with small source-detector separations, *Opt. Lett.* **21**, 546-548 (1996).

59. N. Mohandas, Y.R. Kim, D.H. Tycko, J. Orlik, J. Wyatt and W. Groner, Accurate and independent measurement of volume and hemoglobin concentration of individual red cells by laser light scattering, *Blood* **68**, 506-513 (1986).

60. F. Bevilacqua, P. Marquet, O. Coquoz and C. Depeursinge, Role of tissue structure in photon migration through breast tissues, *Appl. Opt.* **36**, 44-51 (1997).

61. J.T. Bruulsema, J.E. Hayward, T.J. Farrell, M.S. Patterson, L. Heinemann, M. Berger, T. Koschinsky, C.J. Sandahl, H. Orskov, M. Essenpreis, R.G. Schmelzeisen and D. Bocker, Correlation between blood glucose concentration in diabetics and noninvasively measured tissue optical scattering coefficient, *Opt. Let.* **22**, 190-192 (1997).

62. J.S. Maier, S.A. Walker, S. Fantini, M.A. Franceschini and E. Gratton, Possible correlation between blood glucose concentration and the reduced scattering coefficient of tissues in the near infrared, *Optics Letters.* **19**, 2062-2064 (1994).

63. R.H. Champion, J.L. Burton and F.J.G. Ebling, *Textbook of Dermatology*, (Blackwell, Oxford, 1992).

64. W.F. Ganong, *Review of Medical Physiology*, (Appleton & Lange, Connecticut, 1989).

65. M.S. Patterson, B. Chance and B.C. Wilson, Time resolved reflectance and transmittance for the non-invasive measurement of optical properties, *Appl. Opt.* **28**, 2331-2336 (1989).

66. S. Andersson-Engels, R. Berg, A. Persson and S. Svanberg, Multi-spectral tissue characterization using time-resolved detection of diffusely scattered white light, *EQEC European Quantum Electronics Conference*, Firenze, Italy, 1993.

67. R. Cubeddu, A. Pifferi, P. Taroni, A. Torricelli and G. Valentini, Experimental test of theoretical models for time-resolved reflectance, *Med. Phys.* **23**, 1625-1633 (1996).

68. R.F. Bonner, R. Nossal, S. Havlin and G.H. Weiss, Model for photon migration in turbid biological media, *J. Opt. Soc. Am. A* **4**, 423-432 (1987).

69. A.H. Gandjbakhche, G.H. Weiss, R.F. Bonner and R. Nossal, Photon path-length distributions for transmission through optically turbid slabs, *Phys. Rev. E: Statistical Physics* **48**, 810-818 (1993).

70. B. Chance, M. Cope, E. Gratton, N. Ramanujam and B. Tromberg, Phase measurements of light absorption and scatter in human tissue, *Rev. Sci. Instrum.* **69**, 3457-3481 (1998).

71. S. Fantini, M.A. Franceschini-Fantini, J.S. Maier, S.A. Walker, B. Barbieri and E. Gratton, Frequency-domain multichannel optical detector for noninvasive tissue spectroscopy and oximetry, *Opt. Eng.* **34**, 32-42 (1995).

72. J.S. Maier, S.A. Walker and E. Gratton, Frequency-domain optical spectroscopy and imaging of tissues, in *Biomedical Optical Instrumentation and laser-assisted Biotechnology,* eds. A.M. Verga Scheggi, S. Martellucci, A.N. Chester and R. Pratesi, pp. 121-142 (Kluwer Academic Publishers, Dordrecht, 1995).

73. P. Marquet, F. Bevilacqua, C. Depeursinge and E.B. de Haller, Determination of reduced scattering and absorption coefficients by a single charge-coupled-device array measurement, part I: comparison between experiments and simulations, *Opt. Eng.* **34**, 2055-2063 (1995).

74. R. Bays, G. Wagnières, D. Robert, D. Braichotte, J.F. Savary, P. Monnier and H. van den Bergh, Clinical determination of tissue optical properties by endoscopic spatially resolved reflectometry, *Appl. Opt.* **35**, 1756-1766 (1996).

75. J.R. Mourant, T. Fuselier, J. Boyer, T.M. Johnson and I.J. Bigio, Predictions and measurements of scattering and absorption over broad wavelength ranges in tissue phantoms, *Appl. Opt.* **36**, 949-957 (1997).

76. M.G. Nichols, E.L. Hull and T.H. Foster, Design and testing of a white-light, steady-state diffuse reflectance spectrometer for determination of optical properties of highly scattering systems, *Appl. Opt.* **36**, 93-104 (1997).

77. R. Doornbos, R. Lang, M. Aalders, F. Cross and H.J.C.M. Sterenborg, The determination of in vivo human tissue optical properties and absolute chromophore concentrations using spatially resolved steady-state diffuse reflectance spectroscopy, *Phys. Med. Biol.* **44**, 967-981 (1999).

78. G. Kumar and J.M. Schmitt, Optimal probe geometry for near-infrared spectroscopy of biological tissue, *Appl. Opt.* **36**, 2286-2293 (1997).

79. J.M. Schmitt, G.X. Zhou, E.C. Walker and R.T. Wall, Multilayer model of photon diffusion in skin, *J. Opt. Soc. Am.* **7**, 2141-2153 (1990).

80. J.R. Mourant, I.J. Bigio, D.A. Jack, T.M. Johnson and H.D. Miller, Measuring absorption coefficients in small volumes of highly scattering media: source-detector separations for which path lengths do not depend on scattering properties, *Appl. Opt.* **36**, 5655-5661 (1997).

81. E.L. Hull, M.G. Nichols and T.H. Foster, Quantitative broadband near-infrared spectroscopy of tissue-simulating phantoms containing erythrocytes, *Phys. Med. Biol.* **43**, 3381-3404 (1998).

82. F. Bevilacqua, D. Piguet, P. Marquet, J.D. Gross, B.J. Tromberg and C. Depeursinge, In vivo local determination of tissue optical properties: Applications to human brain, *Appl. Opt.* **38**, 4939-4950 (1999).

83. S.L. Jacques, A. Gutsche, J. Schwartz, L. Wang and F. Tittel, Video reflectometry to specify optical properties of tissue *in vivo*, in *Medical Optical Tomography: Functional Imaging and Monitoring,* eds. G.J. Müller, B. Chance, R.R. Alfano,

S.R. Arridge, J. Beuthan, E. Gratton, M. Kaschke, B.R. Masters, S. Svanberg and P. van der Zee, pp. 211-226 (SPIE Optical Engineering Press, Bellingham, Washington, USA, 1993).

84. L. Wang and S.L. Jacques, Use of a laser beam with an oblique angle of incidence to measure the reduced scattering coefficient of a turbid medium, *Appl. Opt.* **34**, 2362-2366 (1995).

85. R. Splinter, G.A. Nanney, L. Littman, C.H. Chuang, R.H. Svenson, J.R. Tuntelder and G.P. Tatsis, Monitoring tissue optical characteristics in-situ using a CCD camera., *Lasers Life Sci.* **6**, 15 (1994).

86. K.M. Cooney, K.W. Gossage, M.J. McShane, M. Motamedi and G. Cote, Development of an optical system for the detection of oral cancer using near-infrared spectroscopy, Proc.IEEE Eng.Med.Biol. vol. **20**, (1998).

87. H. Martens and R. Steiner, Extended multiplicative signal correction and spectral interference subtraction: new preprocessing methods for near infrared spectroscopy, *J. Appl. Physiol.* **9**, 625-635 (1991).

88. A.M.K. Nilsson, R. Berg and S. Andersson-Engels, Measurements of the optical properties of tissue in conjunction with photodynamic therapy, *Appl. Opt.* **34**, 4609-4619 (1995).

89. A.M.K. Nilsson, G.W. Lucassen, W. Verkruysse, S. Andersson-Engels and M.J.C. van Gemert, Changes in optical properties of human whole blood in vitro due to slow heating, *Photochem. Photobiol.* **65**, 366-373 (1997).

90. A. Roggan, M. Friebel, K. Dörschel, A. Hahn and G. Müller, Optical properties of circulating human blood in the wavelength range 400 - 2500 nm, *J. Biomedical Optics* **4**, 36-46 (1999).

91. A.N. Yaroslavsky, I.V. Yaroslavsky, T. Goldbach and H.J. Schwarzmaier, Influence of the Scattering Phase Function Approximation on the Optical Properties of Blood Determined from the Integrating Sphere Measurements, *J. Biomed. Opt.* **4**, 47-53 (1998).

92. J.F. Beek, P. Blokland, P. Posthumus, M. Aalders, J.W. Pickering, H.J.C.M. Sterenborg and M.J.C. van Gemert, *In vitro* double-integrating-sphere optical

properties of tissues between 630 and 1064 nm, *Phys. Med. Biol.* **42**, 2255-2261 (1997).

93. P. Kubelka, New contributions to the optics of intensely light-scattering materials. Part II: nonhomogeneous layers, *J. Opt. Soc. Am.* **44**, 330-335 (1954).

94. J. Reichmann, Determination of absorption and scattering coefficients for nonhomogeneous media. 1: Theory, *Apl. Opt.* **12**, 1811-1815 (1973).

95. CR. Simpson, M. Kohl, M. Essenpreis and M. Cope, Similarity relations for anisotropic scattering in Monte Carlo Simulations of deeply penetrating neutral particles, *Phys. Med. Biol.* **43**, 2465-2478 (1998).

96. T.J. Farrell, B.C. Wilson and M.S. Patterson, The use of a neural network to determine tissue optical properties from spatially resolved diffuse reflectance measurements, *Phys. Med. Biol.* **37**, 2281 (1992).

97. I.J. Bigio, S.G. Bown, G. Briggs, C. Kelley, S. Lakhani, D. Pickard, P.M. Ripley, I.G. Rose and C. Saunders, Diagnosis of breast cancer using elastic-scattering spectroscopy: preliminary clinical results, *J. Biomed. Opt.* **5**, 221-228 (2000).

98. T. Tagaki and M. Sugeno, Fuzzy identifications of systems and its applications to modelling and control, *IEEE Trans. Syst. Man. Cybern.* **15**, 116-132 (1985).

99. R. Bro, *Håndbog i multivariabel kalibrering*, (The Royal Veterinary and Agricultural University, Copenhagen, 1996).

100. H. Martens and T. Naes, *Multivariate Calibration*, (Wiley & Sons Ltd, 1991).

101. K.H. Esbensen, *Multivariate data analysis - in practice*, (Camo, Oslo, 2000).

102. A.M.K. Nilsson, D. Heinrich, J. Olajos and S. Andersson-Engels, Near infrared diffuse reflection and laser-induced fluorescence spectroscopy for myocardial tissue characterisation, *Spectrochim. Acta* **53**, 1901-1912 (1997).

103. C. Eker, S. Montán, E. Jaramillo, K. Koizumi, C. Rubio, S. Andersson-Engels, K. Svanberg, S. Svanberg and P. Slezak, Clinical spectral characterisation of colonic mucosal lesions using autofluorescence and δ aminolevulinic acid sensitisation, *Gut* **44**, 511-518 (1999).

104. M.J. McShane, G. Cote and R. Splinter, Assessment of partial least-squares calibration and wavelength selection for complex near-infrared spectra, *Appl. Opt.* **52**, 878-884 (1998).

Paper I

Determination of tissue optical properties from diffuse reflectance profiles by multivariate calibration

Jan S. Dam, Peter E. Andersen, Torben Dalgaard, and Paul Erik Fabricius

We describe a method for determining the reduced scattering and absorption coefficients of turbid biological media from the spatially resolved diffuse reflectance. A Sugeno Fuzzy Inference System in conjunction with data preprocessing techniques is employed to perform multivariate calibration and prediction on reflectance data generated by Monte Carlo simulations. The preprocessing consists of either a principal component analysis or a new, extended curve-fitting procedure originating from diffusion theory. Prediction tests on reflectance data with absorption coefficients between 0.04 and 0.06 mm^{-1} and reduced scattering coefficients between 0.45 and 0.99 mm^{-1} show the root-mean-square error of this method to be 0.25% for both coefficients. With reference to practical applications, we also describe how the prediction accuracy is affected by using relative instead of absolute reflectance data, by imposing measurement noise on the reflectance data, and by changing the number and the position of detectors. © 1998 Optical Society of America

OCIS codes: 170.0170, 160.4760, 170.7050, 200.4260, 120.4570.

1. Introduction

Light propagation in homogeneous turbid media is determined by the geometry and the four optical properties[1] of the medium, i.e., the absorption coefficient μ_a, the scattering coefficient μ_s, the mean cosine of the single scattering phase function g, and the refractive index n. By measuring the optical properties of a composite, but homogeneous, turbid medium at various wavelengths, the concentrations of the separate components may be calculated, provided that these components have well-characterized absorption and scattering spectra. It has previously been shown[2–8] that μ_a and the reduced scattering coefficient $\mu_s' = \mu_s(1 - g)$ may be extracted from the spatially resolved steady-state diffuse reflectance $R_d(r)$ from a homogeneous single-layer medium. Note that, because of the similarity relations,[9] it is usually difficult to separate the compound parameter μ_s' into μ_s and g by $R_d(r)$ analysis. It has also been shown that μ_s' and μ_a may be determined with good accuracy by using time-resolved[10,11] and frequency-domain[12] reflectance techniques. Yet the steady-state $R_d(r)$ technique is advantageous in many practical applications, because the technology is relatively simple, and thus it offers the possibility of designing low-cost, portable equipment. Although most human tissues are heterogeneous, it is evident that $R_d(r)$ measurements, owing to their simple technology and noninvasive character, have a considerable potential in the field of medical diagnostics. Figure 1 shows a schematic setup for typical $R_d(r)$ measurements. For brevity, $R_d(r)$ is also denoted a reflectance profile.

Before dealing with the inverse problem of extracting μ_s' and μ_a from $R_d(r)$, we must solve the forward problem of modeling light propagation, e.g., $R_d(r)$, from μ_s, μ_a, and g. Two commonly used models for this are (a) diffusion theory[13] and (b) Monte Carlo simulations.[14] Diffusion theory provides analytical solutions to $R_d(r)$ expressed as definite integrals or infinite series. However, diffusion theory is valid only when two general criteria are fulfilled[15]:

$$a' = \mu_s'/(\mu_s' + \mu_a) \approx 1$$
$$MFP' = 1/(\mu_s' + \mu_a) \ll r, t. \qquad (1)$$

Here a' is the reduced albedo, MFP' is the reduced mean-free-path, r is the source–detector distance, and t is the thickness of the medium. Monte Carlo simulation of light propagation provides only numerical estimates of $R_d(r)$. Furthermore the calcula-

---

J. S. Dam, T. Dalgaard, and P. E. Fabricius are with Technology Research Center, Bang & Olufsen Technology A/S, DK-7600 Struer, Denmark. P. E. Andersen is with Technology Research Center/Optics and Fluid Dynamics Department, Risø National Laboratory, P.O. Box 49, DK-4000 Roskilde, Denmark.

Received 17 March 1997; revised manuscript received 2 July 1997.

0003-6935/98/040772-07$10.00/0

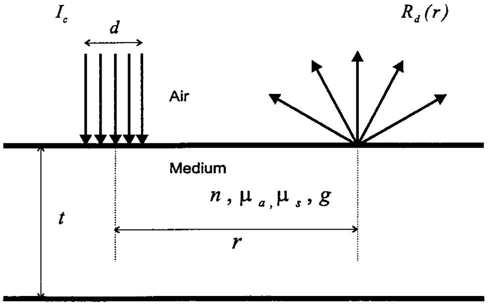

Fig. 1. Schematic setup for $R_d(r)$ measurements. The incident light I_c is a continuous-wave collimated beam with diameter d. The radial source–detection distance is denoted r, and t is the thickness of the medium.

tions are subject to statistical uncertainties and are usually bulky compared with similar diffusion theory calculations. On the other hand, traditional Monte Carlo simulations suffer from no severe restrictions regarding either the optical properties or the geometry of the media.

The nonlinear inverse problem of extracting μ_s' and μ_a from reflectance profiles simulated either by diffusion theory or by Monte Carlo simulations can be solved by performing multivariate calibration on sets of reflectance profiles. This may be done in several ways e.g., by the use of neural networks,[6,7] ordinary partial least-squares methods,[16] or a Sugeno Fuzzy Inference System (SFIS).[17] In this paper we demonstrate how biologically relevant values of μ_s' and μ_a may be extracted from simulated reflectance profiles by use of a SFIS for calibration and prediction. We use this particular method because preliminary tests showed significantly better prediction accuracy compared with ordinary partial least-square methods and because it is more mathematically transparent than neural networks. To model the reflectance profiles, we use Monte Carlo simulations rather than diffusion theory, partly because the Monte Carlo method has shown good agreement with experimental results for a wide range of optical properties[7,18] and partly because we want to avoid the general limitations of the diffusion theory [Eq. (1)]. In conjunction with the SFIS analysis, we also investigate data preprocessing as a means of improving the prediction accuracy, either in the form of principal component analysis[16] (PCA) or in the form of curve fitting to an expression originating from diffusion theory. This expression [Eq. (4)] is an extended version of an expression introduced by Groenhuis *et al.*[2] With reference to practical applications and probe implementation, we also discuss (a) prediction accuracy with relative versus absolute-reflectance profiles, (b) the influence of measurement noise, and (c) the optimum number and position of detectors.

2. Methods

Cheong *et al.*[19] provided a list of human tissue optical properties measured with a variety of *in vitro* techniques. Both the variation between different tissues and the variation between similar tissues measured with different techniques were extreme. Another matter of dispute is whether such *in vitro* properties translate well to the *in vivo* properties. Nevertheless we considered the ranges in inequality (2) to be representative for many living human tissues in the visible region and called them the main space:

$$\begin{gathered} 0.01\ \mathrm{mm}^{-1} < \mu_a < 0.10\ \mathrm{mm}^{-1}, \\ 2.50\ \mathrm{mm}^{-1} < \mu_s < 20.0\ \mathrm{mm}^{-1}, \\ 0.80 < g < 0.99, \\ (0.025\ \mathrm{mm}^{-1} < \mu_s' < 4.00\ \mathrm{mm}^{-1}). \end{gathered} \tag{2}$$

To investigate the performance of the SFIS analysis method on a significantly smaller space, we defined another set of ranges, placed at the center of the comprehensive main space, and called them the subspace:

$$\begin{gathered} 0.04\ \mathrm{mm}^{-1} < \mu_a < 0.06\ \mathrm{mm}^{-1}, \\ 9.00\ \mathrm{mm}^{-1} < \mu_s < 11.0\ \mathrm{mm}^{-1}, \\ 0.91 < g < 0.95, \\ (0.45\ \mathrm{mm}^{-1} < \mu_s' < 0.99\ \mathrm{mm}^{-1}). \end{gathered} \tag{3}$$

According to Bolin *et al.*[20] $1.38 < n < 1.41$ for a number of mammalian tissues; hence we considered $n = 1.4$ to be a valid approximation for the media treated in this paper.

Using the Monte Carlo code provided by Wang and Jacques,[21] we generated two sets of reflectance profiles, covering μ_s, μ_a, and g of the main space and the subspace. To make sure that all of the main space and the subspace range was covered and equally represented, we based each set of profiles on the 125 combinations of a 5 × 5 × 5 matrix with fixed stepwise increments of μ_s, μ_a, and g. The refractive index was set to $n = 1.4$, and the thickness of the medium was $t = 40$ mm. The light source was a flat collimated beam with the diameter $d = 1.0$ mm, and the diffuse reflectance was sampled in the distance range $0.60\ \mathrm{mm} < r < 12\ \mathrm{mm}$ in steps of $\Delta r = 0.25$ mm (i.e., 46 detection spots). In each simulation 10^6 photon packets were traced. Selecting every second profile, we split the main space and the subspace profile sets into a calibration and a prediction subset.

The Monte Carlo code we used employs the Henyey–Greenstein (HG) approximation to the single-scattering phase function. Although the HG approximation is commonly accepted as valid for a wide range of human tissues, small deviations between the HG approximation and the actual phase function(s) of real tissue do occur. Despite identical g values of the HG approximation and the real phase function, these deviations may result in different reflectance profiles.[22] This also affects any analysis of real $R_d(r)$ measurements based on models with the HG approximation.

To perform the calibration and the prediction analysis we used a first-order SFIS.[17] The basic idea of

SFIS analysis is to split a physical or a mathematical system with nonlinear input–output relations into a number of subsystems (i.e., clusters) with relations linear enough to perform a piecewise linear calibration of the total system. In this paper, the actual system is the medium and the incident light I_c depicted in Fig. 1; the input is the optical properties μ_s' and μ_a; and the output is various forms of $R_d(r)$. During calibration with the SFIS, the $R_d(r)$ data of the calibration set were divided into a number of clusters distributed to cover the whole $R_d(r)$ space. Then a rule (i.e., a linear combination) of the $(\mu_s', \mu_a) - R_d(r)$ relations of each cluster was generated with weighted linear regression. This weighting favors $R_d(r)$ data close to the cluster center and thereby attenuates the influence of any outliers. During prediction, the task was to assess the likely optical properties on the basis of a novel reflectance profile from the prediction data set. This was done by assigning the novel $R_d(r)$ data a membership to each cluster in the $R_d(r)$ space. The strength of each membership was calculated from the Euclidian distance between the cluster center and the $R_d(r)$ data in question. The optical properties were then calculated by the application of the rules according to each cluster membership. In this way, the prediction of the optical properties was not based on the rule of one cluster only, but was partially dependent on the rules of all clusters, hence the fuzzy part of the SFIS term. To extract the optimal features from the reflectance profiles before they were introduced to the SFIS, we also employed two preprocessing methods alternately. The first method was an ordinary PCA.[16] During a PCA, one can compress the $R_d(r)$ data set to its most dominant factors by generating a new data set of orthogonal principal components sorted according to decreasing eigenvalues. These eigenvalues indicate the amount of variability each principal component has removed from the original $R_d(r)$ data set.

When PCA was employed, we found that approximately three to six main principal components were sufficient to describe the original $R_d(r)$ data set properly. During analysis including PCA, these main principal components were introduced directly into the SFIS. In the second preprocessing method, we employed curve fitting to reduce the reflectance profiles to a set of fitting parameters. The fitting expression we used was

$$R_d(r) = \frac{z_0}{r^{z_1}} \exp(-z_2 r), \tag{4}$$

which is a general expression for diffuse reflectance, originating from diffusion theory. As opposed to others[2–4] who have used fixed values of z_1 (0.5, 1, and 2) and limited r ranges when fitting reflectance profiles to Eq. (4), we let z_0, z_1, and z_2 all be free fitting parameters and used full-range reflectance profiles (0.6 mm $< r <$ 12 mm). When the fitting method was employed in the analysis, the three z parameters were introduced directly into the SFIS.

All the reported prediction errors below are expressed as ordinary rms errors. In each case, the best calibration model was found by iterative analyses with various combinations of model settings, such as the number of clusters and principal components. Note that the subscripts attached to the PCA rms errors indicate the numbers of principal components used.

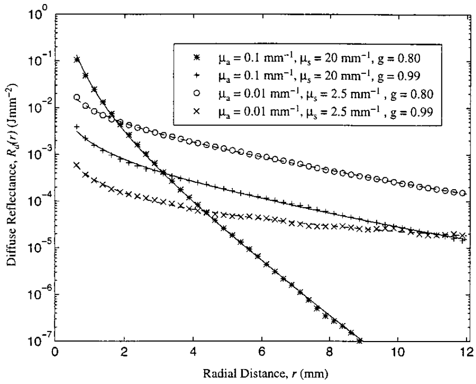

Fig. 2. Monte Carlo-simulated reflectance profiles (symbols) and corresponding fits (solid curves), representing four corners of the main space.

3. Results and Discussion

By letting z_0, z_1, and z_2 from Eq. (4) all be free fitting parameters, and by covering the full r range (0.60 mm $< r <$ 12 mm), we found that Eq. (4) is an excellent fit to all the reflectance profiles from the main space. This is illustrated in Fig. 2. In Fig. 3A, a plane section of optical properties from the main space and the subspace is mapped to the corresponding fitting parameters z_0, z_1, and z_2. The twisted appearance of the main space grid clearly illustrates the nonlinear relations between the optical properties and the reflectance profiles characterized by the fitting parameters. Because of the smaller range, the nonlinearity of the subspace is less pronounced compared with the main space. Looking at Fig. 3B, it is evident that all three fitting parameters (including z_1) are affected by the changes in the optical properties.

In Table 1 we list the prediction errors obtained by SFIS analysis of absolute reflectance profiles from the main space and the subspace. Here the rms errors of the main space are larger than the errors of the subspace. This is attributed partly to the more linearlike relations of the subspace mentioned above and partly to the fact that the increments of the $5 \times 5 \times 5$ subspace matrix of optical properties are much smaller than the increments of the $5 \times 5 \times 5$ main space matrix and thus provides a more fine-meshed covering of the $(\mu_s', \mu_a) - R_d(r)$ relations. Another way of expressing this is that the subspace has a higher profile density than the main space. Either preprocessing method leads to a substantial decrease in the rms errors of Table 1. The PCA method re-

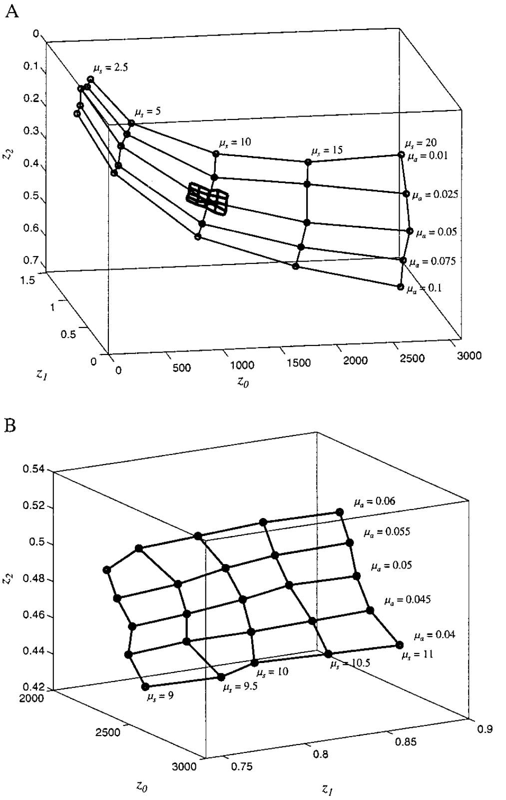

Fig. 3. μ_a, μ_s (mm^{-1}), and g mapped to the fitting parameters z_0, z_1, and z_2 of the reflectance profiles. A, Plane section of subspace (small bold grid) embedded in plane section of main space (g = 0.95). B, Enlarged plane section of subspace (g = 0.91).

sults in the least overall rms errors: 0.24% for μ_s' and 0.25% for μ_a.

One way of obtaining main space rms errors comparable with those of the subspace would be to simply increase the profile density. However, a single calibration model covering all the main space with a profile density similar to the subspace density would be very bulky and would lead to slow prediction calculations. Another way of improving the prediction accuracy of the main space, without introducing extensive calculations, would be to apply the following two-step prediction procedure:

Table 1. Prediction rms Errors of Absolute Reflectance Profiles from the Main Space and the Subspace

	Main Space rms Error (%)		Subspace rms Error (%)	
SFIS Input	μ_s'	μ_a	μ_s'	μ_a
Raw	38	420	0.85	2.08
PCA	4.1_5	13_3	0.24_4	0.25_3
Fit	5.3	9.0	0.21	0.78

Table 2. Prediction rms Errors of Relative Reflectance Profiles from the Main Space and the Subspace

	Main Space rms Error (%)		Subspace rms Error (%)	
SFIS Input	μ_s'	μ_a	μ_s'	μ_a
Raw	1200	510	4.18	7.28
PCA	83_6	24_4	2.06_3	4.07_3
Fit	16	24	1.29	2.44

(1) The unknown $R_d(r)$ is presented to the low-profile-density main space SFIS, and fair estimates of μ_s' and μ_a are returned.

(2) A proper high-profile-density subspace, including the estimates from step 1, is selected from a set of subspaces covering the total range of the main space, and then another (more accurate) prediction is performed by the subspace SFIS in question.

Such a procedure would require a subspace optical property overlapping that is comparable with the prediction errors of the main space. Adjusting the individual subspace sizes according to the nonlinearity of the specific main-space region may further optimize the procedure.

A. Relative Profiles

In real applications, it may be difficult to perform absolute reflectance measurements, e.g., because of unknown conditions regarding the coupling of light at the medium boundary. To circumvent such problems, we have also performed calibration on relative reflectance profiles. Preliminary investigations showed that normalization at the first detection spot (r = 0.625 mm) gave rise to the least rms errors; hence Table 2 gives the rms errors of the reflectance profiles normalized at r = 0.625 mm. During normalization, any information about μ_s' and μ_a related to the absolute levels of the reflectance profiles is reduced, and only information directly related to the shape of the profiles is maintained. The minimum rms errors of μ_s' and μ_a in Table 2 are increased, approximately 5 and 10 times, respectively, compared with the minimum rms errors of the absolute profiles in Table 1. Here it appears that the rms errors of the fitting method are less than those of the PCA method. This indicates a superior shape-recognition property of the fitting method, which may be attributed to the fact that z_0 is the only fitting parameter affected by normalization. Although, in general, normalization leads to increased rms errors (1.29% for μ_s' and 2.44% for μ_a), such relative analysis may be sufficient in some situations, e.g., in purely qualitative assessments.

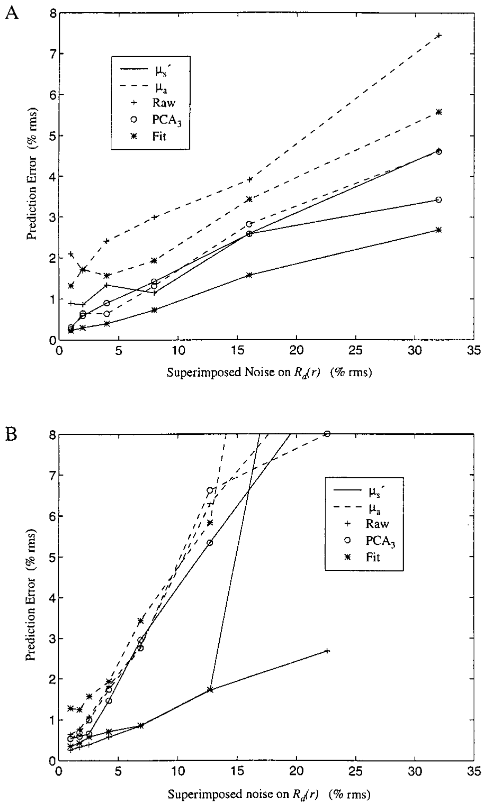

Fig. 4. Prediction errors as a function of noise superimposed on the reflectance profiles from the subspace. The noise rms values are an average of the intensity-dependent noise at each detector of each profile. A, 46 detection spots; B, six detection spots.

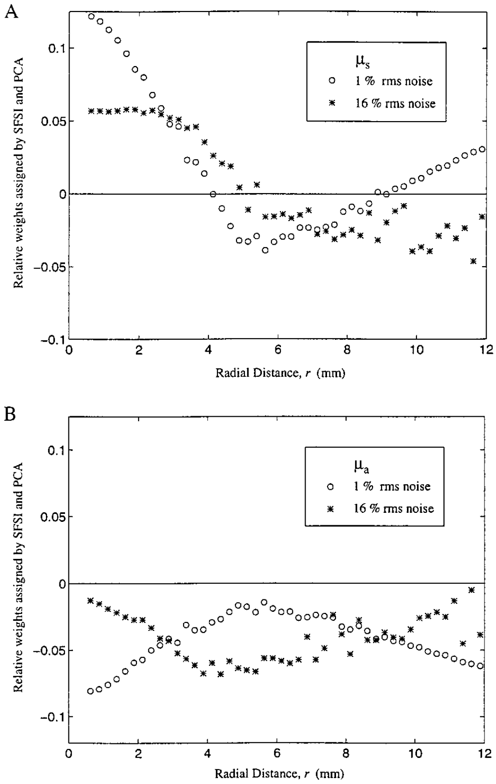

Fig. 5. Noise-dependent distributions of calibration mean weights assigned to each detection spot by the SFIS and the PCA (with three principal components) during calibration on the reflectance profiles from the subspace. The mean weights indicate the amount of information about, A, μ_s' and, B, μ_a collected from each detection spot.

B. Measurement Noise

Reflectance profiles obtained by real measurements are always subject to a certain amount of measurement noise. This noise, introduced by the detector–amplifier system, is inversely proportional to the square root of the light intensity at the detector. Figure 4A shows how the rms errors are influenced when such intensity-dependent noise is superimposed on full-range reflectance profiles from the subspace. The intrinsic noise of the Monte Carlo simulations, which is caused by statistical uncertainties, has been estimated to be approximately 1% rms. All the rms errors of μ_s' and μ_a seem to be approximately proportional to the additional noise. However, by comparing the slopes of the curves in Fig. 4A, the rms errors of μ_a appear to be slightly more sensitive to measurement noise than the errors of μ_s'. Note that the SFIS calibration models used in Fig. 4 have not been optimized separately and therefore should be used for qualitative noise-sensitivity assessments only.

Besides the conspicuous effect on the rms errors, Fig. 5 shows that imposing noise on the profiles also causes a more subtle change in the calibration mean weights. These weights have been derived from the transition loadings generated by the PCA and from the rules and the membership distributions generated by the SFIS during calibration. The absolute values of the calibration mean weights indicate how important the reflectance information from each individual detection spot is in the overall process of predicting the values of μ_s' and μ_a. In the case of almost noiseless profiles (1% rms), it appears that the major part of the information about μ_s' is confined to the close-distance range $r < 3.0$ mm, while the information about μ_a is confined to the distance ranges $r < 4.0$ mm and $r > 7.0$ mm. When additional noise (16% rms) is inflicted on the profiles, the general distribution pattern of mean weights for μ_s' is unaltered, while the mean weights of μ_a indicate that the bulk part of relevant information has moved to the center range 3.0 mm $< r <$ 9.0 mm.

In Fig. 5B it appears that a considerable part of the

Table 3. Prediction rms Errors of Close- and Far-Distance Reflectance Profiles from the Subspace[a]

SFIS Input	Close Range $0.6\text{ mm} < r < 6\text{ mm}$ rms Error (%)		Far Range $3\text{ mm} < r < 12\text{ mm}$ rms Error (%)	
	μ_s'	μ_a	μ_s'	μ_a
Raw	0.36	1.89	2.05	2.67
PCA	0.28_3	0.90_3	1.18_3	0.52_3
Fit	0.31	0.86	0.75	2.32

[a](22 and 36 detectors).

information about μ_a in the low-noise case is confined to the far-distance detection spots. Because of the low $R_d(r)$ intensities at these far distances, the information embedded here is easily corrupted by the intensity-dependent additional noise. This may explain why the PCA–SFIS in Fig. 5B shifts the μ_a mean weight density toward center distances when the additional noise increases. It is important to be aware of this shift when μ_s' and μ_a are extracted from noisy, real $R_d(r)$ measurements. Because, if calibration is performed on practically noiseless simulated profiles, prediction performed on noisy measured profiles may be corrupted. To achieve maximum prediction accuracy in such cases, it may turn out to be advantageous to superimpose equivalent noise on the simulated calibration profiles.

C. Number and Position of Detectors

Table 3 gives the prediction errors when only close- or far-distance detection spots are used. Note that the terms close and far depend on the ranges of the optical properties in question. The results show, as indicated by the weight distributions in Fig. 5A, that μ_s' may be determined by close-distance measurements solely without significant loss of prediction accuracy. However, determining μ_a from close- or far-distance measurements exclusively increases the rms errors.

Reviewing the results from the subspace investigations in Tables 1 and 3, it is obvious that full-range reflectance profiles ($0.6\text{ mm} < r < 12\text{ mm}$) yield minimum rms errors. Note that, in practical applications, it may present difficulties to realize a minimum detector–source distance of $r = 0.625$ mm when a 1-mm light source and a 0.25-mm detector are used.

It is usually inconvenient to use as many detection spots (22–46) as in the cases above. Table 4 gives the prediction errors employing only 6 or 12 equally separated detection spots from full-range reflectance profiles from the subspace. When the number of detectors is reduced from 46 to 6, or to 12, the rms errors of the raw profiles from the subspace show a remarkable decrease. At the same time, the rms errors of the preprocessed profiles are slightly increased. This means that the effect of employing preprocessing is negligible here. Figure 4B shows the rms errors of six-spot reflectance profiles as a function of superimposed noise. The slopes of the curves indicate that six-spot profiles, in general, are more sensitive to noise than the 46-spot profiles of Fig. 4A, and that preprocessing does not have any significant effect in this case either.

Table 4. Prediction rms Errors of Reflectance Profiles from the Subspace with a Reduced Number of Detection Spots

SFIS Input	6 Detection Spots rms Error (%)		12 Detection Spots rms Error (%)	
	μ_s'	μ_a	μ_s'	μ_a
Raw	0.26	0.58	0.35	0.74
PCA	0.26_6	0.50_4	0.38_6	0.43_3
Fit	0.35	1.28	0.35	1.25

The poor effect of preprocessing in the six-spot case, compared with the 46-spot case, is due to the detailed information provided by the 46 inputs without preprocessing, which causes the SFIS to optimize for calibration accuracy at the expense of prediction accuracy. When the number of inputs is reduced, as in the six-spot case, the SFIS calibration model is less strict. This leads to a better prediction accuracy of the raw six-spot profiles, which again leads to comparable prediction rms errors of the raw and the preprocessed six-spot profiles. To this end, we stress that the rms errors of calibration, whenever possible, should be made comparable with the errors of prediction and that the number of input sets should be much larger than the number of inputs in each single set when calibration–prediction systems are tuned.

4. Conclusions

In this paper we have demonstrated how μ_s' and μ_a within typical biological ranges may be extracted from diffuse reflectance profiles by use of multivariate calibration methods. With these methods we were able to determine μ_s' and μ_a with minimum rms errors of approximately 0.25%. Simultaneous determination of μ_s' and μ_a with maximum accuracy requires a large number of detection spots (e.g., 46), PCA preprocessing, and full-range reflectance profiles ($0.6\text{ mm} < r < 12\text{ mm}$). However, μ_s' alone could be determined by close range profiles solely, without loss of accuracy.

Reducing the number of detection spots from 46 to 6 and skipping the preprocessing led to only a doubling of the minimum rms error of μ_a, while the rms error of μ_s' remained unaltered. However, this also led to increased prediction error measurement-noise sensitivity.

Compared with absolute reflectance profiles, calibration and prediction on relative profiles using preprocessing led to a fivefold increase of the μ_s' rms error and a tenfold increase of the μ_a rms error. In this case, the fitting method was superior to the PCA method.

The statements above are all based on a monolayer geometry. In reality, most human tissues may be considered multilayered rather than monolayered. Model experiments[23] have shown that $R_d(r)$ from multilayered models exhibits the same generic form [Eq. (4)] as $R_d(r)$ from a monolayer model. This means that the actual geometry of a medium, i.e., number and thickness of layers, cannot be determined on the basis of $R_d(r)$ alone. However, by incorporating *a priori* knowledge of the layer structure and some of the optical properties of the individual layers, the methods in this paper might still be used to assess selected combinations of μ_s' and μ_a in a multilayer tissue structure.

Through the investigations presented here, we have contributed a set of practical guidelines for determining optical properties from reflectance profile measurements. We have subsequently used these guidelines to build a system for measuring optical properties in the biological range. This system is currently being tested on phantoms and includes a compact optical front end, simultaneous measurements at four arbitrary wavelengths, automatic data acquisition, and flexible real-time data analysis.

References

1. A. J. Welch, M. J. C. van Gemert, W. M. Star, and B. C. Wilson, "Overview of tissue optics," in *Optical-Thermal Response of Laser-Irradiated Tissue*, A. J. Welch and M. J. C. van Gemert, eds. (Plenum, New York, 1995), Chap. 2.
2. R. A. J. Groenhuis, H. A. Ferwerda, and J. J. Ten Bosch, "Scattering and absorption of turbid materials determined from reflection measurements. 2: Measuring method and calibration," Appl. Opt. **22,** 2463–2467 (1983).
3. J. M. Schmitt, G. X. Zhou, E. C. Walker, and R. T. Wall, "Multilayer model of photon diffusion in skin," J. Opt. Soc. Am. A **7,** 2141–2153 (1990).
4. B. C. Wilson and S. L. Jacques, "Optical reflectance and transmission of tissues: principles and applications," IEEE J. Quantum Electron. **26,** 2186–2199 (1990).
5. T. J. Farrell, M. S. Patterson, and B. C. Wilson, "A diffusion theory model of spatially resolved, steady-state diffuse reflectance for the noninvasive determination of tissue optical properties *in vivo*," Med. Phys. **19,** 879–888 (1992).
6. T. J. Farrell, B. C. Wilson, and M. S. Patterson, "The use of neural network to determine tissue optical properties from spatially resolved diffuse reflectance measurements," Phys. Med. Biol. **37,** 2281–2286 (1992).
7. A. Kienle, L. Lilge, M. S. Patterson, R. Hibst, R. Steiner, and B. C. Wilson, "Spatially resolved absolute diffuse reflectance measurements for noninvasive determination of the optical scattering and absorption coefficients of biological tissue," Appl. Opt. **35,** 2304–2314 (1996).
8. J. R. Mourant, T. Fuselier, J. Boyer, T. M. Johnson, and I. J. Bigio, "Predictions and measurements of scattering and absorption over broad wavelength ranges in tissue phantoms," Appl. Opt. **36,** 949–957 (1997).
9. H. C. van de Hulst, *Multiple Light Scattering* (Academic, New York, 1980), Vols. 1 and 2.
10. R. Cubeddu, A. Pifferi, P. Taroni, A. Torricelli, and G. Valentini, "Experimental test of theoretical models for time-resolved reflectance," Med. Phys. **23,** 1625–1633 (1996).
11. S. J. Madsen, B. C. Wilson, M. S. Patterson, T. D. Park, S. L. Jacques, and Y. Hefetz, "Experimental tests of a simple diffusion model for the estimation of scattering and absorption coefficients of turbid media from time-resolved diffuse reflectance measurements," Appl. Opt. **31,** 3509–3517 (1992).
12. S. Fantini, M. A. Franceschini-Fantini, J. S. Maier, and S. A. Walker, "Frequency-domain multichannel optical detector for noninvasive tissue spectroscopy and oximetry," Opt. Eng. **34,** 32–42 (1995).
13. A. Ishimaru, *Wave Propagation and Scattering in Random Media* (Academic, New York, 1978), Vols. 1 and 2.
14. S. L. Jacques and L. Wang, "Monte Carlo modeling of light transport in tissue," in *Optical-Thermal Response of Laser-Irradiated Tissue*, A. J. Welch and M. J. C. van Gemert, eds. (Plenum, New York, 1995), Chap. 4.
15. W. M. Star, "Diffusion theory of light transport," in *Optical-Thermal Response of Laser-Irradiated Tissue*, A. J. Welch and M. J. C. van Gemert, eds. (Plenum, New York, 1995), Chap. 6.
16. H. Martens and T. Næs, *Multivariate Calibration* (Wiley, New York, 1994).
17. T. Tagaki and M. Sugeno, "Fuzzy identifications of systems and its applications to modelling and control," IEEE Trans. Syst. Man Cybern. **15,** 116–132 (1985).
18. S. T. Flock, B. C. Wilson, and M. S. Patterson, "Monte Carlo modeling of light propagation in highly scattering tissues. II. Comparison with measurements in phantoms," IEEE Trans. Biomed. Eng. **36,** 1169–1173 (1989).
19. W. F. Cheong, S. A. Prahl, and A. J. Welch, "A review of the optical properties of biological tissue," IEEE J. Quantum Electron. **26,** 2166–2185 (1990).
20. P. Bolin, L. E. Preuss, R. C. Taylor, and R. J. Ference, "Refractive index of some mammalian tissues using a fiber optic cladding method," Appl. Opt. **28,** 2297–2303 (1989).
21. L. Wang and S. L. Jacques, *Monte Carlo Modeling of Light Transport in Multi-Layered Tissues in Standard C* (University of Texas, M. D. Anderson Cancer Center, Houston, Tex., 1992).
22. J. R. Mourant, J. Boyer, A. H. Hielscher, and I. J. Bigio, "Influence of the scattering phase function on light transport measurements in turbid media performed with small source–detector separations," Opt. Lett. **21,** 546–548 (1996).
23. P. E. Andersen, J. S. Dam, P. M. Pedersen, and P. Bjerring, "Local diffuse reflectance from a multilayered skin tissue model," in *Optical Tomography and Spectroscopy of Tissue: Theory, Instrumentation, Model, and Human Studies II*, B. Chance and R. R. Alfano, eds., Proc. SPIE **2979,** 515–526 (1997).

Paper II

Multiple polynomial regression method for determination of biomedical optical properties from integrating sphere measurements

Jan S. Dam, Torben Dalgaard, Paul Erik Fabricius, and Stefan Andersson-Engels

We present a new, to our knowledge, method for extracting optical properties from integrating sphere measurements on thin biological samples. The method is based on multivariate calibration techniques involving Monte Carlo simulations, multiple polynomial regression, and a Newton–Raphson algorithm for solving nonlinear equation systems. Prediction tests with simulated data showed that the mean relative prediction error of the absorption and the reduced scattering coefficients within typical biological ranges were less than 0.3%. Similar tests with data from integrating sphere measurements on 20 dye–polystyrene microsphere phantoms led to mean errors less than 1.7% between predicted and theoretically calculated values. Comparisons showed that our method was more robust and typically 5–10 times as fast and accurate as two other established methods, i.e., the inverse adding–doubling method and the Monte Carlo spline interpolation method. © 2000 Optical Society of America

OCIS codes: 120.3150, 120.5820, 170.7050, 170.1470, 160.4760.

1. Introduction

In the field of biomedical optics, determination of the optical properties of various biological materials is essential, not only for diagnostic purposes, e.g., whole blood analysis,[1–4] but also in therapeutic applications, e.g., in the development of tissue light propagation models for various types of laser therapy.[5,6] The optical properties,[7] i.e., the absorption coefficient μ_a, the scattering coefficient μ_s, and the anisotropy parameter g, are often determined by measurement of the total diffuse reflectance R and the diffuse transmittance T of a thin sample in an integrating sphere setup. However, it is only possible to determine μ_a and the reduced scattering coefficient $\mu_s' = (1 - g)\mu_s$ from pure R and T measurements. To separate μ_s' into μ_s and g, one often includes measurements of the collimated transmittance T_c as well. Because accurate T_c measurements are difficult to perform, the similarity principle[8–10] is often applied in conjunction with integrating sphere measurements; i.e., only μ_a and μ_s' are determined. R and T measurements may be carried out with either a single- or a double-sphere setup. In the latter, R and T can be determined simultaneously without moving the sample; however, the obtainable accuracy is decreased compared with a single-sphere setup, owing to optical cross talk between the two spheres.[11]

Several methods have been applied to solve the problem of extracting μ_a and μ_s' from R and T measurements, e.g., methods based on Kubelka–Munk theory[12] and diffusion theory.[13] Although both these methods provide analytical expressions for $R(\mu_a, \mu_s')$ and $T(\mu_a, \mu_s')$, the inverse problem of determining $\mu_a(R, T)$ and $\mu_s'(R, T)$ has no analytical solutions. Furthermore, the analytical solutions of $R(\mu_a, \mu_s')$ and $T(\mu_a, \mu_s')$ are not accurate; thus most contemporary approaches are based on numerical methods, which provide more accurate calculations of $R(\mu_a, \mu_s')$ and $T(\mu_a, \mu_s')$, e.g., the inverse adding–doubling (IAD) method[14] or methods involving Monte Carlo simulations.[2–15] For all the above methods it is common that $\mu_a(R, T)$ and $\mu_s'(R, T)$ have to be determined by iterative numerical calculations. This may prove to be to slow in some cases, e.g., applications involving real-time multiwavelength analysis. In this paper we present a method, which is both fast and accurate and thus suitable for such

---

J. S. Dam (jan.sorensen_dam@fysik.lth.se), T. Dalgaard, and P. E. Fabricius are with Bang & Olufsen Medicom a/s, Bredgade 67b, DK-7600 Struer, Denmark. J. S. Dam and S. Andersson-Engels are with the Department of Physics, Lund Institute of Technology, P.O. Box 118, S-221 00 Lund, Sweden.

Received 28 September 1999; revised manuscript received 3 December 1999.

0003-6935/00/01202-08$15.00/0

applications. The method is based on Monte Carlo simulations,[16] polynomial regression, and a Newton–Raphson algorithm[17] for solving nonlinear equation systems. For brevity we denote the method MPR (multiple polynomial regression).

In the following sections we first explain the steps of the MPR method in detail. Next, we present and discuss simulated and measured test results. Finally, we compare the performance of the MPR method with that of the IAD method and another Monte Carlo-based method, the so-called Monte Carlo spline interpolation (MCSI) method.[5]

2. Methods

The purpose of the MPR method is to extract μ_a and μ_s' from integrating sphere measurements of R and T on thin turbid biological samples. This involves several numerical and experimental methods, which we describe in the present section.

A. General Principles

In mathematical terms the first step of the MPR method is to perform two bijective mappings of a relevant subset of the $[\mu_a, \mu_s']$ space onto their images in the R and the T spaces, respectively. Such mappings may of course be obtained from a series of R and T measurements on phantoms are performed with known μ_a and μ_s' values. However, it is faster to apply a proper light-propagation model, e.g., Monte Carlo simulations.

The next step is to create a calibration model, i.e., to find a mathematical description of the $R(\mu_a, \mu_s')$ and $T(\mu_a, \mu_s')$ mappings. A regular and a smooth appearance of simulated R and T images, i.e., R_{sim} and T_{sim}, indicated that these may be fitted well by relatively simple mathematical functions. Thus we tested and used double polynomials with the generic form

$$\begin{aligned} P(\mu_a, \mu_s', m) = {} & (a_0 + a_1\mu_a + a_2{\mu_a}^2 + \cdots + a_m{\mu_a}^m) \\ & \times (b_0 + b_1\mu_s' + b_2\mu_s'^2 + \cdots + b_m\mu_s'^m), \end{aligned} \tag{1}$$

where $(a_0, a_1, a_2, \ldots$ and $b_0, b_1, b_3, \ldots)$ are fitting coefficients determined by least-squares regression and m is the order of the double polynomial. The resulting polynomial fits to R_{sim} and T_{sim} were defined as

$$\begin{aligned} R_{\text{fit}} &= P_R(\mu_a, \mu_s', m), \\ T_{\text{fit}} &= P_T(\mu_a, \mu_s', m). \end{aligned} \tag{2}$$

The final step of the MPR method is to solve the inverse problem of extracting μ_a and μ_s' from real integrating sphere measurements, i.e., R_{meas} and T_{meas}. For this we used a Newton–Raphson algorithm. First, we defined

$$\begin{aligned} F(\mu_a, \mu_s') &= R_{\text{fit}} - R_{\text{meas}}, \\ G(\mu_a, \mu_s') &= T_{\text{fit}} - T_{\text{meas}}. \end{aligned} \tag{3}$$

Then we performed converging iterative calculations of μ_a and μ_s', using the algorithm in Eq. (4):

$$\left.\begin{aligned} -\begin{bmatrix} F(\mu_{a,k}, \mu_{s,k}') \\ G(\mu_{a,k}, \mu_{s,k}') \end{bmatrix} &= \begin{bmatrix} \dfrac{\partial F}{\partial \mu_a} & \dfrac{\partial F}{\partial \mu_s'} \\[2ex] \dfrac{\partial G}{\partial \mu_a} & \dfrac{\partial G}{\partial \mu_s'} \end{bmatrix} \begin{pmatrix} h_{a,k} \\ h_{s,k} \end{pmatrix} \\ \begin{pmatrix} \mu_{a,k+1} \\ \mu_{s,k+1}' \end{pmatrix} &= \begin{pmatrix} \mu_{a,k} \\ \mu_{s,k}' \end{pmatrix} + \begin{pmatrix} h_{a,k} \\ h_{s,k} \end{pmatrix} \end{aligned}\right\}, \quad k = 0, 1, 2, 3, \ldots, \tag{4}$$

where h_a and h_s are correction terms of μ_a and μ_s'. The calculations were continued until h_a and h_s satisfied predefined accuracy requirements. Finally, $\mu_{a,k}$ and $\mu_{s,k}'$ were read.

B. Simulations and Numerical Analysis

We used the Monte Carlo code provided by Wang *et al.*[16] to generate calibration and simulated prediction data sets. To provide a detailed calibration model, we first generated two 20×50 matrices of R_{sim} and T_{sim}, where T_{sim} includes both the collimated and the diffuse transmittance, whereas R_{sim} represents diffuse reflectance only. The values of μ_a and μ_s' in these matrices were incremented in steps of 0.1 and 1 cm^{-1}, respectively, within the typical biological ranges[18,19]:

$$\begin{aligned} 0.1\ \text{cm}^{-1} \le \mu_a &\le 5\ \text{cm}^{-1}, \\ 1\ \text{cm}^{-1} \le \mu_s' &\le 20\ \text{cm}^{-1}, \\ g &= 0.9, \\ n &= 1.4, \end{aligned} \tag{5}$$

where n is the refractive index. Note that both g and n were kept fixed in the simulations. The sample geometry of the simulations was a semi-infinite slab with thickness $d_{\text{sample}} = 0.5$ mm. The slab was placed between semi-infinite glass slides with thickness $d_{\text{slide}} = 1$ mm and refractive index $n_{\text{slide}} = 1.52$. The slab was irradiated by a collimated beam with the diameter $r_{\text{beam}} = 1$ mm. In each simulation, 1×10^6 photons were traced. This extensive R_{sim} and T_{sim} data set was used in the evaluation of the MPR technique to extract μ_a and μ_s' from Monte Carlo simulated prediction data.

To perform prediction tests on data from integrating sphere measurements on phantom models as well, we generated a second calibration model. Referring to the results from the prediction tests on simulated data, the number of simulations used in this calibration model were reduced to include only 117 (9×13) R_{sim} and T_{sim} simulations. The geometry of these simulations were adapted to the single integrating sphere setup geometry in Fig. 1, and the optical properties of the simulations were chosen to

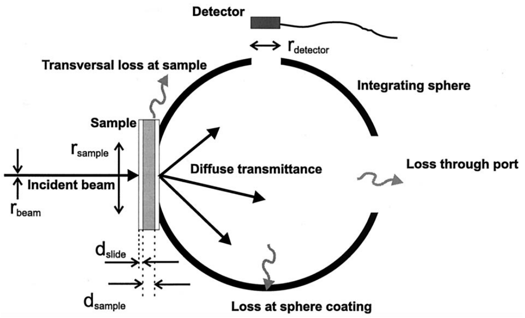

Fig. 1. Setup for R_{meas} and T_{meas} phantom measurements. The sphere is an 8-in. (~20.3 cm) *IS* 080 *SF* from Labsphere, and the parameters are $r_{\text{beam}} = 1$ mm, $d_{\text{sample}} = 2.2$ mm, $d_{\text{slide}} = 1$ mm, $r_{\text{sample}} = 23$ mm, $r_{\text{detector}} = 12.5$ mm, and $\lambda = 633$ nm. Note, during R_{meas} measurements, the sample is placed at the port to the right-hand side.

cover the phantom optical property range sufficiently:

$$\begin{aligned} 0\ \text{cm}^{-1} &\leq \mu_a \leq 3\ \text{cm}^{-1}, \\ 4.4\ \text{cm}^{-1} &\leq \mu_s' \leq 21.8\ \text{cm}^{-1}, \\ g &= 0.92, \\ n &= 1.33. \end{aligned} \tag{6}$$

Except for the Monte Carlo simulations, all numerical analysis and algorithms in this paper were carried out with Matlab 5.2. Thus all matrix manipulation, least-squares fitting, etc., is based on standard Matlab routines.

C. Experimental Setup and Measurements

To carry out MPR tests on experimental data, we measured R_{meas} and T_{meas} of 20 liquid phantoms, each with a distinct set of μ_a and μ_s', using the integrating sphere setup shown in Fig. 1. The phantoms consisted of green food dye and 1.9-μm polystyrene spheres suspended in water. During the measurements the phantoms were contained in cuvettes, consisting of two glass slides separated by a black plastic spacer.

As illustrated in Fig. 1, some of the transmitted and reflected diffuse light is lost in real integrating sphere measurements, owing to the limited diameter of sample port. During the prediction analysis we therefore corrected R_{sim} and T_{sim} to take these transversal losses into account before the polynomial fits R_{fit} and T_{fit} were calculated. We did this by ignoring values of R_{sim} and T_{sim} for radial distances $r > 0.5\ r_{\text{sample}}$. Furthermore, we also had to carry out corrections due to losses through the ports and the reflective coating of the integrating sphere. The measured intensity at the detector P_{out} in an integrating sphere setup is the result of multiple reflections in the sphere originating from the first interaction of the incident light with the sample. This relation is given by

$$\begin{aligned} P_{\text{out}} &= P_0 \delta_d r_w \sum_{n=0}^{\infty} (\alpha_w r_w + \alpha_s r_s + \alpha_d r_d)^n \\ &= P_0 \frac{\delta_d r_w}{1 - \alpha_w r_w - \alpha_s r_s - \alpha_d r_d}, \end{aligned} \tag{7}$$

where r denotes diffuse reflectance coefficients and α denotes normalized areas relative to the total sphere area. The subscripts w, s, and d denote wall, sample, and detector, respectively. The initial reflected or transmitted intensity at the sample is $P_0 = r_s P_{\text{in}}$ or $P_0 = t_s P_{\text{in}}$, respectively, where P_{in} is the intensity of the incident laser beam and r_s and t_s are diffuse reflectance and transmittance coefficients of the sample, respectively. Note that the specular reflectance R_{spec} leaves the sphere through the entrance port and that the collimated transmittance $T_c \ll T_{\text{total}}$; thus both are ignored in this particular setup. To avoid direct exposure of the detector from P_0, it was pulled back from the detector port; thus only diffuse reflectance from a portion of the opposite sphere wall was detected. The normalized area of this portion is denoted δ_d in Eq. (7). Using a well-defined reflectance standard as a reference in conjunction with Eq. (7), we extracted r_s and t_s from the phantom measurements and used these as input to the MPR method during the prediction analysis, i.e., $R_{\text{meas}} = r_s$ and $T_{\text{meas}} = t_s$.

3. Results and Discussion

A. Calibration Model

Figure 2 depicts the two simulated R_{sim} and T_{sim} data sets of the calibration model that we used in the MPR evaluations on simulated prediction data. As we stated above, the overall appearance of the R_{sim} and the T_{sim} plots is smooth and regular and thus well suited for polynomial fitting. Figure 3 shows the resulting fitting errors when two fifth-order double polynomials are used to fit the R_{sim} and T_{sim} plots in Fig. 2. The speckled appearance of the absolute error plots in Figs. 3(a) and 3(b) indicates that any systematic fitting errors due to the fitting algorithm are less significant than errors introduced by the random intrinsic noise of the Monte Carlo simulations. The relative errors of R_{fit} in Fig. 3(c) are significantly higher for low μ_s' values. This is because the low absolute levels of R_{fit} in this region (see Fig. 2) are more easily afflicted by the Monte Carlo noise and that the applied least-squares regression algorithm optimizes the fit on the basis of the absolute—and not the relative—errors. Various preprocessing of R_{sim} and T_{sim} before fitting might reduce the latter error source.

To test the performance of the Newton–Raphson algorithm separately, we also did predictions tests, using the original calibration data sets as input to the Newton–Raphson method, i.e., $R_{\text{meas}} = R_{\text{fit}}$ and $T_{\text{meas}} = T_{\text{fit}}$. The results showed that the mean relative calculation error of both μ_a and μ_s' was approximately 1×10^{-6}. Furthermore, the Newton–

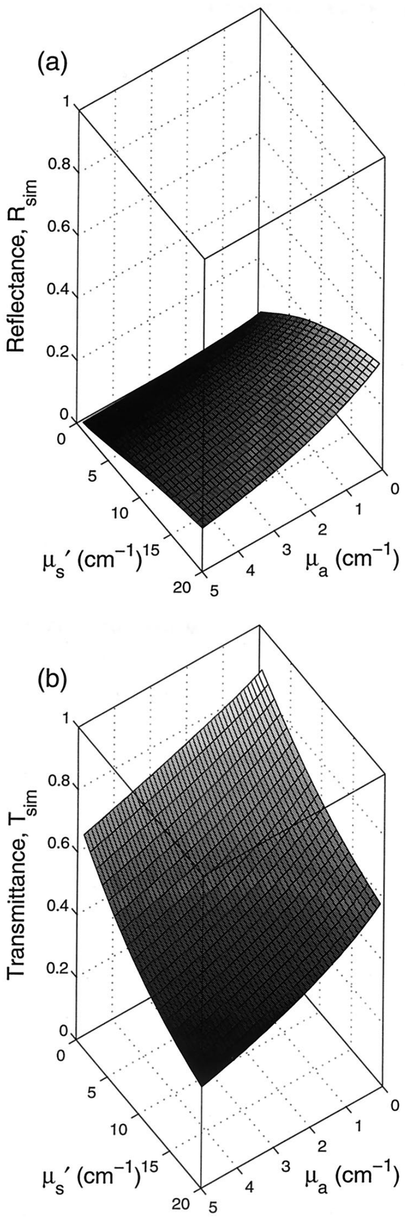

Fig. 2. Total diffuse reflectance R (a) and transmittance T (b) as a function of the absorption coefficient μ_a and the reduced scattering coefficient μ_s' for a thin slab geometry. The R and T data for the plots were generated with Monte Carlo simulations.

Raphson algorithm converged in all cases; thus the specific contribution of the algorithm to the total prediction errors of the MPR method is negligible.

B. Numerical Prediction Tests

We tested the overall prediction performance of the MPR method, using a simulated prediction set of a 100 R_{meas} and T_{meas} data based on random μ_a and μ_s' values within the ranges defined in relation (5). Figure 4 shows the actual random distribution of μ_a and μ_s' in the prediction set. All results discussed in the present subsection are based on this prediction set and the large 20 × 50 calibration set described in Subsection 2.B. Furthermore, all reported errors are relative prediction errors:

$$\mathrm{Err} = 100\% \left| \frac{\mu_{\mathrm{pred}} - \mu_{\mathrm{ref}}}{\mu_{\mathrm{ref}}} \right|, \tag{8}$$

where μ_{pred} is the predicted value and μ_{ref} the true value of either μ_a or μ_s'. The prediction errors of μ_a or μ_s' are denoted Err_a and Err_s, respectively.

1. *Order of Polynomials*

Table 1 gives the prediction errors using R_{fit} and T_{fit} fitting polynomials of orders 3, 4, and 5, respectively. The iterations of the Newton–Raphson algorithm were stopped when both h_a and $h_s < 1 \times 10^{-6}$ [see Eq. (4)]. This criterion was typically satisfied after 5–15 iterations, leading to almost identical calculation times in all three cases. It is evident that the prediction accuracy of the fifth-order polynomials are superior to the third- and fourth-order polynomials. Sixth-order polynomials were also tested but caused rank deficient problems in the regression algorithm and were therefore rejected.

2. *Large-Error Analysis*

The cases in which the prediction errors of μ_a and/or μ_s', i.e., Err_a and/or Err_s were larger than 0.5% with the fifth-order fits from Table 1 are depicted in Fig. 4. It appears that the Err_s values are largest when R is low, whereas the largest Err_a values occur mainly when R is low and T is high (see discussion in subsection 3.A). To analyze the Monte Carlo noise contribution versus the fitting-error contribution to the total prediction error, we generated 10 identical but independent R_{sim} and T_{sim} sets for each of the 14 marked large-error cases in Fig. 4. The results from this analysis are shown in Fig. 5. In cases 1–6 both Err_a and $\mathrm{Err}_s > 0.5\%$ (i.e., the triangles in Fig. 4), whereas in cases 7–14 only $\mathrm{Err}_s > 0.5\%$ (i.e., the open circles in Fig. 4). In each of the 14 cases in Fig. 5 the left-hand bar indicates the maximum deviation from the true value, the middle bar is a measure of the prediction precision error, and the right-hand bar is a measure of the prediction accuracy error. By comparing the middle and the right-hand bars, we can conclude that the errors in cases 1–6 are mainly due to MPR fitting errors in the calibration set, whereas the errors in cases 7–14 are not due to limitations of the MPR method in general but rather to the Monte Carlo noise in the prediction set. Thus only one of the latter eight cases were off by more than 0.5%, when we, in each case, calculated the mean of the ten independent predictions, i.e., the right-hand columns of Fig. 5.

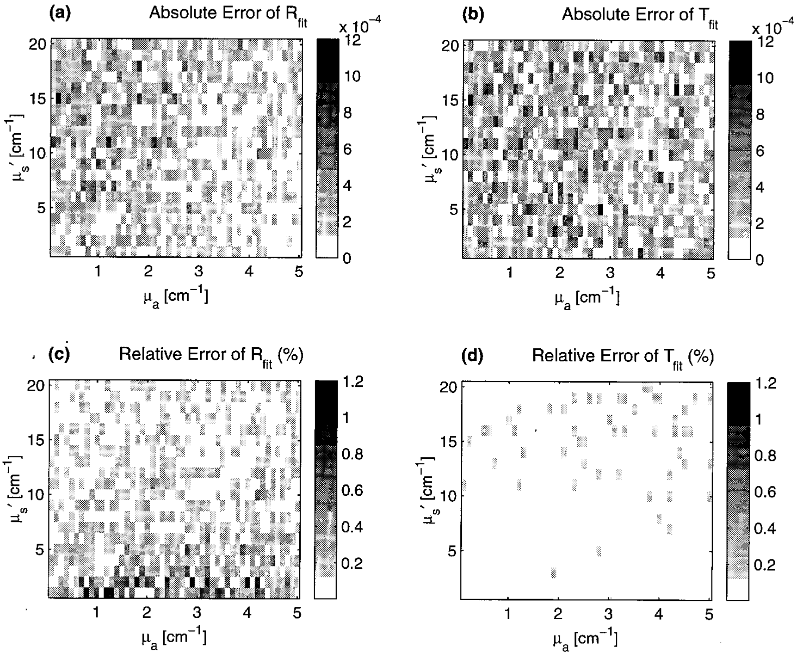

Fig. 3. [(a) and (b)] Absolute and [(c) and (d)] fitting errors of R_{fit} and T_{fit}.

3. *Calculation Speed versus Accuracy*

The applied Newton–Raphson algorithm was implemented in Matlab and run on a 166-MHz Pentium personal computer. As shown in Table 1, one single prediction of μ_a and μ_s' was calculated in ~60 ms. If the algorithms were implemented and compiled in, e.g., the C programming language, the calculations would run even faster. In contrast, it took days to generate the Monte Carlo data for the 20 × 50 calibration model we used. However, the total Monte Carlo calculation time may be reduced by means of either tracing less photons in each simulation or using less simulations to generate the calibration model. The calculation time might also be reduced with the Monte Carlo techniques suggested by Pifferi *et al.*[20] Table 2 shows the resulting prediction errors of four equivalent fifth-order calibration models based on four R_{sim} and T_{sim} sets with two different numbers of simulations and two different numbers of photons per simulation. The results showed no significant increase in the mean prediction errors when either the number of photons or the number of simulations was reduced. Only when both the number of photons and the number of simulations were reduced simultaneously did a significant increase in the prediction errors occur. Consequently, the total calculation time of the calibration set may be reduced at least 10 times without any significant increase in the average prediction errors.

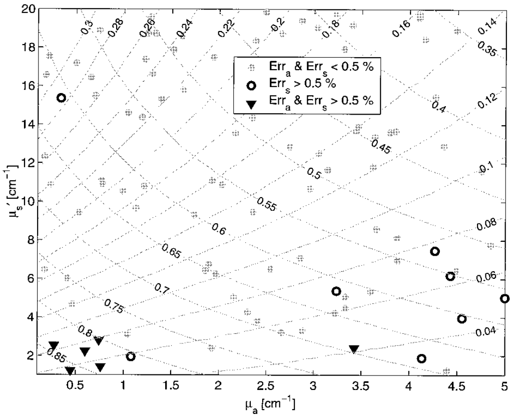

Fig. 4. Solid curves, contour plots of constant R_{sim} and T_{sim} values as a function of μ_a and μ_s'. The curves with positive slopes are R_{sim} plots, and the curves with negative slopes are T_{sim} plots. The markers depict the random distribution of μ_a and μ_s' values in the simulated prediction set. The gray dots indicate cases with prediction errors less than 0.5%. The open circles are cases in which Err$_s$ exceeds 0.5%, and the triangles are cases in which both Err$_a$ and Err$_s$ exceed 0.5%.

4. *Similarity Principle*

When no collimated transmittance data T_c are available during integrating sphere measurements, the similarity principle is often assumed. However, this assumption is strictly valid only for large sample geometries and for $g > 0.9$.[8–10] We tested the validity of the similarity principle, using our calibration model ($g = 0.9$) on a series of simulated R_{meas} and T_{meas} with constant μ_s' but varying g. For constant $\mu_s' = 10\ \text{cm}^{-1}$

Table 1. Prediction Errors, Number of Iterations, and Prediction Calculation Times for Polynomial Fits of Orders 3, 4, and 5

	Err_a (%)		Err_s (%)		Iterations	Calc. Time (ms)
Orders	Mean	Max.	Mean	Max.	Mean	Mean
Third order	1.0	7.8	0.8	6.2	11	54
Fourth order	0.4	3.1	0.4	3.5	11	56
Fifth order	0.2	1.4	0.3	1.1	11	60

we found that the prediction values of μ_s' deviated approximately -2.5% at $g = 0.8$ and $+2.5\%$ at $g = 0.99$, respectively. To determine g in conjunction with R and T measurements, it is necessary to perform T_c measurements also. Because of the practical difficulties involved in T_c measurements, the resulting measurement errors are often more severe than the errors arising from calibration models with a fixed g. However, the MPR method can be readily extended to include determination of μ_s and g as well by generation of calibration models for various g values and application of a simple algorithm for choosing the appropriate model during each prediction.

5. *Comparisons with other Methods*

We also compared the MPR method with the MCSI method[5] and the IAD method.[14] Both the latter methods are capable of extracting the full set of optical properties, i.e., μ_a, μ_s, and g. To do this, they are designed to be fed with collimated transmittance data T_c in addition to the R and T data. In the case of the IAD method it is possible, though, to assume a g value and then use R and T data only. We chose to feed both the MCSI and the IAD method with T_c data calculated with the Beer–Lambert law and the Fresnel law. Table 3 shows the prediction errors, the prediction calculation time, and the number of outliers of the MPR, MCSI, and IAD methods, respectively. The outliers—which we defined as predictions with errors greater than 10%—were excluded from the mean prediction error calculations. All three methods were tested on the same computer.

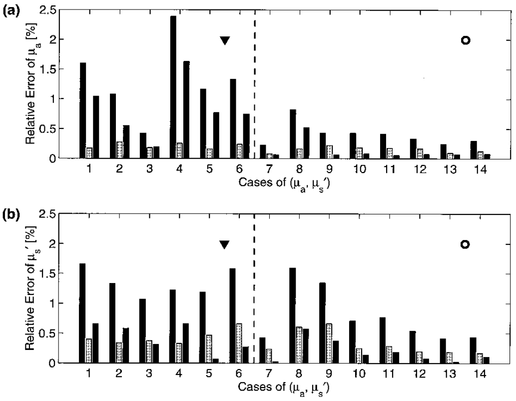

Fig. 5. Analysis of prediction errors greater than 0.5%. The upper graph (a) shows Err_a, and the lower (b) shows the corresponding Err_s. In each single case the three bars indicate the following: left, maximum deviation of ten identical simulations from the true value; middle, average deviation from the mean of the ten simulations; right, deviation of the mean of the ten simulations from the true value.

It appears that the MPR method is significantly faster and more accurate than both the IAD and the MCSI methods. As stated in Subsection 2.B, we applied a finite light source in these experiments. In fact, the IAD method implies uniform illumination; i.e., it is capable of handling one-dimensional light propagation only. This may to some degree account for the lower accuracy. Furthermore, we used only four quadrature points in the IAD calculations. Thus the accuracy of the IAD method may be improved by use of more quadrature points at the expense of the calculation speed.

Although the MCSI and the MPR methods are both based on databases of Monte Carlo simulations, the MPR method yields significantly better accuracy and robustness than the MCSI method. This may be attributed to the fact that the MPR method is less sensitive to the Monte Carlo noise embedded in the databases. The MCSI method is based on spline interpolation of a selection of a few juxtaposed R or T points from the Monte Carlo database. Thus the MCSI fit will pass exactly through all of the selected data points and track any local variation, including intrinsic Monte Carlo noise. Owing to the local variability (i.e., noise) in the Monte Carlo data (see Fig. 3), the interpolated fit may even oscillate widely to pass

Table 2. Prediction Errors with Fifth-Order Polynomial Fits and a Reduced Number of Photon Packets and/or Simulations for the Calibration Model

	1×10^5 Photons/Simulation				1×10^6 Photons/Simulation			
	Err_a (%)		Err_s (%)		Err_a (%)		Err_s (%)	
	Mean	Max.	Mean	Max.	Mean	Max.	Mean	Max.
100 Simulations	0.3	1.2	0.5	2.1	0.2	2.0	0.3	1.6
1000 Simulations	0.2	1.5	0.3	1.4	0.2	1.4	0.3	1.1

Table 3. Prediction Errors, Prediction Calculation Times, and Number of Outliers

Methods	Err_a (%) Mean	Err_s (%) Mean	Calc. Time (ms) Mean	Outliers (%)
MPR	0.2	0.3	60	0
MCSI	1.3	2.0	1350	9
IAD	1.6	2.5	350	9

through all data points and thereby produce unrealistic intermediate values. In contrast, the MPR method is based on two immediate fits including all R and T data points of the Monte Carlo database. In this case the fits are optimized with least-squares regression; thus any local variability in the R and T data will be smoothened out, which in turn will reduce the interference from the random Monte Carlo noise.

C. Phantom Measurements

To further validate the method, we also tested it on R_{meas} and T_{meas} data from phantom measurements. In these experiments we used the small 9 × 13 calibration set described in Subsection 2.C. Assuming that the scattering due to the dye in the phantoms was negligible, we determined the actual μ_a of the 20 phantoms from collimated transmittance measurements of pure dye solutions, using the Beer–Lambert law. Also assuming that the absorption in the polystyrene spheres in the phantoms was negligible, we calculated the actual μ_s' of the phantoms, using Mie theory.[21]

Figure 6 shows correlation plots of the actual optical properties versus optical properties determined from integrating sphere measurements with the MPR method. In this case a few prediction outliers occurred when we used a fifth-order model, whereas a fourth-order model caused no such problems. This is probably because the higher-order models, although they are more accurate in general, may be more sensitive to the inevitable noise in measured prediction data and thus be less robust than lower-order models. As a compromise between accuracy and robustness we therefore used fourth-order models for the predictions presented in Fig. 6. The means of Err_a and Err_s were 1.1% and 1.7%, respectively. In contrast to the errors reported in Subsection 3.B (see Eq. 8), these errors are relative to the dynamic ranges of μ_a and μ_s' in the phantoms:

$$\mathrm{Err} = 100\% \left| \frac{\mu_{\mathrm{pred}} - \mu_{\mathrm{ref}}}{\mu_{\mathrm{ref,max}} - \mu_{\mathrm{ref,min}}} \right| . \tag{9}$$

We used the definition in Eq. (9) in this case, because μ_a includes zero values, leading to division by zero if Eq. (8) is used instead. Although the prediction errors of the measurements are relatively small, they are slightly higher than the errors obtained from similar simulated tests on this model (mean $\mathrm{Err}_a \sim 0.7\%$ and mean $\mathrm{Err}_s \sim 0.2\%$). This is mainly due to uncertainties, partly in the determination of the exact sphere compensation parameters and partly in the stated values of the applied optical properties of microspheres, glass, water, etc. Furthermore, the Monte Carlo simulations employ the Henyey–Greenstein phase function to calculate the scattering properties of the calibration data. However, the

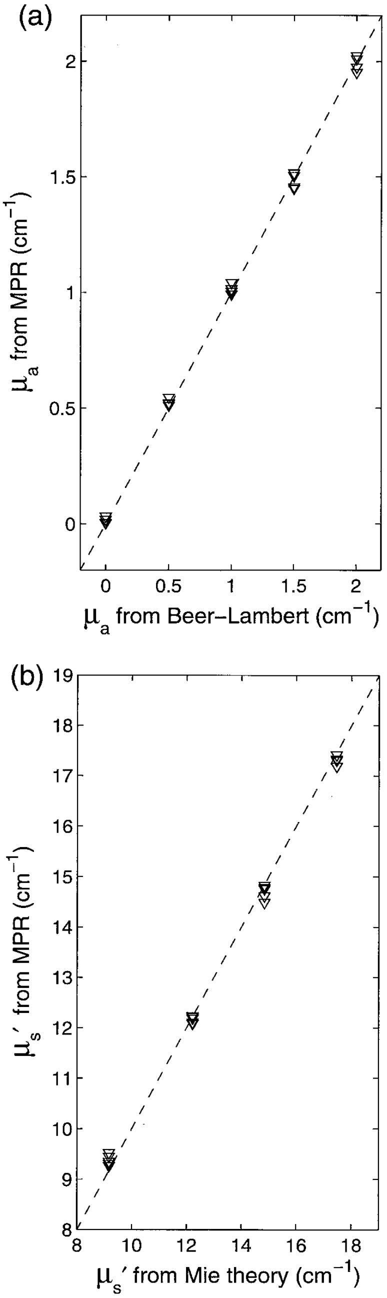

Fig. 6. Correlation plots of theoretical calculations of μ_a (a) and μ_s' (b) versus μ_a and μ_s' values predicted by the MPR method from phantom measurements.

Henyey–Greenstein phase function is an approximation to the more correct and complex phase function obtained from Mie theory calculations. Consequently, this may also account for some of the minor discrepancies between the predicted and the true values of μ_a and μ_s' in Fig. 6.

4. Conclusions

The above results show that the MPR method is accurate, fast, and robust. The minor increase in the prediction errors for low-reflectance levels may be reduced by preprocessing of the calibration data before the fitting is performed. However, if this particular region is of main interest, it would be better to apply a larger sample thickness to increase the reflectance signal level and thereby reduce the effect of the interference from Monte Carlo noise and measurement noise.

It appears that the similarity principle is not strictly valid in the above experiments. Consequently, g variations lead to increased but systematic μ_s' prediction errors of the MPR method. However, if necessary, the MPR method could readily be extended to include direct determination of μ_s and g as well, and thus circumvent any similarity problems.

The calculations of the data for the calibration model suffer from the same advantages and drawbacks as all other Monte Carlo-based methods. The main advantages are the flexibility in sample geometry and the potentially high accuracy. The major drawback is the calculation time needed to obtain this high accuracy. However, the results showed that the MPR method maintained a high level of accuracy when the number of simulations or traced photons in the calibration data set was significantly reduced, i.e., 10 times. In our case this meant that the calculation time of the calibration data could be reduced from days to hours.

The predicted values of μ_a and μ_s' with the MPR method on data from real integrating sphere measurements showed good correlation with theoretically calculated values. These experiments also showed that, when MPR predictions involve real measurement data, it is essential to include proper compensation for the various radiation losses in the setup. Furthermore, it may be necessary to decrease the order of the polynomial fits to obtain robust results on measured (i.e., noisy) data compared with similar experiments on simulated data.

In conclusion, it is evident that, once the calibration model has been implemented, the prediction speed, the accuracy, and the robustness of the MPR method is sufficient for a wide range of real-time spectroscopic analysis applications with integrating sphere measurements.

The authors acknowledge the financial support from the Danish Academy of Technical Sciences.

References

1. N. M. Anderson and P. Sekelj, "Light-absorbed and scattering properties of non-haemolysed blood," Phys. Med. Biol. **12,** 173–184 (1967).
2. A. M. K. Nilsson, G. W. Lucassen, W. Verkruysse, S. Andersson-Engels, and M. J. C. van Gemert, "Changes in optical properties of human whole blood *in vitro* due to slow heating," Photopchem. Photobiol. **65,** 366–373 (1997).
3. A. Roggan, M. Friebel, K. Dörschel, A. Hahn, and G. Müller, "Optical properties of circulating human blood in the wavelength range 400–2500 nm," J. Biomed. Opt. **4,** 36–46 (1998).
4. A. N. Yaroslavsky, I. V. Yaroslavsky, T. Goldback, and H.-J. Schwarzmaier, "Influence of the scattering phase function approximation on the optical properties of blood determined from the integrating sphere measurements," J. Biomed. Opt. **4,** 47–53 (1998).
5. A. M. K. Nilsson, R. Berg, and S. Andersson-Engels, "Measurements of the optical properties of tissue in conjunction with photodynamic therapy," Appl. Opt. **34,** 4609–4619 (1995).
6. W.-C. Lin, M. Motamedi, and A. J. Welch, "Dynamics of tissue optics during laser heating of turbid media," Appl. Opt. **35,** 3413–3420 (1996).
7. A. J. Welch, M. J. C. van Gemert, W. M. Star, and B. C. Wilson, "Overview of tissue optics," *Optical-Thermal Response of Laser-Irradiated Tissue*, A. J. Welch and M. J. C. van Gemert, eds. (Plenum, New York, 1995), Chap. 2.
8. H. C. van de Hulst, *Multiple Light Scattering*, Vols. I and II (Academic, New York, 1980).
9. R. Graff, J. G. Aarnoudse, F. F. M. de MulHenk, and W. Jentink, "Similarity relations for anisotropic scattering in absorbing media," Opt. Eng. **32,** 244–252 (1993).
10. D. R. Wyman, M. S. Patterson, and B. C. Wilson, "Similarity relations for anisotropic scattering in Monte Carlo Simulations of deeply penetrating neutral particles," J. Comp. Physiol. **81,** 137–150 (1989).
11. J. W. Pickering, S. A. Prahl, N. van Wieringen, J. B. Beek, H. J. C. M. Sterenborg, and M. J. C. van Gemert, "A double integrating sphere system for measuring the optical properties of tissue," Appl. Opt. **32,** 399–410 (1993).
12. P. Kubelka, "New contributions to the optics of intensely light scattering materials. Part I," J. Opt. Soc. Am. A **4,** 448–457 (1948).
13. J. Reichmann, "Determination of absorption and scattering coefficients for nonhomogeneous media. 1. Theory," Appl. Opt. **12,** 1811–1815 (1973).
14. S. A. Prahl, M. J. C. van Gemert, and A. J. Welch, "Determining the optical properties of turbid media by using the adding–doubling method," Appl. Opt. **32,** 559–568 (1993).
15. C. R. Simpson, M. Kohl, M. Essenpreis, and M. Cope, "Near Infrared optical properties of ex-vivo human skin and subcutaneous tissues measured using the Monte Carlo inversion technique," Phys. Med. Biol. **43,** 2465–2478 (1998).
16. L.-H. Wang, S. L. Jacques, and L.-Q. Zheng, "MCML—Monte Carlo modeling of photon transport in multi-layered tissues," Comput. Methods Programs Biomed. **47,** 131–146 (1995).
17. S. V. Chapra and R. P. Canale, *Numerical Methods for Engineers* (McGraw-Hill, New York, 1997), Chap. 6.
18. W. F. Cheong, S. A. Prahl, and A. J. Welch, "A review of the optical properties of biological tissue," IEEE J. Quantum Electron. **26,** 2166–2185 (1990).
19. J. F. Beek, P. Blokland, P. Posthumus, M. Aalders, J. W. Pickering, H. J. C. M. Sterenborg, and M. J. C. van Gemert, "*In vitro* double-integrating-sphere optical properties of tissues between 630 and 1064 nm," Phys. Med. Biol. **42,** 2255–2261 (1997).
20. A. Pifferi, P. Taroni, G. Valentini, and S. Andersson-Engels, "Real-time method for fitting time-resolved reflectance and transmittance measurements with a Monte Carlo model," Appl. Opt. **37,** 2774–2780 (1998).
21. C. F. Bohren and D. R. Huffman, *Absorption and Scattering of Light by Small Particles* (Wiley, New York, 1983).

Paper III

Fiber optic probe for non-invasive real-time determination of tissue optical properties at multiple wavelengths

Jan S. Dam[1,2], Carsten B. Pedersen[1], Torben Dalgaard[1], Paul Erik Fabricius[1], Prakasa Aruna[2,3], and Stefan Andersson-Engels[2].

We present a compact, fast, and versatile fiber optical probe system for real-time determination of tissue optical properties from spatially resolved continuous wave diffuse reflectance measurements. The system collects one set of reflectance data from six source-detector distances at four arbitrary wavelengths with a maximum overall sampling rate of 100 Hz. Multivariate calibration techniques based on 2-D polynomial fitting are employed to extract and display the absorption and reduced scattering coefficients in real-time mode. The four wavelengths of the current configuration are 660, 785, 805 and 974 nm, respectively. Cross-validation tests on a 6x7 calibration matrix of Intralipid/dye phantoms shoved that the mean prediction error at e.g. 785 nm was 2.8 % for the absorption coefficient and 1.3 % for the reduced scattering coefficient. The errors are relative to the range of the optical properties of the phantoms at 785 nm, which were 0 - 0.3 /cm for the absorption coefficient and 6 - 16 /cm for the reduced scattering coefficient. Finally, we also present and discuss results from preliminary skin tissue measurements.

OCIS Codes: 170.1470, 170.1580, 170.3890, 170.6510

1. Introduction

The optical properties of human tissue[1], i.e. the absorption coefficient μ_a, the scattering coefficient μ_s, and the anisotropy factor g may provide important information on the composition and the physiological dynamics of the tissue. While μ_a may provide information on tissue chromophores[2-4], μ_s and g may be used to characterize the form, size, and concentration of various scattering components in the tissue[5–8].

Owing to the obvious advantages of non- and minimal-invasive measurements, determination of tissue optical properties based on diffuse reflectance measurements has a significant potential in the fields of biomedical diagnostics and monitoring. Diffuse reflectance measurements may be roughly divided into time-resolved[9,10] (TR), frequency-domain[11,12] (FD), and spatially resolved continuous wave[13–21] (CW) methods. Traditionally, TR and FD based methods have been considered to be more accurate for absolute determination of optical properties than CW based methods. However, TR and FD methods also require more bulky and expensive equipment, and a larger sample volume, which may restrict some biomedical applications, e.g. implementation in portable monitoring equipment or in endoscopes and catheters. Recent work[19] has shown that CW based methods may yield absolute determination of the optical properties of tissue with accuracies similar to the TR and FD methods, which makes CW based methods a better choice for many practical applications.

CW diffuse reflectance methods may be further dived into methods based on probes in contact with the tissue and non-contact methods, i.e. image reflectometry. The latter method is advantageous in clinical applications because of the non-contact and thus sterile properties. The advantage of CW probes is that they can be made small and portable. Therefore, they are

---

[1] Bang & Olufsen Medicom a/s, DK-7600, Struer, Denmark.

[2] Dept. of Physics, Lund Institute of Technology,

P.O. Box 118, SE-22100, Lund, Sweden.

[3] Anna University, 600 025 Madras, India

well suited for (a) optical biopsies of body cavities or organs because a probe may be implemented in existing endoscopic equipment or (b) for long-time monitoring of tissue optical properties, because the probe may be fixed to the skin and still allow the patient to move around. However, there are a number of drawbacks related to skin tissue monitoring using a contact probe system. Firstly, the static mechanical pressure of the probe may influence the tissue optical properties, e.g. by displacing blood in the sample volume. Secondly, physical activities of the patient may lead to motion artifacts, i.e. movements of the probe relative to the skin tissue. Finally, the obstruction of the tissue and sweating may cause long-term changes in the tissue optical properties and the probe/skin optical interface. All such inferences have to be isolated in order to extract the relevant information from diffuse reflectance measurements.

Accurate closed form mathematical analytical expressions for spatially resolved diffuse CW reflectance $R(r)$ as a function of the optical properties is strongly limited by requirements to the range of the optical properties and the specific geometry of the setup[22]. Therefore, methods based on more accurate numerical light propagation models, e.g. Monte Carlo simulations[23], are often used in conjunction with various forms of multivariate analysis[19,24] to solve the inverse problem of extracting the optical properties from $R(r)$ measurements. However, as a consequence of the similarity principle[25,26], normally only μ_a and the reduced scattering coefficient $\mu'_s = (1-g)\mu_s$ are extracted from $R(r)$ measurements.

In this paper, we present a fiber optic probe system for in vivo real-time determination of tissue optical properties based on $R(r)$ measurements at four arbitrary wavelengths. The probe system collects the diffuse reflectance at six distances, extracts the corresponding μ_a and μ'_s and displays the results immediately on a laptop PC. The prediction of μ_a and μ'_s is based on multiple polynomial regression[27] and calibration on a set of Intralipid/dye phantoms with well-known optical properties within a range typical for biological tissue[28] in the visible and near-infrared region. In the following sections we first give a description of the probe specifications and the principles of the calibration and prediction algorithms. Next, we present and discuss the results obtained from phantom measurements and simulated numerical tests with respect to prediction errors, robustness etc. Finally, we present the results of preliminary prediction tests obtained from a series of clinical measurements on normal skin tissue.

2. Methods and Materials

A. Fiber Probe System

Figure 1 shows the basics of the fiber probe system we have used for the measurements described in the following.

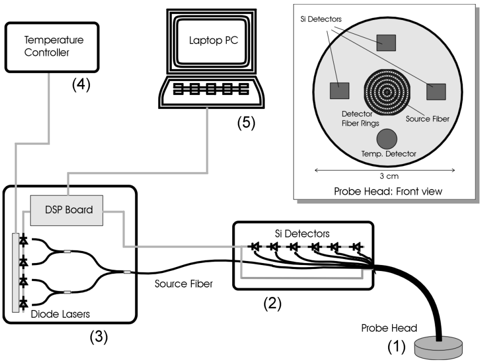

Figure 1 Diagram of the fiber optic system for $R(r)$ measurements applied in this paper. (1) Probe head with source and detector optical fibers mounted in a rotational symmetric configuration. (2) Handheld box with silicon photo diodes and amplifier electronics. (3) Stationary box containing a DSP board and the light sources in the form of diode lasers. (4) External temperature controller to maintain a constant temperature of the diode lasers. (5) Laptop PC to analyze, display, and store the acquired $R(r)$ data.

The system consists of a probe head with a 200 µm source fiber in the center surrounded by five equally spaced concentric rings of 250 µm detector fibers. We chose this ring geometry instead of e.g. a simpler linear geometric configuration, partly to be able to collect more light at the farther distances, and partly to minimize any problems arising from tissue inhomogeneities during clinical measurements. The fibers of each single ring detector are bundled and terminated on separate silicon photo diodes. In addition, three photo diodes and a temperature sensor are mounted directly near the perimeter of the probe head. Thus, $R(r)$ can be collected at six distances, i.e. $r =$ 0.6, 1.2, 1.8, 2.4, 3.0, and 7.8 mm, respectively. These distances were chosen on the basis of previous studies[19]. The gain of each reflectance detector has been calibrated in an integrating sphere setup to obtain equal outputs at constant input light intensities.

The source fiber is coupled into four separate fibers each connected to four replaceable low-power diode lasers. The diode lasers are mounted on a heat sink with a constant temperature maintained by an external controller. Furthermore, a separate reference detector monitors the output of the source fiber at the probe head. The diode lasers may be selected arbitrarily in order to suit different applications. In this paper we have used diode lasers with the wavelengths 660, 785, 805, and 974 nm, which are well suited for applications involving hemodynamic monitoring. The data acquisition and storage is controlled by a laptop PC connected to a digital signal processing (DSP) board. In each $R(r)$ measurement the detector hardware collects data simultaneously in eight parallel channels from the probe head, i.e. from the six detector rings, from the reference detector at the source fiber, and from the temperature sensor. One cycle of four successive measurements (i.e. one at each wavelength) including dark measurements may be performed in about 10 ms, thus the maximum sampling rate of the system is about 100 Hz. To minimize any interference from background light or drift of the light source, the dark measurements are subtracted from the measured reflectance data after which they are normalized relative to the source reference. The DSP board accomplishes this prior to when the data are analyzed, displayed and stored by the PC.

B. Calibration and Prediction Algorithms

In theory, μ_a and μ'_s may be determined using $R(r)$ data from only two of the six detector distances of the fiber probe. Building on our previous work[19,27], we thus applied multiple polynomial regression (MPR) to create a calibration model and subsequently extract μ_a and μ'_s from $R(r)$ measurements at r_1 = 0.6 mm and at r_2 = 7.8 mm. For the sake of clarity we give a summary of the MPR method here. We first measure $R(r)$ at r_1 and at r_2 for a set of calibration samples with well-defined optical properties and denote them $R_{1,cal}$ and $R_{2,cal}$. Then, we find a double-polynomial fit to $R_{1,cal}$ and $R_{2,cal}$:

$$\begin{aligned} R_{1,fit}(\mu_a,\mu'_s,m) &= (a_0 + a_1\mu_a + a_2\mu_a{}^2 + \ldots a_m\mu_a{}^m) \\ &\times (b_0 + b_1\mu'_s + b_2\mu'_s{}^2 + \ldots b_m\mu'_s{}^m) \\ R_{2,fit}(\mu_a,\mu'_s,m) &= (c_0 + c_1\mu_a + c_2\mu_a{}^2 + \ldots c_m\mu_a{}^m) \\ &\times (d_0 + d_1\mu'_s + d_2\mu'_s{}^2 + \ldots d_m\mu'_s{}^m) \end{aligned} \quad (1)$$

Where, the a, b, c, and d's are fitting coefficients determined by least-squares regression. $R_{1,fit}$ and $R_{2,fit}$ thus constitute the calibration model. The next step is to solve the inverse problem of determining μ_a and μ'_s from $R(r)$ measurements on a set of prediction samples, i.e. $R_{1,meas}$ and $R_{2,meas}$. First we define

$$\begin{aligned} F(\mu_a,\mu'_s) &= R_{1,fit} - R_{1,meas} \\ G(\mu_a,\mu'_s) &= R_{2,fit} - R_{2,meas} \end{aligned} \quad (2)$$

Then, we use a Newton-Raphson algorithm to perform converging iterative calculations of μ_a and μ'_s:

$$\left.\begin{aligned} -\begin{bmatrix} \mathrm{F}(\mu_{\mathrm{a,k}},\mu'_{s,k}) \\ \mathrm{G}(\mu_{\mathrm{a,k}},\mu'_{s,k}) \end{bmatrix} &= \begin{bmatrix} \dfrac{\partial F}{\partial \mu_a} & \dfrac{\partial F}{\partial \mu'_s} \\ \dfrac{\partial G}{\partial \mu_a} & \dfrac{\partial G}{\partial \mu'_s} \end{bmatrix} \begin{pmatrix} h_{a,k} \\ h_{s,k} \end{pmatrix} \\ \begin{pmatrix} \mu_{a,k+1} \\ \mu'_{s,k+1} \end{pmatrix} &= \begin{pmatrix} \mu_{a,k} \\ \mu'_{s,k} \end{pmatrix} + \begin{pmatrix} h_{a,k} \\ h_{s,k} \end{pmatrix} \end{aligned}\right\} \quad (3)$$

$$k = 0,1,2,3,\ldots,$$

Where, h_a and h_s are correction terms of μ_a and μ'_s. The calculations continue until h_a and h_s have dropped below predefined maximum values.

Since in this study we want to extract two optical properties only, i.e. μ_a and μ'_s, the MPR method implies exactly two input variables as well, i.e. $R(r_1)$ and $R(r_2)$. However, due to tissue inhomogeneity and/or noisy measurement conditions it might be advantageous to include more source-detector distances during measurements and then subsequently apply some sort of dimension reduction method before the data are fed to the MPR method. In order to test such a procedure, we also applied principal component analysis (PCA) on the data from all six source-detector distances of the probe system and then used the resulting two main principal components P_1 and P_2 as input to the MPR method instead of $R(r_1)$ and $R(r_2)$.

All the prediction algorithms we have applied in this paper were implemented in Matlab and run on a 166 MHz PC. With this configuration, the prediction of a single set of μ_a and μ'_s could be performed in about 60 ms.

C. Phantoms

Due to the unknown numerical apertures of the fiber probe light source and detectors, we chose to calibrate the system directly on a set of phantoms instead of using a mathematical light propagation model. The phantoms consisted of well-defined aqueous solutions of Intralipid and black ink in cylindrical glass containers with a diameter of 10 cm and a height of 4 cm. We determined the scattering and absorption spectra of the Intralipid and the black ink from integrating sphere[27] and traditional transmission spectroscopy measurements. On the basis of these spectra, we mixed a 6x7 matrix of phantoms with μ_a and μ'_s ranges typical for skin tissue (see Table 1). The applied range of Intralipid concentrations were 0.6, 0.8, …1.6 %, and the range of the ink concentrations were 0.0, 0.2, …1.2 %. It should be noted, that the absorption of pure ink is much higher than that of typical biological substances, thus the ink concentrations in the following refers to a premixed basic ink/water solution with a biological relevant absorption level.

Table 1 Optical property ranges of 6x7 matrix of Intralipid/Ink phantoms determined from integrating sphere measurements.

	Optical property range (cm^{-1})	
λ (nm)	μ_a	μ'_s
660	0 - 0.36	7.3 - 19.5
785	0 - 0.32	6.1 - 16.3
805	0 - 0.31	6.0 - 16.0
974	0.45 - 0.68	4.8 - 12.7

To perform the prediction experiments, we calibrated the probe system directly to the concentrations of the Intralipid and the ink in the phantoms, assuming that the absorption of pure Intralipid[29,30] and the scattering of the ink both were negligible. At 660, 785, and 805 nm, we assumed that the background absorption was negligible as well. However, water exhibits substantial absorption[31] at 974 nm ($\mu_{a,water}$= 0.45 cm^{-1}). This was incorporated in the concentration-to-absorption tabulation by assuming a constant water absorption contribution at this particular wavelength (e.g. $c_{ink} = 0\% \Rightarrow \mu_a = 0.45\,\mathrm{cm}^{-1}$).

3. Results

Once the 6x7 matrix of phantoms had been mixed, we determined the actual optical properties of a subset of the phantom matrix using integrating sphere measurements. Figure 2(a) shows the mean absorption spectra of the 6 phantoms with 1% ink concentrations but varying Intralipid concentrations, and Figure 2(b) shows the mean scattering spectra of the 7 phantoms with 1 % Intralipid concentrations but varying ink concentrations. We used the results from Figure 2(a) to relate the concentrations of Intralipid and ink to the optical properties of the phantoms. The resulting optical property ranges of the 6x7 matrix phantoms are listed in Table 1.

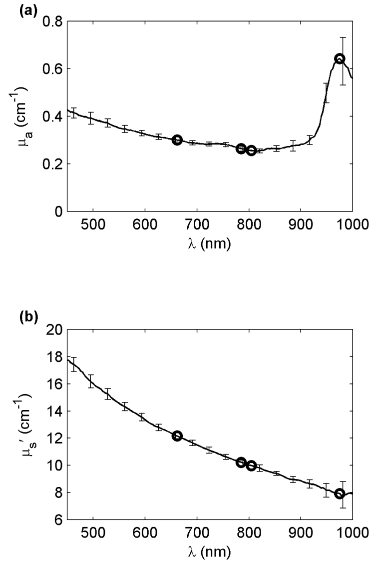

Figure 2 Optical property spectra of the applied Intralipid/ink phantoms. Panel (a) shows the mean of μ_a as a function of the wavelength λ for the six phantoms with 1 % ink concentration, but varying Intralipid concentrations. Likewise, panel (b) shows the mean of μ'_s as a function of the wavelength for the seven phantoms with 1 % Intralipid concentration, but varying ink concentrations. The error bars of the spectra in panel (a) and (b) show the standard deviations of μ_a and μ'_s, respectively. The circles indicate the values at the four wavelengths of the probe. The two spectra were measured and calculated using an integrating sphere setup in conjunction with the MPR method.

Figure 3(a) and Figure 3(b) shows the measured intensity $R(r)$ at 785 nm as a function of μ_a and μ'_s at r = 0.6 mm and r = 7.8 mm, respectively. Corresponding plots at the three remaining wavelengths of the probe, i.e. 660, 805, and 974 nm, showed similar characteristics, i.e. they were also smooth and monotonic, which suggests that they may be fitted well by Eq. (1) using relatively low-order polynomials. Preliminary experiments showed that using Eq. (1) with m = 3 provided the best overall calibration model, concerning accuracy and robustness.

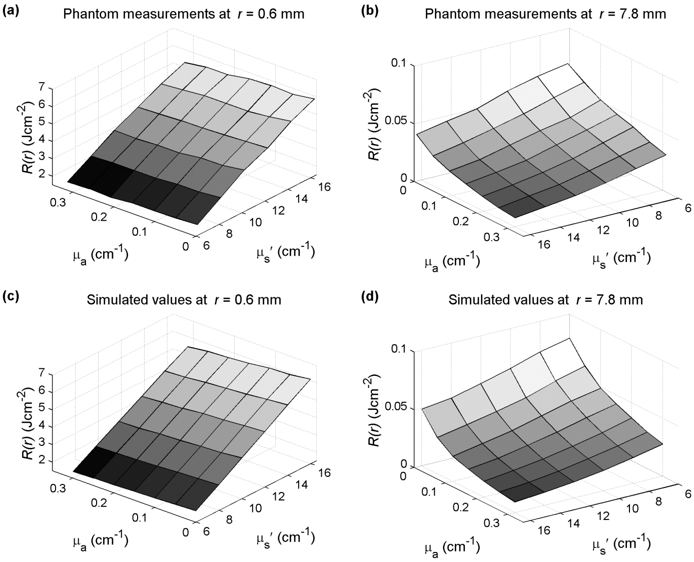

Figure 3 Surface plots of $R(r)$ at $r_1 = 0.6$ mm and $r_2 = 7.8$ mm as a function of μ_a and μ'_s. Panel (a) and (b) show the $R(r)$ plots of the 6x7 Intralipid phantoms at 785 nm, and panel (c) and (d) show the corresponding $R(r)$ plots based on Monte Carlo Simulations. Note that the arbitrary intensity units of measured $R(r)$ plots have been scaled in order to compare them with the simulated plots.

The prediction accuracy of the MPR method was tested using leave-one-out cross validation. This means that we successively performed predictions using the data from one phantom for prediction and the data from the remaining 41 phantoms of the 6x7 matrix for calibration. In order to insure that all $R(r)$ variations were covered by the calibration models, we only carried out predictions on the 4x5 interior subset of the 6x7 matrix. Table 2 presents the results from these cross validation prediction tests.

Table 2. Leave-one-out cross validation prediction tests based on phantom measurements. The errors are relative to the ranges of μ_a and μ'_s of the phantoms. The bracketed values at $\lambda =$ 660 nm, have been corrected for an outlier detected by visual inspection of the measured $R(r)$ data.

	Prediction Errors (%)			
	μ_a		μ'_s	
λ (nm)	Mean	Max.	Mean	Max
660	3.3 (2.5)	18 (6.7)	1.7 (1.7)	3.7 (4.0)
785	2.8	8.3	1.3	3.4
805	2.6	9.0	1.5	4.2
974	3.7	9.7	1.6	3.8

To check our experimental results, and to examine the robustness, noise sensitivity, etc. of the applied calibration model and prediction algorithms we also performed a series of numerical tests based on Monte Carlo simulations with a geometric configuration analogous to fiber probe set-up described in Sect. 2.A. However, unlike the measurements, the simulations were based on a collimated incident beam, a semi-infinite medium, and $1/2\pi$ acceptance angle for collection of the diffuse reflectance. The tests were carried out as follows: (I) First, we generated a basic 6x7 calibration matrix with optical properties corresponding to the 6x7 phantom matrix at $\lambda = 785$ nm and then performed prediction tests similar to the phantom cross validation tests described above. Figure 4 shows a selected set of $R(r)$ profiles from these simulations (see also Figure 3(c) and Figure 3(d)). (II) Next, to test the algorithms with independent calibration and prediction data, we generated a series of 20 $R(r)$ data sets with random μ_a and μ'_s distributions and then performed predictions on this randomized set using a calibration model based on the full 6x7 basic matrix. (III) The basic 6x7 matrix were generated using $1 \cdot 10^6$ photons. In order to examine the impact of random measurement noise on the prediction performance, we generated a second 6x7 matrix with less noise by using $1 \cdot 10^7$ photons and performed identical cross validation tests on this set. (IV) We also wanted to investigate the effect of using a calibration model with a higher μ_a and μ'_s resolution, thus we also carried out cross validation tests on a 11x13 calibration matrix with the same μ_a and μ'_s range and number of photons as the basic 6x7 matrix. (V) Finally, we tested the effect of using PCA for dimension reduction as described in Sect. 2.B. The resulting mean and maximum prediction errors from the numerical tests (I–V) described above are summarized in Figure 5.

In order to validate the optical property range of the applied calibration model we performed a series of probe measurements on the inner forearm of 5 healthy individuals. Figure 6 shows how the mean $R(r)$ of all 5 individuals (circles) at each probe distance is situated relative to the $R(r)$ ranges of the calibration model (vertical bars). Figure 6 also shows the predicted optical properties at all four wavelengths calculated from the mean $R(r)$ data using Eq. (1) - (3). It can be seen that the measured skin tissue at $\lambda = 660$ nm and $r =$ 7.8 mm is outside the calibration model range, and therefore, it is not possible to predict μ_a and μ'_s correctly in this case.

4. Discussion

A. Geometry Considerations

In Figure 4(a) and (b) μ'_s is kept constant at values of 6 cm^{-1} and 16 cm^{-1}, respectively. In these two cases, it appears that changes in μ_a have a negligible effect on $R(r)$ at distances close to the source. In Figure 4(c) and (d), μ_a is kept constant at values of 0 cm^{-1} and 0.3 cm^{-1}, respectively. Here, it is notable that there is very little variation in $R(r)$ at $r \approx$ 0.35 cm in Figure 4(c) and at $r \approx$ 0.3 in Figure 4(d). With a figure of speech, we say that there is a “pivot point” in the $R(r)$ graphs at $r \approx$ 0.3 cm, when μ_a is kept constant. The simulations in Figure 4(a) and Figure 4(b) indicates that μ'_s may be determined with good accuracy from close distance measurements only. To determine μ_a as well, Figure 4(c) and (d) suggest that $R(r)$ measurements close to the pivot point should be included, since there is little variation in $R(r)$ as a function of μ'_s at this point.

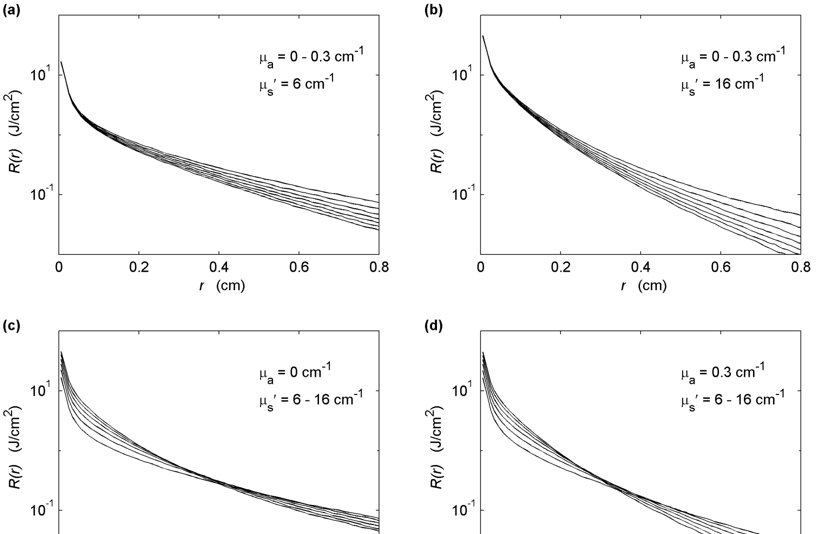

Figure 4 Monte Carlo simulated $R(r)$ data for various combinations of μ_a and μ'_s within ranges typical for skin tissue at 785 nm. In (a) and (b), μ'_s is kept constant at 6 cm^{-1} and 16 cm^{-1}, respectively while μ_a is varied within the range 0 – 0.3 cm^{-1}. In (c) and (d), μ_a is kept constant at 0 cm^{-1} and 0.3 cm^{-1}, respectively while μ'_s is varied within the range 6 – 16 cm^{-1}.

Although, other authors[32,33] support this argumentation, we have based our experiments in this paper on close range distances in conjunctions with distances well beyond the pivot point. We did this, because our previous studies[19] showed that this geometrical configuration provided a better accuracy than a configuration with close range distances in conjunction with distances near the pivot point.

B. Phantom Measurements

The prediction tests using Intralipid/ink phantoms show a good accuracy (see Table 2). The mean prediction error at all four wavelengths is roughly 3 % for μ_a, and 1.5% for μ'_s, while the maximum prediction errors for μ_a and μ'_s is about 11 % and 4 %, respectively. The prediction algorithm converged in all cases; however, the maximum error of μ_a at $\lambda =$ 660 nm is remarkably high (18 %). A visual inspection of the raw $R(r)$ data at 660 nm revealed an outlier at $r =$ 7.8 mm in one of the phantom measurements. This outlier could be due to an air bubble or a piece of dirt at one of the three 7.8 mm detectors in this particular measurement. When we removed the outlier from the calibration and prediction analysis at $\lambda =$ 660 nm, we obtained the improved results shown in brackets in Table 2.

In general, the prediction errors of μ_a are about twice as high as the errors of μ'_s. This may partly be attributed to the fact that μ_a is mainly determined on the basis of the $R(r)$ data at $r =$ 7.8 mm, while μ'_s is almost solely determined from $R(r)$ data at $r =$ 0.6 mm, where the signal level is about 1000 times the level at $r =$ 7.8 mm. The μ_a predictions are therefore more sensitive to any background noise interference during the measurements.

With reference to the comments on the pivot point in Sect. 4.A we also performed a series of prediction tests, where we replaced the $R(r)$ probe data at $r_2 =$ 7.8 mm with probe data at the pivot point $r_{pivot} =$ 3.0 mm. This had no significant effect on the μ'_s prediction errors, but both the mean and the maximum μ_a prediction errors increased roughly 30 % compared to results reported in Table 2.

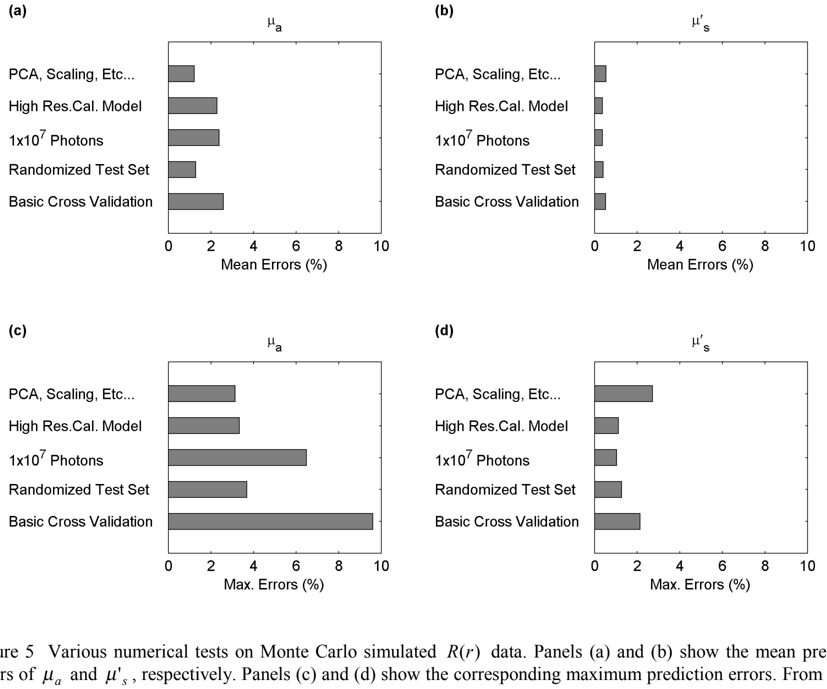

Figure 5 Various numerical tests on Monte Carlo simulated $R(r)$ data. Panels (a) and (b) show the mean prediction errors of μ_a and μ'_s, respectively. Panels (c) and (d) show the corresponding maximum prediction errors. From below: (I) Cross validation on a basic 6x7 calibration matrix corresponding to phantom measurements at 785 nm. (II) Predictions on data with random μ_a and μ'_s distribution. (III) Cross validation on 6x7 matrix generated using $1 \cdot 10^7$ photons. (IV) Cross validation on a high resolution 11x13 calibration matrix. (V) Cross validation on the basic 6x7 calibration matrix using principal component analysis.

C. Numerical Tests

The general shape of the measured and the simulated $R(\mu_a, \mu'_s)$ plots in Figure 3 are very similar at corresponding detector distances. However, the simulated plots do show slightly higher $R(\mu_a, \mu'_s)$ levels for low μ_a and μ'_s values at $r =$ 7.8 mm. This difference is severe enough to prevent the direct use of a calibration model based on Monte Carlo simulations for prediction analyses of $R(r)$ data collected with the fiber probe. The difference between the simulated and the measured $R(r)$ data in Figure 3(b) and (d) may be attributed to the different numerical apertures of the sources and the detectors in the two cases, e.g. the Monte Carlo simulations employ a collimated source beam, while the probe source beam is divergent.

The μ_a prediction errors of the simulated data shown in Figure 5(a) and (c) are comparable with the errors of the measured data Table 2, while the μ'_s prediction errors of the simulated data (Figure 5(b) and (d)) are lower than the errors of the measured data. In both cases the μ_a prediction errors are significantly higher than the μ'_s errors, probably owing to the noise sensitivity at $r =$ 7.8 mm as discussed above. Figure 5 also shows a drop in the prediction errors when using a randomized prediction data set. This may be due to the fact that the quality of the calibration model fit during leave-one-out cross validation is reduced in the vicinity of the μ_a and μ'_s to be predicted. Consequently, the fiber probe system may perform better during real measurements on samples with unknown optical properties, than the results in Table 2 indicates.

From Figure 5 it also appears that a reduction in measurement noise (i.e. more photons) or using calibration model with a higher μ_a and μ'_s resolution in both cases lead to a significant drop in maximum prediction errors, while the effect on the mean prediction errors is moderate. Finally, it can be seen from Figure 5 that the use of PCA before calibration and prediction has a positive effect on the μ_a prediction errors, while the μ'_s prediction errors are slightly increased. In summary, the prediction accuracy obtained from calibration and prediction on phantoms are comparable with the accuracy obtained from calibration and prediction on Monte Carlo simulated data. The numerical tests suggest that the prediction accuracy may be improved slightly by using more samples when creating the calibration model. However, the improvements may hardly justify the additional efforts of creating more calibration phantoms.

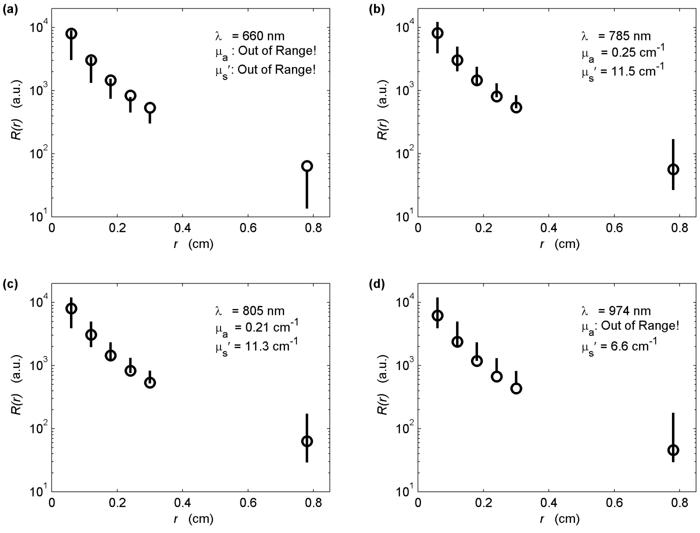

Figure 6 Mean optical properties at all four wavelengths determined from $R(r)$ measurements on the forearm of five healthy individuals. The vertical bars indicate the valid range of the applied calibration model at various distances and wavelengths, and the circles indicate the mean measured $R(r)$ of the five individuals. At each of the four wavelengths, the stated values of μ_a and μ'_s were determined on the basis of the mean $R(r)$ values at $r_1 =$ 0.6 mm and $r_2 =$ 7.8 mm.

D. Clinical Measurements

From Figure 6 it appears that the range of calibration model covers the span of the measured tissue $R(r)$ data in most cases, except at $\lambda =$ 660 nm. At this wavelength, the mean of the measured $R(r)$ at $r_2 =$ 7.8 mm is above the range of the calibration model. This suggests that either μ_a or μ'_s (or both) of the skin tissue are lower than the minimum values of the calibration model. In the case of μ_a this is not possible, since the model range at $\lambda =$ 660 nm is 0 – 0.36 cm^{-1}. The minimum value of μ'_s of the model at this wavelength is 7.3 cm^{-1}, and it is not likely that the measured μ'_s should be beneath this limit either. At the three remaining wavelengths the measured $R(r)$ at $r_1 =$ 0.6 mm and $r_2 =$ 7.8 mm are within the limits of the calibration mode, and the extracted μ_a or μ'_s show a reasonable correlation with other studies[20,34]. However, at 974 nm, it appears that the measured $R(r)$ data, at some of the intermediate distances (i.e. at r = 2.4 and 3.0 mm) are not within the ranges of the calibration model, i.e. the shape of the tissue $R(r)$ profiles are different from the shape of phantom profiles. There may be several reasons for this. Firstly, in contrast to the phantoms, the volume of the skin tissue sampled by the probe is not homogeneous but basically consists of distinct layers, i.e. the stratum corneum, the vivid epidermis, the epidermis, etc. Each of these layers has specific optical properties, and therefore the predicted values of μ_a or μ'_s in Figure 6 are a compound of the optical properties of each separate layer. Secondly, the ratio of the refractive indexes between the probe and the sample (n_{probe} / n_{sample}) is different in the two cases, i.e. $n_{tissue} \approx$ 1.40[35] and $n_{phantom} \approx$ 1.33. Finally, the probe tissue interface may not have been optimal, which in turn may lead to light piping effects between the probe and the stratum corneum. Such effects may cause an increase of the farther $R(r)$ values relative to the values close to the light source, which also might explain the "out of range" problems encountered at $\lambda =$ 660 nm. To summarize, it is essential to ensure a proper optical contact and apply a uniform and reproducible mechanical pressure in order to obtain valid predictions from contact probe measurements.

E. Acquisition and Analysis Speed

As we stated in Sect. 2.A the maximum acquisition rate of the fiber probe system for all four wavelengths is about 100 Hz, which is sufficient for analyzing the optical property dynamics of most physiological systems. The current software implementation of the prediction algorithms leads to an analysis time for one set of μ_a or μ'_s of about 50 ms, i.e. an analysis rate of 5 Hz when all four wavelengths are included. To match the analysis rate to the acquisition rate of the probe system, the speed of the prediction algorithms may be increased substantially by applying a more contemporary PC and/or by compiling the algorithms in e.g. the C programming language.

5. Conclusions

We have demonstrated a versatile, fast and accurate probe system for real-time non-invasive determination of tissue optical properties from continuos wave spatially resolved diffuse reflectance measurements. The current calibration of the system was intended to match a typical range of absorption and reduced scattering coefficients of skin tissue, and preliminary clinical trials on a set of healthy individuals showed a good consistency except at $\lambda =$ 660 nm. At this wavelength, the measured tissue data was outside the range of the calibration model in some occasions. This problem may be solved by extending the range of the calibration model, but the problem may also originate in the fact that the system was calibrated on homogeneous one-layer phantoms, while skin tissue is a inhomogeneous multi-layer structure. Furthermore, the clinical trials clearly demonstrated that is imperative to ensure proper and reproducible refractive index matching and mechanical contact properties to obtain valid results. All things considered, the system and the method we have presented here provide a sound basis for future development of compact and dedicated systems for non- or minimal-invasive medical diagnostics and monitoring. Still, further work is required to explore the applicability for specific biomedical implementations.

The authors acknowledge the financial support from the Danish Academy of Technical Sciences

References

1. Welch J., van Gemert M. J. C., Star W. M., and Wilson B. C., "Overview of tissue optics," *Optical-Thermal Response of Laser-Irradiated Tissue,* A. J. Welch and M. J. C. van Gemert, eds. (Plenum, New York, 1995), Chap. 2.

2. Feather J. W., Ellis D. J., and Leslie G., "A portable reflectometer for the rapid quantification of cutaneous haemoglobin and melanin," Physics in Medicine and Biology 33, 711-722 (1988).

3. Jacques S. L., “Reflectance spectroscopy with optical fiber devices, and transcutaneous bilirubinometers,” in *Biomedical optical instrumentation and laser-assisted biotechnology,* A. M. Verga Scheggi, S. Martellucci, A. N. Chester, and R. Pratesi, eds., 83-94 (1996).

4. Franceschini M. A., Gratton E., and Fantini S., “Noninvasive optical method of measuring tissue and arterial saturation: an application to absolute pulse oximetry of the brain,” Opt. Let. 24 829-831 (1999).

5. Jacques S. L. “Origins of tissue optical properties in the UVA, Visible, and NIR regions,” OSA TOPS on Advances in Optical Imaging and Photon Migration 2, 364-369, eds. RR Alfano, JG Fujimoto, publ. Optical Society of America (1996).

6. Hielscher A. H., Mourant J. R., and Bigio I. J., “Influence of particle size and concentration on the diffuse backscattering of polarized light from tissue phantoms and biological cell suspensions,” Appl. Opt. 36**,** 125-135 (1997).

7. Mourant J. R., Freyer J. P., Hielscher A. H., Eick A. A., Shen D., and Johnson T. M., “Mechanisms of light scattering from biological cells relevant to noninvasive optical-tissue diagnotics,” Appl. Opt. 37**,** 3586-3593 (1998).

8. Bruulsema J. T., Hayward J. E., Farrell T. J., Patterson M. S., Heinemann L., Berger M., Koschinsky T., Sandahl C. J., Orskov H., Essenpreis M., Schmelzeisen R. G., and Bocker D., “Correlation between blood glucose concentration in diabetics and noninvasively measured tissue optical scattering coefficient,” Opt.Let. 22, 190-192 (1997).

9. Patterson M. S., Chance B., and Wilson B. C., “Time resolved reflectance and transmittance for the non-invasive measurement of tissue optical properties,” Appl. Opt. 28, 2331-2336 (1989).

10. Andersson-Engels S., Berg R., Persson A., and Svanberg S., “Multispectral tissue characterization with time-resolved detection of diffusely scattered white light,” Opt. Let. 18, 1697-1699 (1993).

11. Chance B., Cope M., Gratton E., Ramanujam N., and Tromberg B., “Phase measurement of light absorption and scatter in human tissue,” Rev. Scient. Instr. 69, 3457-3481 (1998).

12. Fantini S., Franceschini M.A., Maier J. S., Walker S. A., Barbieri B., and Gratton E., “Frequency-domain multichannel optical detector for noninvasive tissue spectroscopy and oximetry,” Opt. Eng. 34, 32-42 (1995).

13. Farrell T. J., Patterson M. S., and Wilson B., “A diffusion theory model of spatially resolved, steady-state diffuse reflectance for noninvasive determination of tissue optical properties *in vivo*,” Med. Phys. 19**,** 879-888 (1992).

14. Marquet P., Bevilacqua F., Depeursinge C., and De-Haller E. B., “Determination of reduced scattering and absorption coefficients by a single charge-coupled-device array measurement. I. Comparison between experiments and simulations,” Opt. Eng. 34, 2055-2063 (1995).

15. Kienle A., Lilge L., Patterson M. S., Hibst R., Steiner R., and Wilson B. C., “Spatially resolved absolute diffuse reflectance measurements for noninvasive determination of the optical scattering and absorption coefficients of biological tissue,” Appl. Opt. 35**,** 2304-2314 (1996).

16. Bays R., Wagnieres G., Robert D., Braichotte D., Savary J. F., Monnier P., and van-den B. H., “Clinical determination of tissue optical properties by endoscopic spatially resolved reflectometry,” Applied Optics 35, 1756-1766 (1996).

17. Mourant J. R., Fuselier T., Boyer J., Johnson T. M., and Bigio I. J., “Predictions and measurements of scattering and absorption over broad wavelength ranges in tissue phantoms,” Appl. Opt. 36**,** 949-957 (1997).

18. Nichols M. G., Hull E. L., and Foster T. H., “Design and testing of a white light, steady state diffuse reflectance spectrometer for determination of optical properties of highly scattering systems,” Appl. Opt. 36, 93-104 (1997).

19. Dam J. S., Andersen P. E., Dalgaard T., and Fabricius P. E., “Determination of tissue optical properties from diffuse reflectance profiles by multivariate calibration,” Appl. Opt. **37,** 772-778 (1998).

20. Doornbos R. M., Lang L., Alders R., Cross F. W., and Sterenborg H. J. C. M., “The determination of in vivo human tissue optical properties and absolute chromophore concentrations using spatially resolved steady-state diffuse reflectance spectroscopy,” Phys. Med. Biol. 44, 967-981 (1999).

21. Pham T. H., Bevilacqua, F., Spott T., Dam J. S., Tromberg B. J., and Andersson-Engels S., “Quantifying the absorption and reduced scattering coefficients of tissue-like turbid media over a

broad spectral range using a non-contact Fouirier interferometric, hyperspectral imaging system.," Appl. Opt. (accepted!)

22. Wang L. V. and Jacques S. L., "Source of error in calculation of optical diffuse reflectance from turbid media using diffusion theory," Comp. Meth. Prog. Biomed. 61, 163-170 (2000).

23. Wang L-H, Jacques, S.L. and Zheng L-Q, "MCML - Monte Carlo modeling of photon transport in multi-layered tissues," Compt. Meth. Prog. Biomed. 47, 131-146 (1995).
24. Farrell T. J., Wilson B. C., and Patterson M. S., "The use of a neural network to determine tissue optical properties from spatially resolved diffuse reflectance measurements," Phys. Med. Biol. 37, 2281 (1992).
25. van de Hulst H. C., *Multiple Light Scattering*, Vols. I and II, (Academic, New York, 1980).
26. Graff R., Aarnoudse J. G., de MulHenk F. F. M., and Jentink W., "Similarity relations for anisotropic scattering in absorbing media," Opt. Eng. 32, 244-252 (1993).
27. Dam J. S., Dalgaard T., Fabricius, P. E. and Andersson-Engels S., "Multiple polynomial regression method for determination of biomedical optical properties from integrating sphere measurements," Appl. Opt. 39, 1202-1209 (2000).
28. Cheong W. F. Prahl S. A., and Welch A. J., "A review of the optical properties of biological tissue," IEEE J. Quantum Electron. 26 2166-2185 (1990).
29. van Staveren H. J., Moes C. J. M., van Marle J., Prahl S. A., and van Gemert M. J. C., "Light scattering in Intralipid-10 % in the wavelength range of 400-1100 nm," Appl. Opt. 30, 4507-4514 (1991).
30. Flock S. T., Jacques S. L., Wilson B. C., Star W. M., and van Gemert M. J. C., "Optical properties of Intralipid: A phantom medium for light propagation studies," Lasers Surg. Med. 12, 510-519 (1992).
31. Matcher S. J., Cope M., and Delpy D. T., "Use of the water absorption spectrum to quantify tissue chromophore concentration changes in near-infrared spectroscopy," Phys. Med. Biol. 39, 177-196 (1994).
32. Mourant J. R., Bigio I. J., Jack D. A., Johnson T. M., and Miller H. D., "Measuring absorption coefficients in small volumes of highly scattering media: Source-detector separations for which path lenths do not depend on scattering properties," Appl. Opt. 36, 5655-5661 (1997).
33. Kumar G. and Schmitt J. M., "Optimal probe geometry for near-infrared spectroscopy of biological tissue," Appl. Opt. 36, 2286-2293 (1997).
34. Simpson C. R., Kohl M., Essenpreis M., and Cope M., "Near-infrared optical properties of ex vivo human skin and subcutaneous tissues measured using the Monte Carlo inversion technique," Phys. Med. Biol. 43, 2465-2478 (1998).
35. Bolin F. P., Preuss L. E., Taylor R. C., and Ference R. J., "Refractive index of some mammalian tissues," Appl. Opt. 28 2297-2303 (1989).

Paper IV

Quantifying the absorption and reduced scattering coefficients of tissue-like turbid media over a broad spectral range using non-contact Fourier-transform hyperspectral imaging.

Tuan H. Pham[1,2], Frederic Bevilacqua[2], Thorsten Spott[3], Jan S. Dam[1,4], Bruce J. Tromberg[2], and Stefan Andersson-Engels[1]

Absorption (μ_a) and reduced scattering (μ_s') spectra of turbid media were quantified using a non-contact imaging approach based on a Fourier transform interferometric imaging system (FTIIS). FTIIS was used to collect hyperspectral images of the steady-state diffuse reflectance from turbid media. Spatially-resolved reflectance data from Monte Carlo simulations were fit to the recorded hyperspectral images in order to quantify μ_a and μ_s' spectra in the region of 550-850 nm. A simple and effective calibration approach was introduced to account for the instrument response. Using reflectance data that were close to and far from the source (0.5-6.5 mm), μ_a and μ_s' of homogenous, semi-infinite turbid phantoms with optical property ranges comparable to tissues were determined with an accuracy of ±7% and ±3%, respectively. Prediction accuracy for μ_a and μ_s' degraded to ±12% and ±4%, respectively, when only reflectance data close to the source (0.5-2.5 mm) were used. Results indicate that reflectance data close to and far from the source are necessary to optimally quantify μ_a and μ_s'. The spectral properties of μ_a and μ_s' values were used to determine the concentrations of absorbers and scatterers, respectively. Absorber and scatterer concentrations of two-chromophore turbid media were determined with a percent accuracy of ±5% and ±3%, respectively.

1. Introduction

The absorption and reduced scattering parameters (μ_a and μ_s', respectively) of turbid media, such as tissue, can be used to characterize its composition and structure. For instance, μ_a and μ_s' of tissue can provide information on a variety of physiological processes. Wavelength-dependent absorption is used to quantify the concentration of biologically important chromophores, such as hemoglobin, myoglobin, water, fat, and near-infrared absorbing drugs[1-5]. Wavelength-dependent scattering properties offer insight into the composition, density, and organization of tissue structures, such as cells, sub-cellular organelles, and connective tissue/extracellular matrix[6-10]. Since changes in these components generally accompany pathologic transformations and physiologic processes, techniques for non-invasively quantifying μ_a and μ_s' *in vivo* have generated intense interest.

One approach for characterizing μ_a and μ_s' of turbid media is to use spatially-resolved, steady-state diffuse reflectance. Two strategies for spatially resolved reflectance measurements of turbid, semi-infinite media have been demonstrated: contact probe detection using fiber-optic arrays[11-15] and image reflectometry[16-19]. Systems based on contact probe detection often have the capacity to measure the reflectance for a continuous range of wavelengths but require that the detection fibers touch the tissue. Imaging reflectometry has the advantage that measurements can be performed remotely. Non-contact detection can be particularly useful in clinical settings where fiberoptic probes may contribute to a number of problems, including contaminating sterile fields, altering regional tissue perfusion (via probe-induced pressure) and increasing measurement uncertainty due to irreproducible fiber/tissue coupling.

When a light source is launched onto tissue, diffuse reflectance signals close to and far from the injection point do not have equal sensitivity to bulk media optical properties. The reflectance profile close to the source, i.e. approximately less than 1 transport length $l_{tr} = (\mu_a + \mu_s')^{-1}$, depends strongly on the phase function, anisotropy factor, scattering property[20,21], and source volumetric distribution; but exhibits weak dependence on absorption[15,21,22]. Far from the source (> 5 l_{tr}), diffuse reflectance profiles depend

---

[1] Department of Physics, Lund Institute of Technology, P.O. Box 118, SE-22100, Lund, Sweden

[2] Beckman Laser Institute and Medical Clinic,Laser Microbeam and Medical Program (LAMMP),1002 Health Sciences Road East, Irvine, Ca 92612

[3] Department of Physical Electronics, Norwegian University of Science and Technology (NTNU), N-7034 Trondheim, Norway

[4] Bang & Olufsen Medicom a/s, DK-7600, Struer, Denmark

significantly on absorption, but less so on the phase function and source volumetric distribution[22,23]. In addition, photons that are diffusely reflected close to the source mainly probe superficial regions of the medium, while photons reflected distal to the source have diffused into deeper regions[24,25]. Accordingly, parameters such as scattering and anisotropy of superficial regions may be optimally characterized using diffuse reflectance information close to the source. Diffuse reflectance profiles far from the source may be optimal for quantifying the absorption and scattering properties of deeper regions. Thus, source-detector separation, i.e. the distance between the source and the location of light re-emission, is an important parameter to consider in analyzing diffuse reflectance images[26].

Imaging reflectometry systems often have limited spectral range, typically consisting of only a few discrete wavelengths[16,17,27]. For many tissue applications, broad spectral dynamic range is desirable. This is due to the fact that detailed absorption and scattering spectra can be used to determine the physiologic and structural properties of tissues and are diagnostically valuable in characterizing pathology[28-30]. Calibration procedures are generally difficult and complex, since the instrument response depends not only on the spatial and wavelength performance of the CCD, but also on the point spread function of the imaging system. Consequently, techniques that extend the wavelength dynamic range and facilitate rapid, accurate calibration are of considerable interest for spectroscopy and imaging of turbid media.

In this study, we investigate the feasibility of using diffusely reflected hyperspectral images to quantify μ_a and μ_s' over a continuous and broad spectral range. A Fourier transform interferometric imaging system (FTIIS) is used to collect hyperspectral diffuse reflectance images from tissue-like phantoms containing Intralipid (a light scattering fat emulsion) and absorbing dyes. We fit Monte Carlo simulations to measured image data in order to characterize the wavelength-dependent optical properties of the phantoms. Wavelength-dependent μ_a, and μ_s' are used to quantify, respectively, dye and fat emulsion concentrations. Additionally, we examine how the range of source-detector separations used in the image analysis affects the determination of μ_a and μ_s'.

2. Material and Methods.

A. Fourier Transform Interferometric Imaging System (FTIIS):

Figure 1 schematically illustrates the main components of the hyperspectral imaging device. White light from a broadband halogen source is coupled onto a 0.16 NA, 200 μm diameter optical fiber. Light exiting the fiber is re-focused to form a 250-μm diameter point source that is launched onto tissue-like phantoms at an incidence angle of 25 degrees relative to the surface normal. At this angle, specularly reflected light is not collected by the imaging optics and the diffuse reflectance distribution is minimally affected[17]. Hyperspectral images are collected using a Fourier-transform interferometric imaging system (FTIIS), (SpectraCube® imaging system, Applied Spectral Imaging, Migdal HaEmek 10511, Isreal).

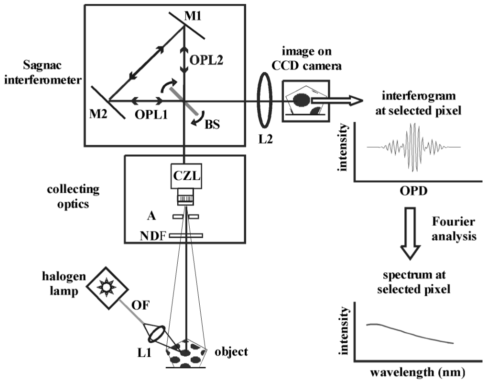

Figure 1. Experimental setup of the Fourier transform interferometric imaging system used to collect hyperspectral images of the diffuse reflectance from turbid media. The principle components of the system are the halogen white light source, collection optics, Sagnac interferometer, and a cooled 12-bit CCD camera (CCD). Interference patterns of the object are collected for a sequential series of optical path differences (OPD) by incrementally rotating the beamsplitter (BS). Interferogram is generated at each pixel, which corresponds to a particular region of the object. Inverse Fourier transform of the interferograms yields the hyperspectral images. Data acquisition and processing were performed using a PC. A full description of the setup is provided in the text. Abbreviations: optical fiber (OF), aperture (A), camera zoom lens (CZL), neutral density filter (NDF), lens to focus the white light source (L1), lens to image the recombined beams onto the CCD (L2), mirror (M), and optical pathlength (OPL).

FTIIS employs a cyclic (Sagnac) interferometer[31] to construct hyperspectral images. The principle components of FTIIS are the collection optics, a Sagnac interferometer, and a 12-bit CCD camera (Model TE-CCD-512-EFT/UV, Princeton Instruments, Inc., Trenton, NJ, USA). The collection optics consist of a commercial camera zoom lens (a 50-mm focal length, f1.2 to f16) and a neutral density filter (NDF). The achromatic zoom lens allows for adjustable image magnification and acceptance angle. NDFs were placed in front of the camera lens to prevent saturation of the CCD pixels that image the regions near the source, where the intensity is maximal.

Light entering the collection optics is split into two beams and directed along different optical paths (OPL1 and OPL2). The two beams are then recombined at the CCD. The optical path difference (OPD) between the beams, which is a function of the beamsplitter's angular position, generates interference patterns of the object on the CCD. To obtain hyperspectral images, interference patterns are collected for sequences of OPDs, generated by step-wise rotation of the beam splitter. In this manner an interferogram is constructed for each pixel in the image. Fourier analysis of the interferograms is used to produce wavelength spectra. The selected magnitude, range, and spacing of the OPDs determine spectral range and resolution. Images can occupy up to 512x512 pixels (for a given wavelength), and depending on the selected magnification, objects with sizes on the order of 1-50 mm can be imaged. In this study, we set the FTIIS parameters such that hyperspectral images for wavelengths ranging from 550-850 nm were generated. Twenty-four wavelengths were obtained with images unevenly spaced within the wavelength range. On average, the spacing was 8 nm for shorter wavelengths and 17 nm for longer wavelengths. Image size was 170 x 170 pixels, corresponding to a physical (object) dimension of 25 x 25 mm. At these settings, hyperspectal images were acquired in 40 seconds.

B. Phantoms:

Fifteen turbid phantoms with unique and randomly selected pairs of μ_a and μ_s' were made from absorbing dyes (Nigrosin and Janus Green B, Sigma, St. Louis, MO, USA) and fat emulsion scatterers (Intralipid 200 mg/ml (20%), Pharmacia & Upjohn Sverige AB, Stockholm, Sweden). The range of optical properties for the phantoms was comparable to tissues[32], i.e. μ_a and μ_s' values were $1\text{x}10^{-3}$ – 0.20 mm^{-1} and 0.30 – 2.50 mm^{-1}, respectively. For each phantom, known concentrations of aqueous dye solutions were prepared, followed by the addition of Intralipid scatterers. Conventional absorption spectrophotometry was performed on a small sample (2-ml) collected from the aqueous dye mixture, i.e. prior to adding scatterer, in order to independently measure μ_a. Expected phantom absorption values from 500 to 900 nm were calculated using these measured extinction coefficients. These calculated values were then used as "gold standards" in the evaluation of FTIIS accuracy.

Expected reduced scattering (μ_s') values were calculated according to van Staveren *et al.*[33], who used Mie theory to relate the scattering coefficient and anisotropy factor of Intralipid to the optical wavelength. According to that work, the scattering coefficient (μ_s) and the anisoptropy factor (*g*) of 10% Intralipid can be expressed as a function of the optical wavelength, λ:

$$\mu_s(\lambda) = 16\lambda^{-2.4} \tag{1}$$

$$g(\lambda) = 1.1 - 0.58\lambda \tag{2}$$

where λ is given in micrometers and μ_s in mm^{-1}. Values obtained from Eq. 1 and 2 were shown to have an accuracy of ±6%. The reduced scattering coefficient for 10% Intralipid was calculated from μ_s and *g* using the similarity relation, $\mu_s' = \mu_s(1-g)$, which is satisfied when the source-detector separation, ρ, is greater than approximately one transport length[34]. μ_s' for Intralipid can be expressed as $\mu_s' = \sigma C_{\%}$, where $\sigma = \mu_s(1-g)/10$ and $C_{\%}$ is the Intralipid concentration in percent volume. This relationship has been shown to be valid when Intralipid concentration is less than 10% by volume[33]. Optical property values obtained from fits of the hyperspectral data were compared to expected coefficients in order to determine the percent accuracy and spectral fidelity of quantifying μ_a and μ_s'.

C. Monte Carlo simulations:

Monte Carlo simulations were performed to generate a database of diffuse reflectance from a finite-diameter (250-µm) source in homogenous, semi-infinite media. We elected to use Monte Carlo simulation instead of the diffusion approximation, because the numerical approach readily accounts for the effects of boundary, source distribution, and media geometry on the diffuse reflectance. In addition, reflectance data from Monte Carlo simulations are more accurate for highly absorbing media as well as for positions close to the source. The Henyey-Greenstein phase function was used in the simulations, since various investigators have used this to successfully model the scattering phase function of fat emulsions. The range of optical properties used to generate the database encompassed values typically found in tissues: μ_a and μ_s' were $1x10^{-3} – 0.30$ mm^{-1} and 0.30-2.50 mm^{-1}, respectively, with μ_a equally spaced by $1x10^{-2}$ mm^{-1} and μ_s' by 0.20 mm^{-1}. The refractive index was set to that of water. Because of cylindrical symmetry, Monte Carlo data for diffuse reflectance and other parameters were organized using cylindrical coordinates. For example, diffuse reflectance data were arranged in concentric rings surrounding the source. The radial bin thickness of the concentric rings was 50 μm. The number of photons was empirically set at $N = (\mu_a / \mu_s')^{'' \,\urcorner} x10'$ so that the noise characteristics of data simulated using different optical properties would be comparable[17]. Simulated data were normalized to ring area in order to account for differences in ring size. The diffuse reflectance was recorded as a function of the radial distance from the source and stored as photon probability per unit area.

An interpolation procedure was used to obtain simulated reflectance data for optical properties that were not the same as the simulated values, e.g. for values lying in between the simulated μ_a, μ_s' pairs. In particular, we used a three-dimensional spline function[35,36] to model the Monte Carlo reflectance database as a function of μ_a, μ_s', and ρ. The spline function was then used to interpolate radially resolved reflectance data for arbitrary μ_a and μ_s' values within the simulated range.

D. Data fitting:

Monte Carlo simulations were fit to the hyperspectral images to determine μ_a and μ_s' values in the visible and near-infrared regions. Prior to data fitting, a calibration procedure was performed in order to account for the instrument response (IR) of the imaging system, i.e. instrument factors such as the point spread function, spectral sensitivity of the CCD, and uniformity of the CCD response. The calibration procedure consisted of three main steps. First, we collected an image of a marked ruler and counted the number of pixels corresponding to a unit length on the ruler. The ratio of length to pixel count is the factor that relates the pixel count to the physical size of the object. Second, hyperspectral images of the diffuse reflectance were acquired from a reference phantom, which was constructed from Intralipid and dyes, in order to determine the IRs at the measured wavelengths. Calibration images were obtained using experimental settings, such as numerical aperture (NA) and magnification factor, that were identical to those used to construct hyperspectral images of the test samples. Third, the IR of the system was calculated using the calibration images and the known optical properties of the reference phantom. For this purpose, the calibration image at each wavelength was Fourier transformed into the spatial frequency domain (SFD). Likewise, the Monte Carlo simulated image (MCSI) corresponding to the reference phantom optical properties was transformed into the SFD. The overall instrument response of FTIIS at each wavelength was calculated from the spatial transforms of the calibration and MCSI via the relation:

$$\Im(IR) = \Im(I) / \Im(MCSI), \tag{3}$$

where $\Im$(I), $\Im$(MCSI), and $\Im$(IR) are the spatial Fourier transforms of the calibration image, the Monte Carlo simulated image, and instrument response, respectively.

To perform data fitting, the MCSI corresponding to a particular set of optical properties was effectively convolved with the instrument response at the evaluated wavelength, i.e. MCSI⊗IR where the symbol "⊗" denotes a convolution. However, the convolution was performed indirectly in the spatial frequency domain. MCSI was first transformed into the spatial-frequency domain, $\Im$(MCSI). The spatial-frequency transform of MCSI was multiplied by $\Im$(IR) to account for the instrument response. The product, $\Im$(MCSI)$\Im$(IR), was inversely Fourier transformed into the spatial domain to yield MCSI⊗IR. The sample image at each wavelength and MCSI⊗IR were binned radially. That is, the images were divided into concentric rings, and pixel values in each ring were summed and normalized to the pixel count of the ring. Radial binning of data conferred two advantages: 1) pixel values from different quadrants were averaged and thus noise was reduced, and 2) computational demand of fitting was reduced since fitting was performed on data of one dimension instead of two. A simplex minimization algorithm (Nelder-Meads) was used to perform least-squares fitting of the radially binned MCSI⊗IR to the corresponding binned sample image. Fit of the hyperspectral data was performed independently on one image at a time and proceeded sequentially until all images of the spectrum were fit. Different initial guess values of the fit parameters (μ_a and μ_s') were used to avoid local minima, and the fit parameters were selected from the trial with the lowest least-squares residuals.

In order to examine how the range of source-detector separations affects the accuracy of quantifying μ_a and μ_s', we fit MCSI to sample data for various ranges of ρ. Three ranges of ρ were examined: 1) distances covering the full-range (0.5-6.5 mm), 2) distances close to the source (0.5-2.5 mm), and 3) distances far from the source (4-6.5 mm).

E. Concentrations:

The μ_a spectra obtained from the fit were used to determine the dye concentrations. μ_a values are related to the dye concentrations as expressed by the matrix,

$$\begin{bmatrix} \mu_a^{\lambda 1} \\ \mu_a^{\lambda 2} \\ \cdot \\ \cdot \\ \mu_a^{\lambda n} \end{bmatrix} = \begin{bmatrix} \varepsilon_{d1}^{\lambda 1} & \varepsilon_{d2}^{\lambda 1} & \cdot & \cdot & \varepsilon_{dm}^{\lambda 1} \\ \varepsilon_{d1}^{\lambda 2} & \cdot & & & \cdot \\ \cdot & \cdot & & & \cdot \\ \cdot & \cdot & & & \\ \varepsilon_{d1}^{\lambda n} & \varepsilon_{d2}^{\lambda n} & \cdot & & \varepsilon_{dm}^{\lambda n} \end{bmatrix} \begin{bmatrix} C_{d1} \\ C_{d2} \\ \cdot \\ \cdot \\ C_{dm} \end{bmatrix}, \qquad (4)$$

where ε is the extinction coefficient (ml/mg mm^{-1}) of the dye, *di*, at wavelength λi, and C is the dye concentration (mg/ml). In this study, the concentration vector consisted of two elements, since only two dyes were used to make the phantoms. Extinction coefficients of Nigrosin and Janus Green over the wavelength range were determined from absorption spectrophotometer measurements. A least-squares solution of Eq. 4 was determined for the concentration vector, with the constraint that the concentration values be positive[37]. Within a certain range, the macroscopic μ_s' is proportional to the scatterer concentration and can be expressed in matrix form similar to Eq. 4. The fit-derived μ_s' spectra were then used to determine percent Intralipid in a manner analogous to the dye concentration calculation.

All programs were written in the Matlab® environment, except for the Monte Carlo algorithm, which was written in C, compiled and linked to, and made executable within the Matlab® environment.

3. Results

The hyperspectral images of 15 tissue-like phantoms were examined to select an outer distance to be used in the fit. An outer distance of 6.5 mm was selected to guarantee that the image intensities used in data fitting were higher than the CCD dark noise, and the signal-to-noise ratio was on average greater than 2 at the outer distances (~6.5 mm). Because of the broad range of spectral data collected from the phantoms, it is not practical to show the full-range of data for all the phantoms. Accordingly, the data from the figures are selected from different phantoms at various wavelengths in order to highlight examples that are representative of the complete data set. Panel (a) of figure 2 schematically presents the organization of the hyperspectral image data. In panel (b), the image intensity is plotted as a function of spatial coordinates (x, y) for a representative diffuse reflectance image. The image was collected from a medium with μ_a = 0.028 mm^{-1} and μ_s' = 1.16 mm^{-1} at 630 nm. The uncalibrated image contained contributions from both the diffuse reflectance as well as the instrument response. An example of the instrument response obtained from calibration measurement is shown in panel (a) of Figure 3 for 630 nm, labeled as *IR*. Figure 3 depicts the procedure for fitting MCSI to the sample image. MCSI for a set of μ_a and μ_s' values were interpolated from the Monte Carlo data base. MCSI were convolved with the instrument response (IR) to form MCSI⊗IR.

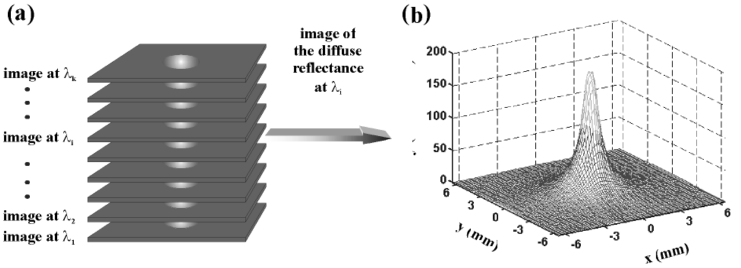

Figure 2. (a) A schematic showing the data organization of hyperspectral images obtained from FTIIS measurements. Image at each wavelength may contain up to 512x512 pixels at 12-bit dynamic range. Panel **(b)** show a typical image of the diffuse reflectance collected on a phantom with μ_a = 0.0281 mm^{-1} and μ_s' = 1.163 mm^{-1} at 630 nm. Neutral density filters were placed in front of the imaging optics to prevent CCD saturation near the source.

Figure 3(a) shows an example of the Monte Carlo simulated image and MCSI⊗IR for μ_a and μ_s' values of 0.028 mm^{-1} and 1.16 mm^{-1}, respectively. As shown in panel (b), the sample images and MCSI⊗IR were radially binned, and the binned data were then fit for the specified distances from the source. Figure 4 shows typical fit results for intensity vs. ρ using three ranges of ρ (a) 0.5 to 6.5 mm, (b) 0.5 to 2.5 mm, and (c) 4.0 to 6.5 mm. In the interest of showing representative data at various wavelengths and optical property values, the data for figure 4 are selected from a sample with μ_a = 0.0708 mm^{-1} and μ_s' = 0.316 mm^{-1} at 745 nm.

Representative μ_a and μ_s' results derived from fitting reflectance data over the full range of ρ are shown in figure 5. Data are acquired from two different phantoms with μ_a values that span from low to high absorption. Results from the phantom with low μ_a values are shown in panels (a) and (b). Specifically, panel (a) plots the fit vs. expected μ_a values from 550 to 850 nm, while panel (b) plots the fit vs. expected values for μ_s'. Similarly, fit vs. expected μ_a values for the highly absorbing phantom are plotted in panel (c), and fit vs. expected μ_s' values are plotted in panel (d). Filled diamonds are fit values, dashed curves are expected values, and solid curves are the constrained least-squares solution of Eq.4 to the fit-derived data in order to yield concentrations.

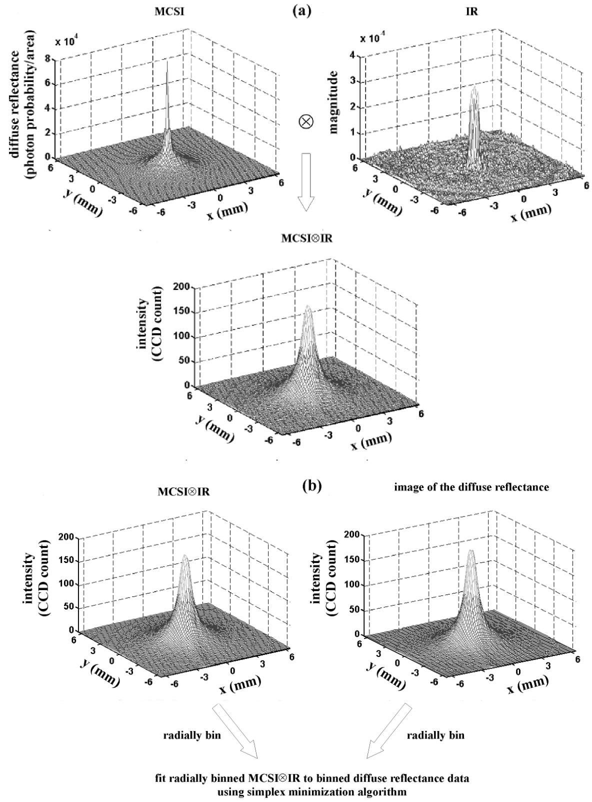

Figure 3. Panel (a) shows an example of the 1) Monte Carlo simulated image for μ_a and μ_s' values of 0.028 mm^{-1} and 1.16 mm^{-1}, respectively, and 2) FTIIS instrument responses (IR) at 630 nm. IRs were calculated from the hyperspectral images collected on a reference phantom and the corresponding MCSI generated from its optical properties. To fit Monte Carlo simulations to the image of the diffuse reflectance, MCSI was first convolved with IR at the appropriate wavelength to generate MCSI⊗IR. In panel (b), sample image of the diffuse reflectance and MCSI⊗IR are radially binned, thereby taking advantage of radial symmetry to reduce computational demands. Radially binned reflectance profiles were then fit using simplex minimization algorithm.

Fit μ_a and μ_s' values are in excellent agreement with expected values for wavelengths in the range of 550-850 nm. Percent error between the expected and fit optical property was calculated at each wavelength for all 15 samples. We pooled the percent error values from all samples and calculated the root mean square error, which we defined as the percent accuracy in quantifying μ_a and μ_s'. Table 1 summarizes the percent accuracy for quantifying μ_a and μ_s' using three sets of fitting distances, i.e. column 1 for ρ from 0.5 to 6.5 mm, column 2 for $0.5 < \rho < 2.5$ mm, and column 3 for $4.0 < \rho < 6.5$ mm.

Table 1. Percent accuracy of quantifying μ_a and μ_s' for different range of fitting distances

	distances close to and far from source $0.5 \text{ mm} < \rho < 6.5 \text{ mm}$ ($\sim 0.25\ l_{tr}$ to $\sim 16\ l_{tr}$)	only distances close to source $0.5 \text{ mm} < \rho < 2.5 \text{ mm}$ ($\sim 0.25\ l_{tr}$ to $\sim 5\ l_{tr}$)	only distances far from source $4.0 \text{ mm} < \rho < 6.5 \text{ mm}$ ($\sim 8\ l_{tr}$ to $\sim 16\ l_{tr}$)
$\pm\mu_a$ (%)	7	12	29
$\pm\mu_s'$ (%)	3	4	23

The optimal result was obtained using ρ from 0.5 to 6.5 mm, with the percent accuracy for μ_a and μ_s' of ±7% and ±3%, respectively. When reflectance data close to the source ($0.5 < \rho < 2.5$ mm) were fit, the percent accuracy for μ_a degraded to ±12% while μ_s' accuracy remained unchanged. The percent accuracies for μ_a and μ_s' are significantly worse when the fitting was performed only on the reflectance data distal to the source ($4.0 < \rho < 6.5$ mm).

To examine how sensitive prediction accuracy is to absorption (μ_a), results from the full-range fit were further divided. Specifically, μ_a and μ_s' data from all phantoms at all wavelenghts were pooled and grouped into four absorption ranges: 0-0.05 mm^{-1}, 0.05-0.10 mm^{-1}, 0.10-0.15 mm^{-1}, and 0.15-0.20 mm^{-1}. The percent accuracies for μ_a and μ_s' within each range were calculated and tabulated in Table 2. For the fixed range of distances used, the percent accuracies for media with low absorption were worse than the accuracy values for media with high absorption.

Table 2. Percent accuracy of quantifying μ_a and μ_s' for media with different range of absorption[a]

	μ_a range 0.001-0.05 (mm^{-1})	μ_a range 0.05-0.10 (mm^{-1})	μ_a range 0.10-0.15 (mm^{-1})	μ_a range 0.15-0.20 (mm^{-1})
$\pm\mu_a$ (%)	11	6	7	3
$\pm\mu_s'$ (%)	5	3	3	4

[a] Results are from the fit that used the full range of distances. The majority of the data is within the μ_a ranges of 0.05-0.10 mm^{-1} and 0.10-0.15 mm^{-1}.

Absorption, μ_a, and scattering, μ_s', values from the full-range fit were used to calculate, respectively, the phantom dye and Intralipid concentrations. Examples of the constrained least-squares solution to Eq. 4 are shown as solid curves in Figure 5. For the particular sample shown in panels (a) and (b), the constrained least-squares solution yielded Nigrosin, Janus Green, and Intralipid concentrations of 0.0014 mg/ml, 0.0324 mg/ml, and 1.01%, respectively. These values deviated from the expected concentrations by approximately 4% for Nigrosin, 6% for Janus Green, and 1% for Intralipid. Measured vs. expected concentrations for the 15 phantoms are plotted in figure 6: (a) Nigrosin, (b) Janus Green, and (c) Intralipid. The measured concentrations for Nigrosin and Janus Green agreed with the expected values to within ±5%, while the measured Intralipid concentrations agreed with the expected values to within ±3%

4. Discussion and Conclusion

Quantitative, hyperspectral imaging of diffuse reflectance from turbid media offers several key advantages over contact fiber probe strategies. First, the image contains a complete two-dimensional profile of diffuse reflectance over a continuous and adjustable range of distances from the source. This feature may be important in the spectroscopy of biological tissues, because the full image offers the possibility of identifying inhomogeneous regions. Second, image detection can be performed in non-contact or remote mode, an important feature well suited for certain clinical measurements. Third, conventional bright field images of the medium can be collected in conjunction with diffuse reflectance, making it possible to simultaneously visualize superficial structure and underlying composition. Finally, FTIIS has an intrinsically broad spectral dynamic range (visible to near-infrared), overcoming limitations of single or multi-source imaging devices. Consequently, FTIIS is effective for both imaging and spectroscopy of turbid media, such as tissues.

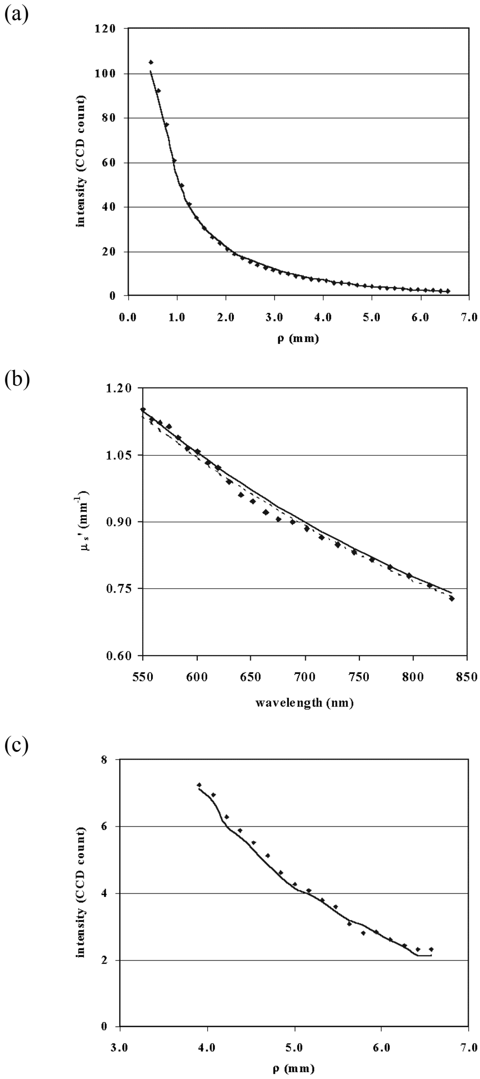

Figure 4. Examples showing typical results from fitting radially binned MCSI⊗IR to radially binned diffuse reflectance data at 745 nm: (a) ρ from 0.5 to 6.5 mm, (b) ρ from 0.5 to 2.5 mm, and (c) ρ from 4.0 to 6.5 mm. Diffuse reflectance data are from a phantom with expected μ_a and μ_s' of 0.0708 mm^{-1} and 0.316 mm^{-1}, respectively, at 745 nm. Note that the binned reflectance and the Monte Carlo simulated data contain significantly more noise at large ρ as compare to the shorter distances.

In this study, we demonstrate that μ_a and μ_s' of homogenous turbid media can be accurately determined from FTIIS hyperspectral images of diffuse reflectance. In the process, we show that the calibration method used to account for the instrument response is both simple and effective. When Monte Carlo simulations are fit to hyperspectral images, μ_a and μ_s' in the visible and near-infrared can be determined with accuracies of ±7% and ±3 %, respectively. These values are applicable to homogenous, turbid media of semi-infinite geometry with optical properties in the specified range (μ_a and μ_s' = $1\text{x}10^{-3}$ – 0.30 mm^{-1} and 0.30-2.50 mm^{-1}, respectively). Moreover, for a fixed range of source-detector separation, μ_a accuracy degrades when the medium has low absorption. It remains to be determined whether these accuracies can be obtained for μ_a and μ_s' in the case of heterogenous tissues with more complex geometries. Similarly, accuracy values for fits that use small source-detector separations may change when other phase functions are assumed. However, since Monte Carlo solutions to the transport equation were used to model diffuse reflectance, we expect this technique can be easily extended to media with other geometries, optical property ranges, layered structures and phase functions.

An important goal of this work was to determine chromophore concentration(s) despite the confounding contribution of multiple light scatterering. μ_a and μ_s' spectra were used to quantify, respectively, the concentration of absorbers and scatterers in tissue phantoms. Dye concentrations were determined with an accuracy of ±5%, while the Intralipid percent volume was determined with an accuracy of ±3%.

We also examined the effect of source-detector separation on the accuracy of quantifying μ_a and μ_s'. Our results suggest that μ_a and μ_s' accuracies are optimal when the distances used in the fit encompass spatial regions close to (≤ 0.5 l_{tr}) and far (≥ 5 l_{tr}) from the source, provided of course, that the reflectance signals remain larger than the noise. This result is consistent with a number of previously-reported observations[15,22,23,26,38,39]. The accuracy of determining μ_a degraded slightly (±12%) when we fit only the diffuse reflectance data close to the source, while μ_s' accuracy was minimally affected (±4%). Interestingly, results from reflectance data close to the source support a previous finding that small source-detector separations can yield accurate optical properties[14].

However, careful consideration of the phase function is essential when using small source-detector separations (≈ 1 l_{tr}). Indeed, in such a case, the diffuse reflectance is sensitive to the shape of the scattering phase function[20,22,40]. As shown by Bevilacqua *et al.*[20] for source-detector separations around one transport mean-free-path, the important parameter of the phase function to be considered is the ratio $(1-g)/(1-g_2)$ where g_2 is the second moment of the phase function (the anisotropy factor, g, is the first moment of the phase function). The scattering phase function of Intralipid has been successfully modeled by various phase functions matching the first and second moment of the Henyey-Greenstein phase function[41]. Moreover, the excellent accuracies obtained in this study support the validity of the Henyey-Greenstein phase function for such fat emulsions. Accuracy values for determining μ_a and μ_s' quoted in this study may worsen if an inaccurate phase function is used[14,20], particularly for fits that use only the short source-detector separations. Nevertheless, it must be noted that using the same type of media for the calibration and measurements may also significantly reduce errors since, under these conditions, phase function differences should not exist.

Far from the source, the effects of noise play a critical role in the accurate quantification of μ_a and μ_s' for several reasons. First, the decay of the reflectance profile is approximately given by $\exp(-\rho/l_{tr})$, making it difficult to separate μ_a from μ_s' because of the single decay constant. Second, the signal-to-noise ratio decreases dramatically with ρ because the diffuse reflectance intensity decays but the CCD noise remains relatively constant.

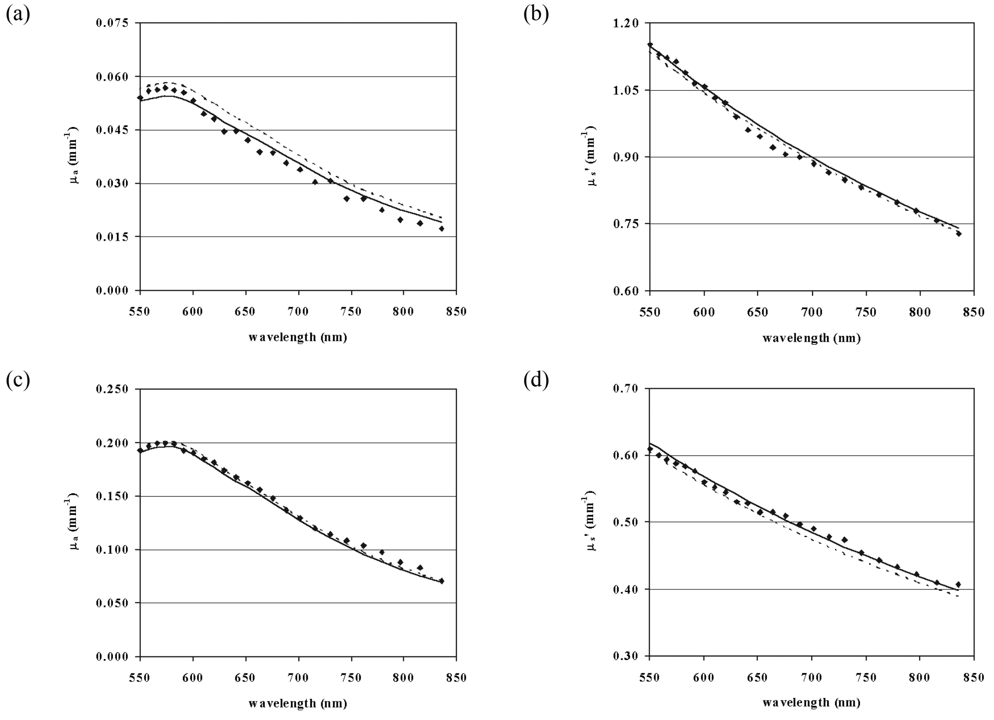

Figure 5. Fit-derived (♦) and expected (dashed curves) μ_a and μ_s' values from one of the phantom are plotted as a function of wavelengths. Solid curves represent constrained least-square solution to Eq. 4 that was used to determine the concentrations from the spectra of fit values. Data for panel (**a**) and (**b**) are from a representative phantom with low absorption values, while data for panel (**c**) and (**d**) are from a phantom with high absorption values. Expected μ_a values were determined from the chromophore concentrations and independently verified with absorption spectrophotometer. Expected μ_s' values were determined from the phantom's Intralipid percent volume. Fit μ_a and μ_s' values for the measured wavelengths agree well with expected values. Based on the results from 15 phantoms, the constrained least-squares solution to the fit μ_a and μ_s' data yielded concentration values for the dyes and Intralipid that were, respectively, within 5% and 3% of the true concentrations.

Finally, the signal-to-noise in the Monte Carlo simulation decreases for larger distances, since fewer photons are collected at distances far from the source. Note that the latter two reasons are practical and not fundamental limitations. The signal-to-noise ratio of the diffuse reflectance data and the Monte Carlo simulations can be improved, respectively, by using a low noise, high dynamic range CCD and launching more photons during the simulation step. In practical terms, however, these factors contribute to poor accuracy only when fits are performed on reflectance data far from the source. Consequently, optimal fit results are obtained when using reflectance data that are close to as well as far from the source. This conclusion is reasonable when we take into consideration the instrumental limitations as well as complications that arise from an incomplete knowledge of the phase function for a particular medium.

To reliably record data from distances close to and far from the source, a high dynamic range CCD is required. Since these systems are quite expensive, an alternative approach could involve using a specially designed neutral density filter (NDF) that has variable attenuation along the radial direction, i.e. the optical density is high near the center and decreases radially away from the center. This would compensate for the rapid attenuation of the diffuse reflectance away from the source, create a flatter image intensity decay profile, and reduce the need for using a high dynamic range CCD.

Presently, direct least-squares fitting of the Monte Carlo simulations to the data is too computationally intensive for rapid analysis of the hyperspectral images. Data fitting of the hyperspectral images using a simplex algorithm requires as much as half an hour on a 400-MHz Pentium II PC. Note that the computational demands are primarily due to the least-squares fits, not the Monte Carlo simulations. In fact, the interpolation algorithm used to generate the simulated data from the Monte Carlo database is computationally efficient and rapid. Alternative approaches to direct fitting may significantly decrease computational demands. One such empirical approach could involve analyzing hyperspectral reflectance images using chemometrics e.g. partial least squares (PLS). In the future, we plan to examine the feasibility of this strategy for directly calculating optical properties and chromophore concentrations. With continued improvements in modulating CCD dynamic range requirements and enhanced data analysis, we expect FTIIS will find important applications in non-contact tissue spectroscopy.

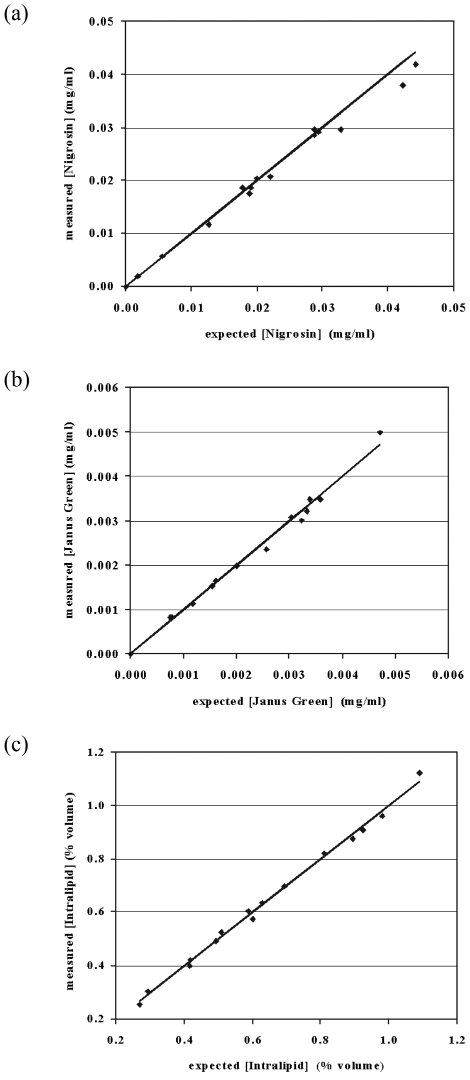

Figure 6. The least-squares method was used to fit the absorption values in the range of 550-850 nm in order to determine the chromophore concentrations of the phantoms. Similarly, Intralipid percent volume was determined from wavelength-dependent fit μ_s' values. Measured (♦) and expected (solid curves) values for (a) Nigrosin concentration, (b) Janus Green concentration, and (c) Intralipid percent volume are plotted for the 15 phantoms. Measured concentrations agree well with expected values. Differences between measured and expected concentrations yield the percent accuracy values of ±5%, ±5%, and ±3% for Nigrosin, Janus Green, and Intralipid, respectively.

The authors gratefully thank Jan Åke Jönsson for providing access to the spectrophotometer, and Philippe Thueler for the insightful discussions on data fitting. This work was supported by the Swedish Research Council for Engineering Sciences, the Knut and Alice Wallenberg Foundation, and the National Institutes of Health Laser Microbeam and Medical Program (NIH RR01192). T.H.P. gratefully acknowledges support provided by the Fulbright Fellowship and the Whitaker Foundation Graduate Fellowship. F.B. gratefully acknowledges support from the Swiss National Science Foundation.

References.

1. B.J. Tromberg, R.C. Haskell, S.J. Madsen and L.O. Svaasand, "Characterization of Tissue Optical Properties Using Photon Density Waves," Comments Mol. Cell. Biophys. **8**, 359-386 (1995).

2. C.E. Elwell, M. Cope, A.D. Edwards, J.S. Wyatt, D.T. Delpy and E.O.R. Reynolds, "Quantification of adult cerebral hemodynamics by near-infrared spectroscopy," J. Appl. Physiol. **77**, 2753-2760 (1994).

3. B. Chance, "Near-infrared images using continuous, phase-modulated, and pulsed light with quantitation of blood and blood oxygenation," Ann. N. Y. Acad. Sci. **838**, 29-45 (1998).

4. J. Fishkin, A. Cerussi, P.T.C. So, S. Fantini and M.A. Franceschini-Fantini, "Frequency-domain method for measuring spectral properties in multiple-scattering media: methemoglobin absorption spectrum in a tissue-like phantom," Appl. Opt. **34**, 1143-1155 (1995).

5. R.A. Weersink, J.E. Hayward, K.R. Diamond and M.S. Patterson, "Accuracy of noninvasive *in vivo* measurements of photosensitizer uptake based on a diffusion model of reflectance spectroscopy," Photochem. Photobiol. **66**, 326-335 (1997).

6. N. Mohandas, Y.R. Kim, D.H. Tycko, J. Orlik, J. Wyatt and W. Groner, "Accurate and independent measurement of volume and hemoglobin concentration of individual red cells by laser light scattering," Blood **68**, 506-513 (1986).

7. J.R. Mourant, J.P. Freyer, A.H. Hielscher, A.A. Eick, D. Shen and T.M. Johnson, "Mechanisms of light scattering from biological cells relevant to noninvasive optical-tissue diagnostics," Appl. Opt. **37**, 3586-3593 (1998).

8. A.H. Hielscher, J.R. Mourant and I.J. Bigio, "Influence of particle size and concentration on the diffuse backscattering of polarized light from tissue phantoms and biological cell suspensions," Appl. Opt. **36**, 125-135 (1997).

9. F. Bevilacqua, P. Marquet, O. Coquoz and C. Depeursinge, "Role of tissue structure in photon migration through breast tissues," Appl. Opt. **36**, 44-51 (1997).

10. I.S. Saidi, S.L. Jacques and F.K. Tittel, "Mie and Rayleigh modeling of visible-light scattering in neonatal skin," Appl. Opt. **34**, 7410-7418 (1995).

11. T.J. Farrell, M.S. Patterson and B. Wilson, "A diffusion theory model of spatially resolved, steady-state diffuse reflectance for noninvasive determination of tissue optical properties *in vivo*," Med. Phys. **19**, 879-888 (1992).

12. R. Doornbos, R. Lang, M. Aalders, F. Cross and H.J.C.M. Sterenborg, "The determination of in vivo human tissue optical properties and absolute chromophore concentrations using spatially-resolved steady-state diffuse reflectance spectroscopy," Phys. Med. Biol. **44**, 967-981 (1999).

13. E.L. Hull, M.G. Nichols and T.H. Foster, "Quantitative broadband near-infrared spectroscopy of tissue-simulating phantoms containing erythrocytes," Phys. Med. Biol. **43**, 3381-3404 (1998).

14. F. Bevilacqua, D. Piguet, P. Marquet, J.D. Gross, B.J. Tromberg and C. Depeursinge, "In vivo local determination of tissue optical properties: applications to human brain," Appl. Opt. **38**, 4939-4950 (1999).

15. R. Bays, G. Wagnières, D. Robert, D. Braichotte, J.F. Savary, P. Monnier and H. van den Bergh, "Clinical determination of tissue optical properties by endoscopic spatially resolved reflectometry," Appl. Opt. **35**, 1756-1766 (1996).

16. S.L. Jacques, A. Gutsche, J. Schwartz, L. Wang and F. Tittel, "Video reflectometry to specify optical properties of tissue *in vivo*," in *Medical Optical Tomography: Functional Imaging and Monitoring,* G.J. Müller, B. Chance, R.R. Alfano, S.R. Arridge, J. Beuthan, E. Gratton, M. Kaschke, B.R. Masters, S. Svanberg and P. van der Zee, eds., SPIE Institute Series vol. **ISII**, 211-226 (1993).

17. A. Kienle, L. Lilge, M.S. Patterson, R. Hibst, R. Steiner and B.C. Wilson, "Spatially resolved absolute diffuse reflectance measurements for noninvasive determination of the optical scattering and absorption coefficients of biological tissue," Appl. Opt. **35**, 2304-2314 (1996).

18. L. Wang and S.L. Jacques, "Use of a laser beam with an oblique angle of incidence to measure the reduced scattering coefficient of a turbid medium," Appl. Opt. **34**, 2362-2366 (1995).

19. R. Splinter, G.A. Nanney, L. Littman, C.H. Chuang, R.H. Svenson, J.R. Tuntelder and G.P. Tatsis, "Monitoring tissue optical characteristics in situ using a CCD camera," Laser Life Sci. **6**, 15-25 (1994).

20. F. Bevilacqua and C. Depeursinge, "Monte Carlo study of diffuse reflectance at source-detector separations close to one transport mean free path," J. Opt. Soc. Am. A **16**, 2935-2945 (1999).

21. F. Bevilacqua, "Local Optical Characterization of Biological Tissues In Vitro and In Vivo," Ph.D. Dissertation (Ecole Polytechnique Federale De Lausanne, Lausanne, Switzerland, 1998).

22. V. Venugopalan, J.S. You and B.J. Tromberg, "Radiative transport in the diffusion approximation: An extension for highly absorbing media and small source-detector separations," Phys. Rev. E **58**, 2395-2407 (1998).

23. A. Kienle and M.S. Patterson, "Determination of the optical properties of semi-infinite turbid media from frequency-domain reflectance close to the source," Phys. Med. Biol. **42**, 1801-1819 (1997).

24. L.O. Svaasand, B.J. Tromberg, P. Wyss, M.-T. Wyss-Desserich, Y. Tadir and M.W. Berns, "Light and drug distribution with topically administered photosensitizers," Lasers Med. Sci. **11**, 261-265 (1996).

25. L.O. Svaasand, L.T. Norvang, E.J. Fiskerstrand, E.K.S. Stopps, M.W. Berns and J.S. Nelson, "Tissue parameters determining the visual appearance of normal skin and port-wine stains," Lasers Med. Sci. **10**, 55-65 (1995).

26. M.G. Nichols, E.L. Hull and T.H. Foster, "Design and testing of a white-light, steady-state diffuse reflectance spectrometer for determination of optical properties of highly scattering systems," Appl. Opt. **36**, 93-104 (1997).

27. P. Marquet, F. Bevilacqua, C. Depeursinge and E.B. de Haller, "Determination of reduced scattering and absorption coefficients by a single charge-coupled-device array measurement, part I: comparison between experiments and simulations," Opt. Eng. **34**, 2055-2063 (1995).

28. D.M. Haaland, H.D.T. Jones and E.V. Thomas, "Multivariate classification of the infrared spectra of cell and tissue samples," Appl. Spectr. **51**, 340-345 (1997).

29. H. Key, R.E. Davies, P.C. Jackson and P.N. Wells, "Optical attenuation characteristics of breast tissues at visible and near-infrared wavelengths," Phys. Med. Biol. **36**, 579-590 (1991).

30. V.G. Peters, D.R. Wyman, M.S. Patterson and G.L. Frank, "Optical properties of normal and diseased human breast tissues in the visible and near infrared," Phys. Med. Biol. **35**, 1317-1334 (1990).

31. W.H. Steel, "*Interferometry*," (Cambridge University Press, Cambridge, 1983).

32. F.A. Duck, "*Physical Properties of Tissue*," (Academic Press Ltd., London, 1990).

33. H.J. van Staveren, C.J.M. Moes, J. van Marle, S.A. Prahl and M.J.C. van Gemert, "Light scattering in Intralipid-10 % in the wavelength range of 400-1100 nm," Appl. Opt. **30**, 4507-4514 (1991).

34. D.R. Wyman, M.S. Patterson and B.C. Wilson, "Similarity relations for anisotropic scattering in Monte Carlo simulations of deeply penetrating neutral particles.," J. Comput. Phys. **81**, 137-150 (2000).

35. C. de Boor, "*A Practical Guide to Splines*," (Springer-Verlag, New York, NY, 1978).

36. The MathWorks Inc., "*MATLAB Reference Guide*," (The MathWorks, Inc., Natick, MA, 1994).

37. C.L. Lawson and R.J. Hanson, "*Solving Least Squares Problems*," (Prentice-Hall, New York, NY, 1974).

38. J.S. Dam, P.E. Andersen, T. Dalgaard and P.E. Fabricius, "Determination of tissue optical properties from diffuse reflectance profiles by multivariate calibration," Appl. Opt. **37**, 772-778 (1998).

39. A. Kienle and M.S. Patterson, "Improved solutions of the steady-state and the time-resolved diffusion equations for reflectance from a semi-infinite turbid medium," J. Opt. Soc. Am. A-Optics Image Science and Vision **14**, 246-254 (1997).

40. J.R. Mourant, J. Boyer, A.H. Hielscher and I.J. Bigio, "Influence of scattering phase function on light transport measurements in turbid media performed with small source-detector separations," Opt. Lett. **21**, 546-548 (1996).

41. J.W. Pickering, S.A. Prahl, N. van Wieringen, J.F. Beek, H.J.C.M. Sterenborg and M.J.C. van Gemert, "Double-integrating-sphere system for measuring the optical properties of tissue," Appl. Opt. **32**, 399-410 (1993).

Paper V

Monte Carlo study on optical characterization of thin turbid samples using angular and spatially- resolved measurements.

Jan S. Dam[1,2], Carsten B. Pedersen[1], Torben Dalgaard[1], Paul Erik Fabricius[1],
and Stefan Andersson-Engels[2].

We present a novel and accurate method for real-time determination of the absorption coefficient, the scattering coefficient, and the anisotropy factor of thin turbid samples. The three optical properties are determined using multivariate calibration on Monte Carlo simulated recordings of the angularly resolved transmittance, the spatially resolved diffuse reflectance, and the spatially resolved diffuse transmittance. The applied calibration and prediction techniques are based on multiple polynomial regression in combination with a Newton-Raphson algorithm. Numerical test showed mean prediction errors of approximately 0.5 % for all three optical properties within ranges typical for biological media. Finally, we suggest a set-up for practical implementation of the presented method.

1. Introduction

The optical properties of a turbid medium[1], i.e. the absorption coefficient μ_a, the scattering coefficient μ_s, and the anisotropy factor g may provide important information on the composition and the dynamics of the medium. While μ_a provide information on various chromophores[2,3], μ_s and g may be used to characterize the form, size, and concentration of various scattering components in the medium[4,5]. Therefore, determination of the optical properties of turbid media is a useful and important in numerous fields of science, industry, health care, environmental technology, etc. Some examples are (a) tissue characterization in cancer diagnostics and therapy[6], (b) medical diagnostics using biological fluids[7], (c) process control in breweries and dairies[8], and (d) environmental monitoring. Still, most of the existing methods for optical analysis of turbid media are not able to extract μ_a, μ_s, and g simultaneously. Many methods focus on either the absorption- or the scattering properties; i.e. the scattering effects are treated as interference during absorption measurements or vice versa.

Other methods rely on removal of the scattering components prior to absorption measurements, e.g. some types of clinical blood analysis, where the blood cells are hemolysed, i.e. the cell walls are crushed, and subsequently removed from the sample either by means of sedimentation or centrifugation.

Integrating sphere (IS) measurements[9-11] are widely used as and reference method for determination μ_a, μ_s, and g. Here, the optical properties are extracted from measurements of the total diffuse reflectance R_{tot} and the total diffuse transmittance T_{tot} of either a thin turbid slab or a turbid solution in a thin cuvette. IS measurements may be carried out using a single- or a double sphere set-up. In the latter, R_{tot} and T_{tot} can be recorded simultaneously without moving the sample, but due to optical cross-talk between the two spheres, the accuracy is often decreased compared to a single-sphere setup. However, it is only possible to determine μ_a and the reduced scattering coefficient $\mu_s' = (1-g)\mu_s$ from pure R_{tot} and T_{tot} measurements. In order to separate μ_s' into μ_s and g it is necessary to perform additional measurements of the collimated transmittance T_c in a separate set-up, i.e. the sample has to be moved once again. Moreover, it is complicated to perform accurate T_c measurements in practice, thus IS based methods are applied for research purposes mainly.

In summary, the existing methods for determination of optical properties from thin turbid samples either imply (a) more or less accurate interference compensation techniques, (b) bulky equipment, (c) inconvenient sample handling, or (d) complicated measuring techniques. Hence, there is an obvious need

---

[1] Bang & Olufsen Medicom a/s, DK-7600, Struer, Denmark.

[2] Dept. of Physics, Lund Institute of Technology, P.O. Box 118, SE-22100, Lund, Sweden.

for more compact, handy, and accurate techniques for this type of measurements.

In the following of this paper we present a novel method for real-time simultaneous determination of μ_a, μ_s, and g from thin turbid samples using multivariate calibration. We first describe the geometrical configuration of the set-up and the principles of the applied calibration and prediction techniques, which are based on multiple polynomial regression (MPR)[11] in conjunction with a Newton-Raphson algorithm[12]. Then, we show, using Monte Carlo (MC) simulated data[13], how the optical properties may be determined from four (or less) recordings of a) the angularly resolved transmittance, b) the spatially resolved diffuse transmittance, and c) the spatially resolved diffuse reflectance of the sample. Finally, we suggest a set-up for practical implementation of the presented method.

2. Methods

As stated above, the purpose of the work described in this paper is to extract μ_a, μ_s, and g from MC simulated recordings of various combinations of angularly and spatially resolved reflected and transmitted intensities from a thin turbid sample using multivariate calibration. The basic geometrical configuration of the set-up we used for the simulations in our analyses is shown in Figure 1.

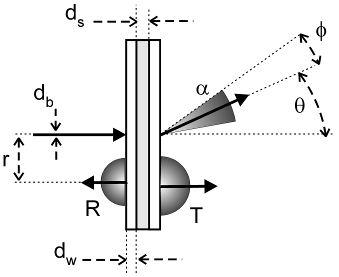

Figure 1. Geometric configuration of setup for measuring μ_a, μ_s, and g. Where, R and T is spatially resolved diffuse reflectance and transmittance, respectively with radial distance r. The angularly resolved transmittance is denoted α, where θ is the deflection angle and ϕ is the acceptance angle. Finally, d_s is the sample thickness, d_b is the diameter of the collimated source beam, and d_w is the thickness of the cuvette walls.

The set-up imitates a cuvette with sample thickness d_s = 1 mm, wall thickness d_w = 1 mm, and beam diameter d_b = 1 mm. The refractive indices of the sample n_s, the wall n_w, and the surrounding media n_m were 1.33, 1.49, and 1.00, respectively.

During each single MC simulation, we thus recorded: (a) the spatially resolved diffuse reflectance R as a function of the radial distance r_R, (b) the spatially resolved diffuse transmittance T as a function of the radial distance r_T, and (c) the angularly resolved total transmittance α as a function of the deflection angle θ and the acceptance angle ϕ.

As a first step to solve the inverse problem of extracting μ_a, μ_s, and g using multivariate calibration, we generated a database of MC simulations using the geometrical configuration in Figure 1 and a set of optical properties within typical biological ranges:

$$\begin{gathered} 0 < \mu_a < 2\,\mathrm{cm}^{-1} \\ 10 < \mu_s < 200\,\mathrm{cm}^{-1} \\ 0.85 < g < 0.99 \end{gathered} \tag{1}$$

The simulated reflectance and transmittance recordings were tabulated and stored in a 21x19x11 calibration matrix, i.e. a data base containing all combinations of 21 values of μ_a, 19 values of μ_s, and 11 values of g. The single simulations of the calibration model was generated using on $1 \cdot 10^6$ *photons*.

Next, we applied multiple polynomial regression (MPR) in conjunction with a Newton-Raphson (N-R) algorithm to calculate μ_a, μ_s, and g from R, T, and α recordings of MC simulated prediction data with random distributions of optical properties. Based on preliminary investigations, we chose to use third-order polynomials for our further analyses. Thus, the principle of the applied three-dimensional MPR/N-R method is as follows:

First, we select the relevant R, T, and/or α data from the simulated 21x19x11 calibration matrix and denote them $X_{1-3,cal}$. Then, we find triple-polynomial fits to $X_{1-3,cal}$:

$$\begin{aligned} &[X_{1,fit} \quad X_{2,fit} \quad X_{2,fit}] = [1 \quad \mu_a \quad \mu_a{}^2 \quad \mu_a{}^3] \\ &\times \mathbf{A} \cdot [1 \quad \mu_s \quad \mu_s{}^2 \quad \mu_s{}^3]\mathbf{B} \cdot [1 \quad g \quad g^2 \quad g^3]\mathbf{C} \end{aligned} \tag{2}$$

Where, $X_{1-3,fit}$ are functions of μ_a, μ_s, and g, and $\mathbf{A}$, $\mathbf{B}$ and $\mathbf{C}$ are 4x3 matrices of fitting coefficients determined by least-squares regression. Thus, $X_{1-3,fit}$ constitute the calibration model. The next step is to solve the inverse problem of determining μ_a and μ'_s from recordings of the simulated prediction data sets $X_{1-3,meas}$

$$\begin{aligned} F(\mu_a, \mu_s, g) &= X_{1,fit} - X_{1,meas} \\ G(\mu_a, \mu_s, g) &= X_{2,fit} - X_{2,meas} \\ H(\mu_a, \mu_s, g) &= X_{1,fit} - X_{1,meas} \end{aligned} \tag{3}$$

Then, we use the Newton-Raphson algorithm to perform converging iterative calculations of μ_a, μ_s, and g:

$$\left.\begin{array}{l} -\begin{bmatrix} \mathrm{F}(\mu_{\mathrm{a,k}},\mu_{s,k},g_k) \\ \mathrm{G}(\mu_{\mathrm{a,k}},\mu_{s,k},g_k) \\ \mathrm{H}(\mu_{\mathrm{a,k}},\mu_{s,k},g_k) \end{bmatrix} = \begin{bmatrix} \frac{\partial F}{\partial \mu_a} & \frac{\partial F}{\partial \mu_s} & \frac{\partial F}{\partial g} \\ \frac{\partial G}{\partial \mu_a} & \frac{\partial G}{\partial \mu'_s} & \frac{\partial G}{\partial g} \\ \frac{\partial H}{\partial \mu_a} & \frac{\partial H}{\partial \mu'_s} & \frac{\partial H}{\partial g} \end{bmatrix} \begin{pmatrix} h_{a,k} \\ h_{s,k} \\ h_{g,k} \end{pmatrix} \\ \begin{pmatrix} \mu_{a,k+1} \\ \mu'_{s,k+1} \\ g_{k+1} \end{pmatrix} = \begin{pmatrix} \mu_{a,k} \\ \mu_{s,k} \\ g_k \end{pmatrix} + \begin{pmatrix} h_{a,k} \\ h_{s,k} \\ h_{g,k} \end{pmatrix} \end{array}\right\} \quad (4)$$

$$k = 0,1,2,3,...,$$

Where, h_a, h_s, and h_g are correction terms of μ_a, μ_s, and g, respectively. The calculations continue until h_a, h_s, and h_g have dropped below predefined maximum values.

Figure 2 shows the schematics of the four different R, T, and α configurations we have analyzed in this paper. In configuration (a) we used the transmittance at three angles α_{1-3} to extract μ_a, μ_s, and g. In (b) we extracted μ_s and g from α_1 and α_2 only. Configuration (c) was used to extract μ_a and μ'_s from R and T. Finally, in configuration (d) we used a combination of configuration (b) and (c) to extract all three optical properties μ_a, μ_s, and g.

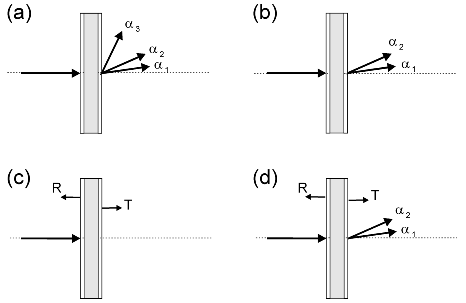

Figure 2. Four different set-ups for predicting optical properties using various combinations of spatially and/or angularly resolved data. Each single set-up may be used for determination of respectively (a): μ_a, μ_s, and g, (b): μ_s and g, (c): μ_a and μ'_s, and (d): μ_a, μ_s, and g. See Figure 1 for nomenclature.

In configuration (c) and (d) in Figure 2 we have to variables only, i.e. (α_1, α_2) or (R, T). In these two cases Eq.(2)-(4) are reduced to two dimensions during calibration and prediction, i.e. we use X_1 and X_2 only. In addition, μ_s are replaced by μ'_s during analysis on configuration (c). In configuration (d) we have four variables. Since the MPR/N-R method implies exactly three variables in order to predict μ_a, μ_s, and g, we have to apply some sort of dimension reduction. For this we use Principal Component Analysis (PCA), that is, we perform PCA on the 21x19x11 calibration matrix and then use the resulting three main principal components as input i.e. X_{1-3} to the calibration and prediction algorithms.

All the prediction errors we have reported in the following are mean errors relative to the total optical property ranges of the applied prediction test data.

3. Results

In order to test the prediction performances of the four configurations in Figure 2, we first generated a set of prediction data with 20 random combinations of optical properties within the ranges:

$$\begin{aligned} &0 < \mu_a < 2\,\mathrm{cm}^{-1} \\ &50 < \mu_s < 100\,\mathrm{cm}^{-1} \qquad (5) \\ &0.85 < g < 0.95 \end{aligned}$$

The prediction data were generated using $1 \cdot 10^7$ photons, and Table 1 shows the results from the prediction tests using these data in conjunction with the four configurations in Figure 2. In each case the prediction errors were minimized by finding the optimal combinations of angles α and distances r, using error plots similar to Figure 3.

Table 1 Mean prediction errors from the analyses on the four set-ups in Figure 2.

	Mean Prediction Errors (%)			
	μ_a	μ_s	g	μ'_s
(a)	0.83	0.47	0.68	-
(b)	-	0.95	3.9	-
(c)	0.84	-	-	0.23
(d)	0.17	0.45	0.43	-

Table 2 shows the optimal angles and the distances corresponding to errors listed in **Table 1**.

Table 2 Optimum angles and distances of the four set-ups in Figure 2.

	Angles θ (°)			Distances r (mm)	
	α_1	α_2	α_3	T	R
(a)	0	3	60	-	-
(b)	0	3	-	-	-
(c)	-	-	-	0.7	2.0
(d)	0	5	-	2.0	2.5

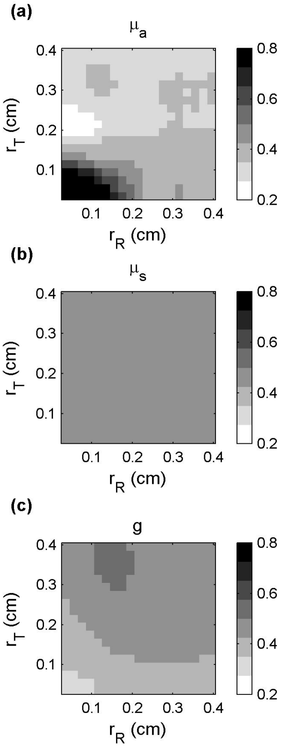

Figure 3 Prediction errors of (a) μ_a, (b) μ_s, and (c) g as a function of r_T and r_R using set-up (d) in Figure 2 in conjunction with a prediction data set defined by Eq. (5). The angles α_1 and α_2 were 0° and 5°, respectively.

The μ_s range of the above prediction data only covers a part of the range spanned by the calibration model (see Eq. (1)). In order to test the performance of the prediction algorithms on a wider range of the calibration model, we therefore generated two additional test sets with μ_a and g ranges similar to Eq. (5), but with the following μ_s ranges: ($10<\mu_s<50\text{cm}^{-1}$) and ($100<\mu_s<150\text{cm}^{-1}$), respectively. The prediction errors for all three μ_s ranges are given in Table 3.

Table 3 Prediction errors for various μ_s-ranges using set-up (d) in Figure 2.

	Mean Prediction Errors (%)		
	μ_a	μ_s	g
$10 < \mu_s < 50\ \text{cm}^{-1}$	1.7	0.10	0.28
$50 < \mu_s < 100\ \text{cm}^{-1}$	0.17	0.45	0.43
$100 < \mu_s < 150\ \text{cm}^{-1}$	8.6	36	14

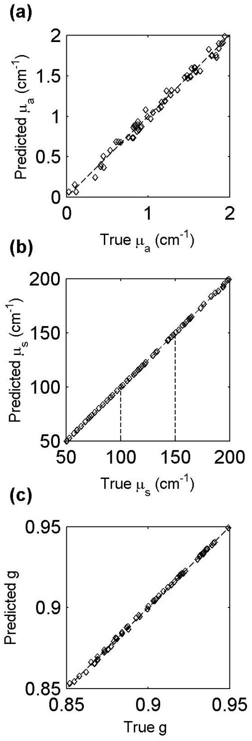

Figure 4. Predicted values of (a): μ_a, (b): μ_s, and (c): g as a function of the true values, using set-up (d) in Figure 1 (d_s = 1.0 mm) in conjunction with downscaled prediction data (d_s = 0.5 mm). The corresponding prediction errors of μ_a, μ_s, and g are 2.2, 0.40, and 0.59 %, respectively. The dashed lines in (b) indicates the μ_s ranges of three sub-sets of calibration and prediction data. The resulting μ_a, μ_s, and g prediction errors using these sub-ranges are 0.59, 0.58, and 0.26, respectively.

In some cases, the sample thickness d_s = 1mm of the applied calibration model may be too large for proper prediction of large μ_a and μ_s values. Applying a calibration model with a smaller d_s may of course solve this problem. Another solution is to feed downscaled prediction data[14] to the original calibration model and then subsequently multiply the predicted μ_a and μ_s values by the scaling factor. Figure 4 shows the resulting correlation plots of true and corrected predicted values of μ_a, μ_s, and g, when using prediction data with d_s = 0.5mm as input to the original calibration model with d_s = 1mm.

By splitting the prediction data in Figure 4 into three μ_s sub-ranges (indicated by the dashed lines in panel (b)) and apply three corresponding calibration sub-models as well, the mean of the μ_a and g prediction errors dropped from 2.2 to 0.59% and from 0.59 to 0.26%, respectively. While, the μ_s prediction error showed a slight increase, rising from 0.40 to 0.58%.

During the analysis of the data in Table 1 the acceptance angles ϕ_{α_2}, ϕ_{α_3} = 1°, while ϕ_{α_1} = 0.25°. Such a relatively small angle may be difficult to realize in practice, thus Figure 5(a) shows the prediction errors of μ_a, μ_s, and g as a function of ϕ_{α_1}. Noise is another problem encountered during real measurements. To illustrate the effect of random noise in the prediction data set, Figure 5(b) shows the prediction errors of μ_a, μ_s, and g as a function of the applied number of photons m for five, otherwise similar prediction sets. The optical property ranges for the prediction data in both Figure 5(a) and (b) are given by Eq. (5).

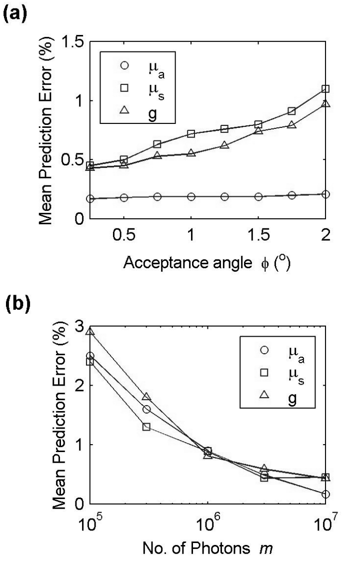

Figure 5. Prediction errors of μ_a, μ_s, and g as a function of (a) the acceptance angle θ_a of α_1, and (b) number of photons used to generate the prediction data. The optical property ranges of the prediction data are in both cases defined by Eq. (5), and d_s = 1 mm.

4. Discussion

A. Optimum Set-up

The results in Table 1 show that it is possible to predict μ_a, μ_s, and g with errors less than 1% using the purely angularly resolved configuration (a) in Figure 2. However, the relatively large optimum angle of α_3 (θ_{α_3} = 60 °) in this configuration, may be inconvenient to implement in real applications. Thus, in search of a more feasible geometrical configuration, we tested configuration (b) and (c) in Figure 2 as well. Configuration (b) was chosen due to its similarity to integrating sphere measurements, hence we chose to perform prediction tests on μ_a in combination with μ'_s instead of μ_s. The results in Table 1 show that both optical properties may be predicted with good accuracies using this setup. Now, that we were able to perform accurate determination of μ_a and μ'_s, the next step was to find a feasible geometrical configuration for accurate determination of either μ_s or g. In principle, it would then be possible to determine all three optical properties by combining the two configurations. Based on our experience with configuration (a), we chose to apply configuration (c) for the μ_s and g prediction tests. From Table 1 it appears that at least μ_s may be predicted well using this configuration, while the prediction accuracy of g is moderate. Still, according to the above considerations, we only required the prediction of μ_s or g to be accurate, thus we combined configuration (b) and (c) finally leading to the hybrid configuration (d) in Figure 2.

Configuration (d) obviously has four out-put variables, i.e. α_1, α_2, T and R. Due to the fact, that the applied MPR/N-R algorithms imply exactly three variables in order to determine the three requested optical properties, i.e. μ_a, μ_s, and g, we chose to apply PCA to reduce the dimension of the variables from four to three. In short, the PCA procedure extracts the relevant information in a set of calibration variables and generates a new set of variables, so-called *principal components*, i.e. PC_1, PC_2, etc., which are sorted according to their respective variances. In our case, this means that almost all information on μ_a, μ_s, and g from α_1, α_2, T, and R is embedded in $PC_{1\text{-}3}$, while most of the random noise from the MC simulations are isolated in PC_4, which is disregarded during calibration and prediction. As a bonus, the use of PCA decreases the noise-sensitivity of the applied prediction methods; i.e. the robustness of the method is increased.

Initially, we performed prediction tests on configuration (d) using the optimal angles and distances found during the analysis of configuration (b) and (c) (see Table 2). This also yielded good results, but the short optimal distance of T (r_t = 0.7 mm), may be difficult to implement if goniometric measurements at α_1 and α_2 are to be performed simultaneously. We therefore carried out the error analysis depicted in Figure 3. The results showed that the choice of r_T, and r_R in configuration (d) was uncritical as long as 1.5< (r_T, r_R) < 3.0mm, where the lower limit was determined by the prediction errors of μ_a and the upper limit by the prediction errors of g. It also appeared, that the prediction errors of μ_s was practically independent of r_T, and r_R in the range 0 < (r_T, r_R) < 4mm. The results depicted in Figure 3 is based on θ_{α_1} = 0° and θ_{α_2} = 5°. We carried out similar analyses for the range 1° < θ_{α_2} < 10° as well. The results showed that the prediction accuracies of all three optical properties were practically invariant to the value of θ_{α_2} in this range. Due to these loose restrictions on the geometrical configuration of α_1, α_2, T, and R, configuration (d) in Figure 2 appears to be relatively simple and straightforward to implement. As a consequence, we based all our further analyses on this configuration using the values of θ_{α_1}, θ_{α_2}, r_T, and r_R listed in Table 2.

Table 3 shows that the prediction performance of configuration (d) is good in the lower- and the middle μ_s-ranges. However, the prediction error of μ_a in the lower μ_s-range is significantly larger than the other errors. This may be due to fact that the calibration model was optimized on the middle-range. Moreover, the analyses on configuration (b) and (c) suggest that the information on μ_a, to a large extent, is embedded in the spatially resolved recordings of R and T. Thus, if μ_s = 10 cm^{-1}, this statistically speaking leads to one single scattering event if d_s = 1 mm. Consequently, only a very few photons will be recorded at r_T = 2.0 mm and r_R = 2.5 mm, leading to poor prediction of μ_a. In this case it may be advantageous to apply a larger d_s. The prediction accuracy of the upper μ_s-range in Table 3 is inadequate. Here, a large sample thickness in conjunction with large μ_s values lead to an almost complete diffuse transmittance, i.e. it is difficult to extract any information on μ_s and g from the goniometric recordings of α_1 and α_2, which in turn makes it difficult to determine μ_a as well. In this case it may be advantageous to decrease d_s.

B. Model Scaling

As discussed in Sect 4.A the sample thickness d_s = 1 mm may be too large for proper prediction of large values of μ_s. As mentioned in Sect. 3 above, this problem may be solved by applying a calibration model and prediction data with a smaller d_s. However, in some practical implementations, it may too tedious to generate a new calibration model. Therefore, we tried to feed downscaled prediction data, i.e. d_s = 0.5 mm to the original calibration model (d_s = 1 mm) and then subsequently correct the results by multiplying the predicted μ_a and μ_s by 2. During such a procedure, it is important to remember that r_T, r_R and d_b of the prediction data have to be scaled as well, in opposition to the α data, which are invariant to any scaling of d_s. The results given in Figure 4 shows a good prediction accuracy for both μ_a, μ_s, and g, in spite of the μ_s-range is substantially wider than e.g. the individual tests reported in Table 3. Still, the prediction error of μ_a = 2.2 % may be unacceptable in some cases. However, as stated in Sect. 3 this error may be substantially reduced by splitting the calibration model used in Figure 4 into three sub-models. As a trade off the prediction error of μ_s is slightly increased, probably owing to the reduced μ_s resolution of the three calibration sub-models compared to the full-range model. In a real application demanding high accuracy and wide optical property ranges, a two-step prediction algorithm thus could be introduced. This could carried out by first making a rough estimate of μ_a, μ_s, and g, and then subsequently zoom in on the relevant sub-model to perform a second more accurate prediction of μ_a. In summary, the results in Figure 4 actually suggest that a calibration model with d_s = 0.5 mm would be a better choice as a general-purpose model for the optical property ranges defined by Eq. (1), than the model with d_s = 1 mm we started out with.

C. Acceptance Angle and Noise Considerations

During the analysis corresponding to the results in Table 3 the acceptance angle ϕ_{α_1} was 0.25°. Owing to the fact that such a relatively small angle may be difficult to implement in some applications, we carried out a series of prediction tests with varying ϕ_{α_1}. The results from these tests are shown in Figure 5(a). It appears that the prediction error of μ_a is unaffected by the changes in ϕ_{α_1}, and that the prediction errors of both μ_s and g increase more or less linearly as function of ϕ_{α_1}. This is agrees well with the discussions in Sect. 4.A which suggest that μ_a is mainly determined from the R and T data, in opposition to μ_s and g, which are mainly determined from α_1 and α_2. The increase in the errors of μ_s and g is most likely due to the fact that, when ϕ_{α_1} increases so does the probability that the photons leaving the sample may have been scattered twice or more and still be within the limits of the acceptance cone spanned by ϕ_{α_1}. In other words, two (or more) scattering events with $\mu_{s,1}$ and g_1 may be interpreted as one scattering event with $\mu_{s,2}$ and g_2. However, the results in Figure 5(a) also show that θ_{α_1} may be increased to at least 2° without any serious reduction of the overall prediction accuracy. In the light of the practical problems encountered during T_c measurements in connection with IS measurements (see Sect. 1), this result is interesting, because it is considerably simpler to perform α_1 measurements with a finite acceptance angle ($\phi_{\alpha_1} \approx 1^{\circ}$), than T_c

measurements with $\phi_{T_c} = 0^{\circ}$. The above discussion also suggests that predictions on data with higher g values may cause problems. Thus, we tested our method on a set of prediction data with μ_a- and μ_s-ranges similar to Eq. 5, but with a g-range defined by: $0.9 < g < 0.98$. The results showed prediction errors < 0.7 % for all three optical properties. This leads to the conclusion, that our method may be extended to include at least $g \leq 0.98$ without any problems.

As we mentioned in Sect. 3, noise is another practical problem encountered during real measurements. The decay of the prediction errors shown in Figure 5(b) agrees well with the theoretical $P_{noise} \propto \sqrt{1/m}$ relation between the random MC noise P_{noise} and the number of applied photons m. Furthermore, it appears that all three errors have dropped below 1% already at $m = 1\cdot10^6$. These results only stress the importance of minimizing the noise sources during real measurements.

5. Conclusions

We have developed a novel method for accurate real-time determination of the optical properties μ_a, μ_s, and g from spatially and/or angularly resolved measurements on a thin turbid sample, i.e. a solid slab or a cuvette. However, all analyses and conclusions we have presented are based on Monte Carlo simulated data and experimental verification therefore remains to be carried out. This may of course introduce new problems, e.g. it may prove be difficult to obtain a prediction performance comparable to the simulated cases, due to noise and/or discrepancies between the applied MC model and real measurements. Still, during our previous work using MC on other geometrical configurations we have obtained experimental prediction accuracies comparable to the accuracies we obtained using simulated test data. Moreover, should any problems arise due to the applied MC simulations, e.g. the implicit *Henyey-Greenstein* phase function[15], it would be relatively simple to apply the calibration and prediction algorithms on data from a set of new or modified simulations. In the last resort, it is of course also possible to carry out calibration on a set of phantoms with well-defined optical properties. Thus, we are confident that it is feasible to implement the presented method in compact and cost-effective practical instrumentation maintaining prediction performances sufficient for a variety of applications. Such instrumentation is especially interesting due to its obvious advantages compared to IS based methods, i.e. no T_c measurements are required, the sample does not have be moved during the measurements, and no bulky spheres are needed. Figure 6 illustrates how the implementation may be carried out in a simple way merely using a beam-splitter, five detectors, and a lens. Such a set-up is currently under construction, and our future work will therefore be aimed at experimental tests and verifications of the theoretical methods we have presented here.

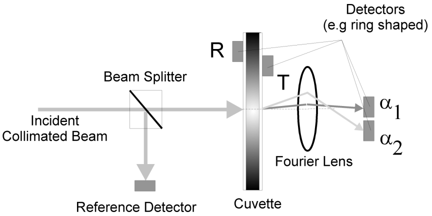

Figure 6. Practical realization of configuration (d) in Figure 2.

The authors acknowledge the financial support from the Danish Academy of Technical Sciences.

References

1. A.J. Welch, M.J.C. van Gemert, W.M. Star and B.C. Wilson, Definitions and overview of tissue optics, in *Optical-Thermal Response of Laser-Irradiated Tissue,* eds. A.J. Welch and M.J.C. van Gemert, (Plenum Press, New York, NY, 1995).

2. J.W. Feather, D.J. Ellis and G. Leslie, A portable reflectometer for the rapid quantification of cutaneous haemoglobin and melanin, *Phys. Med. Biol.* **33**, 711-722 (1988).

3. S.L. Jacques, Reflectance spectroscopy with optical fiber devices, and transcutaneous bilirubinometers, in *Biomedical optical instrumentation and laser-assisted biotechnology,* eds. A.M. Verga Scheggi, S. Martellucci, A.N. Chester and R. Pratesi, pp. 83-94 (Kluwer Academic Publishers, Dordrecht, 1996).

4. J.R. Mourant, J.P. Freyer, A.H. Hielscher, A.A. Eick, D. Shen and T.M. Johnson, Mechanisms of light scattering from biological cells relevant to noninvasive optical-tissue diagnotics, *Appl. Opt.* **37**, 3586-3593 (1998).

5. S.L. Jacques, Origins of tissue optical properties in the UVA, Visible, and NIR regions, eds. R.R.

Alfano and J.G. Fujimoto, pp. 364-369 (Optical Society of America, 1996).

6. A.M.K. Nilsson, R. Berg and S. Andersson-Engels, Measurements of the optical properties of tissue in conjunction with photodynamic therapy, *Appl. Opt.* **34**, 4609-4619 (1995).

7. A. Roggan, M. Friebel, K. Dörschel, A. Hahn and G. Müller, Optical properties of circulating human blood in the wavelength range 400 - 2500 nm, *J. Biomedical Optics* **4**, 36-46 (1999).

8. S.R. Kamath, C.V. Morr and T. Shenz, Laser Light Scattering and Microscopic Properties of Milkfat Globules in Swiss Cheese Whey Low Density Lipid-containing Fraction, *Lebensmittel-Wissenschaft & -Technologie* **31**, 274-278 (1998).

9. J.W. Pickering, S.A. Prahl, N. van Wieringen, J.F. Beek, H.J.C.M. Sterenborg and M.J.C. van Gemert, Double-integrating-sphere system for measuring the optical properties of tissue, *Appl. Opt.* **32**, 399-410 (1993).

10. A.N. Yaroslavsky, I.V. Yaroslavsky, T. Goldbach and H.J. Schwarzmaier, Influence of the Scattering Phase Function Approximation on the Optical Properties of Blood Determined from the Integrating Sphere Measurements, *J. Biomed. Opt.* **4**, 47-53 (1998).

11. J.S. Dam, T. Dalgaard, P.E. Fabricius and S. Andersson-Engels, Multiple polynomial regression method for determination of biomedical optical properties from integrating sphere measurements, *Appl. Opt.* **39**, 1202-1209 (2000).

12. S.V. Chapra and R.P. Canale, *Numerical Methods for Engineers*, (MacGraw-Hill, 1997).

13. L. Wang, S.L. Jacques and L. Zheng, MCML-Monte Carlo modeling of light transport in multi-layered tissues, *Computer Methods and Programs in Medicine* **47**, 131-146 (1995).

14. A. Pifferi, P. Taroni, G. Valentini and S. Andersson-Engels, Real-time method for fitting time-resolved reflectance and transmittance measurements with a Monte Carlo model, *Appl. Opt.* **37**, 2774-2780 (1998).

15. L.G. Henyey and J.L. Greenstein, Diffuse radiation in the galaxy, *Astrophys. J.* **93**, 70-83 (1941).

Paper VI

Local diffuse reflectance from three-layered skin tissue structures

Peter E. Andersen[a†], Jan S. Dam[b], Paul M. Petersen[a], and Peter Bjerring[c]

[a] Optics and Fluid Dynamics Department, Risø National Laboratory, P.O. Box 49,
DK-4000 Roskilde, Denmark
[b] Technology Research Center, Bang & Olufsen Technology A/S, DK-7600 Struer, Denmark
[c] Department of Dermatology, Marselisborg Hospital, University of Aarhus,
DK-8000 Aarhus, Denmark

Abstract

We consider two different skin structure models. The first structure consists of epidermis, dermis/blood, and subcutaneous tissue. The second structure consists of epidermis/dermis, adipose tissue and muscle tissue. A new solution based on diffusion theory of the CW local diffuse reflectance from a three-layered skin tissue structure is presented. Comparisons with Monte Carlo simulations are carried out favorably. It is shown that the functional form of the radial dependence of the diffuse reflectance from multilayer and single layer models are identical. We use a modified expression originating from diffusion theory to fit the diffuse reflectance. We discuss the sensitivity of the local diffuse reflectance as a function of the optical properties of separate layers in both structures. Moreover, we investigate the influence on the local diffuse reflectance with changes in the optical properties corresponding to normal changes in tissue glucose concentration and blood volume. The necessity of multilayer models lies within their ability to provide a detailed description of the light-tissue interaction rather than their applicability to practical data analysis of the local diffuse reflectance measurements.

Keywords: diffuse reflectance, multilayer diffusion theory models, layered skin structures

1. Introduction

Human skin consists of bounded layers with distinct optical properties. Depending on the specific diagnostic application it may be necessary to distinguish between these layers when light-tissue interactions are modeled. Diffusion theory[1] and Monte Carlo simulations[2] (MCS) are commonly used for describing the light propagation in tissues. Time-domain, frequency-domain, and continuous wave (CW) measurement techniques may be modeled using the above models. In the present work, we are considering CW measurement techniques only.

The diffusion approximation to transport theory has been widely used to describe light propagation in turbid media for a variety of geometries and source functions. Reynolds *et al.*[3] used diffusion theory to describe the scattering from a monolayered slab with collimated illumination and modeled scattering from whole blood in a cuvette. Good agreement between theory and experimental results was obtained. Diffuse reflectance from two-layer tissue structures has also been investigated[4,5,6,7,8,9,10]. For example, Takatani and Graham[9] investigated the diffuse reflectance and transmittance from a two-layer tissue structure illuminated by a collimated beam. Their analysis was extended by Schmitt *et al.*,[10] who included a thin attenuating layer on top of the two-layer structure. Moreover, they obtained good agreement between the model and their experimental investigation. Recently, Svaasand *et al.*[11] presented an analysis of a three-layered skin structure consisting of epidermis, dermis, and a port-wine stain layer. They used a simple diffusion theory analysis where the illumination is a plane wave (of infinite width) and obtained a one-dimensional solution. Despite the simple analysis, acceptable agreement between computations and clinical results was obtained.

[†] P. E. A. (correspondence), phone: +45 46 77 45 55, fax: +45 46 75 40 64. e-mail: peter.andersen@risoe.dk, WWW: http://kon-hp.risoe.dk/

The validity of the diffusion approximation is, however, limited.[1] Firstly, the albedo $W_0 = \mu_s/(\mu_s + \mu_a)$ of the medium must be in the range of unity, where μ_s is the scattering and μ_a the absorption coefficients. This is fulfilled in most cases regarding tissues. Secondly, the approximation is not valid close to the source where the injected photons not yet have become diffuse. Usually the photons are considered diffuse after a few mean free paths, i.e., for distances exceeding $1/(\mu_a + \mu_s')$, where $\mu_s'=(1-g)\mu_s$ is the transport reduced scattering coefficient. Finally, the diffusion approximation breaks down at boundaries and border layers. However, good agreement between experiments and the diffusion theory has been demonstrated throughout the literature.

The localized diffuse reflectance from single and multilayer structures may also be obtained using MCS.[2] This is a purely numerical method with the major advantages that is valid for all values of the albedo and valid close to sources and at boundaries. Naturally, it lacks the ability to provide analytical expressions for the reflectance and transmittance. One important assumption is commonly made in MCS: the single scattering phase function $p(\cos\theta)$ is assumed to follow the Henyey-Greenstein approximation.[2] Nevertheless, the methods agrees extraordinary well with experiments for most tissues. It should be noted, however, that MCS using a Mie theory calculation of the single scattering phase function has been presented[12,13,14]. In particular, Mourant *et al.*[14] demonstrated a substantial discrepancy in the diffuse reflectance close to the source using the Mie theory calculated $p(\cos\theta)$ as compared to the Henyey-Greenstein approximation.

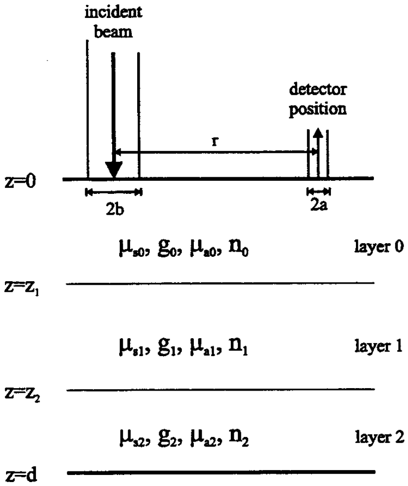

Figure 1. Geometry of the three-layer structure.

In our work, we are primarily concerned with measuring the glucose content of skin tissue *in vivo* from CW diffuse reflectance measurements, see Figure 1. In this geometry, we obtain the local diffuse reflectance *R*(*r*), or reflectance profile, as a function of the source-detector separation *r*. We model different skin structures depending on the geometry of our experimental setup. Structure #1 consists of an epidermal layer, a dermal/blood layer, and a subcutaneous tissue layer. This structure may be used to model the operation of devices with small source-detector separation, e.g. fiber-optic devices. Structure #2 consists of an epidermal/dermal/blood layer, a fat layer, and a layer of muscle-like tissue. Such a structure is suitable for modeling devices with relatively large source-detector separation. Our calculations are carried out at a single wavelength. However, the wavelength range may easily be extended by including the spectral dependence of the optical properties. We use diffusion theory to derive a novel expression for the diffuse reflectance from a three-layer structure thus extending the work of Takatani *et al.*[9] The functional form of *R*(*r*) from a single layer and a multilayer structure is identical. Hence, practical experiments are made cumbersome by this fact. We compare our computations using diffusion theory with MCS and obtain good agreement. We fit the reflectance profile using a novel fitting expression.[15] A sensitivity analysis of *R*(*r*) based on the fitting parameters with respect to changes in the optical parameters in each layer including both skin structures is carried out. Furthermore, for both skin structures we investigate the sensitivity of *R*(*r*) on changes in the optical properties according to physiological changes in blood volume and glucose concentration.

2. Theoretical considerations

The geometry of the problem is shown in Figure 1. The diameter of the collimated incident beam is 2*b* and the detector with diameter 2*a* is placed at position *r*. The total thickness of the structure is *d*. In the following, we give the result for calculating the diffuse reflectance from a three-layer structure.

The local diffuse reflectance *R*(*r*) is given by:

$$R(r) = \left| -D_0 \frac{\partial \psi_0}{\partial z} \right|_{z=0} \tag{1}$$

where $D_i = 1/3(\mu'_{si} + \mu_{ai}) = 1/3\mu'_{ti}$ is the diffusion constant for the i'th layer (i=0,1,2) and ψ_0 the diffuse intensity. The diffusion equation has to be solved for the diffuse intensity $\psi_i(r,z)$ for each layer. By doing so and inserting in Eqn. (1) we obtain:

$$\begin{gathered} R(r) = D_0 \sum_n^{\infty} \frac{k_{n0} \cos\gamma_{n0}}{\lambda_n^2 N_n} \left\{ \frac{b^2}{2} - rbI_1(\lambda_n b) K_1(\lambda_n r) \right\} \\ \left[\frac{\mu_{s0}'}{D_0} z_{n0} + \frac{\mu_{s1}' n_1}{D_1 n_0} \exp\{-\mu'_{t0} z_1\} z_{n1} + \frac{\mu_{s2}' n_2}{D_2 n_1} \exp\{-\mu'_{t0} z_1 - \mu'_{t1}(z_2 - z_1)\} z_{n2} \right] \end{gathered} \tag{2}$$

where I_1 is the first-order modified Bessel function of the first kind and K_1 is the first-order modified Bessel function of the second kind. Note, that whenever n is used as subscript it refers to the summation variable. The functions z_{n0}, z_{n1}, and z_{n2} are given by:

$$\begin{aligned} z_{n0} &= \frac{1}{\left(k_{n0}^2 + \mu'^2_{t0}\right)} \left[k_{n0} \cos\gamma_{n0} + \mu'_{t0} \sin\gamma_{n0} \right. \\ &\qquad \left. - \exp\{-\mu'_{t0} z_1\} \left(k_{n0} \cos(k_{n0} z_1 + \gamma_{n0}) + \mu'_{t0} \sin(k_{n0} z_1 + \gamma_{n0})\right)\right] \\ z_{n1} &= \frac{A_{01}}{\left(k_{n1}^2 + \mu'^2_{t1}\right)} \left[-k_{n1} \cos(k_{n1}(z_2 - z_1) + \gamma_{n1}) + \mu'_{t1} \sin(k_{n1}(z_2 - z_1) + \gamma_{n1}) \right. \\ &\qquad \left. + \exp\{-\mu'_{t1}(z_2 - z_1)\} \left(k_{n1} \cos\gamma_{n1} - \mu'_{t1} \sin\gamma_{n1}\right)\right] \\ z_{n2} &= \frac{A_{12}}{\left(k_{n2}^2 + \mu'^2_{t2}\right)} \left[-k_{n2} \cos(k_{n2}(d - z_2) + \gamma_{n2}) + \mu'_{t2} \sin(k_{n2}(d - z_2) + \gamma_{n2}) \right. \\ &\qquad \left. + \exp\{-\mu'_{t2}(d - z_2)\} \left(k_{n2} \cos\gamma_{n2} - \mu'_{t2} \sin\gamma_{n2}\right)\right] \end{aligned} \tag{3}$$

The normalization factor N_n of the coupled Green's functions is given by:

$$\begin{aligned} N_n &= \frac{1}{4k_{n0}} \left[\sin 2\gamma_{n0} + 2k_{n0} z_1 - \sin[2(\gamma_{n0} + k_{n0} z_1)]\right] \\ &+ \frac{A_{01}^2}{4k_{n1}} \left[\sin 2\gamma_{n1} + 2k_{n1}(z_2 - z_1) - \sin[2(\gamma_{n1} + k_{n1}(z_2 - z_1))]\right] \\ &+ \frac{A_{12}^2}{4k_{n2}} \left[\sin 2\gamma_{n2} + 2k_{n2}(d - z_2) - \sin[2(\gamma_{n2} + k_{n2}(d - z_2))]\right] \end{aligned} \tag{4}$$

The boundary and continuity equations yield the two constants A_{01} and A_{12}:

$$\begin{aligned} A_{01} &= \frac{\sin(k_{n0} z_1 + \gamma_{n0})}{\sin(k_{n1}(z_2 - z_1) + \gamma_{n1})} \left(\frac{n_1}{n_0}\right)^2 \\ A_{12} &= A_{01} \frac{\sin(\gamma_{n1})}{\sin(k_{n2}(d - z_2) + \gamma_{n2})} \left(\frac{n_2}{n_1}\right)^2 \end{aligned} \tag{5}$$

where n_i represents the refractive index of the i'th layer. Furthermore, from the same set of equations the transcendental equation for the eigenvalues k_{ni} may be found:

$$\frac{\tan(k_{n0}z_1+\gamma_{n0})}{D_0 n_0^2 k_{n0}} = -\frac{\tan(k_{n1}(z_2-z_1)+\gamma_{n1})}{D_1 n_1^2 k_{n1}} \tag{6}$$

In these equations the phase functions are given by:

$$\begin{aligned} \gamma_{n0} &= \tan^{-1}(2b_0 D_0 k_{n0}) \\ \gamma_{n1} &= \tan^{-1}\left(\frac{D_1 k_{n1} n_1^2}{D_2 k_{n2} n_2^2}\tan(k_{n2}(d-z_2)+\gamma_{n2})\right) \\ \gamma_{n2} &= \tan^{-1}(2b_2 D_2 k_{n2}) \end{aligned} \tag{7}$$

where b_0 and b_2 are determined by the refractive indices of each layer and the surrounding medium.[16] In the case of index matching, $b_0=b_2=1$. Finally the parameter λ_n is found:

$$\lambda_n^2 = k_{n0}^2 + \frac{\mu_{a,0}}{D_0} = k_{n1}^2 + \frac{\mu_{a,1}}{D_1} = k_{n2}^2 + \frac{\mu_{a,2}}{D_2} \tag{8}$$

The local diffuse reflectance $R(r)$ in Eqn. (2) is found from an infinite series. However, only a limited number of eigenvalues is necessary for the series to converge. Solving the transcendental eigenvalue equation in Eqn. (6), the local diffuse reflectance may be computed within seconds (on a personal computer). Hence, the advantage of using diffusion theory over MCS is that a large number of $R(r)$ profiles may be generated in a short time. The agreement between the diffusion theory and experiments may be less accurate than the agreement obtained with MCS. However, for the purpose of a sensitivity analysis of $R(r)$ with respect to the optical properties of the multilayered structure, the accuracy of the diffusion theory is sufficient.

It is obvious that the expression in Eqn. (2) for the diffuse reflectance $R(r)$ does not provide a simple relation between the reflectance and the optical properties of the underlying layers. This is a well known fact and various neural network approaches have been demonstrated to provide the necessary relation in the monolayer case.[17] The *inverse* problem may thus be solved for the single layered structure.

The functional form of the reflectance profile $R(r)$ from a multilayer structure cannot, however, be distinguished from a monolayer structure. This is obtained by comparison of Eqn. (2) to the corresponding expression in Ref. 3 (Eqn. (16)). The functional form of the r-dependent term is identical in both cases and therefore the $R(r)$ profiles from single and multilayer structures would have similar shapes. In practical measurements it is impossible to determine the number of layers (and their thickness) making up the skin structure from the reflectance profile itself. The inverse problem is thereby ill posed. Moreover, solving the inverse problem using neural network processing based on multilayered models is will not provide a unique answer: the number of variables in the system is simply too large for most practical cases.

What is then the need of modeling light propagation in multilayered tissue structures? Obviously, the *forward* problem, i.e. predictions of $R(r)$ with known optical properties and geometry, may be thoroughly investigated by such models. For example, the change in $R(r)$ due to physiological blood volume changes or tissue glucose concentration may be investigated providing valuable information during design of an experiment or a device. An example of such an investigation is carried out in Section 3.

In the present work, we investigate two different skin structures. We have used values representative of the tissues, which are modeled.[18] In the following, all layers have the same refractive index: $n_0=n_1=n_2=1.4$. The two structures, #1 and #2, are surrounded by air with unity refractive index. Structure #1 consists of an epidermal layer, a dermal/blood layer, and a subcutaneous layer. The thickness of each layer is 0.12 mm, 1 mm, and 10 mm, respectively. The mean cosine of the scattering phase function is assumed constant in these calculations and we have chosen g_0=0.92, g_1=0.88, and g_2=0.85, respectively. Structure #2 consists of an epidermal/dermal layer, a layer of adipose tissue, and a layer of muscle tissue. The thickness of each layer in structure #2 are 1 mm, 1 mm, and 20 mm, respectively, and g_0=0.90, g_1=0.85, and g_2=0.89, respectively.

In the following we give a few examples of comparisons between our calculations obtained with diffusion theory and MCS. We used the MCS program provided by Wang and Jacques.[19] The first comparison is carried out using skin structure #1. The absorption coefficients of the first and third layers are: μ_{a0}=0.02 mm^{-1} and μ_{a2}=0.01 mm^{-1}. The scattering coefficients of the first and third layers are: μ_{s0}=35 mm^{-1} and μ_{s2}=15 mm^{-1}. The scattering coefficient μ_{s1} of the middle layer is varied with values: 10 mm^{-1}, 15 mm^{-1}, and 25 mm^{-1}. In this case the absorption coefficient is μ_{a1}=0.05 mm^{-1}. In Figure 2a the comparison between MCS (solid lines) and the corresponding diffusion theory calculations (dashed lines) is shown. The comparison between MCS and the diffusion theory with varying absorption of the middle layer is shown in Figure 2b. The scattering coefficient is μ_{s1}= 20 mm^{-1}. The absorption coefficient μ_{a1} is varied with values: 0.02 mm^{-1}, 0.05 mm^{-1}, and 0.10 mm^{-1}. Qualitatively we observe good agreement between the two methods.

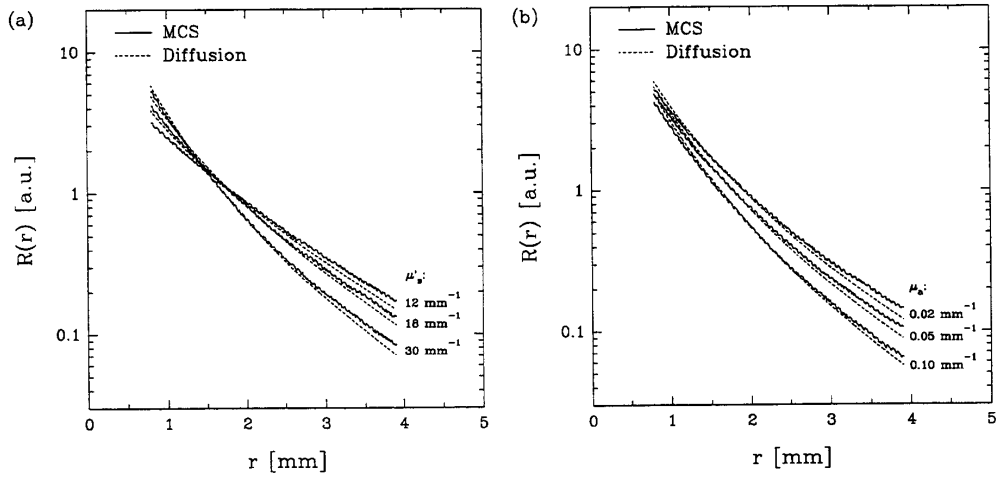

Figure 2 The diffuse reflectance $R(r)$ as a function of the source-detector separation r for skin structure #1. (a) the scattering coefficient of the middle layer is varied (parameters in the text). (b) the absorption coefficient of the middle layer is varied (parameters in the text).

We also compared the diffusion theory to MCS for skin structure #2. The absorption coefficients of the three layers are: μ_{a0}=0.01 mm^{-1}, μ_{a1}=0.005 mm^{-1}, and μ_{a2}=0.01 mm^{-1}. The scattering coefficients of the second and third layers are: μ_{s1}=35 mm^{-1}, and μ_{s2}=50 mm^{-1}. The scattering coefficient μ_{s0} of the first layer is varied with values: 20 mm^{-1}, 25 mm^{-1}, and 30 mm^{-1}. The results are shown in Figure 3a, where MCS are shown as solid lines and the diffusion theory calculations are shown as dashed lines. In Figure 3b, the absorption coefficients of the three layers are: μ_{a0}= 0.001 mm^{-1}, μ_{a1}=0.005 mm^{-1}, and μ_{a2}=0.01 mm^{-1}. The scattering coefficients of the two first layers are: μ_{s0}=20 mm^{-1} and μ_{s1}=35 mm^{-1}. The scattering coefficient μ_{s2} of the third layer is varied: 40 mm^{-1}, 50 mm^{-1}, and 60 mm^{-1}. The comparison displayed in Figure 3 reveals good agreement between the two methods. Hence, we conclude that the three-layered diffusion theory presented above is adequate for investigating the local diffuse reflectance.

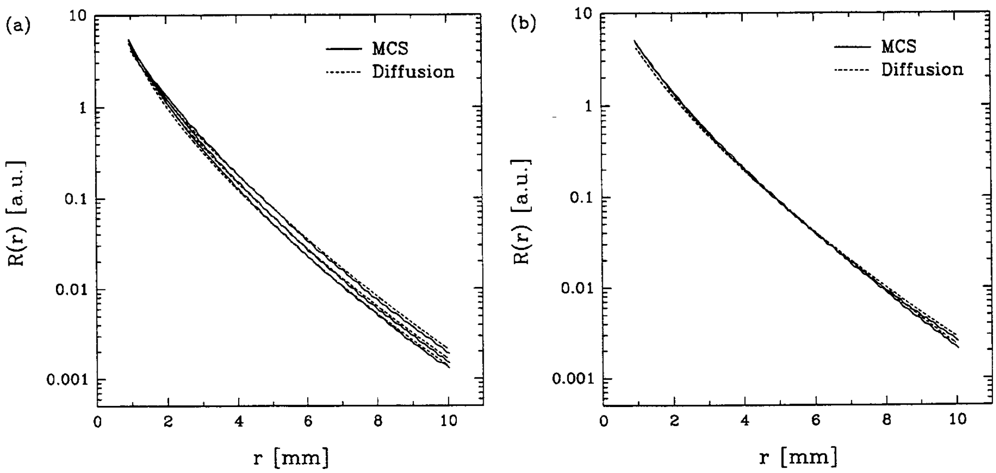

Figure 3 The diffuse reflectance $R(r)$ as a function of the source-detector separation r for skin structure #2. (a) the scattering coefficient of the first layer is varied (parameters in the text). (b) the scattering coefficient of the third layer is varied (parameters in the text).

3. Numerical results and discussion

In the following we present the results of our sensitivity analysis of the two skin structures. In the analysis we investigate the sensitivity of the diffuse reflectance with respect to (relatively large) changes in the optical properties of each layer. Moreover, we investigate the sensitivity of the reflectance modeling physiological cases, e.g., tissue glucose concentration and blood volume changes. The reflectance profile may be fitted using the expression:[15]

$$R(r) = k_1 \frac{\exp\{-k_2 r\}}{r^x} \tag{9}$$

where k_1, k_2, and x are all functions of the optical properties. Note, that in contrast to previous results[10] the parameter x is in this paper considered a function of the optical properties. It has been shown that this dependence is pronounced even for subtle changes in the optical properties.[15] The advantage of using the above expression to fit the profile is that it fits the reflectance extremely well for *all* radial distances.[15] Furthermore, throughout the investigation we assume the wavelength of the light in the 600 to 900 nm range.

In the following investigation, the assessment of the local diffuse reflectance profiles is carried out as follows: All diffuse reflectance profiles are generated using Eqn. (2). Each profile is then fitted using the curve fitting expression given in Eqn. (9) yielding three fitting parameters k_1, k_2, and x. When the optical parameters are varied, the three fitting parameters change accordingly. These parameters are then displayed as a function of optical parameter in question. Note, that the three fitting parameters may serve as input to a neural network, which has been demonstrated in the monolayer case.[15]

3.1 Sensitivity analysis

In the present section, the results of the sensitivity analysis is presented for skin structure #1. We vary the absorption μ_{ai} and scattering μ_{si} of each layer separately. The absorption coefficients of the second and third layers are 0.05 mm^{-1} and 0.01 mm^{-1}. The scattering coefficients of the second and the third layers are 20 mm^{-1} and 15 mm^{-1}. In Figure 4 the fitting parameters are shown as a function of the absorption coefficient of the first layer with scattering coefficient μ_s=35 mm^{-1}. There is a slight decrease in k_1 and increase in k_2 with increasing absorption. The reason for the small changes is that the first layer is only 120 μm thick. In Figure 4b the three fitting parameters are shown as a function of the scattering coefficient of the first layer with absorption coefficient

μ_a=0.02 mm^{-1}. As the scattering increases more light is reemitted close to the source and hence less light is reemitted far away. This is in accordance with the increase in the amplitude k_1 and attenuating factor k_2. Moreover, the parameters x decreases, since the profile flattens out. Note, that the optical properties are changed far beyond the range occurring in real tissues. Even in this case, the change in reflectance is relatively small. This may once again be attributed to the small thickness of the first layer.

Next, we investigate how the optical properties of the second layer influence the diffuse reflectance $R(r)$. The absorption coefficients of the first and third layer are 0.02 mm^{-1} and 0.01 mm^{-1}. The scattering coefficients of the second and the third layers are 35 mm^{-1} and 15 mm^{-1}. The three fitting parameters are shown as a function of the absorption coefficient of the middle layer in Figure 4c with scattering coefficient μ_s=20 mm^{-1}. The behavior vaguely exhibited in Figure 4a is now more pronounced. In Figure 4d, the fitting parameters are shown as a function of the scattering coefficient with absorption coefficient μ_a=0.03 mm^{-1}. The behavior of k_1 and k_2 clearly is similar to Figure 4b. However, the exponent x behaves differently. It is clear though, from Figure 4, that the exponent x is a function of the optical parameters in accordance with Ref. 15.

The above changes in the optical properties are much larger than normally occurring in human tissues. Consequently, the changes in the diffuse reflectance profile is large and easily detectable. However, the primary aim of working with multilayer models is to investigate the resulting changes in reflectance as the parameters are varied comparable with their true physiological values. In the following we assume that the tissue glucose concentration affects the scattering coefficient μ_s only. Moreover, we assume that only the scattering coefficients of the dermis/blood layer and the subcutaneous tissue layer are affected. Varying the tissue glucose concentration from a minimum value of 3.5 mmol/l to a maximum of 18 mmol/l corresponds to a change in μ_s' of approximately 2.5%.[20] For the computations, we have used the optical parameters: μ_{a0}=0.02 mm^{-1}, μ_{a1}=0.03 mm^{-1}, μ_{a2}=0.01 mm^{-1}, μ_{s0}=35 mm^{-1}, μ_{s1}=20 (±7.5%) mm^{-1}, μ_{s2}=15 (±6.6%) mm^{-1} (the remaining parameters have been given above). To mimic a physiological system, we have extended the range for variations in the scattering coefficients for the two bottom layers. The fitting parameters k_1, k_2, and x are shown as a function of the scattering coefficients of the bottom layers in Figure 5. Note, that the scattering coefficient of both layers are changed from its minimum to its maximum value simultaneously. For example we can estimate the change in the fitting parameters according to the maximum change in glucose concentration from Figure 5. Such a change (2.5%) results in a change of less than 1% in each of the fitting parameters with k_1 being the most sensitive. Moreover, this assessment is based on an assumption that absolute measurements are possible as opposed to relatively measurements. In other words, the resulting change in the diffuse reflectance profile is extremely small and consequently high accuracy of the practical measurement system is needed.

The above computations showed small changes in the diffuse reflectance as a function of tissue glucose concentration. However, how does the above changes compare against blood volume changes in dermis and subcutaneous tissue (middle and bottom layer)? To answer this question, we have changed the absorption coefficients of these layers to simulate the change in blood volume e.g. due to temperature changes. The absorption of the middle layer is changed from 0.1 mm^{-1} down to 0.004 mm^{-1} and the absorption of the bottom layer from 0.01 mm^{-1} down to 0.005 mm^{-1}. The changes in the scattering coefficients are similar to those of Figure 5. In Figure 6 we have shown the fitting parameters as a function of the scattering coefficients of the two bottom layers. Note, that the absorption changes from its maximum to its minimum value. In this case the maximum glucose concentration change (2.5%), which is found by considering only part of the curves, superposed by a change in absorption from 0.065 mm^{-1} to 0.049 mm^{-1} (layer 2, 25%) and 0.0081 mm^{-1} to 0.0073 mm^{-1} (layer 3, 10%), results in changes of the fitting parameters between 1.25% and 3%, and again k_1 is the most sensitive parameter. Hence, the change in fitting parameters due to tissue glucose concentration is smaller than the corresponding change in blood volume in comparison to the estimates related to Figure 5. Ultimately, this may lead to difficulties in determination of the tissue glucose concentration from $R(r)$ measurements. Moreover, these calculations suggest

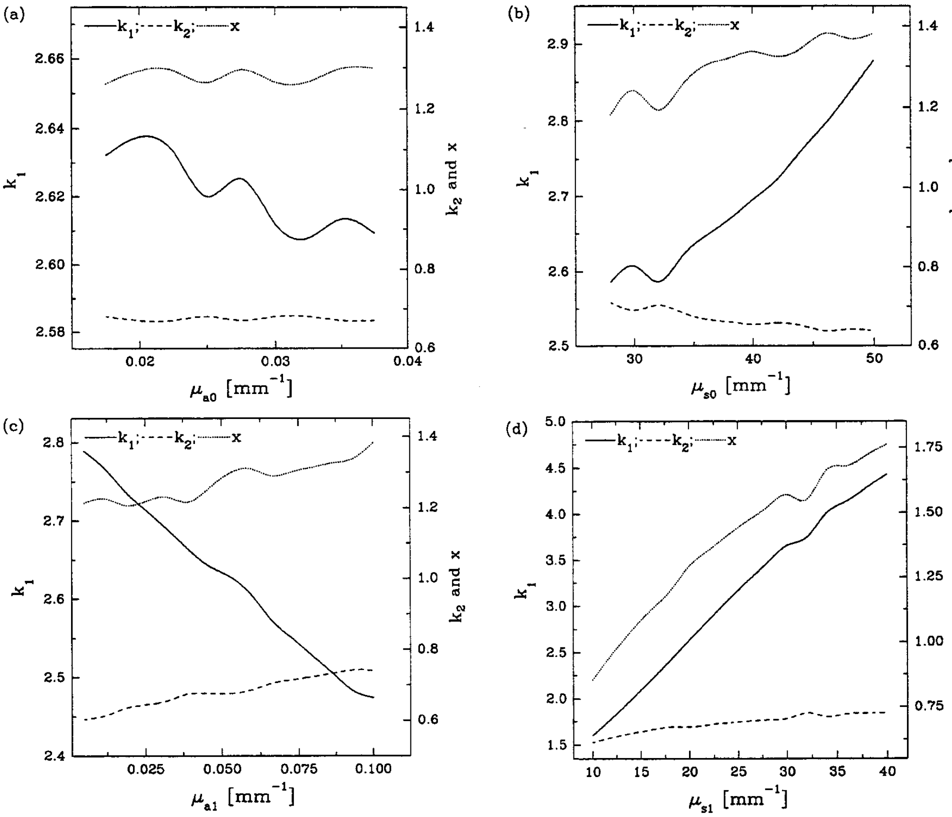

Figure 4 The fitting parameters k_1, k_2, and x as a function of the optical parameters for skin structure #2. (a) absorption change of the first layer. (b) scattering change of the first layer. (c) absorption change of the middle layer. (d) scattering change of the middle layer.

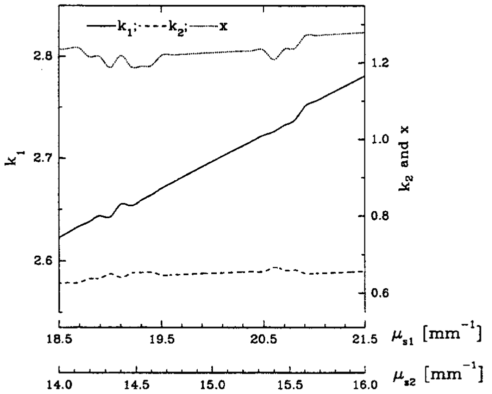

Figure 5 The fitting parameters as a function of the scattering coefficients of layer 2 and 3 for skin structure #1 (absorption kept constant).

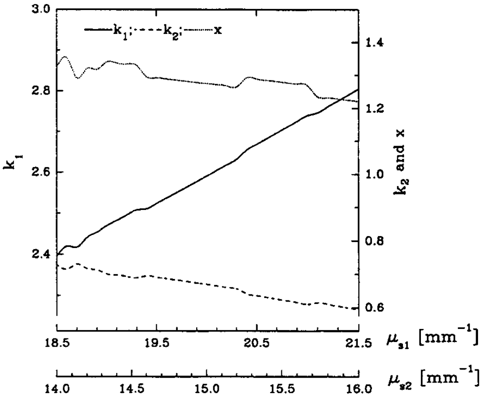

Figure 6 The fitting parameters as a function of the scattering coefficients of layer 2 and 3 for skin structure #1. The absorption of layer 2 and 3 are changed according to normal blood volume changes.

that a single wavelength is not sufficient to extract information of the tissue glucose contents from diffuse reflectance profiles. The proper set of wavelengths for measuring tissue glucose has to be identified with respect to determining various biological interferences.

Skin structure #2 consists of an epidermal/dermal/blood layer, a layer of adipose tissue, and a muscle layer. In our investigation of this structure we have mostly been concerned with changes of optical parameters in the first and third layer. The reason being that the fat layer changes its optical properties in time much slower than skin and muscle tissues. The optical properties of this layer is: μ_{a1}=0.005 mm^{-1} and μ_{s1}=35 mm^{-1}. In the following we give an example of the sensitivity of $R(r)$ with changes in the scattering of the top and bottom layer, respectively. Finally, we give an example of the complicated relationship between the fitting parameter (or reflectance profile) and the underlying optical properties.

For the first calculations the absorption coefficient of the top and bottom layers are μ_{a0}=μ_{a2}=0.01 mm^{-1}. The scattering coefficient of the bottom layer is μ_{s2}=50 mm^{-1} and the scattering of the top layer is varied. In Figure 7a we have shown the fitting parameters as a function of the scattering of the top layer. The behavior of the fitting parameters is similar to the case using skin structure #1, see e.g. Figure 4. However, the fitting parameters is now more influenced by the optical property change due to the increased thickness of the layers yielding increased interaction paths. Therefore, more pronounced changes in the reflectance are occurring in this case. The scattering coefficient of the bottom layer is then varied with fixed scattering coefficient of the top layer: μ_{s0}=20 mm^{-1}. The result is shown in Figure 7b, where the fitting parameters are shown as a function of the scattering coeffi-

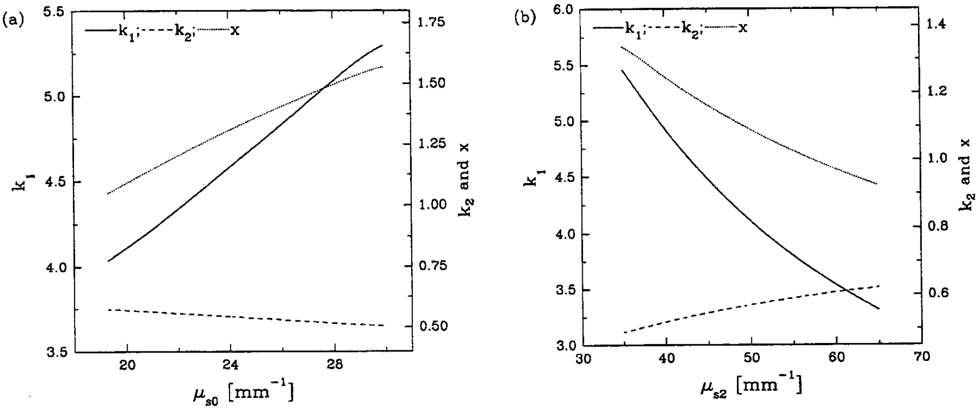

Figure 7 The fitting parameters as a function of the scattering coefficients for skin structure #2 (absorption kept constant). (a) scattering coefficient varied in top layer. (b) scattering coefficient varied in bottom layer.

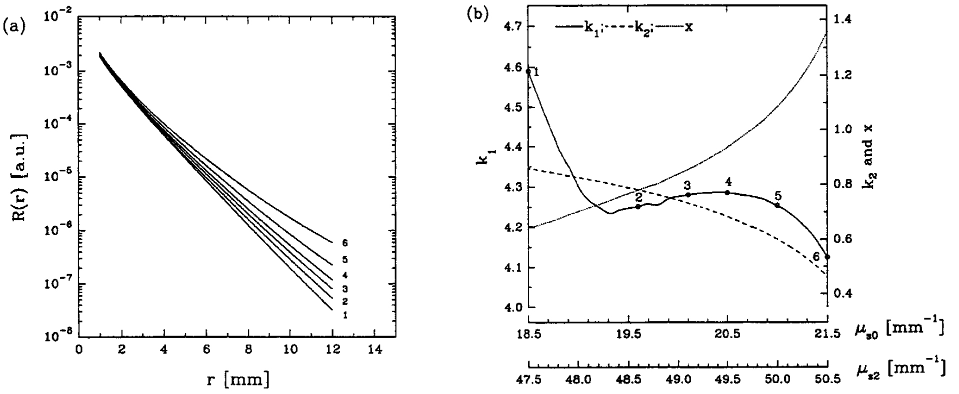

Figure 8 (a) The diffuse reflectance $R(r)$ as a function of r. The numbers refer to certain absorption coefficients given in Table 1 of the top and bottom layer. (b) The fitting parameters as a function of the scattering coefficients. The markers refer to a profile in (a).

cient. As before the behavior is similar to the previous case, but with more pronounced effects on the fitting parameters when compared to Figure 4.

The primary goal of our work has been to investigate the influence on the reflectance profile with optical property changes in physiological relevant ranges. Moreover, the analysis involving the fitting procedure clearly demonstrates the complicated relationship between the diffuse reflectance profiles and the optical properties. In the following example we vary the scattering of the top and bottom layers within the range of maximum glucose concentration changes and the absorption coefficient of both layers simulating blood volume changes. The absorption coefficients for both layers are changed from their maximum 0.05 mm^{-1} value to their minimum value 0.005 mm^{-1}. In Figure 8a, the diffuse reflectance profiles are shown for a few sets of optical properties. The numbers in Figure 8a refer to the absorption coefficients of layer 0 and 2, see Table 1. A straightforward relationship between the reflectance profiles and the optical properties seems to exists judging from Figure 8a. This is, however, not the case. Previously neural networks have been used to model this relation in the case of a single layer model.[17] In the case of multilayered structures, a complicated relation between the diffuse reflectance profile and the optical properties also exists. This is exemplified in Figure 8b showing the fitting parameters as a function of the scattering coefficients of the top and bottom layers. The circles with markers indicate the set of fitting parameters describing the diffuse reflectance profile in Figure 8a. Hence, one should apply data analysis algorithms capable of handling nonlinear relations between input and output, e.g., neural networks. Finally, the change in the fitting parameters due to tissue glucose concentration changes is again smaller than the change due to blood volume changes. The demands for exact quantification of the blood volume change or similar interferences are therefore high.

4. Conclusions

We have investigated two skin structures: the first consisted of an epidermal layer, a dermal/blood layer, and a layer of subcutaneous tissue. The second structure consisted of an epidermal/dermal/blood layer, a layer of adipose tissue, and a muscle tissue layer. We have modeled the local diffuse reflectance using a three-layered diffusion theory and compared our calculations favorably to Monte Carlo simulations. We have investigated the sensitivity of the local diffuse reflectance $R(r)$ with respect to the optical properties of each layer through a curve fitting procedure of $R(r)$. Using the multilayer diffusion theory model, we simulated typical tissue glucose concentration changes and blood volume changes. Typically, the change in fitting parameters due to glucose changes was smaller than the corresponding change due to blood volume changes. Hence, the demands for accurate de-

Table 1 Absorption coefficients of top and bottom layers used for the calculations on skin structure #2 (Figure 8).

Profile number	1	2	3	4	5	6
Absorption coefficient μ_{a0} and μ_{a2} (mm^{-1})	0.05	0.032	0.0245	0.0185	0.011	0.005
Scattering coefficient μ_{s0} (mm^{-1})	18.5	19.7	20.2	20.6	21.1	21.5
Scattering coefficient μ_{s2} (mm^{-1})	47.5	48.7	49.2	49.6	50.1	50.5

termination of various biological interferences, e.g. blood volume changes, are high. Finally, we demonstrated the complicated relationship between the reflectance profile $R(r)$ (or the fitting parameters) and the underlying optical properties.

References

1. A. Ishimaru, *Wave propagation and scattering in random media, Vol. I*, Academic Press, New York, 1978.
2. See e.g., S.L. Jacques and L. Wang, "Monte Carlo modeling of light transport in tissues," *Optical-Thermal response of laser-irradiated tissue (eds. A.J. Welch and M.J.C. van Gemert)*, Chapter 4, Plenum Press, New York, 1995.
3. L. Reynolds, C. Johnson, and A. Ishimaru, "Diffuse reflectance from a finite blood medium: applications to the modeling of fiber optic catheters", Appl. Opt. **15**, 2059-2067 (1976).
4. M. Keijzer, W.M. Star, and P.R.M. Storchi, "Optical diffusion in layered media", Appl. Opt. **27**, 1820-1824 (1988).
5. R. Nossal, J. Keifer, G.H. Weiss, R. Bonner, H. Taitelbaum, and S. Halvin, "Photon migration in layered media", Appl. Opt. **27**, 3382-3391 (1988).
6. H. Taitelbaum, S. Havlin, and G.H. Weiss, "Approximate theory of photon migration in a two-layer medium", Appl. Opt. **28**, 2245-2249 (1989).
7. W. Cui and L.E. Ostrander, "The relationship of surface reflectance measurements to optical properties of layered biological media", IEEE Trans. Biomed. Eng. **39**, 194-201 (1992).
8. A.H. Hielscher, H. Liu, B. Chance, F.K. Tittell, and S.L. Jacques, "Time resolved photon emission from layered turbid media", Appl. Opt. **35**, 719-728 (1996).
9. S. Takatani and M.D. Graham, "Theoretical analysis of diffuse reflectance from a two-layer tissue model", IEEE Trans. Biomed. Eng. **BME-26**, 656-664 (1979).
10. J.M. Schmitt, G.X. Zhou, E.C. Walker, and R.T. Wall, "Multilayer model of photon diffusion in skin", J. Opt. Soc. Am. A **7**, 2141-2153 (1990).
11. L.O. Svaasand, L.T. Norvang, E.J. Fiskerstrand, and E.K.S. Stopps, "Tissue parameters determining the visual appearance of normal skin and port-wine stains", Laser Med. Sci. **10**, 55-65 (1995).
12. J. Boyer, J.R. Mourant, and I.J. Bigio, "Theoretical and experimental investigations of elastic scattering spectroscopy as a potential diagnostic for tissue pathologies", Proc. OSA: Advances in optical imaging and photon migration, **21**, R.R. Alfano, ed., 265-268 (1994).
13. J. Boyer, J.R. Mourant, and I.J. Bigio, "Monte Carlo investigations of elastic scattering spectroscopy applied to latex spheres used as tissue phantoms", Proc. SPIE **2389**, 103-112 (1995).
14. J.R. Mourant, J. Boyer, A.H. Hielscher, and I.J. Bigio, "Influence of the scattering phase function on light transport measurements in turbid media performed with small source-detector separations", Opt. Lett. **21**, 546-548 (1996).
15. J. S. Dam, P.E. Andersen, T. Dalgaard, and P.E. Fabricius, " Determination of tissue optical properties from diffuse reflectance profiles by multivariate calibraiton", *submitted March 1997 for publication in Applied Optics*.

16. W.M. Star and J.P.A. Marijnissen, "Calculating the response of isotropic light dosimetry probes as a function of the tissue refractive index", Appl. Opt. **28**, 2288-2291 (1989).

17. T.J. Farrell, B.C. Wilson, and M.S. Patterson, "The use of a neural network to determine tissue optical properties from spatially resolved diffuse reflectance measurements", Phys. Med. Biol. **37**, 2281-2286 (1992).

18. W.-F. Cheong, "Appendix to Chapter 8: Summary of optical properties", *Optical-Thermal response of laser-irradiated tissue (eds. A.J. Welch and M.J.C. van Gemert)*, App. to Chap. 8, Plenum Press, New York, 1995.

19. L. Wang and S.L. Jacques, *Monte Carlo modeling of light transport in multilayered tissues in Standard C*, Univ. of Texas, M.D. Anderson Cancer Center, Houston, Texas (1992).

20. J.S. Maier, S.A. Walker, S. Fantini, M.A. Franceschini, and E. Gratton, "Possible correlation between blood glucose concentration and the reduced scattering coefficient of tissues in the near-infrared", Opt. Lett. **19**, 2062-2064 (1994).

Paper VII

Comparison of spatially and temporally resolved diffuse reflectance measurement systems for determination of biomedical optical properties at 785 nm

Johannes Swartling, Claes af Klinteberg, Jan S. Dam, Thomas Johansson, Jonathan Roth,
Stefan Andersson-Engels

We have performed a comparative study of the performance of two systems used for determining the absorption and reduced scattering coefficients at 785 nm; one spatially resolved and one time-resolved. The spatially resolved system recorded the diffuse reflectance from a diode laser by means of a fiber-bundle probe in contact with the sample. The time-resolved system utilized ultra-short laser pulses and a single-photon counting detection scheme. Additional measurements were made with an integrating sphere set-up. The results showed 1-60% variation in the evaluation of the reduced scattering between the systems for Intralipid phantoms and 130-330% for *in vivo* measurements. For the absorption coefficient, the corresponding variations were 9-60% and 55%.

1. Introduction

Measuring the optical properties of biological tissue has grown into a mature procedure in the field of biomedical optics. Knowing the light scattering and absorption properties of tissue is the basis of a wide range of both diagnostic and therapeutic applications. Examples include laser-induced fluorescence to diagnose malignant tissue,[1,2] as well as laser-induced thermotherapy[3-5] and photodynamic therapy[6,7] to treat diseased tissue.

A number of different techniques have been developed to measure the optical properties of tissue. Common for most methods is a measurement of the diffuse reflectance or transmittance from a sample of the tissue, either *in vitro* or *in vivo*. The data is then related to the optical properties by means of a suitable inversion algorithm, based on either a theoretical light propagation model, or calibration against standards with known scattering and absorption properties. When spatially resolved measurements are performed, the sample is illuminated by a continuous wave light source in a spot, and the diffuse reflectance is recorded at different radial distances.[8-14] Time-resolved measurements, on the other hand, utilize sub-nanosecond pulses from a laser. After passing through a portion of the tissue, the time dispersion of the pulse can be measured.[15-22] Both these methods are two-parameter techniques, *i.e.*, the extracted properties are the absorption coefficient μ_a and the reduced scattering coefficient μ'_s.

Even though measurements of these two types are now common in biomedical optics, no systematic investigation to experimentally compare the performance of various systems seems to have been done. In this work, we have evaluated the performance of one spatially resolved and one time-resolved system on the same samples. In addition, we compared the results with those from integrating-sphere measurements, which are known to give very accurate results for *in vitro* samples.[7,23-25] When a measurement of the collimated transmittance is added to the integrating-sphere measurements, this technique becomes a three-parameter method, and allows the determination of μ_a, the scattering coefficient μ_s and the scattering anisotropy factor g. The reduced scattering coefficient μ'_s is defined as $\mu'_s = (1 - g)\,\mu_s$.

In order to evaluate the performance of the systems, measurements were carried out in three steps. First, tissue phantoms were prepared from diluted Intralipid (for scattering) and a dye (for absorption). In the next step, measurements on pork and chicken meat were performed. As a final step, *in vivo* measurements on the arms of the experimenters were made. The aim of the study was to compare the results and investigate

---

Department of Physics, Lund Institute of Technology,
P.O. Box 118, SE-221 00 Lund

the limitations of the different systems, especially in the case of inhomogeneous samples such as tissue.

In the following four sections, each of the three systems will be briefly presented, with references to publications where more thorough descriptions may be found regarding the technical details and the data evaluation methods.

2. Bang & Olufsen Fiber Probe System

A. Fiber Probe System

The fiber probe system, constructed by Bang & Olufsen Medicom a/s, Denmark, has been extensively described in Ref. [9]. The system was designed with real-time measurements of the skin surface in a clinical environment in mind. It consists of a probe head with a 200 µm source fiber in the center surrounded by five equally spaced concentric rings of 250 µm detector fibers. The fibers of each single ring detector are bundled and terminated on separate silicon photodiodes. In addition, three photodiodes and a temperature sensor are mounted directly near the perimeter of the probe head. Thus, $R(r)$ can be collected at six distances, *i.e.*, $r = 0.6$, 1.2, 1.8, 2.4, 3.0, and 7.8 mm, respectively. The source fiber is coupled into four separate fibers each connected to four replaceable low-power diode lasers. Furthermore, a separate reference detector monitors the output of the source fiber at the probe head. The diode lasers may be selected arbitrarily in order to suit different applications. In this paper only the diode laser at the wavelength 785 nm was used. The data acquisition and storage is controlled by a laptop PC connected to a digital signal processing (DSP) board. One cycle of four successive measurements (*i.e.*, one at each wavelength) including dark measurements may be performed in about 10 ms, thus the maximum sampling rate of the system is about 100 Hz. To minimize any interference from background light or drift of the light source, the dark measurements are subtracted from the measured reflectance data after which they are normalized relative to the source reference. The DSP board accomplishes this prior to when the data are analyzed, displayed and stored on the PC.

B. Calibration and Prediction Algorithms

In theory, μ_a and μ'_s may be determined using $R(r)$ data from only two of the six detector distances of the fiber probe. A multiple polynomial regression (MPR) was applied to create a calibration model and subsequently extract μ_a and μ'_s from $R(r)$ measurements at $r_1 = 0.6$ mm and at $r_2 = 7.8$ mm. The properties $R(r)$ at r_1 and at r_2 were measured for a set of calibration samples with well-defined optical properties. These were then fitted to double polynomials using least-squares regression. The next step was to solve the inverse problem of determining μ_a and μ_s' from $R(r)$ measurements on a set of prediction samples. This was done using a two-dimensional Newton-Raphson algorithm. Due to the unknown numerical apertures of the fiber probe light source and detectors, the system was calibrated directly on a set of phantoms instead of using a mathematical light propagation model. The phantoms consisted of well-defined aqueous solutions of Intralipid and black ink. The scattering and absorption spectra were determined from integrating-sphere and traditional transmission spectroscopy measurements. The range of optical properties used in the calibration phantoms was for μ_a, 0 – 0.32 cm^{-1}, and for μ'_s, 6.1 – 16.3 cm^{-1}.

3. Time-resolved System

A. Set-up for Time-resolved Measurements

A passively mode-locked Ti:Sapphire laser (Mira 900, Coherent, Santa Clara, CA) pumped by a frequency-doubled Nd:YAG-laser (Millennia, Spectra Physics, Mountain View, CA) was used as a light source. This laser system provided 150-fs light pulses with a wavelength of 785 nm at a repetition rate of 76 MHz. The light was brought to the sample by a 600-µm-diameter optical fiber. A similar fiber was used to collect the diffusely reflected light at a distance of 1.4 cm and guide it to the detector, a microchannel plate photomultiplier tube (R2566U-07, Hamamatsu Photonics K.K., Japan). A time-correlated single-photon counting technique[26] was employed to record the time-dispersion curves. The overall temporal response function of the system was approximately 60 ps (full width half maximum).

B. Data Evaluation

The absorption and transport scattering coefficients were assessed through fitting the solution of the diffusion equation for a semi-infinite homogenous medium with an extrapolated boundary[27] to the measured data. The diffusion coefficient, D, was assumed to be independent of the absorption of the medium, *i.e.*, $D = 1/3\mu'_s$.[28] The theoretical curve was convoluted with the instrumental transfer function, as measured with the source and detector fiber facing each other. The resulting curve was fitted to the data over a range, starting at 10% of the maximum intensity on the rising edge and ending at 1% on the tail. The best fit was reached with a Levenberg-Marquardt algorithm[29] by varying μ_a, μ'_s, and a free time-shift, t_0, in order to minimize the reduced χ^2.

4. Integrating Sphere System

A. Optical Set-up

The integrating sphere set-up was similar to the one used in Ref. [7], except that an external cavity diode laser (SDL Inc., San Jose, CA), operating at 785 nm, was used as the light source. The sphere (Oriel Corp., Stratford, CT) allows detection of the total transmittance T and the total reflectance R from a sample placed at either the entrance or exit port. The light was modulated with a mechanical chopper, then guided to the sphere using a 600 μm-diameter fiber, and collimated using a lens and a pair of apertures. A photodiode connected to a lock-in amplifier (SR-830, Stanford Research Systems, CA) was used for detection. The collimated transmittance was measured in a separate set-up, where a series of co-linear apertures served to suppress the scattered light so that only the non-scattered light was detected by the photodiode. Attenuation filters were used to increase the dynamic range of this measurement, which yielded the transport attenuation coefficient $\mu_t = \mu_a + \mu_s$ from Beer-Lambert's law. The Intralipid suspensions were poured into 1 mm thick cuvettes made from microscope slides. The meat samples were cut into 1 mm thick slices and placed between microscope slides with pieces of slides used as spacers, and then clamped together.

B. Determination of Optical Properties

The optical properties were extracted from the measured values R, T and μ_t using a multiple polynomial regression method based on Monte Carlo simulations,[30] in principle similar to the method used for the fiber probe system. A pre-computed database of R and T spanning the expected range of optical properties was fitted to a polynomial model. The properties μ_a, μ_s and g were extracted from the model using a Newton-Raphson algorithm. Unlike the method described in Ref. [30], where a fixed value of g was used, three-dimensional rather than two-dimensional polynomials were used in the regression. Due to the limited size of the ports of the integrating sphere, there were light losses at the outer parts of the sample. This effect was incorporated in the Monte Carlo simulations, since otherwise the losses would lead to an overestimation of the absorption properties.[31] In principle, it would be sufficient to measure the port diameters and the diameter of the light beam and use this data as input for the Monte Carlo simulations. In practice, however, simulations showed that an error in these parameters of only one millimeter corresponded to a one percent error in the T or R values, and it was practically difficult to measure the beam diameter to such an accuracy. Very accurate values of T and R are necessary to be able to extract μ_a in low-absorbing samples, since the inverse model is then ill-conditioned. For this reason, the measured diameters were only used as a first approximation in the Monte Carlo simulations. Measurements of T and R on an Intralipid sample with known absorption properties were then performed. The extracted values of μ_s and g were used as input for the Monte Carlo program, and the input entrance and exit diameters were changed in steps of 0.1 mm until the simulated values corresponded to the measured values. The resulting values of the diameters were then used for the entire database computation.

5. Test Samples

A. Intralipid Phantoms

Twenty-five phantoms were prepared from Intralipid 200 mg/ml (20%) (Pharmacia & Upjohn Sverige AB, Stockholm, Sweden) and the dye Nigrosin (Sigma, St. Louis, MO), at five different concentrations of each. Expected reduced scattering coefficients were calculated according to van Staveren *et al.*[32] At 785 nm, this results in an anisotropy factor $g = 0.645$, and a scattering coefficient $\mu_s = 0.286$ ml^{-1} l cm^{-1}, where (ml^{-1} l)$^{-1}$ should be read as milliliter Intralipid-10% per liter total diluted suspension. These values are valid for concentrations up to 100 ml Intralipid-10% per liter.[32] The phantoms were prepared so that μ'_s would be 6.0, 8.5, 11.0, 13.5, and 16.0 cm^{-1}, corresponding to 59 – 157 ml l^{-1}. Three of the phantoms were thus outside of the range of the valid numbers of the scattering coefficient, so we did not necessarily expect to find exactly the values of μ'_s quoted above in the measurements. A stock solution of Nigrosin was prepared and diluted to different concentrations in the various phantoms. The absorbance of the stock solution was measured in the collimated transmittance arrangement at the integrating sphere set-up. The absorption coefficients due to the dye in the phantoms were 0.024, 0.048, 0.095, 0.19, and 0.38 cm^{-1}. The water absorption at 785 nm is 0.022 cm^{-1}, which should be added to these values when the dye is in an aqueous solution.[33] Provided that the absorption of the lipid particles in the Intralipid is negligible, this is the absorption we would expect from the measurements. The Intralipid and Nigrosin were diluted to their proper concentrations with phosphate buffered saline (PBS) to prevent possible acidity of the dye to affect the Intralipid. For each phantom, a total of 450 ml solution was prepared.

B. Tissue Samples

Bone-free pork chops and chicken breasts were purchased at the local supermarket on the same day as the measurements, and were kept wrapped in plastic in room temperature for 1 – 2 hours. The pork meat was cut in ~4-cm-thick slices and the measurements commenced immediately on the freshly cut side. The chicken breasts were arranged in a stack, and the muscle membrane of the upper one was removed with a sharp knife, leaving a flat surface exposed to perform the measurement on.

When the measurements with the spatially and temporally resolved systems were finished, pieces of the meat were cut out for the integrating-sphere measurements.

C. C. In Vivo Measurements

Measurements were also performed on the inside of the forearm of two of the experimenters. The procedure was otherwise identical to the measurements of the *in vitro* samples. However, the intensity of the Ti:Sapphire laser was reduced to 10 mW average power after the source fiber, to assure a safe level.

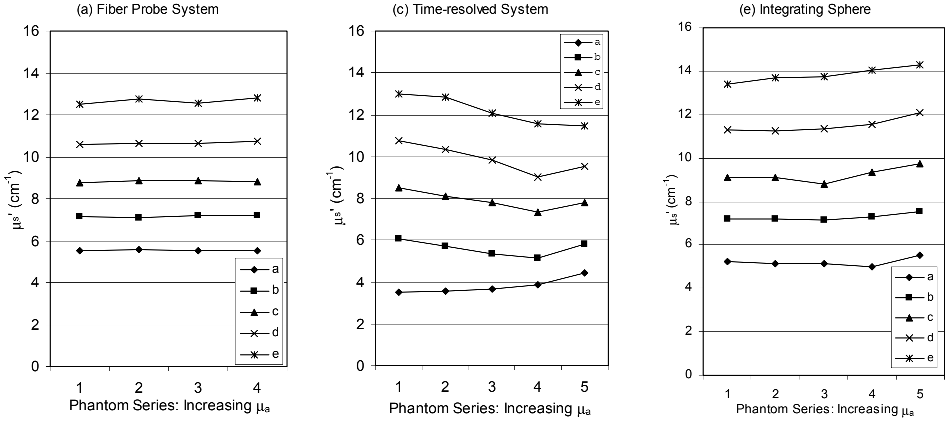

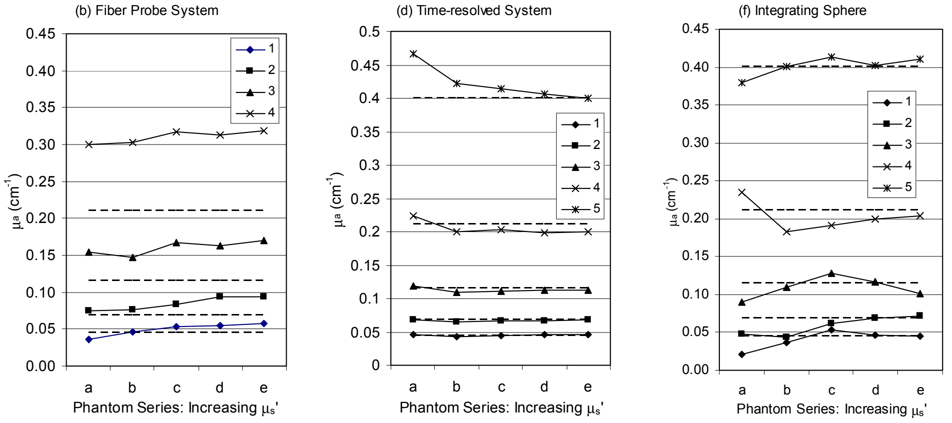

Figure 1. The values of μ'_s and μ_a of the Intralipid phantoms, as determined by the three different systems. The dashed lines show the expected values of μ_a. The theoretical values of μ'_s are not shown, because they did not correspond well to the measurements. (a), (b) show μ'_s and μ_a from the fiber probe system; (c), (d) the time-resolved system; (e), (f) the integrating sphere system.

6. Results

A. Intralipid Phantoms

Figures 1(a) – (f) shows the values of μ'_s and μ_a obtained from the different systems, together with the expected values for μ_a.

The fiber probe system was not calibrated above $\mu_a = 0.32\ \mathrm{cm}^{-1}$. Thus, no data are available for the five samples with the highest concentration of the dye. The absorption coefficients measured with this system [Figure 1(b)] are about 40% higher than the predicted values. The time-resolved system yielded absorption coefficients very close to the expected values for the low-absorption phantoms [Figure 1(d)], but there is an apparent overestimation of μ_a in the phantoms with low scattering and high absorption. This is not surprising as the diffusion equation loses some validity under those conditions. The values of μ'_s are generally lower than predicted [Figure 1(c)], but comparable to those obtained by the fiber probe system, although there appear to be artifacts due to varying absorption. The correspondence is worse for the phantoms with low scattering and those with high absorption. Furthermore, μ'_s seems to be overestimated in the phantoms with the highest absorption. This is consistent with the integrating-sphere measurements, which is an indication that the Intralipid was in some way affected by the addition of the Nigrosin, and thus that it is a real effect rather than an inverse-model artifact.

The integrating-sphere measurements yielded values of μ'_s within 10% of those obtained by the fiber probe system [Figure 1(e)], while the correspondence with the time-resolved system was worse for the low-scattering phantoms/high-absorption phantoms, differences ranging from 5% up to 30% for the low-scattering phantoms. Looking at the values of μ_s and g (see Figure 2), from which μ'_s is calculated, it seems evident that the scattering properties of the Intralipid were strongly affected by the addition of the Nigrosin. This is despite the fact that Nigrosin was chosen as the absorber because it was thought to be a relatively inert dye. This effect is of no serious concern, since the purpose of the investigation was to compare the different systems, and not to test them against calibrated phantoms.

The values of μ_a correspond fairly well to the predicted values [Figure 1(f)], but the errors are larger than for the time-resolved measurements. The primary reason for this is that extracting μ_a in samples with very low absorption using the integrating sphere technique is an ill-conditioned inverse problem.

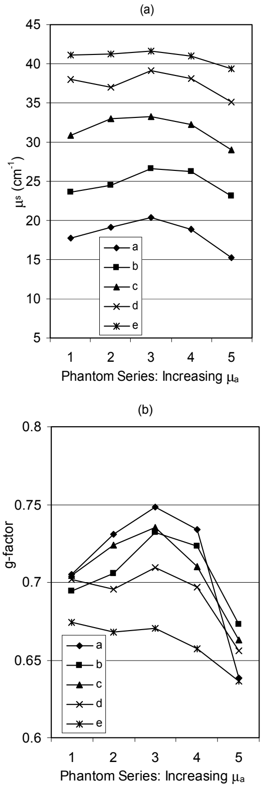

Figure 2. Integrating-sphere results for the Intralipid phantoms: (a) the scattering coefficient, μ_s; (b) the scattering anisotropy factor, g.

B. Tissue Samples

For the fiber probe system, unfortunately all tissue samples were outside the calibration range. It had been designed to be used primarily for clinical skin-contact measurements, where the scattering coefficients are higher than the muscle tissue used in this investigation. The results obtained by the other two systems are presented in Table 1.

Table 1. The optical properties of the pork and chicken samples from the FTIIS, the time resolved and the integrating sphere systems.

	Time-resolved		Integrating Sphere			
Sample	μ'_s (cm^{-1})	μ_a (cm^{-1})	μ'_s (cm^{-1})	μ_s (cm^{-1})	g	μ_a (cm^{-1})
Pork #1	1.8	0.07	2.4	62	0.96	0.39
Pork #2	2.4	0.07	4.7	81	0.94	0.22
Pork #3	1.6	0.04	3.0	69	0.96	0.14
Chicken	1.8	0.08	1.5	49	0.97	0.09

C. In Vivo Measurements

Although *in vivo* measurements of the skin surface present an inhomogeneous sampling volume, while all measurements were evaluated with the assumption of homogeneity, the systems were tested on the forearms of two of the experimenters. The results are presented in Table 2.

Table 2. The optical properties obtained from *in vivo* measurements on the inside of the forearm of two volunteers, from the fiber probe system, the FTIIS and the time-resolved system.

	Fiber Probe		Time-resolved	
Person	μ'_s (cm^{-1})	μ_a (cm^{-1})	μ'_s (cm^{-1})	μ_a (cm^{-1})
#1	10.6	0.31	2.5	0.20
#2	11.8	0.31	5.0	0.20

7. Discussion

Starting with the measurements on the Intralipid phantoms, the predicted absorption coefficients, based on the measurements of the stock solution of the dye, were regarded as representing the most correct values. For the reduced scattering coefficients, the predicted values were mistrusted for several reasons. Firstly, it is not clear whether the composition of the Intralipid could be regarded to be identical to the one used by van Staveren *et al.* in 1991.[32] Possible causes for different scattering characteristics are the use of 20% Intralipid rather than 10%, changes in the production conditions of the Intralipid, variations in the raw materials used, etc. One has to keep in mind that Intralipid is intended to be used for intravenous nutrition and not light-propagation experiments. Secondly, the integrating-sphere results showed that the addition of the dye probably altered the composition of the scattering lipid particles. Thirdly, three of the concentrations were higher than the range where the formula given by van Staveren *et al.* was valid, and the other two were close to the limit. For these reasons, the integrating-sphere results for μ'_s were regarded as representing the most true values. The integrating-sphere method has a proven record of producing accurate values for the scattering coefficient, verified by tests on polystyrene micro-spheres in water suspensions, where the scattering can be calculated exactly using Mie theory.[30] The method used to extract the optical properties, the MPR method based on Monte Carlo simulations, was also regarded to be state-of-the-art in terms of inverse algorithms for integrating-sphere measurements. The apparent change in scattering characteristics after addition of the dye was unfortunate, but did not compromise the investigation since the main objective was to compare the systems on identical samples.

It is worthwhile noting that even though both μ_s and g varied strongly with the dye concentration (see Figure 2), these variations almost cancelled out when combined in μ'_s. It seems that μ'_s was largely determined by the mass concentration of scatterers, rather than the exact composition of the particle sizes. The absorption coefficients extracted by the integrating-sphere method had larger errors, but this was expected since the evaluation of μ_a is ill-conditioned when μ_a is low. Monte Carlo simulations showed that the difference between no dye and the lowest concentration of dye corresponds to less than one percent difference in the measurement of R or T, and thus the evaluation is susceptible to measurement noise. The time-resolved method, on the other hand, produced very accurate values of μ_a for the low-absorption phantoms. The fiber probe system overestimated the absorption by about 40%, for which there may be two explanations. Either, there was a systematic error in the calibration standards when the system was calibrated. Or, the system needed re-calibrating, possibly because of wear or a thin layer of dirt accumulating on the probe head. The latter of these explanations was regarded as the most plausible. As for the scattering, the fiber probe system yielded values of μ'_s within 10% of the integrating-sphere results, usually in the 1-7% range. This is not surprising, given that the calibration standards were measured using an integrating-sphere system. The scattering results from the time-resolved system present a more complex case. The determination of μ'_s was somewhat sensitive to assumptions made in the fitting process. The best fit, in terms of the lowest value of χ^2, was achieved by allowing the starting time, t_0, of the time dispersion curve to be a fitting parameter, together with μ'_s and μ_a. However, this seems unphysical when the actual value of t_0 is known from the reference pulse in the measurement. The values of μ'_s obtained this way also seems to be underestimated by about 20-30% compared with the integrating-sphere results. These results are a bit surprising as Cubeddu *et al.* presented absolute errors in both μ_a and μ'_s less than 10% under similar conditions.[34] Since it is known that the diffusion approximation is less accurate for early times, Cubeddu *et al.* used the 80% point of the rising flank of the curve as the starting point of the fitting, and the 1% point of the trailing flank as the end point. Using this approach on our data, however, resulted in larger deviations in both μ_a and μ'_s.

In the case of the tissue samples, there is less motivation for regarding the integrating-sphere results as the "golden standard." Although the method is just as accurate, the probing volume is smaller than for the diffuse reflectance systems, which allows for small inhomogeneities in the tissue that are averaged out in the other systems to yield different values of the optical properties. Also, there is a concern that the somewhat brutal preparation of the samples may affect the optical properties.

As has been pointed out, the sampling volume in the *in vivo* measurements is inhomogeneous, because the skin and the underlying tissues are a layered structure. This would pose no problem in the comparison of the systems if the probing volume were the same, since the inhomogeneities would average out. This is not the case, however, which is obvious when comparing the measurement geometry of the time-resolved with the spatially resolved system. The 1.4 cm fiber spacing for the time-resolved system means that the detected light will have traveled along a deeper path than the detected light in the spatially resolved system. For that system, the scattering properties are primarily determined from the signal recorded by the innermost detector, *i.e.*, at $r = 0.6$ mm. The photons registered by this detector have penetrated approximately 0.2-0.3 mm, and thus mainly carry information on the uppermost layer of the skin. For the evaluation of the absorption, on the other hand, the outermost detector, *i.e.*, at $r = 7.8$ mm, is of most importance. The light collected at this distance have penetrated further down in the tissue, approximately 2-4 mm. Since the skin and the subcutaneous layer scatter more than the muscle tissue, the spatially resolved systems consequently yielded higher values of μ'_s than the time-resolved (Table 2).

The *in vivo* measurements were included in this work to illustrate the performance of the systems in a realistic measurement situation. The discrepancies of the results point to one important observation, that quantitative measurements of the optical properties are often impossible to perform using the assumption of homogeneous tissue. Only when a homogeneous material for certain can approximate the tissue, such measurements are useful. In other cases, either relative measurements, which may be system dependent, will have to suffice, or one has to utilize more sophisticated inverse models based on assumptions of inhomogeneous tissue.

The authors wish to thank Dr. Antonio Pifferi (Department of Physics, Politecnico di Milano, Milan, Italy) for the software used for the evaluation data recorded by the time-resolved system.

References

1. M. Sinaasappel and H. J. C. M. Sterenborg, "Quantification of the hematoporphyrin derivative by fluorescence measurement using dual-wavelength excitation and dual-wavelength detection," Appl. Opt. **32,** 541-548 (1993).
2. G. A. Wagnières, W. M. Star, and B. C. Wilson, "*In vivo* fluorescence spectroscopy and imaging for oncological applications," Photochem. Photobiol. **68,** 603-632 (1998).
3. G. J. Müller and A. Roggan, eds., "Laser-Induced Interstitial Thermotherapy," (SPIE Press, Bellingham, WA, 1995).
4. J. A. S. Brookes, W. R. Lees, and S. G. Bown, "Interstitial laser photocoagulation for the treatment of lung cancer," Am. J. Rad. **168,** 357-358 (1997).
5. K. Ivarsson, J. Olsrud, C. Sturesson, P. H. Möller, B. R. Persson, and K.-G. Tranberg, "Feedback interstitial diode laser (805 nm) thermotherapy system: ex vivo evaluation and mathematical modeling with one and four-fibers," Lasers Surg. Med. **22,** 86-96 (1998).
6. B. C. Wilson, P. J. Muller, and J. C. Yanch, "Instrumentation and light dosimetry for intra-operative photodynamic therapy (PDT) of malignant brain tumours," Phys. Med. Biol. **31,** 125-133 (1986).
7. A. M. K. Nilsson, R. Berg, and S. Andersson-Engels, "Measurements of the optical properties of tissue in conjunction with photodynamic therapy," Appl. Opt. **34,** 4609-4619 (1995).
8. T. H. Pham, F. Bevilacqua, T. Spott, J. S. Dam, B. J. Tromberg, and S. Andersson-Engels, "Quantifying the absorption and reduced scattering coefficients of tissue-like turbid media over a broad spectral range using a non-contact Fourier interferometric, hyperspectral imaging system," Appl. Opt. (2000). In press.
9. J. S. Dam, C. B. Pedersen, T. Dalgaard, P. E. Fabricius, P. Aruna, and S. Andersson-Engels, "Fiber optic probe for non-invasive real-time determination of tissue optical properties at multiple wavelengths," (2000). Manuscript.
10. S. L. Jacques, A. Gutsche, J. Schwartz, L. Wang, and F. Tittel, "Video reflectometry to specify optical properties of tissue *in vivo*," in *Medical Optical Tomography: Functional Imaging and Monitoring,* G. J. Müller, B. Chance, R. R. Alfano, S. R. Arridge, J. Beuthan, E. Gratton, M. Kaschke, B. R. Masters, S. Svanberg, and P. van der Zee 211-226 (1993).

11. T. J. Farrell, M. S. Patterson, and B. Wilson, "A diffusion theory model of spatially resolved, steady-state diffuse reflectance for noninvasive determination of tissue optical properties *in vivo*," Med. Phys. **19,** 879-888 (1992).

12. A. Kienle, L. Lilge, M. S. Patterson, R. Hibst, R. Steiner, and B. C. Wilson, "Spatially resolved absolute diffuse reflectance measurements for noninvasive determination of the optical scattering and absorption coefficients of biological tissue," Appl. Opt. **35,** 2304-2314 (1996).

13. R. M. P. Doornbos, R. Lang, M. C. Aalders, F. W. Cross, and H. J. C. M. Sterenborg, "The determination of *in vivo* human tissue optical properties and absolute chromophore concentrations using spatially resolved steady state diffuse reflectance spectroscopy," Phys. Med. Biol. **44,** 967-981 (1999).

14. R. Bays, G. Wagnières, D. Robert, D. Braichotte, J. F. Savary, P. Monnier, and H. van den Bergh, "Clinical determination of tissue optical properties by endoscopic spatially resolved reflectometry," Appl. Opt. **35,** 1756-1766 (1996).

15. S. Andersson-Engels, R. Berg, and S. Svanberg, "Effects of optical constants on time-gated transillumination of tissue and tissue-like media," J. Photochem. Photobiol. B **16,** 155-167 (1992).

16. K. Suzuki, Y. Yamashita, K. Ohta, and B. Chance, "Quantitative measurement of optical parameters in the breast using time-resolved spectroscopy. Phantom and preliminary in vivo results," Invest. Radiol. **29,** 410-414 (1994).

17. S. L. Jacques, "Time-resolved reflectance spectroscopy in turbid tissues," IEEE Trans. Biomed. Eng. **36,** 1155-1161 (1989).

18. S. J. Madsen, B. C. Wilson, M. S. Patterson, Y. D. Park, S. L. Jacques, and Y. Hefetz, "Experimental tests of a simple diffusion model for the estimation of scattering and absorption coefficients of turbid media from time-resolved diffuse reflectance measure," Appl. Opt. **31,** 3509-3517 (1992).

19. J. Kölzer, G. Mitic, J. Otto, and W. Zinth, "Measurements of the optical properties of breast tissue using time-resolved transillumination," in *Photon Transport in Highly Scattering Tissue,* S. Avrillier, B. Chance, G. J. Müller, A. V. Priezzhev, and V. V. Tuchin (Soc. Photo-Opt. Instrum. Eng., Bellingham, WA, 1995), pp. 143-152.

20. R. Cubeddu, M. Musolino, A. Pifferi, P. Taroni, and G. Valentini, "Time resolved reflectance: a systematic study for the application to the optical characterization of tissue," IEEE J. Quant. Electr. **30,** 2421-2430 (1994).

21. X. Liang, L. Wang, P. P. Ho, and R. R. Alfano, "True scattering coefficients of turbid media," in *Optical Tomography, Photon Migration and Spectroscopy of Tissue and Model Media: Theory, Human Studies, and Instrumentation,* B. Chance and R. R. Alfano (Soc. Photo-Opt. Instrum. Eng., Bellingham, WA, 1995), pp. 571-574.

22. M. Ferrari, Q. Wei, L. Carraresi, R. A. De Blasi, and G. Zaccanti, "Time-resolved spectroscopy of the human forearm," J. Photochem. Photobiol. B **16,** 141-153 (1992).

23. J. W. Pickering, S. A. Prahl, N. van Wieringen, J. F. Beek, H. J. C. M. Sterenborg, and M. J. C. van Gemert, "Double-integrating-sphere system for measuring the optical properties of tissue," Appl. Opt. **32,** 399-410 (1993).

24. A. Roggan, H. Albrecht, K. Dörschel, O. Minet, and G. J. Müller, "Experimental set-up and Monte-Carlo model for the determination of optical tissue properties in the wavelength range 330-1100 nm," in *Laser interaction with hard and soft tissue II,* H. J. Albrecht, G. P. Delacretaz, T. H. Meier, R. W. Steiner, L. O. Svaasand, and M. J. van Gemert (Soc. Photo-Opt. Instrum. Eng., Bellingham, WA, 1995), pp. 21-46.

25. A. M. K. Nilsson, C. Sturesson, D. L. Liu, and S. Andersson-Engels, "Changes in spectral shape of tissue optical properties in conjunction with laser-induced thermotherapy," Appl. Opt. **37,** 1256-1267 (1998).

26. S. Andersson-Engels, R. Berg, O. Jarlman, and S. Svanberg, "Time-resolved transillumination for medical diagnostics," Opt. Lett. **15,** 1179-1181 (1990).

27. R. C. Haskell, L. O. Svaasand, T.-T. Tsay, T.-C. Feng, M. S. McAdams, and B. J. Tromberg, "Boundary conditions for the diffusion equation in radiative transfer," J. Opt. Soc. Am. A **11,** 2727-2741 (1994).

28. K. Furutsu and Y. Yamada, "Diffusion approximation for a dissipative random medium and the applications," Phys. Rev. E **50,** 3634-3640 (1994).

29. W. H. Press, S. A. Teukolsky, W. T. Vetterling, and B. P. Flannery, "Numerical recipes in C: The art of scientific computing," (Cambridge University Press, New York, 1992).

30. J. S. Dam, T. Dalgaard, P. E. Fabricius, and S. Andersson-Engels, "Multiple polynomial regression method for determination of

biomedical optical properties from integrating sphere measurements," Appl. Opt. **39,** 1202-1209 (2000).

31. G. de Vries, J. F. Beek, G. W. Lucassen, and M. J. C. van Gemert, "The effect of light losses in double integrating spheres on optical properties estimation," IEEE Journal of Selected Topics in Quantum Electronics **5,** 944-947 (1999).
32. H. J. van Staveren, C. J. M. Moes, J. van Marle, S. A. Prahl, and M. J. C. van Gemert, "Light scattering in Intralipid-10 % in the wavelength range of 400-1100 nm," Appl. Opt. **30,** 4507-4514 (1991).
33. G. M. Hale and M. R. Querry, "Optical constants of water in the 200-nm to 200-µm wavelength region," Appl. Opt. **12,** 555-563 (1973).
34. R. Cubeddu, A. Pifferi, P. Taroni, A. Torricelli, and G. Valentini, "Experimental test of theoretical models for time-resolved reflectance," Med. Phys. **23,** 1625-1633 (1996).